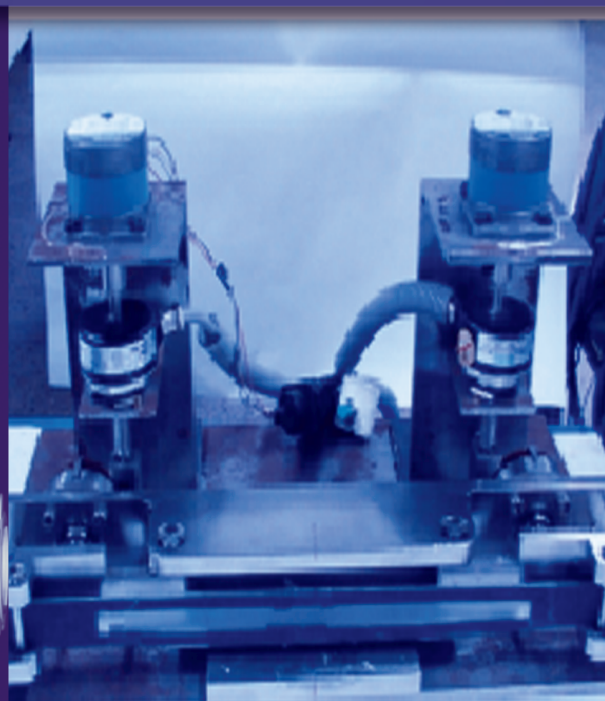
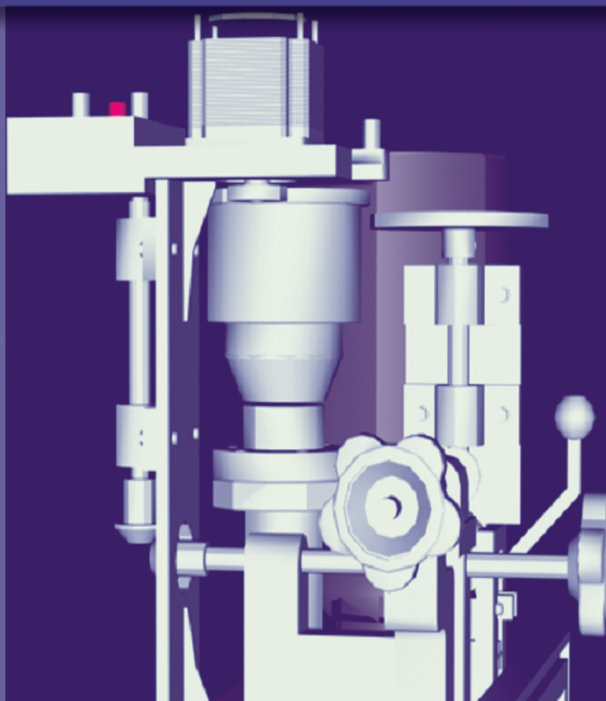


# BARC

## HIGHLIGHTS



PHYSICAL  
SCIENCES

**BARC**  
HIGHLIGHTS

**PHYSICAL  
SCIENCES**



भारत सरकार  
Government of India

**भाभा परमाणु अनुसंधान केंद्र  
BHABHA ATOMIC RESEARCH CENTRE**

स्वर्ण जयंती वर्ष  
GOLDEN JUBILEE YEAR  
2006-2007

For further details contact:

**Dr. J. V. Yakhmi**

Associate Director, Physics Group,  
Bhabha Atomic Research Centre, Trombay, Mumbai - 400 085, India.

E mail: [yakhmi@barc.gov.in](mailto:yakhmi@barc.gov.in)

Published by :

**Dr. Vijai kumar**

Associate Director, Knowledge Management Group and  
Head, Scientific Information Resource Division,  
Bhabha Atomic Research Centre, Trombay, Mumbai - 400 085, India.

E mail: [vijai@barc.gov.in](mailto:vijai@barc.gov.in)

## FOREWORD

Bhabha Atomic Research Centre (BARC) is celebrating its golden jubilee year during 2006-07. On 20<sup>th</sup> January, 1956, Pandit Jawaharlal Nehru formally inaugurated the Atomic Energy Establishment Trombay (AEET), which was renamed as Bhabha Atomic Research Centre (BARC) on January 22, 1967. As a premier R & D centre of the Department of Atomic Energy (DAE), BARC has a mandate to provide R & D support to the nuclear power programme, to pursue all activities related to nuclear fuel cycle, to operate research reactors for supporting neutron beam research and supplying radioisotopes for various applications, to conduct frontline basic research in physical, chemical, biological and engineering sciences all of which leading towards improving the quality of life of our people. The achievements BARC has made over the last 50 years are well known not only to the scientific community in the country but also to our people at large. Scientific achievements made by this premier research centre are well documented in various publications of DAE including the series "BARC Highlights". During this golden jubilee year, we have made an effort to bring out some glimpses of recent research and development accomplishments in the form of 8 volumes, highlighting the following areas:

1. Nuclear Fuel Cycle
2. Physical Sciences
3. Chemical Science and Engineering
4. Materials Science and Engineering
5. Life Sciences
6. Reactor Technology and Engineering
7. Electronics, Instrumentation and Computers
8. Environmental Science and Engineering

These volumes will showcase the latest work in the aforementioned areas and will demonstrate how each of these is directed towards achieving the overall goal of using nuclear energy for the benefit of our people.

Nuclear energy programme in India has now reached a level of maturity. Today, India is self-sufficient in building nuclear power stations of 540 MWe capacities and has gained mastery over the entire fuel cycle. We are at the threshold of entering the second stage of nuclear power programme, in which a rapid growth in installed capacity is expected through the fast reactor programme. In the area of basic research in science and engineering, BARC has been maintaining a lead position both in national and international scenario. One of the strongest points of basic research in BARC lies in its capability in building sophisticated research facilities in-house. The core competence of the scientists and engineers in our centre covers a very wide range as is reflected in the 8 companion volumes getting released on the occasion of the golden jubilee year.

Nuclear Physics research is focussed on nuclear collisions at high energies and formation of hot and dense nuclear matter, study of nuclei with large spins and deformations and underlying symmetries and investigation of nuclei away from the line of stability and formation of super-heavy nuclei. The experimental programmes have been pursued at the Pelletron accelerator facilities at Mumbai and Delhi. Current research in astronomy and astrophysics are directed towards gaining an in-sight into the non-thermal processes in the Universe and also to understand the sources of high energy cosmic radiation and the processes which enable charged particles to be accelerated to energies of upto 1020 eV and beyond. Research activities in the emerging areas in atomic and molecular spectroscopy include cluster physics using supersonic molecular beam, laser spectroscopy, spectroscopy of trapped ions, single molecule spectroscopy, mass spectrometry of bio-molecules and spectroscopy of quantum solids. R & D efforts in the development of specialized optical components, devices, data acquisition and control system and instruments were also continued.

Significant contributions have been made in the development of various beamlines on synchrotron radiation sources at Raja Ramanna Center for Advanced Technology, Indore. Recently, three beamlines namely, the High Resolution Vacuum Ultra Violet (HRVUV), Photo Physics (PP), Angle Resolved Photo Electron Spectroscopy (ARPES) were established at synchrotron sources at Indus-I. The Angle

Resolved Photoelectron Spectroscopy (ARPES) beamline has been used to study photo-emission spectroscopy for probing electronic states in atoms, molecules and solid surfaces and High resolution VUV beamline, has been employed in high resolution studies in the range 700–2000 Å. The Photoabsorption Spectroscopy Study beamline is under installation and will be used for near-to-absorption edge (17–225 Å) spectrum analysis in terms of local electronic structure. Photo Electron Spectroscopy (PES) beamline will use X-rays in the energy range from 0.8 keV to 15 keV. The heart of the beamline is an indigenously developed double crystal monochromator.

BARC has developed multi-channel Raman spectrometer for analysis of microparticles, scanning monochromator for isotopic analysis and electron spectrometers meet some of the increasing demands for improved analysis of materials. An optical periscope has been specially designed for video recording of objects with a resolution of 0.7 mm in the core of Fast Breeder Test Reactor. A notable development were the room temperature operating sensors based on Te and conducting polymer thin films. BARC has made significant contributions to the development of mass spectrometric techniques in nuclear areas and has expertise in areas like HV/UHV technology, precision mechanical engineering and fabrication, magnet technology, ion optics, sensitive and stable analog and digital electronics, data systems that are important to develop sophisticated mass spectrometers such as Isotopic Ratio Mass Spectrometers (IRMS), Inductively Coupled Plasma source Mass Spectrometer (ICPMS), Quadrupole Mass Spectrometer (QMS) and double focusing mass spectrometer.

New radiation detectors and imaging systems such as X-ray diffraction, tomography, EXFAS, X-ray holography are developed at BARC for nuclear, defence and space technology applications. BARC continues research in advanced functional materials for nuclear reactors, synchrotron sources, lasers and other applications. Cylinders of high temperature superconductors have been fabricated for application in superconducting motors. Thin films and multilayer coatings have been prepared for laser resonators, optical components for synchrotrons and analytical instruments. Single crystals, glasses and glass-ceramics for nuclear particle detectors, lasers, hermetic seals and vacuum components are routinely prepared and fundamental studies on superconducting and colossal magnetoresistive materials have been carried out.

In the area of electron beam technology, with a view of its wide ranging industrial applications for radiation processing like modification of bulk polymers, cross linking of plastic films, foam and cables, sterilization of medical products and food preservation, BARC has developed 500 keV to 10 MeV particle energy and 10 to 30 kW beam power Electron accelerators (DC and RF) and a 10 MeV RF *linac*. Gigawatt single and multi-pulse systems in strategic applications for high power microwave generation and pulsed high magnetic fields for EM welding of metal to ceramic joints are other accomplishments. Shock wave studies using ultra short lasers, development of tunable dye lasers, laser cooling of atoms in traps in 100 micro Kelvin and laser produced plasmas by resonant ionization are some of the areas intensely pursued in BARC. Besides, development of laser-based instrumentation for applications in nuclear fuel cycle and plasma torches with long lives are the other highlights in this area.

In this volume accomplishments of the last few years in the front line areas of physical sciences have been discussed.

Srikumar Banerjee  
Director

## PREFACE

Fundamental research in different branches of Physics, such as condensed matter, lasers, accelerators, neutron scattering, protein crystallography, high pressure physics and nuclear physics employing sophisticated techniques is carried out with zeal at BARC. Simultaneously, there have been consistent attempts to apply the expertise gained towards indigenous development of high-tech instruments/systems and processing of new functional materials and fabrication of devices. Notable accomplishments include the development of particle accelerators, high power gas-gun, radiation detection and imaging systems, high power fast lasers, high-resolution mass spectrometers, neutron diffractometers, beamlines on synchrotron radiation sources Indus-1 and Indus-2. State-of-the-art facilities and expertise have been developed to prepare/process and characterize different materials such as ceramics, glasses, oxide semiconductors, high-  $T_c$  superconductor, etc. in the form of polycrystalline bulk, multilayer thin films and single crystals for basic as well as applied research and for device applications. The Centre also has a strong base to carry out theoretical studies and simulation work in basic as well as applied physics.

This volume of Highlights provides a summary of some of the activities in many areas of research and development in Physics at BARC, conducted during recent years. Physics-based activity is spread over many Divisions/Sections of BARC. The account of work presented here is by no means complete but only representative of the current activities. These activities are briefly described in fourteen sections. References to only a few representative publications are made at the end of each write-up so as to provide information about the contact persons to enable the prospective readers easy access to further details of the work. The write-ups have been kept brief to convey the essence of the activity and it is hoped that the contents will be useful to readers. It may also be mentioned here that the present volume primarily covers the basic research aspects of Physics-based programmes at BARC and technological spin-offs have been presented in related parallel volumes of the current series.

J.V. Yakhmi



P H Y S I C A L   S C I E N C E S

# CONTENTS

## **FOREWORD**

## **PREFACE**

<b>PARTICLE ACCELERATORS AND RELATED ACTIVITIES</b>	<b>1</b>
1.1 500 KeV, 10KW industrial DC electron accelerator for material processing	2
1.2 20 MeV, 10 KW industrial RF electron Linac for material processing	3
1.3 3 MeV, 30 KW industrial DC electron accelerator for material processing	4
1.4 Development of a GW pulsed electron accelerators and their applications	5
1.5 Repetitively pulsed linear induction accelerator	5
1.6 Generation & application of pulsed high magnetic fields	6
1.7 Development of high current proton ECR source	7
1.8 Electron beam RF Linac for cargo inspection	8
1.9 Superconducting RF cavity development for particle accelerators	9
1.10 Utilization of 14-MeV neutron generator to study the neutronic behaviour of an accelerator driven sub-critical assembly	10
<b>2. STUDIES IN HIGH PRESSURE PHYSICS</b>	<b>13</b>
2.1 Experimental condensed matter physics:material behaviour under high pressure	14
2.2. Shock-wave physics related activities	19
2.3 Pulsed high energy density related activities.	22
2.4 Mechanical resilience of Single-Walled Carbon Nanotubes (SWNTs)	26
2.5 Structural and magnetic behaviour on Fe-filled Multi-Walled carbon Nanotubes (MWNTs)	27
2.6 Irreversible amorphization of negative thermal expansion materials	27
2.7 Structural changes in cristobalite- $\text{AlPO}_4$ under high pressures	28

2.8	Scheelite structured compounds	29
2.9	Molecular solids under high pressures	30
2.10	Development of high pressure optical absorption set-up: study on red-HgI <sub>2</sub>	31
<b>3.</b>	<b>RADIATION DETECTION AND IMAGING</b>	<b>33</b>
3.1	Radiation Imaging:Advanced imaging with X-rays and neutrons	34
3.2	Neutron measurements using SSNTD technique during PFBR & AHWR shielding experiments	36
3.3	Standards and calibration	37
3.4	Measurement and simulation of fluence and dose build-up at electron storage ring INDUS-1	38
3.5	Depth dose profile measured in water with Victoreen survey meter 450P at front end	38
3.6	Al <sub>2</sub> O <sub>3</sub> based phosphors for radiation detection	39
3.7	Development and fabrication of semiconductor radiation detectors	40
3.8	TLD Badges for personnel monitoring	40
<b>4.</b>	<b>LASERS AND PLASMA RELATED STUDIES</b>	<b>41</b>
4.1	Intense picosecond and femtosecond Nd:glass Lasers to generate multi-megabar shocks and study intense laser matter interaction	42
4.2	Barium photoplasma studies	44
4.3	Novel scheme for spatial filtering of laser beams using saturable absorber	45
4.4	Optical nonlinearity in atomic vapour	46
4.5	Extended tunability of a binary dye-mixture laser	46
4.6	Safe and superior water and heavy water based solvents for laser dyes	47
4.7	Photo-stability of laser dyes:role of stimulated emission	47
4.8	Differential wavelength meter:an improved technique	48
4.9	Optical parametric oscillators	49
4.10	Solid state dye laser.	50
4.11	Development of a Single Longitudinal Mode (SLM) dye oscillator:pre-amplifier system pumped by copper vapor laser	51
4.12	A pre-prototype digital beam profiler for Infrared Lasers	51
4.13	Kinetics of isotope-selective multi-step photoionization for laser spectroscopy and trace analysis	52

4.14	Non-linear dynamic study of arc root dynamics	53
4.15	Thermo-physical properties of thermal plasmas	54
4.16	Computational Fluid Dynamics (CFD) of thermal plasmas	54
4.17	Similarity analysis for plasma torches and jets	55
4.18	Innovative diagnostics:time resolved temperature measurement in a spray plasma jet	56
4.19	Laser cooling of atoms	56
4.20	Laser- based instruments for diameter measurement and rebound velocity measurement	57
4.21	Laser-based instrument for projectile speed measurement	58
4.22	Laser-based instrument for free surface level measurement of liquid metal	58
4.23	CCRF discharge studies and development of a 40 MHz, 5 kW RF power supply for a diffusion cooled slow flow slab type CO <sub>2</sub> laser	59
4.24	Operation of a helium-free TEA CO <sub>2</sub> laser	60
<b>5.</b>	<b>MATERIALS IN DEVICE APPLICATIONS</b>	<b>61</b>
5.1	Laser decontamination and analysis of Zircaloy clad surface	62
5.2	Fabrication of hollow cylinders of high temperature oxide superconductors	62
5.3	Development of multilayer coatings for the resonators of chemical oxygen iodine laser	63
5.4	Achievement of ordered 3D island structures in zirconia films by stabilizing with silica	64
5.5	Engineering morphological control over thin film surface for the development of low-scatter deep ultraviolet coatings	65
5.6	Structure and function of class-B bacterial non-specific acid phosphatase of <i>S typhimurium</i> : Lys154	66
5.7	An ideal tool for roughness characterization: Neutron reflectometry	67
5.8	Study of magnetic nanoparticles	67
5.9	CMR/HTSC thin films and multilayers	68
5.10	Studies on MgB <sub>2</sub> superconductor	69
5.11	Growth of single crystals by Czochralski technique	70
5.12	B <sub>2</sub> O <sub>3</sub> substituted (PbO) <sub>0.5</sub> (SiO <sub>2</sub> ) <sub>0.5</sub> glasses	71
5.13	Structural properties of machineable magnesium alumino-silicate glasses and their glass-ceramics	71
5.14	Interface study of lithium zinc silicate (LZS) glass-ceramics to copper and SS-321 hermetic seals	72
5.15	Some studies on Cs diffusion and corrosion in borosilicate glasses	73

5.16	Order-disorder transition in vortex matter	74
5.17	Magnetic response of superconductors	74
5.18	Magnetic semiconductors	75
<b>6.</b>	<b>CRYSTAL STRUCTURE AND LATTICE DYNAMICS</b>	<b>77</b>
6.1	Metal clusters	78
6.2	Molecular electronics	79
6.3	Coulomb explosion in methyl iodide clusters	79
6.4	Magnetic structures in $\text{La}_{1-x}\text{Ca}_x\text{MnO}_3$ ( $x=0.4, 0.5, 0.6$ )	80
6.5	Structure and interaction in protein solutions as studied by small-angle neutron scattering	81
6.6	Physics of the earth's interior: neutron inelastic scattering lattice dynamics and molecular dynamics simulation	82
6.7	Hydrogen bonding in thiourea: diethyl oxalate complex in 2:1 ratio	83
6.8	Origin of negative thermal expansion in cubic $\text{ZrW}_2\text{O}_8$ , $\text{HfW}_2\text{O}_8$ and $\text{ZrMo}_2\text{O}_8$ as revealed by neutron inelastic scattering at high pressures	84
6.9	Structural and magnetic properties of hexacyanometallate based molecular magnets	85
6.10	Temporal evolution of mesoscopic structure and dynamical scaling of structure factor for some non-Euclidean systems	86
6.11	Dynamics in monolayer protected metal-nano Clusters	87
6.12	Molecular Reorientation in nO.m type Liquid Crystal	88
<b>7.</b>	<b>THEORETICAL STUDIES AND SIMULATIONS</b>	<b>90</b>
7.1	Computational physics - equation of state: Actinides	91
7.2	Shock simulation and molecular dynamics	92
7.3	Non-LTE model for radiation hydrodynamics	93
7.4	Theoretical modeling of transversely pumped pulsed dye lasers	94
7.5	Direct simulation Monte-Carlo development	94
7.6	Electronic relaxation in atomic vapour jets	94
7.7	BEST (Basic Electron-beam Simulation in Three Dimension)	95
7.8	Analysis of dynamical systems	95
7.9	Quantum simulations	
7.10	Classical simulations: Disordered systems (liquid and amorphous)	96
7.11	Nuclear electromagnetic pulse	97
7.12	Hydrodynamic phenomena	98



P H Y S I C A L   S C I E N C E S

7.13	Chaos based cryptography	99
7.14	Neutron-Gamma transport for nuclear science applications	100
7.15	Viracator modelling and simulation	101
7.16	Radiative transfer	102
<b>8.</b>	<b>ASTRONOMY AND ASTROPHYSICS</b>	<b>104</b>
8.1	VHE astronomy and astrophysics	105
8.2	GeV astronomy and astrophysics	105
8.3	Low energy cosmic ray neutron monitor	106
8.4	Theoretical astrophysics	106
8.5	Scattering of cosmic muons transmitted through slabs of concrete, iron, lead and uranium	106
<b>9.</b>	<b>INSTRUMENTATION IN PHYSICAL SCIENCES</b>	<b>108</b>
9.1	Design & Development of a Multichannel Spectrograph using CCD as a Detector	109
9.2	Scanning Monochromators (0.5 m) for Isotopic Analysis of Molecules such as <sup>15</sup> N- <sup>14</sup> N in Nitrogen Gas	109
9.3	Nuclear optical Instrument	110
9.4	Development of Thermoelectric Generators	111
9.5	Room Temperature operating Gas Sensors	112
9.6	Conducting Polymers based Sensors and Actuators	112
9.7	High Resolution Electron Spectrometer	113
9.8	New electrode design for Triode Sputter Ion Pump	114
<b>10.</b>	<b>MASS SPECTROMETR</b>	<b>115</b>
10.1	Mass Spectrometers for RMP, Mysore	116
10.2	Thermal Ionization Mass Spectrometer TIMS	116
10.3	Quadrupole Mass Spectrometers QMS	117
10.4	Mass Spectrometers for Heavy Water Analysis	118
10.5	Mass Spectrometers for Heavy Water Board	119
10.6	Indigenously Developed Matrix assisted Laser Desorption Time of Flight Mass Spectrometry (MALDI-TOFMS)	119
10.7	Electrostatic Ion Trap	
10.8	High Resolution Reflectron Time-of-flight Mass Spectrometer	121
<b>11.</b>	<b>SYNCHROTRON BEAMLINE INSTRUMENTATION</b>	<b>122</b>
11.1	Angle Resolved Photoelectron Spectroscopy Beamline at Indus-1	123
11.2	Photophysics Beamline at Indus-1	123
11.3	High Resolution VUV Beamline at Indus-1	124
11.4	Development of a crystal bender for extended X-ray Absorption Fine Structure (EXAFS) beamline at Indus-II synchrotron source	125



P H Y S I C A L   S C I E N C E S

11.5	Photo-Absorption Spectroscopy Studies beamline	126
11.6	Photo-electron Spectroscopy beamline	127
<b>12.</b>	<b>SPECTROSCOPIC STUDIES</b>	<b>128</b>
12.1	Multicolor photoionization opto-galvanic spectroscopy of Uranium	129
12.2	Laser Induced Fluorescence Spectroscopy of Lanthanide.	129
12.3	High Resolution Laser Spectroscopy of Actinides	130
12.4	Laser Induced Fluorescence Spectroscopic Studies on Zirconium Atoms; Zirconium Oxide Molecules	131
12.5	Fourier Transform Emission Spectroscopy of the $A^1\Pi-X^1\Sigma^+$ transition in $^{74}\text{Ge}^{80}\text{Se}$	131
12.6	Fabrication of precision optical components	133
12.7	Interferometric testing of optical components	134
12.8	Fourier Transform Spectroscopic Studies of Atoms, Molecules and Transient Species	135
12.9	CCD-based Raman Spectrometer	135
<b>13.</b>	<b>STUDIES IN NUCLEAR PHYSICS</b>	<b>136</b>
13.1	Fission of Super Heavy Nuclear Systems	137
13.2	Transfer followed by breakup with stable and weakly bound projectiles	137
13.3	Heavy-ion Induced Fission Fragment Mass, total Kinetic Energy and Angular Distributions	138
13.4	Measurement of Pre-fission n, p, $\alpha$ and GDR $\gamma$ -ray Multiplicities in $^{28}\text{Si} + ^{175}\text{Lu}$ System	139
13.5	Study of Giant Dipole Resonance Built on 15.1 MeV T=1 State In $^{12}\text{C}$	140
13.6	Direct Observation of $4^+$ To $2^+$ Gamma Transition in $^8\text{Be}$	141
13.7	Enigma in Angular Momentum Gated Particle Spectrum in $^{12}\text{C}+^{93}\text{Nb}$ Reaction	142
13.8	Anomaly in the Nuclear Charge Radii of Zr Isotopes	142
13.9	ENSTAR Detector in the Search for a New State of Nuclear Matter	143
13.10	Relativistic Heavy Ion Collisions	144
13.11	Development and Utilizations of Ion Accelerators	145
13.12	Astrophysical $S_{17}(0)$ from $^2\text{H}(^7\text{Be},^8\text{B})\text{n}$ Reaction at $E_{\text{c.m.}} = 4.5$ MeV	146
13.13	Application of Pulse Shape Discrimination in Si Detector for Fission Fragment Angular Distribution Measurements	147
<b>14.</b>	<b>DESIGN AND FABRICATION OF MECHANICAL ASSEMBLIES</b>	<b>149</b>
14.1	Annular Parallel Plate Avalanche Counter	150
14.2	Alpha Spectrometer	151
14.3	On-line Linear Sample Changer for (TIMS) Mass Spectrometer	151



## **1. PARTICLE ACCELERATORS AND RELATED ACTIVITIES**

### **INTRODUCTION**

Particle accelerators have important applications in industry, defence and R & D. Industrial electron accelerators (DC and RF) with 500 keV to 10 MeV particle energy and 10 to 30 kW beam power have been developed for radiation processing applications like modification of bulk polymers, cross linking of plastic films, foam and cables, sterilization of medical products and food preservation. A 10 MeV RF *linac* is employed for cargo inspection. Gigawatt single and multi pulse systems have applications in defence for high power microwave generation and flash radiography. Pulsed high magnetic fields are employed for EM welding of metal to ceramic joints. High current proton ECR source, superconducting elliptical cavities, 14 MeV neutron source, RFQ accelerators and Monte Carlo method simulations have applications in Accelerator Driven Sub critical Systems (ADSS). A brief description of the developments in each of these areas is given in the following sections.

### 1.1 500 keV, 10 kW INDUSTRIAL DC ELECTRON ACCELERATOR FOR MATERIAL PROCESSING

A 500 keV, 20 mA, 10 kW DC Cockcroft Walton industrial electron accelerator for various applications such as polymerization, paint curing, cross linking of polymers, grafting of rubber and Teflon degradation etc. has been designed and developed. This is the first indigenously designed and built industrial accelerator in the country that is operational at high beam power. A detailed view of the full facility and its extended views are shown below. It mainly consists of EHV supply, electron beam system, accelerator tank, computer control system, vacuum system, radiation shield and product handling system. Some of the other auxiliary facilities include low conductivity water plant, gas handling plant, ozone exhaust duct fitted with blowers etc. The basic scheme for generating 500 kV DC comprises of a ten stage balanced Cockcroft Walton cascade voltage multipliers. The accelerator consists of a  $\text{LaB}_6$ -based cathode electron gun, which

can deliver a beam of about 20 mA at a voltage of 5 kV. The beam, after getting accelerated to 500 keV in accelerating tubes, passes through the magnetic sweep scanner, scan horn and brought into air through a titanium foil of  $25\ \mu$  thickness. Since this was the first indigenously built accelerator, several technical problems encountered were addressed one by one. The stability in beam energy and current is measured and found within  $\pm 1\%$  and  $\pm 3.5\%$  respectively. The products can be irradiated by putting them on a static and also on a movable conveyor belt system. The accelerator installed at BRIT, Vashi, is routinely operated for surface irradiation experiments.

K.C. Mittal, R. Majumder, K.Nanu, A. Jain, S.Acharya, Ritu Aggarwal, R.I. Bakhtsingh, A.R. Chindarkar, S.R. Ghodke, D. Jayaprakash, S. Khole, Mukesh Kumar, Mahendra Kumar, R.L. Mishra, G.P. Puthran, R.N. Rajan, S.R. Raul, P.C. Saroj, D.K. Sharma, Vijay Sharma, S.K. Srivastava and R.C. Sethi, Proc. DST-BARC Indo Bulgarian Workshop on Electron Beam Technology and Applications, November 19-21, 2003, Mumbai, pp- 243.

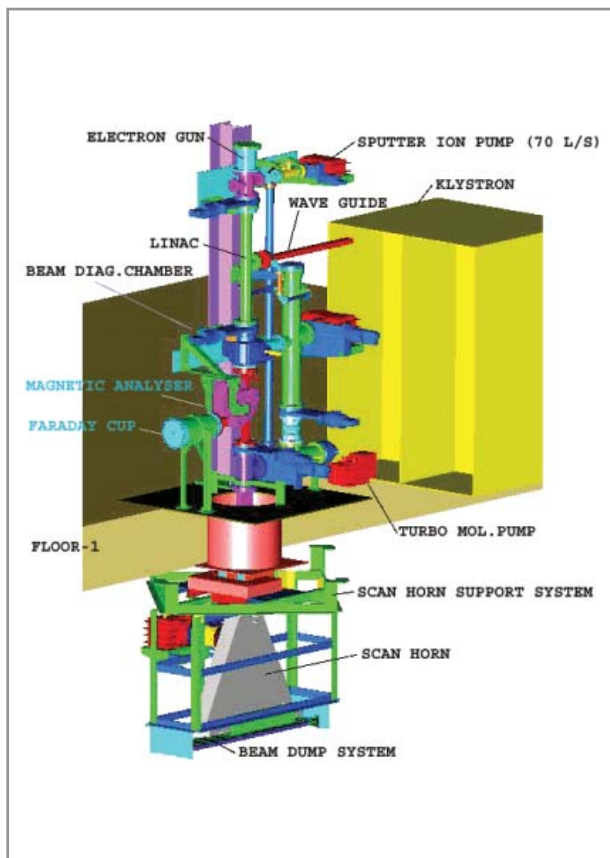
500 keV Electron Beam Irradiator Facility, BRIT, Vashi, Navi Mumbai



A view of the 500 keV Accelerator

## 1.2 10 MeV, 10 kW INDUSTRIAL RF ELECTRON LINAC FOR MATERIAL PROCESSING

This is an on-axis coupled cavity, standing wave type of RF linac. A schematic is shown below. A 50 keV electron beam injected into the RF linac is accelerated to the desired energy. The linac is designed to work at a duty factor of 0.4 %. The total length of the linac cavity is about 0.9 m. The energy analysis of the beam is accomplished through a magnetic analyzer and the current by a current transformer. A 5-10 Hz scanner is used to scan the beam. A vacuum of about  $10^{-8}$  Torr can be maintained in the entire accelerator with the help of a Turbo & sputter ion pump combination. A klystron-based microwave source with a peak power of 6 MW and an average power of 24 kW is used to feed the linac. The design has been conceived for a frequency of 2856 MHz. The beam is brought into air through a 50  $\mu$  thick tantalum foil. The irradiation of the products is accomplished by putting them on a moving conveyor belt mechanism.



Schematic of 10 MeV RF Electron Linac



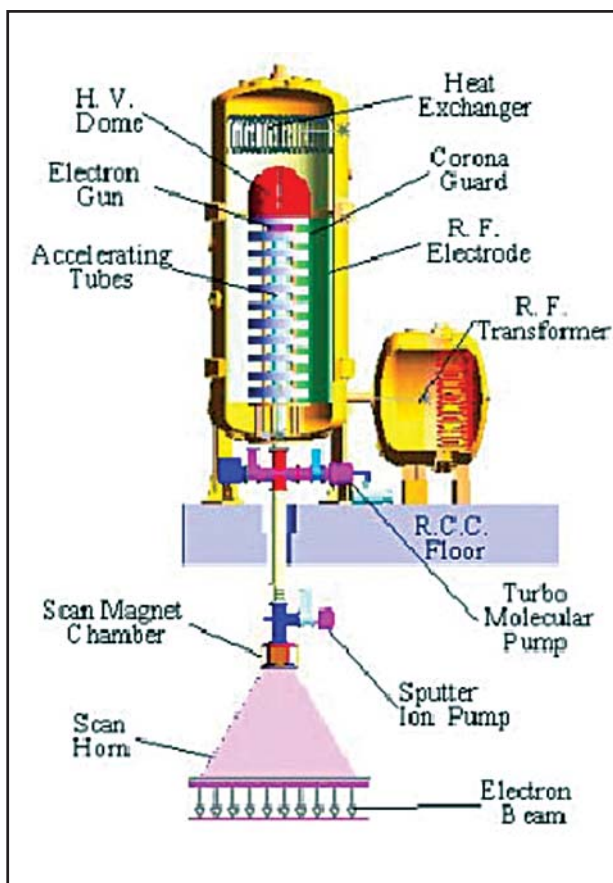
10 MeV Linac installed at EBC, Kharghar

The linac has been assembled and installed. A view of the same is shown in figure. Linac cavity has been brazed and characterized. The difference in frequency before & after the brazing is found to be within 0.5 MHz. The field deviations inside the cavity are measured to be within 2 %. Electron Gun has been tested up to 50 kV & 0.8 A. The magnetic analyzer & the beam current transformer have been calibrated. A vacuum of the order of  $3 \times 10^{-7}$  Torr has been obtained in the entire accelerator assembly. All the accelerator parameters can be set, varied and controlled through the control console of the control room. The microwave source is being built by SAMEER, Mumbai.

R.C.Sethi, V.T.Nimje, K.P.Dixit, D.Bhattacharjee, P.Roychoudhary, V.Yadav, R.B.Chavan, Mukesh Kumar, A.S.Dhawale, P.Jain, R.S.Sardesai, K.C.Mittal, A.R.Chindarkar, S.Acharya, Arvind Jain, Mukesh Kumar, P.S.Kaurav, Vijay Sharma, S.B.Jawale, R.S.Vohra, K.Mahajan, S.Guha, Abhay Kumar, G.Chakrabarty, J.R.Mulwadkar, S.Y.Kulkarni, Jagmohan Singh, Proceedings of the Indian Particle Accelerator Conference, Kolkata, March 1-5, 2005 (InPAC 2005), p-122.

### 1.3 3 MeV, 30 kW INDUSTRIAL DC ELECTRON ACCELERATOR FOR MATERIAL PROCESSING

The accelerator with 3 MeV electron energy and 30 kW beam power can be considered as the work horse for industrial radiation processing applications like modification of bulk polymers, cross linking of plastic film, foam and cables, degradation of scrap Teflon and cellulose materials, sterilization of medical products and food irradiation. A detailed 3D layout of this accelerator is shown in figure. The accelerator comprises of several sub systems. The high voltage column comprises of corona rings, which are interconnected by rectifier stacks. The split RF electrodes are energized through a high frequency oscillator having specifications as 150-0-150 kV, 120 kHz. The power to the RF electrodes is fed via a 10 MVA air core transformer. There are 70 rectification stages & each stage is designed to give an effective DC voltage of 50 kV. The tank houses the electron gun,



3 MeV, 30 kW DC Accelerator

acceleration tubes, high voltage multiplier column, the dome and a motor alternator drive assembly. The voltage insulation is provided through 6 atmospheres of SF<sub>6</sub>. The tank is approximately 7 m long and 2 m in diameter and has been built in three sections. Thermistor type beam sensing devices have been incorporated for monitoring beam transportation.

The pressure vessel has been installed and tested and high voltage dome has been delivered at EBC, Kharghar. Also, a 50 kW, 120 kHz oscillator has been built and tested. 150-0-150 kV, 10 MVA air core transformer (see Fig.) has been built. The electron gun has been made. The magnetic scanner and its power supplies are ready. The SF<sub>6</sub> storage tanks have been installed. The voltage divider and rectifier stacks have been built. The remaining parts are in the advanced stage of fabrication and assembly.



150-0-150 kV, 10 MVA Air cored transformer

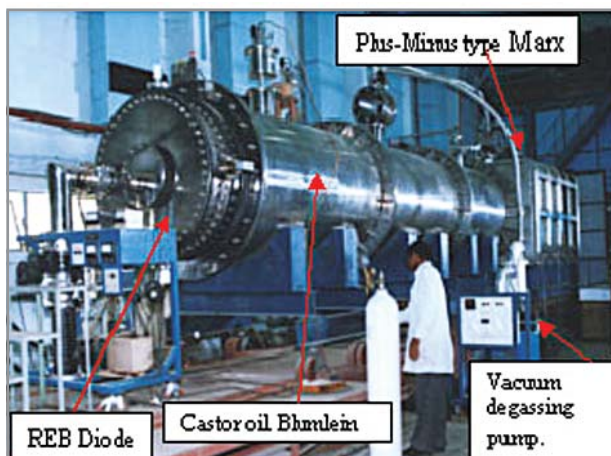
R.Majumder, K.C. Mittal, K.Nanu, A. Jain, K.V. Nagesh, S. Acharya, R.I. Bakhtsingh, M. Balakrishnan, A.S. Chawla, A.R. Chindarkar, S.R. Ghodke, D. Jayaprakash, S. Khole, Mukesh Kumar, Mahendra Kumar, R.L. Mishra, G.P. Puthran, R.N. Rajan, P.K. Sarma, P.C. Saroj, D.K. Sharma, Vijay Sharma, S.K. Srivastava and R.C. Sethi, Proc. DST-BARC Indo Bulgarian Workshop on Electron Beam Technology and Applications, November 19-21, 2003, Mumbai, pp-258

#### 1.4 DEVELOPMENT OF A GW PULSED ELECTRON ACCELERATORS AND THEIR APPLICATIONS

The photograph of KALI-5000 system is shown below. This system consists of (i) a Marx generator rated as 1.5 MV, 25 kJ, 1ms, (ii) three electrodes, castor oil Blumlein rated as 1MV, 40 kA, 12  $\Omega$ , 100 ns, 5 kJ, (iii) SF<sub>6</sub> sparkgap, (iv) REB diode rated as 1MV, 12  $\Omega$ , 100 ns and (v) charging power supply & controls. This Marx generator consists of five modules of 300 kV, three stages of  $\pm 50$  kV, 0.7 $\mu$ F (pair) capacitors, 15 nitrogen gas insulated sparkgap switches of Bruce profile and nichrome wire wound resistors of 2.5 k $\Omega$  and 20 k $\Omega$  for charging and ground resistance respectively in "Z" configuration.

This Marx generator has been housed in a stainless steel tank of 1.7 m x 1.6 m x 3 m length with transformer oil as insulation. The transmission line in the present pulse power system is a three electrode coaxial Blumlein with castor oil as the dielectric. This consists of three coaxial cylinders of diameters 0.8 m, 1.0 m & 1.2 m and 4 m length.

This inductor is used for SF<sub>6</sub> gas inlet to the SF<sub>6</sub> sparkgap chamber, made of Perspex cylinder with nylon tie rods.



KALI-5000 System (1MV, 40kA, 100ns, 5kJ).

Intense Relativistic Electron Beams (REB) can be generated by applying a high voltage pulse across a field emission diode made of graphite cathode and copper mesh anode. The high field emission current densities of 10<sup>8</sup> to 10<sup>9</sup> A/cm<sup>2</sup> resulting from E fields of greater than 10<sup>6</sup> MV/cm, lead to thermal explosion of

micro-projections on the cathode & formation of plasma on cathode surface. This system has been assembled and commissioned at 650 kV, 100 ns pulse on the Blumlein. A current of  $\sim 71$  kA has been extracted with 2-2.5 kg/cm<sup>2</sup> pressure SF<sub>6</sub> gas. The pulsed HPM is generated by injecting electron beam in to microwave devices such as Vircator. The virtual cathode formed due to passing of REB at low pressure reflects the electron beam that in turn oscillates between cathode & virtual cathode. This oscillation results in generation of HPM. The range parameters of frequency, peak power and efficiency for this device are 1-10 GHz/1-20 GW/1-5%, respectively. This system has been used for generation of HPM along with suitable cavity and a power of  $\sim 1$  GW HPM has been obtained at the parameters of 600 kV, 70 kA, 100 ns. Experiments for X-ray generation with KALI-5000 system will start shortly.

K.V.Nagesh, Archana Sharma, Ritu Agarwal, S.R.Raul, K.C.Mittal, G.V.Rao, J.Mondal and R.C.Sethi, Proceedings of the Indian Particle Accelerator Conference, Kolkata, March 1-5, 2005 (InPAC 2005), p-120.

#### 1.5 REPETITIVELY PULSED LINEAR INDUCTION ACCELERATOR

In this Linear Induction accelerator, inductive adder configuration has been adopted for high voltage beam generation. The high voltage at the output of the induction adder is applied through a field emission cathode to produce the electron beam. These devices can operate in either polarity to produce negatively or positively charged particle beams. The assembly of various subsystems is shown in Fig. The basic scheme of present solid state switching based power modulator comprises of IGBT inverter (30 kHz) and ferrite core step-up transformer with constant current control feedback. It charges a 100  $\mu$ F energy storage capacitor up to 2.5 kV by command resonance charging in 9 ms for 100Hz operation.

This energy is transferred to an amorphous core based toroidal pulse transformer rated 2.5 kV/20 kV, 20  $\mu$ s through ABB make laser triggered high power SCR in 10-100Hz. Two pulse transformers are used in the initial stages for stepping up the voltage. In the first pulse transformer, voltage is stepped up from 2.5 kV to 20 kV, at 20  $\mu$ s. Here six cores of size:



200keV, 5kA, 10-100Hz, 50ns Linear Induction Accelerator.

160/240/25 mm toroids are used. In the second stage, 20 kV, 5  $\mu$ s pulse is stepped up to 200 kV pulse with 8-cores of similar size. Resetting of these cores is done with built-in DC reset supply along with a blocking inductor. This transformer has been designed, fabricated and assembly is in progress. There are four magnetic switches in this accelerator to compress the pulse in stages of 20  $\mu$ s/5  $\mu$ s; 5  $\mu$ s/1  $\mu$ s, 1  $\mu$ s/250 ns and 250 ns/100 ns with turns of 13, 37, 7 and 1 respectively. First switch is between the two pulse transformers and it has separate reset supply. The remaining three switches and induction cavities are reset by a 400 A DC supply using a blocking inductor made of amorphous cores.

Three induction cavities, consisting of two cores of size 220/390/25 mm each, rated 75 kV, 100 ns have been used to obtain a beam voltage of 200 kV. Conical Perspex insulators of 30 mm thickness are inserted between consecutive cavities to form the oil-vacuum interface. The high voltage pulse input from the PFL will be fed to the cavities. A field emission diode with appropriate area and gap will be used to realize a proper electron beam. A blocking inductor of 400 mH, is designed to reset three magnetic switches at 200 kV level and induction cavities (with 100 A DC) and block 200 kV, 5  $\mu$ s pulses from the pulse transformer of the accelerator. The linear induction accelerator LIA-200 is expected to be operational in burst mode of few seconds duration shortly.

Archana Sharma, K.V.Nagesh, S.Acharya, R.Rehim, D.K.Sharma, P.C.Saroj, Ritu Agrawal, Manoj Pande, G.V.Rao, K.C. Mittal and R.C.Sethi, Proceedings of the Indian Particle Accelerator Conference, Kolkata, March 1-5, 2005 (InPAC 2005), pp-124.

## 1.6 GENERATION & APPLICATIONS OF PULSED HIGH MAGNETIC FIELDS

Generation of pulsed high magnetic field is important for several activities in the area of Physical sciences. For generation of such fields a high voltage source is required which was developed using energy storage capacitor banks. To understand the material behaviour at high magnetic fields few such experiments were carried out in APPD and are presented here. The EM welding equipment was developed in-house. The sample of Aluminum tube (15 mm diameter, 1 mm wall thickness), shown in Fig. was compressed in our laboratory to near solid form (~6 mm dia rod) at an estimated strain rate of 10<sup>6</sup>/s.

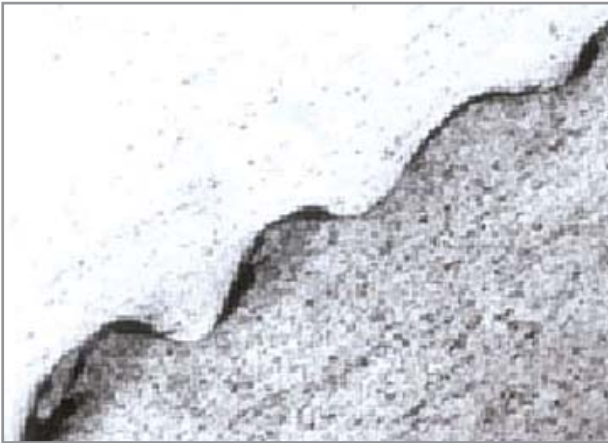
Another experiment carried out for joining the metals to insulators. A leak tight vacuum joint (leak rate < 10<sup>-10</sup> std cc/s) was achieved between 0.4 mm thick annealed copper sleeves and Alumina rods and tubes using high magnetic field pulses. The welding of Aluminum metal was also carried out using high magnetic field. Micrograph of an Al-to-Al welded using EMF welding technique, is shown.



10kV, 20kJ Electromagnetic Welding Equipment developed with AFD.



Metal-Ceramic joint using EMF.



150X – Micrograph of Al-to-Al weld.



Aluminium tube compressed at  
~10<sup>6</sup>/s Strain rate.

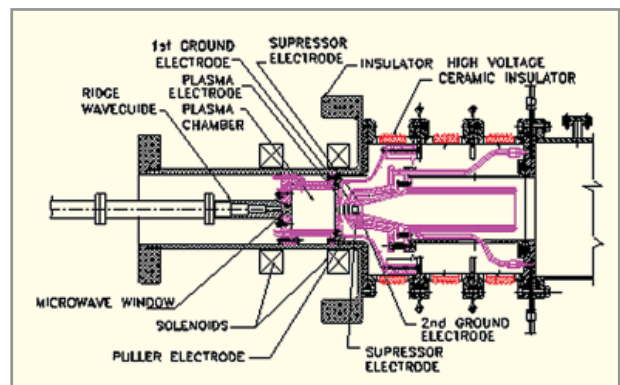
R.K.Rajawat, S.V. Desai, M.R. Kulkarni, Dolly Rani, K.V. Nagesh, R.C. Sethi, 3rd Asian Particle Accelerator Conf, APAC 2004, Gyeongju, Korea, March 22-26, 2004

## 1.7 DEVELOPMENT OF HIGH CURRENT PROTON ECR SOURCE

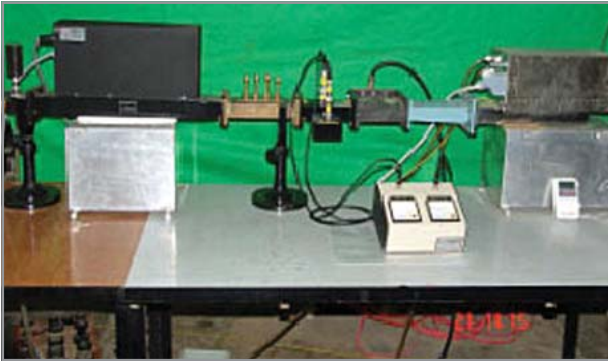
APPD/BARC has initiated a program of designing & developing a 50 kV, 50 mA, DC ECR based proton ion source shown schematically in Fig. It consists of 1) Microwave generator, 2) Microwave transmission components, 3) Plasma chamber, 4) Solenoids, 5) Ion extraction assembly, 6) Vacuum systems, 7) Gas injection assembly, 8) Beam diagnostics, 9) Einzel lenses and 10) Power supplies for operating the source. The plasma is initiated by a microwave discharge in the presence of a magnetic field created through a pair of solenoids. The microwave power is generated by a 2.45 GHz, 2 kW cw Magnetron. This power to the ion source is fed via an RF plumbing line consisting of a circulator, dual directional coupler, four-stub auto-tuner, waveguide break, ridge waveguide and a microwave window.

The ion source rms normalized emittance has been theoretically estimated to be ~ 0.1 p mm-mrad, which corresponds to an ion temperature of  $kT_i = 1.5$  eV. The minimum value of the emittance has been estimated at a puller voltage of 40 kV. The ECR discharge will be attained at an axial magnetic field of  $B_{ECR} \sim 875$  G using two independently controlled and water-cooled solenoids.

A turbo pump is used to evacuate the source and the flow of hydrogen/deuteron gas is monitored through a flow meter. The plasma chamber has been made and tested. The microwave generator comprising of a magnetron and a plumb line is shown in Fig.. This has been tested up to 1.8 kW. The generator will be



Schematic of the 50 keV, 50 mA ECR  
proton ion source.



Testing 2.45 GHz ECR Microwave Generator

operated through a remotely controlled micro-controller, managed through a PC. The ECR ion source will be commissioned by 2007.

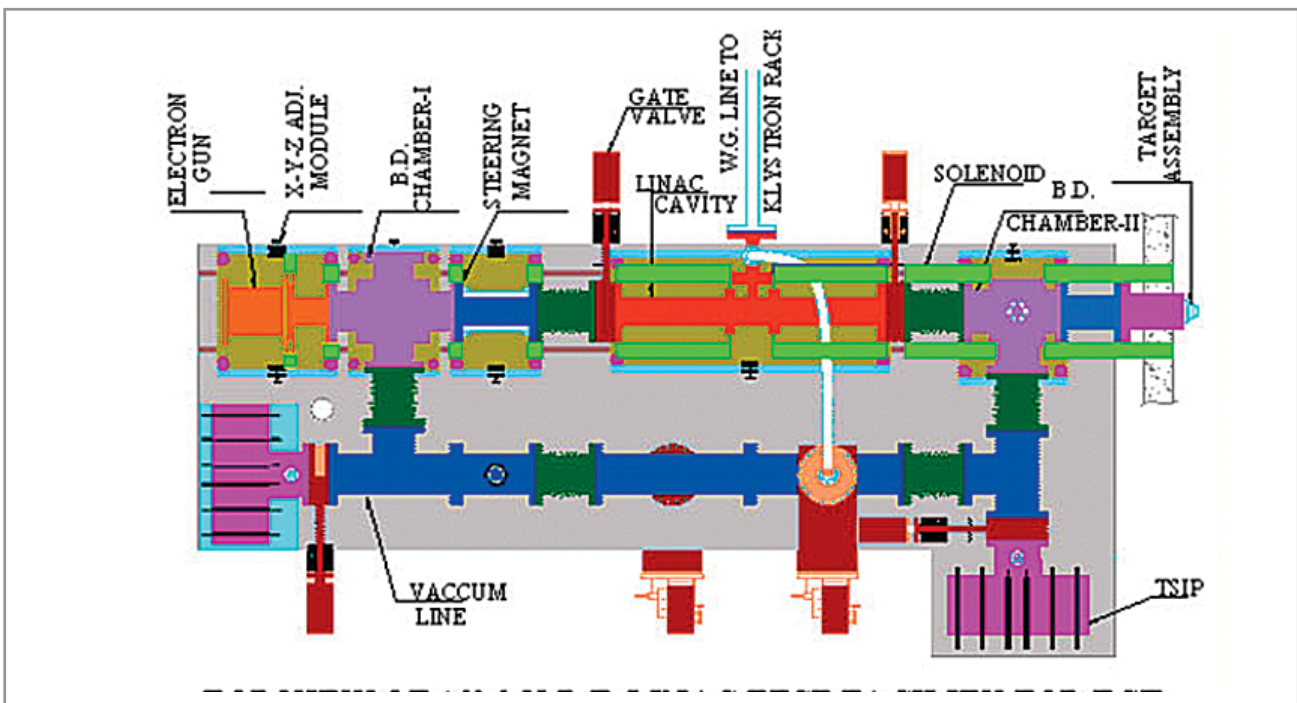
P. Roychowdhury, P.Jain, K.P. Dixit, V. Ydadav, S. Chandan, and R.C. Sethi, Proceedings of the Indian Particle Accelerator Conference, Kolkata, March 1-5, 2005 (InPAC 2005), p-316.

### 1.8 ELECTRON BEAM RF LINAC FOR CARGO INSPECTION

APPD/BARC in collaboration with ECIL (Electronics Corporation of India, Ltd.), have initiated a project to develop a prototype cargo scanning system. A Cargo Scanning Source has three major components: (a) electron accelerator for generating the X-rays, (b) radiographic and imaging techniques for constructing and viewing the images and (c) container handling system inclusive of overall electromechanical controls. The role of APPD is to supply the electron accelerator.

The developed prototype machine will have a beam energy of about 10 MeV with an average beam current of about 0.2 mA. The expected X-rays dose rate is 30 Gy/min m.

The required X-ray beam focal spot size is about 2 mm with a field uniformity of  $\pm 5\%$  at  $\pm 7.5$  deg, off the central axis. The leakage of radiation will be confined to 0.1% for X-ray field, spanning to an area of 30 degrees with respect to the axis. Except for the power level, the X-ray source specifications are



Top View of 10 MeV RF LINAC facility for ECIL

similar to the 10 MeV, 10 kW electron beam RF linac, already taken up by APPD. Therefore, this RF linac will be duplicated by restricting the power level to 2 kW. A schematic of the proposed X-rays source is shown in fig..

The entire operation of the developed machine is computer controlled.

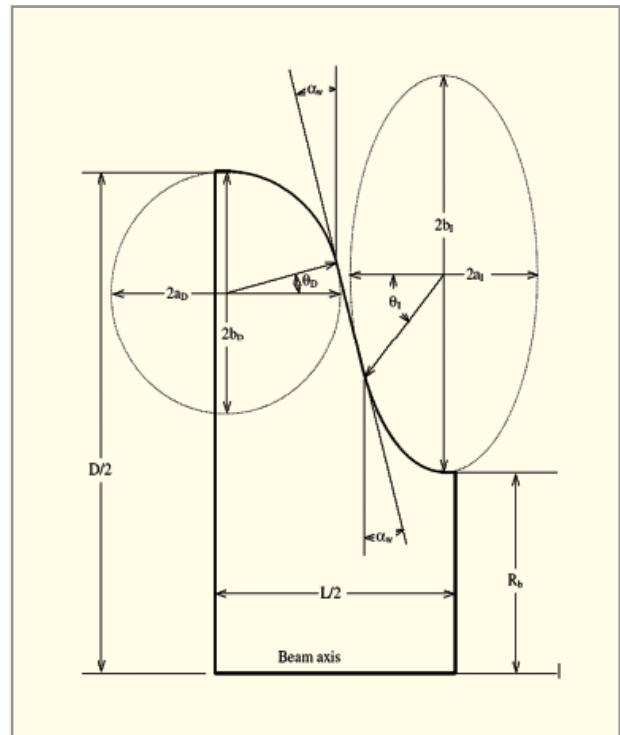
R.C.Sethi, V.T.Nimje, K.P.Dixit, D.Bhattacharjee, P.Roychoudhury, V.Yadav, R.B.Chavan, Mukesh Kumar, P. Jain, R.S.Sardesai, K.C.Mittal, A.R.Chindarkar, S.Acharya, Arvind Jain, S.B.Jawale, R.S.Vohra, K.Mahajan, A.K. Sinha, G.Chakrabarty, Jagmohan Singh and G.P. Shrivastava, Internal Report No: APPD/RFAS/2/2003

### 1.9 SUPERCONDUCTING RF CAVITY DEVELOPMENT FOR PARTICLE ACCELERATORS

Normal conducting (NC) copper cavities and superconducting (SC) cavities at cryo-temperatures in various configurations are commonly employed in modern high-energy accelerators. SC cavities are preferred because these consume around 200 times less power compared to a NC cavity for similar level of operation.

Considering the importance of SC RF technology and its applications towards ADSS, the Accelerator & Pulse Power Division (APPD) has worked out a plan to develop SC RF single-cell and multiple-cell niobium cavities for high current accelerators for different beta values from 0.42 to 1.0. These cavities will be used for accelerating high current protons from 100 MeV onwards up to 1 GeV for ADSS program of BARC.

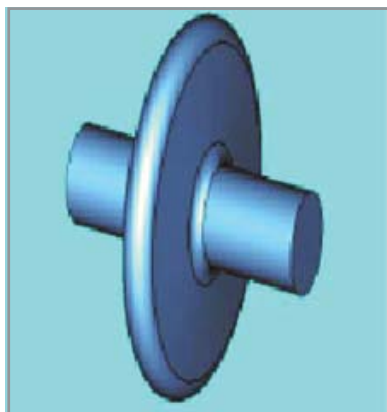
A single cell prototype elliptical niobium cavity having beta=0.42, operating at 700 MHz with accelerating field gradient of 5 MV/m at liquid helium temperature is being developed. A symmetric half cell has been shown in Fig. Detailed simulations have been carried out and RF design values of various cavity parameters were arrived at and are listed in the Table. A suitable power coupler has also been designed. The cavity with these parameters is being developed using OFHC copper. Later niobium coated over copper and bulk niobium cavity will also be developed. Possible trapped modes in the cavity have been analyzed. Fig. shows a typical symmetric elliptic cavity.



Symmetric half cell

Accelerating Gradient	5 MV/m
Bore Radius $R_b$	5 cm
Cell Length L	8.994 cm
Cavity Diameter D	37.384
Wall Angle $\alpha_w$	4°
Iris $a_I/b_I$	0.45
Dome Ellipse $a_D/b_D$	1
Dome Radius $R_D$	2.5 cm
$E_{pk}/E_{acc}$	1.6027
$H_{pk}/E_{acc}$	3.7325
Q	$0.61 \times 10^9 @$
	4.2° K
r/Q	8.069 $\Omega$

Single Cell Elliptical Niobium  
Cavity Parameters



Symmetric Elliptical cavity.

A.Roy, J. Mondal, K. C. Mittal and R. C. Sethi, Proceedings of the Indian Particle Accelerator Conference, Kolkata, March 1-5, 2005 (InPAC 2005), p-394.

A.S.Dhavale And K.C.Mittal, Proceedings of the Indian Particle Accelerator Conference, Kolkata, March 1-5, 2005 (InPAC 2005), p-398.

### 1.10 UTILISATION OF 14-MeV NEUTRON GENERATOR TO STUDY THE NEUTRONIC BEHAVIOUR OF AN ACCELERATOR DRIVEN SUB-CRITICAL ASSEMBLY

The physics of ADS and its Sub-Critical Assembly (SCA) is fairly well understood. However, several concepts are new and their understanding requires experimental verification. It has been shown that in the absence of a spallation source, another well known and economical source of 14 MeV neutrons can be used to drive the SCA. An experimental program has been initiated at BARC to study the neutronic characteristics of an SCA using the 14-MeV n-source located at Purnima. Main objective is to study the physics characteristics of a SCA to validate the calculation tools and neutron cross-section data sets and to gain confidence in the prediction of the basic safety features of ADS.

#### ■ 14 MeV Neutron Source:

A 14-MeV (D,T) neutron generator has been fabricated and installed at Purnima to validate sub-critical validation. 14 MeV neutrons are produced when 100-200  $\mu\text{A}$  D<sup>+</sup> ion current accelerated up to 300 KV is bombarded on a 10 Ci Tritium target. Measured neutron yield is  $3 \times 10^9$  n/s.



Neutron Generator

#### ■ Theoretical treatment by Monte-Carlo Method:

The presence of an External n-Source and a SCA results in a neutron distribution which is more complex in terms of its space, energy and angle variation. For this reason the analysis of the neutronic behaviour of ADS is carried out by the Monte Carlo methods. This approach is more versatile as it can treat the complicated 3-D reactor geometry as it actually exists and it can treat the complex variation of the point neutron cross section with energy accurately. The transport of high energy spallation neutrons produced by the interaction of  $\sim 1$  GeV protons with the target like lead/Bismuth are treated by using high energy transport codes like LAHET, FLUKA or SHIEL. They follow the protons down to zero energy while neutrons are tracked down to 20 MeV below which they are treated by standard Monte-Carlo codes like MCNP. The physics design and analysis of the neutronic behaviour of the Purnima Sub-SCA is carried out using 3-Dimensional MCNP code employing latest unnormalized ENDF/B cross section data libraries.

#### ■ Development of the Ion Source and RFQ based accelerators

A few improvements were carried out in the design of the RF-Ion Source which resulted in the enhancement of the pre-accelerated D<sup>+</sup> ion-current up to  $\sim 1$  ma. This will be useful in enhancing the 14 MeV neutrons yield to about  $10^{10}$  n/s. The 50 kV high energy platform along with 1 mA RF type ion source of

the existing accelerator at Purnima is also being utilized for simultaneous development of a RFQ based 400 kV accelerator which will be used to produce higher intensity neutrons ( $> 10^{10}$  n/s) of 14-MeV which is planned to be used to drive the Purnima sub-critical assembly.

■ **Design of Purnima Sub-Critical Assembly by Monte-Carlo Method:**

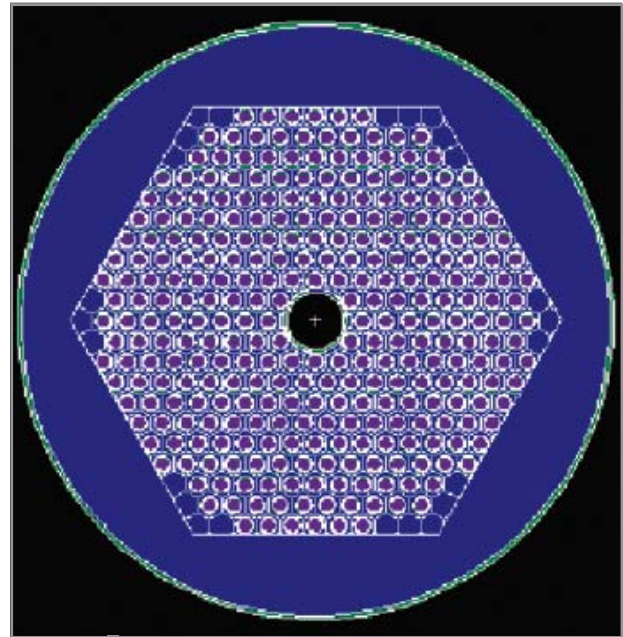
The objective was to get max.  $k_{eff}$  ( $k_{eff} \sim 0.9$ ) using Nat.-U rods with Ord.-water. The assembly should be easily accommodated at the available space in front of the 14-MeV n-source and should also have a central hole through which the beam tube of the accelerator could be inserted to place the n-source at its centre. The  $k_{eff}$  of the final assembly was found to be slightly lower than that calculated by standard reactor physics techniques based on deterministic methods. The calculated  $k_{eff}$  was found to be  $k_{eff}(\text{Monte-Carlo}) = 0.873 \pm 0.001$ .

■ **Simulation of  $k_{eff}$  Measurement by dynamic method:**

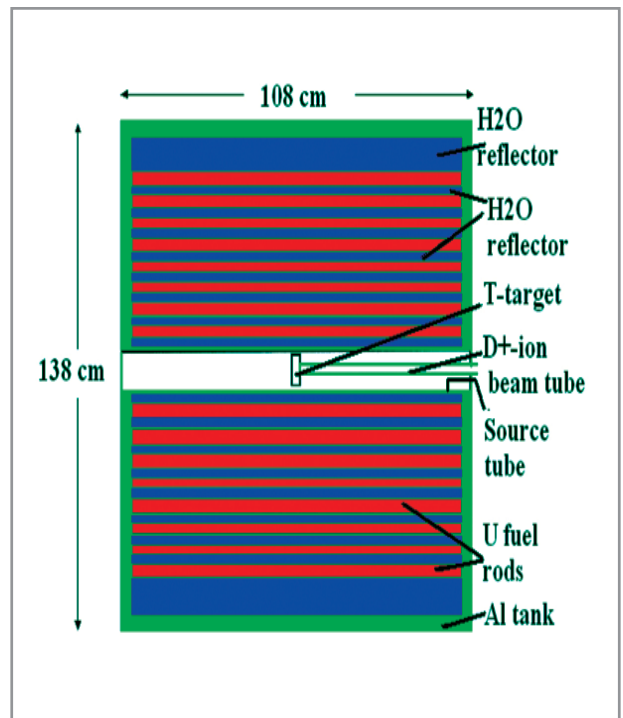
In a thermal system the counting rates were found to decrease exponentially with time as,  $N(t) = N_0 \cdot \text{Exp}(-\alpha t)$ ; where  $\alpha = \{(\rho - \beta) / l_{eff}\}$  from the measurement of the slope of the decay curve,  $\rho$  and hence  $k_{eff}$  can be obtained.  $k_{eff}$  can be measured at any time during the operation of actual ADS. This method requires the source to operate in the pulsed mode. Decay plot of He-3(n,p) detector located at the middle of Ring No.1 and Ring No.5 of Pu-SCA is shown in figure.

■ **Simulation Calculations for Reaction Rates and Neutron Spectra inside Pu-SCA:**

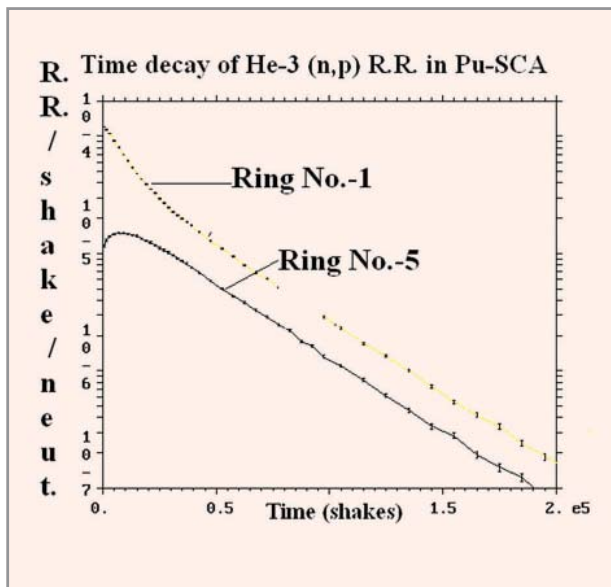
Detailed 3-D simulations were done for Pu-SCA to estimate the Reaction Rates of the following important activation detectors like  $^{27}\text{Al}(n,\alpha)$ ,  $^{56}\text{Fe}(n,p)$ ,  $^{93}\text{Nb}(n,2n)$ ,  $^{197}\text{Au}(n,\gamma)$  and  $^{235}\text{U}(n,f)$  for a central isotropic source of 14-MeV neutrons with Monte-Carlo method using latest ENDF point data cross sections. The reaction rates are also known as spectral indices as they can be used to estimate the neutron spectrum and flux distributions inside the Pu-SCA. Simulated values of RR for  $^{235}\text{U}(n,f)$  are shown in figure.



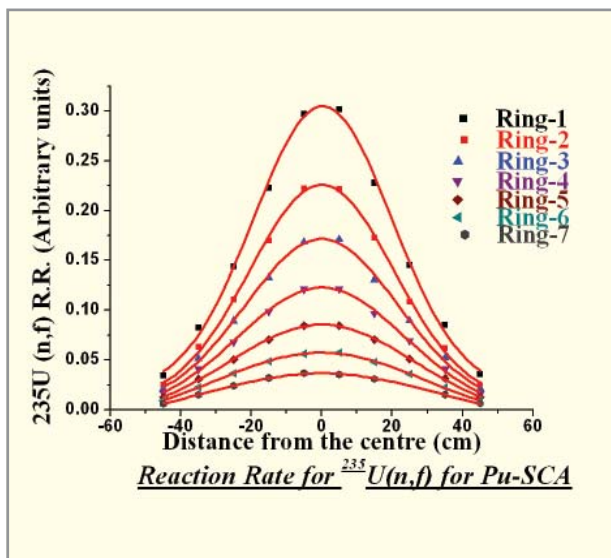
Cross sectional view of Purnima-SCA



Elevation of Purnima-SCA



Decay Plot of  $^3\text{He}(n,p)$  RR at middle of Ring-1 and Ring-5 of Purnima-SCA



Simulated Reaction Rates for  $^{235}\text{U}(n,f)$  reaction inside Purnima SCA



## **2. STUDIES IN HIGH PRESSURE PHYSICS**

### **INTRODUCTION**

The response of materials may depend upon the nature of high pressure loading viz. static or dynamic. In BARC, both kinds of studies are being carried out. The investigations under static high pressures are done using various kinds of diamond anvil cells (X-ray diffraction, Raman and resistivity), piston-cylinder device (compressibility) and WC Bridgeman anvils (transport properties). Single stage gas gun is used for the studies under shock loading. Using these, several materials - metals and alloys, organic and inorganic compounds and nano-crystalline materials have been investigated to obtain an equation of state and the nature of the phase transformations. This chapter provides a brief summary of the kind of investigations carried out over the last few years. This also includes the pulsed high energy density activity related to the high magnetic fields generated through capacitor bank or with the exploding foil accelerator.

## 2.1 EXPERIMENTAL CONDENSED MATTER PHYSICS: MATERIAL BEHAVIOUR UNDER HIGH PRESSURE

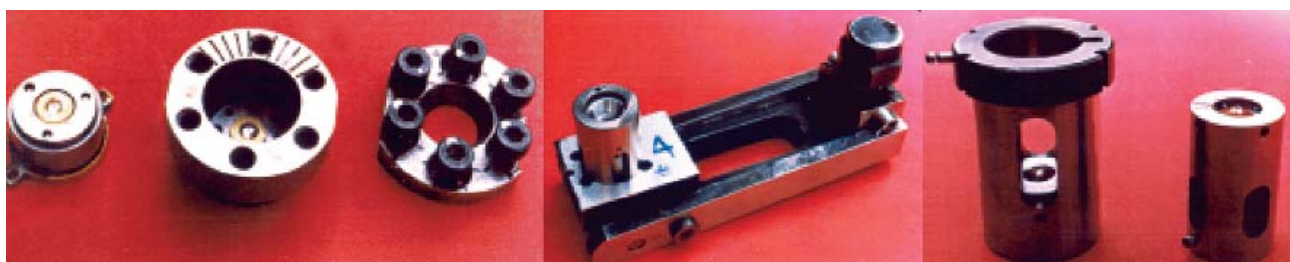
General nature of investigations being perused are on materials of current interest / exotic properties, synthesized in-house or obtained through collaboration. A program for the investigation of Actinides and their compounds under pressure has also been initiated. Transport properties (R & TEP), Electronic transition, structural evolution, structural transition, P-V relation, HP-HT synthesis, comparison with theory [transition pressure, equation of state (EOS), details of electronic structure (anomalous EOS, Electronic Topological Transition, ETT, etc)] are the type of material behaviour being investigated. Variety of high pressure generating equipment like diamond anvil cells, piston-cylinder apparatus,

and room temperature was confirmed by electrical resistance (R) data and details of the band structure.

In  $MgB_2$ , R measurements up to 30 GPa revealed a discontinuous fall by approximately 30 % near 18 GPa. This is due to a phonon mediated ETT in  $MgB_2$ .

In  $Cd_8Hg_2$ , high-pressure angle dispersive X-ray diffraction measurements up to 40 GPa carried out at PURNIMA showed absence of any structural phase transition. However, the c/a ratio variation as a function of pressure show a small anomaly between 8 and 11 GPa. This anomaly could be due to the Van Hove singularity as observed in Cd and its isostructural alloys.

Alka B. Garg, B.K. Godwal, S. Meenakshi, P. Modak, R.S. Rao, S.K. Sikka and V. Vijayakumar, J. Phys.: Condense Matter 14, 10605



Diamond anvil cells—Diamond anvil cells have been adopted for angle dispersive X-ray powder diffraction, Optical spectroscopy, High temperature high pressure (HT-HP), and Electrical resistance measurements.

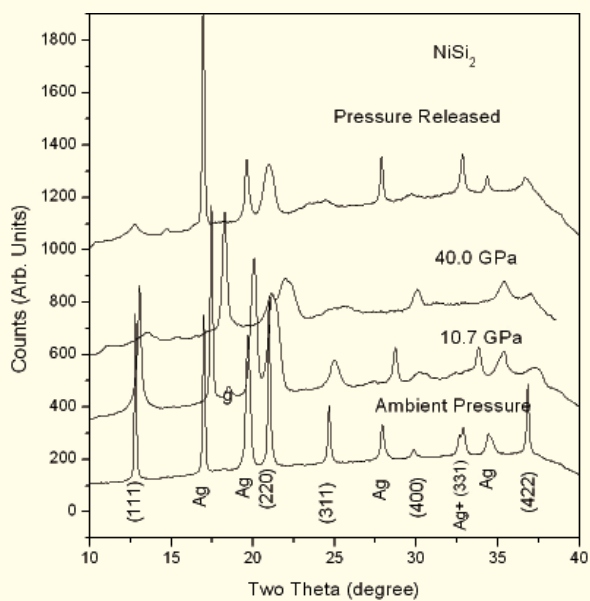
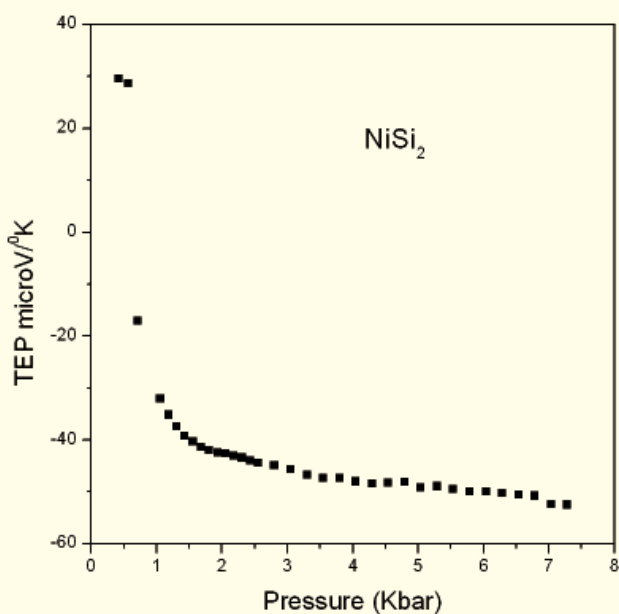
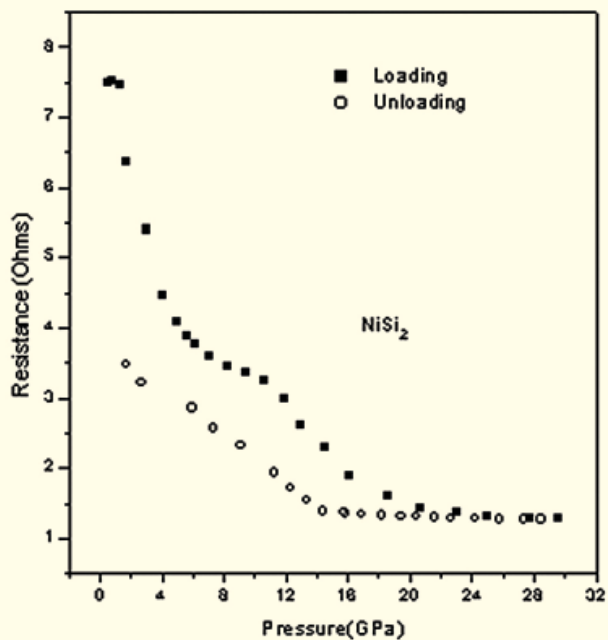
Toroid apparatus and Bridgman anvil apparatus have been fabricated and adopted to various measurements on condensed matter.

### ■ Electronic Topological Transition (ETT) at high pressures

An ETT involves changes in the Fermi surface topology, which takes place due to the modification of the band structure at extreme conditions of pressure. Transport properties and Equation Of State (EOS) are expected to show it's signature. Several materials were investigated by electrical resistance and EOS measurements. In Zn the presence of an ETT near 10 GPa

### ■ Investigations on intermetallics with $CaF_2$ structure

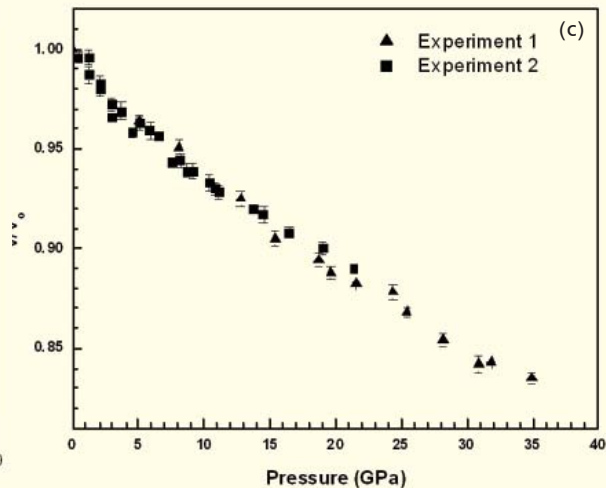
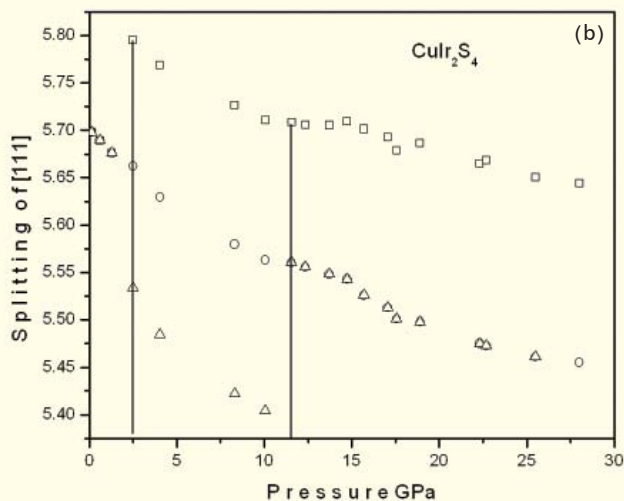
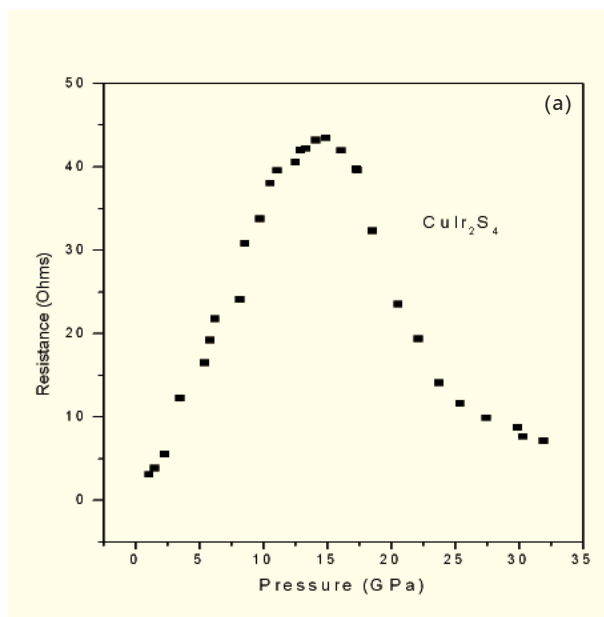
Intermetallics with  $CaF_2$  structure may undergo electronic and structural transitions and may transform into disordered phases under pressure. This is due to various reasons; most of them are entropy stabilized phases (volume expansion on compound formation), have partial covalent bonding, have a reduced transition metal d-orbital overlap etc. Several of these materials have been investigated ( $AuIn_2$ ,  $AuAl_2$ ,  $AuG_2$ ,  $PtAl_2$ ,  $NiSi_2$ ) with several interesting results (Electronic transition, structural transition, disordered phases etc). An interesting example is that of  $NiSi_2$ . This material exhibits a change in sign of TEP at 0.5 GPa, and a gradual structural disorder under pressure.



Electrical resistance, TEP and structure variation with pressure for NiSi<sub>2</sub>

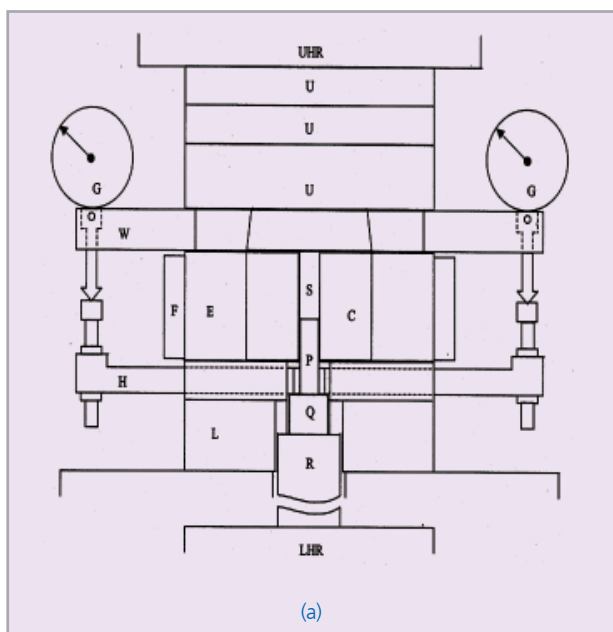
■ Investigations on strongly correlated systems

$\text{CuIr}_2\text{S}_4$  with spinel structure is a highly correlated system being investigated for several reasons. It exhibits interplay of structure, transition metal mixed valence ( $\text{Ir}^{3+}/\text{Ir}^{4+}$ ), magnetic ordering, metal-insulator transition,  $\text{Ir}^{4+}-\text{Ir}^{4+}$  dimerization, stabilization of an insulating phase at low temperature and high pressure etc. Investigations on  $\text{CuIr}_2\text{S}_4$  revealed the existence of a re-entrant metallic phase in it above 30 GPa (Fig. a) and two structural transitions (Fig. b). The manganese based intermetallics,  $\text{Mn}_3\text{GaC}$ , with cubic antiperovskite type structure falls in to an intermediate class of materials between the rare earth manganites and the normal metallic alloys. High pressure angle dispersive X-ray diffraction investigations on  $\text{Mn}_3\text{GaC}$  up to 35 GPa (Fig. c) aimed at investigating the signatures of the strong interaction between the magnetic and the structural properties of  $\text{Mn}_3\text{GaC}$  on the compressibility and its structural stability under pressure did not reveal any anomalies.

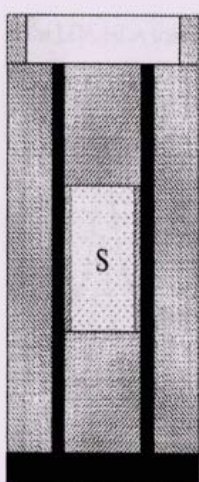


■ High temperature compressibility measurements

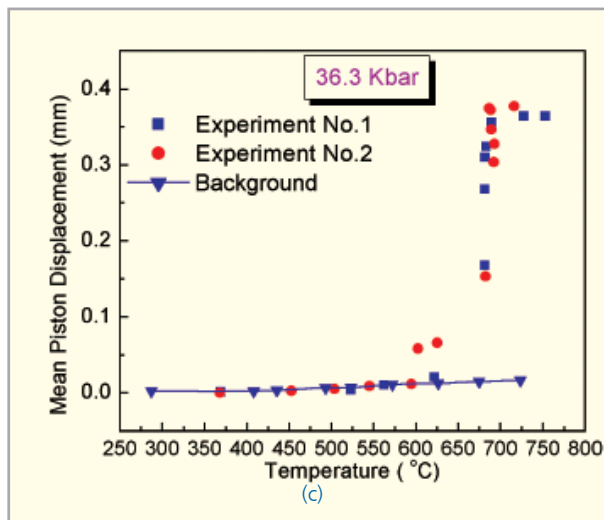
Compressibility measurements on solids at high temperature in the piston-cylinder high pressure (PC) apparatus (Fig. a & b), were performed on fused quartz. An apparently first order transition in fused quartz with a volume change of about 20% at 3.6 GPa and 680 °C was observed (Fig. c). The X-ray powder diffraction (XRD) and Raman measurements (Fig. d) on the quenched sample showed the transition to be from a low



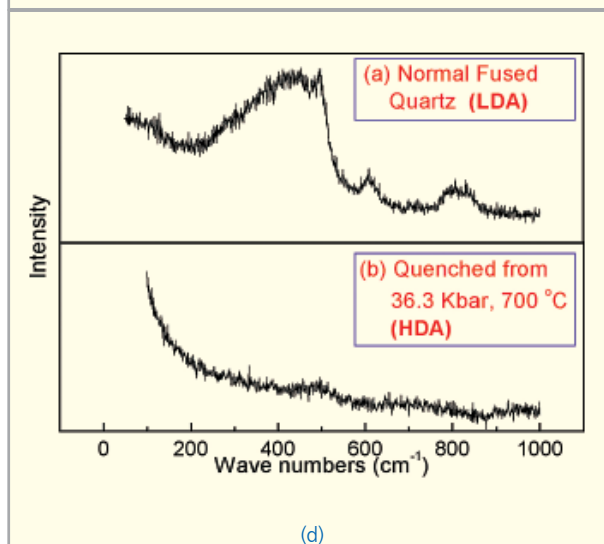
(a)



(b)



(c)



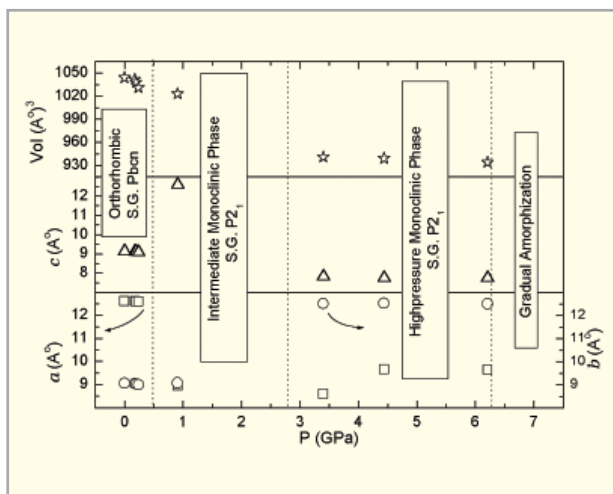
(d)

density amorphous phase to another high density amorphous phase. This work is the first application of PC set up for high temperature compressibility measurement.

Alka B. Garg, A. K. Verma, V. Vijayakumar, R. S. Rao and B. K. Godwal, Phys.Rev B (2005).

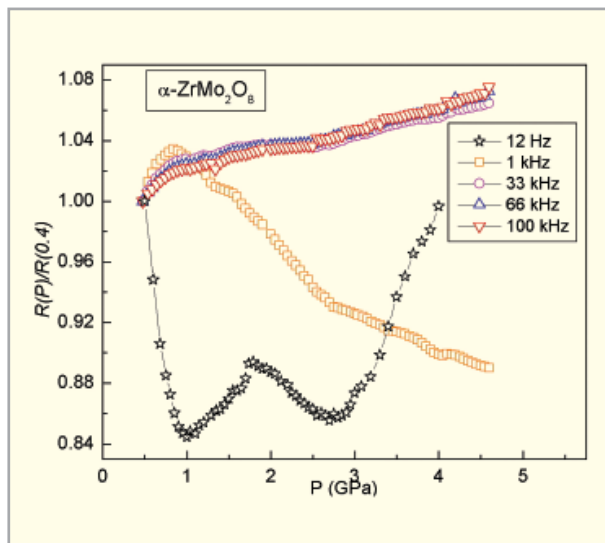
High pressure and high temperature studies on negative thermal expansion materials

Negative Thermal Expansion (NTE) is observed in the low-density phases of ionic compounds with  $MO_2$ ,  $AO_3$ ,  $AM_2O_7$ ,  $A_2M_3O_{12}$  and  $AMO_5$  stoichiometry (A & M are octahedral and tetrahedral cations), which have a three-dimensional open network structures with corner sharing polyhedra. NTE materials predisposed to display interesting behavior at high pressure and high temperature. Also such ceramic materials that exhibit NTE are of technological importance because of the ionic conductivity facilitated by cation disorder in them and because of the possibility to tune the thermal expansion of NTE-normal material composites. On our ongoing investigations on these NTE materials we have carried out high pressure and high temperature investigations on  $Al_2(WO_4)_3$ ,  $HfMo_2O_8$ ,  $ZrMo_2O_8$  and  $NbOPO_4$  belonging to a new subclass of compounds.

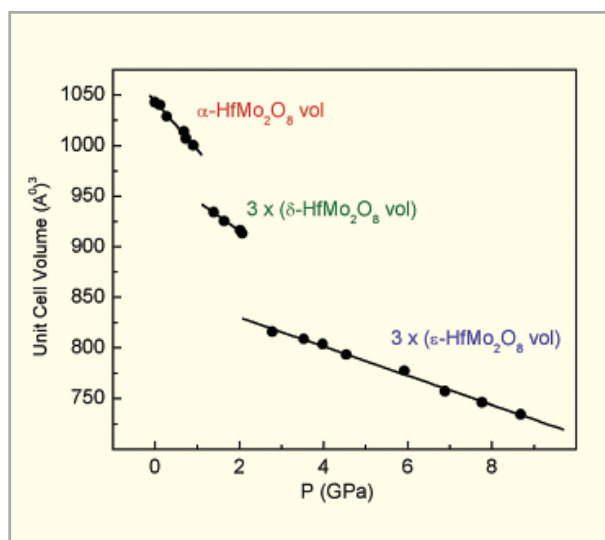


$Al_2(WO_4)_3$  phase diagram

Several structural transitions, a linear pressure volume relation or unusually large variation of bulk modulus over limited pressure region, pressure induced amorphization that fall into two categories (Kinetic hindrance to bond reconstructive transitions and decomposition) and a possibility of synthesis of new phases at high temperature and pressure are the highlights of these investigations.



R~P for  $ZrMo_2O_8$



EOS of  $HfMo_2O_8$

G.D.Mukherjee, V.Vijayakumar, A.S.Karandikar, B.K.Godwal, S.N. Achary, A.K. Tyagi, A.Lausi and E.Busetto, J.Solid State Chem., 178 (2005) 8.

## 2.2 SHOCK WAVE PHYSICS RELATED ACTIVITIES

### ■ Gas gun facility at BARC

For studying the response of material to high stress and strain rates a gas gun facility has been developed at our laboratory (Fig.). The gun is capable of accelerating the projectile upto the velocity of 1 km/s, and generating the pressure of 40 GPa in the target material.

The gun has three main parts: breech, barrel and target catcher system. The breech contains a gas at high pressure and breech opening mechanism provides within a few



Photograph of Gas Gun facility.

milliseconds the unrestricted flow of gas behind the projectile. The barrel is a 3 meter long high tensile strength steel pipe with outer diameter of 114 mm and inner diameter of 63 mm. A straight slot, 3 mm wide and 1.9 mm deep, has been machined in the internal surface of the barrel. Also, a 2.5 mm long brass key with the same cross-sectional dimensions as that of slot is fitted to the projectile. This key is guided through the slot during the acceleration of the projectile and facilitates the impacts of inclined parallel plates for compression-shear experiments. The target catcher system consists of two sections separated by a thick mylar diaphragm. The first section (target chamber) permanently mounted to the muzzle end of the barrel is evacuated to 10 millitorr using a rotary and roots vacuum pumps. The second section is movable and contains the projectile and target stopping mechanism. The firing of

the projectile is done with a remote control unit. The amplitude of the stress pulse in the target depends on the velocity of the impactor. The duration of shock (a few  $\mu\text{s}$ ) in the target is determined by the impactor thickness (a few mm) and impedance of the impactor and target material. The projectile can be accelerated to the desired velocity by suitably selecting the breech pressure. Diagnostic techniques like electrical pins, manganin gauge technique, self shorting pins, ionization pins and optical pins are used for measurement of projectile velocity, shock pressure and shock velocity. A series of four pairs of electrical pins are used to measure the projectile velocity just before the impact. The manganin gauge technique is used for measurement of time resolved stress profile and shock velocity in the shock-loaded target. The self-shortening pins, ionization pins and optical pins are used to measure the shock velocity in the target. For investigation of shock induced structural phase transitions in powder or brittle sample a special capsule (recovery fixture) is used for holding the sample. In these experiments, termed as recovery experiments, shock pressure in the sample is determined indirectly from the hydrodynamic code in conjunction with measured projectile velocity. The sample recovered after unloading from peak shock pressure is characterized through X-ray diffraction and Raman measurements for any irreversible phase transition.

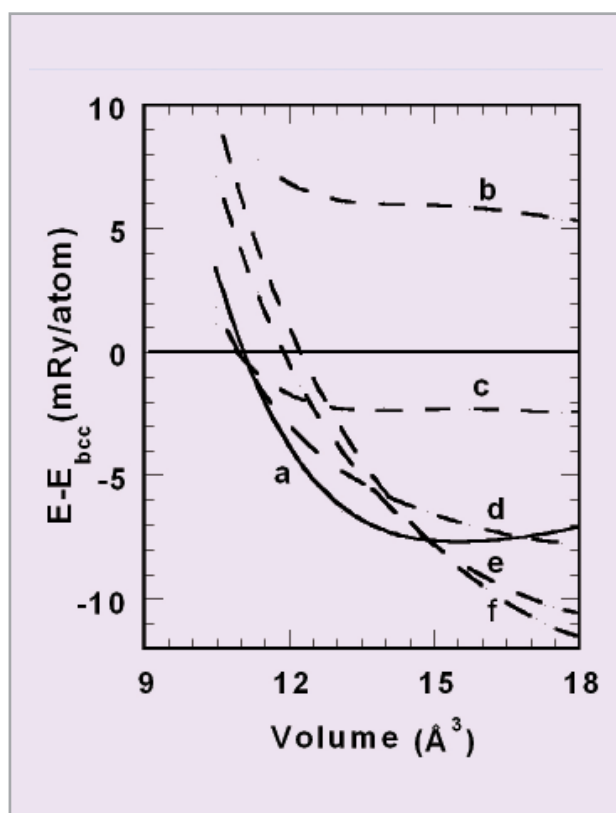
Satish C.Gupta, R.G. Agarwal, J.S. Gyanchandani, S. Roy, N. Suresh, S.K. Sikka, A. Kakodkar and R. Chidambaram, in Shock Compression of Condensed Matter-1991 (ed. S.C Schmidt, R.D. Dick, J.W. Forbes and D.G. Tasker) pp. 839.

Satish C. Gupta, R.G. Agarwal, J.S. Gyanchandani, S. Roy, N. Suresh, S.K. Sikka, A. Kakodkar and R. Chidambaram, BARC Report No. BARC/1995/E/017.

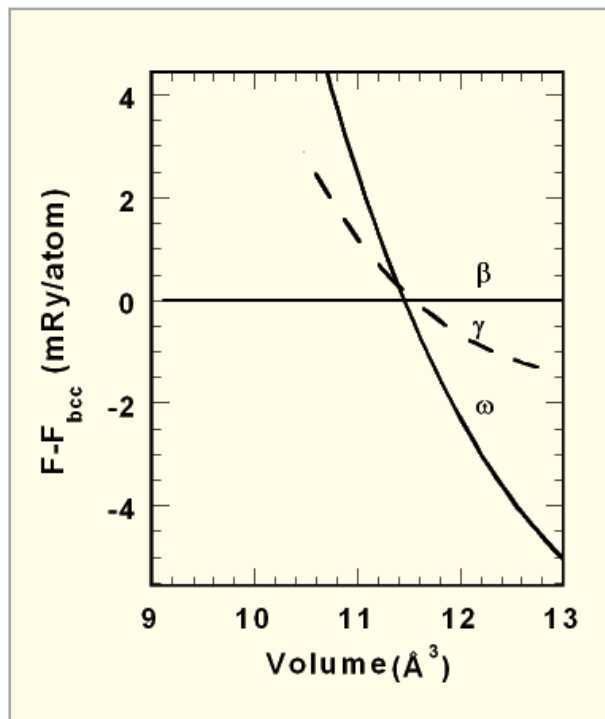
### ■ Theoretical Investigation of Pressure Induced Phase Transition in Ti at High Pressures

The group IV B elements are expected to undergo  $s-d$  electron transfer under pressure and, thus, mimic the transformation sequence  $\alpha \rightarrow \omega \rightarrow \beta$  shown by these elements with increasing number of  $d$  electrons on alloying with  $d$ -electron rich neighbors. This structural sequence under pressure is well established for Zr and Hf. However, Ti metal has been reported to undergo a transition from hexagonal phase ( $\omega$ ) to an orthorhombic phase (distorted hcp,  $\gamma$ -phase) at 116 Gpa,

whereas there are also reports that titanium undergoes a transition to the  $\gamma$ -phase from the  $\omega$ -phase. To resolve this we have carried out total energy calculations employing the FP-LAPW method to examine the stability of the  $\gamma$  and  $\delta$  phase with respect to the  $\omega$  and  $\beta$  structures. Our analysis predicts at 0 K the  $\omega$ -phase transforms to  $\beta$ -phase via intermediate  $\gamma$ -phase, whereas at 300 K the  $\omega$ -phase transforms to  $\beta$  structure directly and the  $\gamma$ -phase becomes most competing metastable structure in the pressure range of  $\beta$ -phase stability. The  $\delta$ -phase, however, is not at all stable at any compression. It suggests that the  $\gamma$ -phase observed in the experiments is a metastable phase that could be formed due to the shear stresses present in the experiments and the  $\omega \rightarrow \gamma$  structural transition does not represent the phenomenon expected under hydrostatic conditions.



Calculated energy difference of the  $\omega$  and  $\gamma$ -phase with respect to  $\beta$ -phase as a function of volume of unit cell. The curve 'a' corresponds to the  $\omega$  phase; b, c, d, e and f correspond to the  $\gamma$ -phase with  $y$  as 0.08, 0.10, 0.12, 0.14 and 0.16, respectively.



Free energy at 300 K plotted with respect to  $\beta$ -phase as a function of volume for the  $\omega$ ,  $\beta$  and  $\gamma$  ( $y = 0.1$ ) phases.

K.D. Joshi, G. Jyoti, Satish C. Gupta and S.K. Sikka, Phys. Rev. B 65, 0252106, 2002.

K.D. Joshi, G. Jyoti, Satish C. Gupta and S.K. Sikka, J. Phys. Cond. Matter, 14, 1, 2002.

#### ■ *Ab-initio* Calculations for Comparison of Hardness of Osmium and Diamond

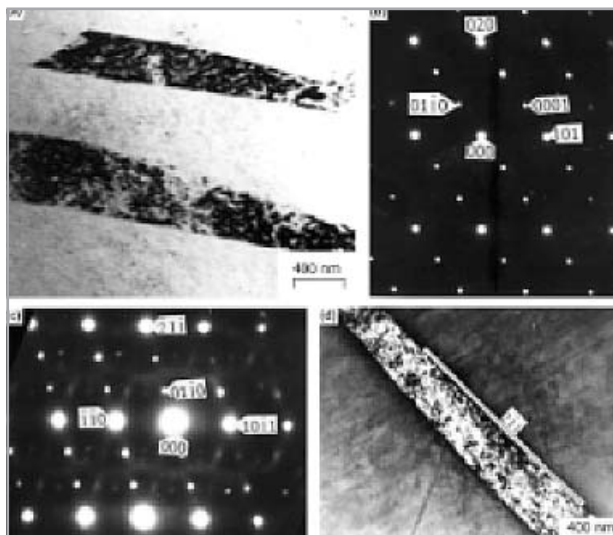
On the basis of the high-pressure diamond anvil cell experiments on Os metal, Cynn et al. have reported that the bulk modulus of this metal is 462 GPa, higher than that of diamond (445 GPa), the hardest material known so far. Based on this they concluded that it has lower compressibility than diamond. We have reanalyzed the experimental data of Cynn et al and found that the bulk modulus of Os (434 GPa) and diamond are close to each other, implying that Os metal is as incompressible as the diamond but not more. We also, performed the first principles total energy calculations on Os and diamond using full potential linearised augmented plane wave method under both Local Density Approximation (LDA) and Generalized Gradient Approximation (GGA). For LDA calculation the value of  $B_0$  estimated from Birch –Murnaghan fit is 461 GPa for

osmium and 464 GPa for diamond. From GGA calculations, this parameter is estimated as 436 GPa and 432 GPa, respectively, for the two elements. Thus, we find the theoretical values of  $B_0$  for Os are comparable to the corresponding values of diamond for both LDA and GGA calculations.

K.D. Joshi, G. Jyoti, and Satish C. Gupta, High Press. Res., 23, 403, 2003.

### ■ TEM Study on Shock Compressed Zr-20 Nb Alloy

The TEM study on shock compressed Zr-20 %Nb alloy have been done in collaboration with Materials Science Division, BARC. This alloy having bcc ( $\beta$ ) structure at ambient condition was subjected to a peak shock pressure of 15 GPa in a 63 mm bore gas gun at our laboratory. The electron diffraction measurements of the retrieved sample confirmed the  $\beta \rightarrow \omega$  transformation. The  $\beta \rightarrow \omega$  transformation has been observed for the first time in an alloy under shock compression. The  $\omega$ -phase so formed has plate shape morphology and orientation relationship have been found same as that observed



Microstructure after shock loading of  $\beta$ -Zr-Nb:  
 (a) Bright field electron micrograph shows plate shaped  $\omega$  phase,  
 (b) SAD Pattern along zone axis [1 1 0],  
 (c) SAD Pattern: zone axis [1 1 3], (d) bright field electron micrograph shows steps and waviness at the  $\omega/\beta$  interface.

in  $\omega$ -phase formed on thermal treatment of the alloy. The formation of the  $\omega$ -phase has been explained on the basis of shear and shuffle of atoms on  $\{112\}\beta$  planes.

G.K. Dey, R. Tewari, S. Banerjee, G. Jyoti, Satish C. Gupta, K.D. Joshi and S. K. Sikka, Phil. Mag. Lett. 82, 333, 2002.

G.K. Dey, R. Tewari, S. Banerjee, G. Jyoti, Satish C. Gupta, K.D. Joshi and S. K. Sikka, Acta Materialia. 52, 3243, 2004.

### ■ Theoretical Spall Strength and Equation of State of Materials in Negative Pressure Regime

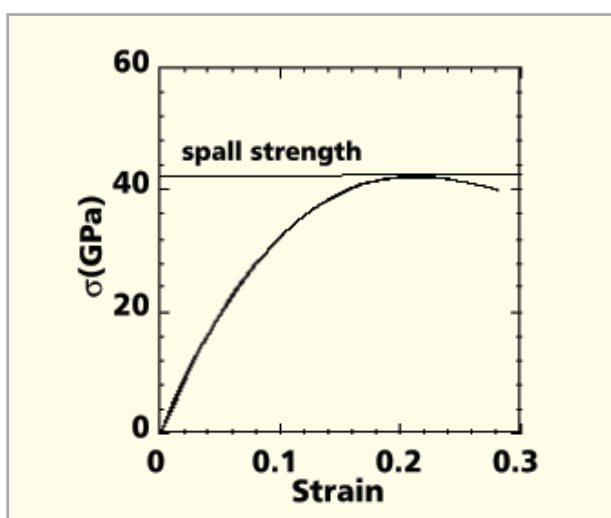
The shock compression experiments generate not only the compressive high pressures but also high tensile stresses. Sophisticated diagnostic techniques like VISAR and ORIVIS, used recently to measure such tensile stresses, throw light on the material behavior in the negative pressure regimes. We have determined the ideal spall strength ( $\sigma_s$ ) and also, the equation of state (EOS) in the negative pressure region for Mo and group IV B metals (Ti, Zr and Hf) from first principles total energy calculations using full-potential linearised augmented plane wave (FP-LAPW) method (WIEN97 Package). For Mo, we have calculated the ideal tensile strength ( $\sigma_T$ ) and the elastic constants also. The  $\sigma_s$  is calculated using uni-axial strain i.e. without allowing the Poisson contraction, however for  $\sigma_T$  the Poisson contraction was also allowed.

The calculated  $\sigma_s$  along [1 0 0] for Mo is 41 GPa as compared to the experimental value of 16.5 GPa measured after unloading the sample from peak pressure of 75 GPa (strain rate  $\sim 3 \times 10^7/s$ ). Our calculated  $\sigma_T$  value is 23 GPa. The calculated equilibrium volume is  $15.96 \text{ (\AA)}^3/\text{atom}$ , elastic constants  $c_{11}$ ,  $c_{12}$ ,  $c_{44}$  are 439, 175, 100 GPa, and  $B_0$ ,  $Y(1 0 0)$ ,  $Y(111)$  are 272, 339, 266 GPa, respectively.

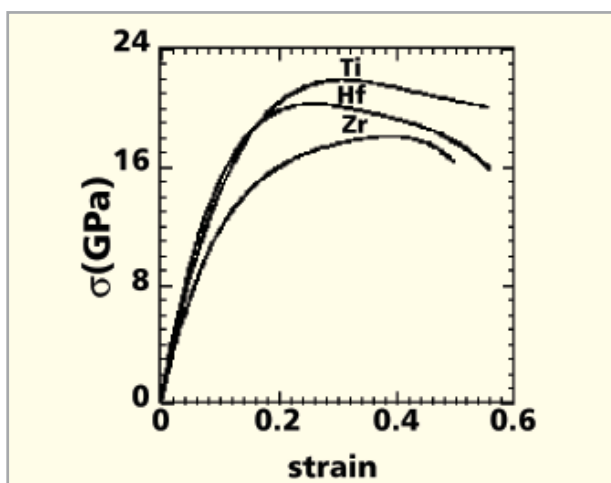
For Ti, Zr and Hf we have determined  $\sigma_s$  along [0001] direction for hcp ( $\alpha$ ) and three atom hexagonal phase ( $\omega$ ). The calculated  $\sigma_s$  for  $\alpha$  phase of Ti, Zr and Hf is 22, 18 and 20 GPa, and for the  $\omega$  phase is 24.2, 19.5 and 23.6 GPa, respectively. The  $\omega$  phase is found to be harder than  $\alpha$  phase in agreement with available experimental results. The trend in the group IV B indicates that  $\sigma_s$  for Ti is largest followed by Hf and then Zr for both  $\alpha$  and  $\omega$  structures. The theoretical  $\sigma_s$  for Ti is much

higher than  $\sim 4.2$  GPa measured at strain rates of  $\sim 10^6/s$ . The bulk modulus of 110, 96 and 115 GPa, respectively for Ti, Zr and Hf, determined from the theoretical EOS in the negative pressure region, are in good agreement with experiments.

The theoretical value of the  $\sigma_s$  for Mo and Ti are higher than the available experimental values. This discrepancy could be associated with the material defects, which dominantly control the spalling at such strain rates. For determination of ideal  $\sigma_s$ , experiment should be performed at still higher stresses (and higher strain rates) to minimize the effects of material defects.



Tensile stress as a function of strain for Mo



Tensile stress as a function of strain for Ti, Zr and Hf

K.D. Joshi and Satish C. Gupta, Joint-AIRAPT International Conference on High Pressure Science and Technology, 2005.

K.D. Joshi and Satish C. Gupta, APS Topical Conference on Shock Compression of Condensed Matter, 2005.

### 2.3 PULSED HIGH ENERGY DENSITY RELATED ACTIVITIES

#### ■ Pulsed High Magnetic Field Generation for Material Compression and EMP Generation Studies

High magnetic fields (greater than 100 Tesla) are generally produced in pulsed ( $\mu s$ -ms range) form using capacitor banks. These fields may be further enhanced through compression of metallic liners (cylindrical shells) in which initial magnetic field may be trapped and then compressed using secondary energy source such as another capacitor bank or chemical explosives. When the current is along the Azimuthal direction of the cylinder, the configuration is known as Theta-pinch or otherwise if it along the axial direction of the cylinder, the configuration is termed as Z-pinch. As a first step towards experiments on the mega gauss field generation at Applied Physics Division, field compression devices using Z-pinch and  $\theta$ -pinch as also single turn coils have been developed.

#### Experiments on Magnetic Field Generation for Material Compression:

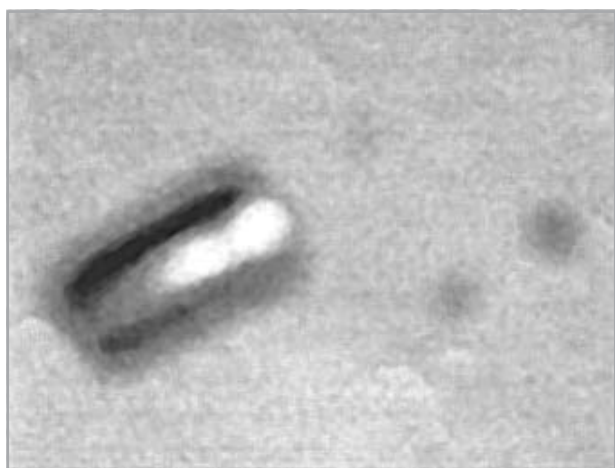
Experiments have been carried out to investigate material compression using single turn coils made out of copper with 10 mm central hole for magnetic field generation. These coils have been fired on MAGIC-280 capacitor bank (340.8 mF/ 40 kV) at peak currents of 2-2.5 MA. An estimated peak magnetic field of 150-160 Tesla was produced in several shots. In some of the experiments, a titanium chip suitably confined in metallic layers to minimize the effect of induced currents (thereby avoid pre-heating) was placed to look for phase transitions.

#### Field compression device in Z-pinch configuration:

The Z-pinch field compression device consists of initial magnetic field system, accelerating field system and imploding liner system. The initial magnetic field system includes a coil and



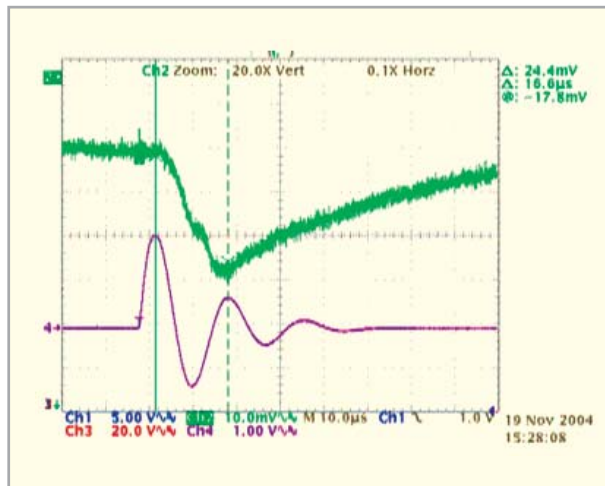
Coil before and after shot (2.2 mA unconfirmed geometry)



Recovered Titanium chip

2.5 mF/5 kV Capacitor bank. The bank is configured to give 60 kA at 100 micro-sec when charged to 5 kV. The initial field with suitably designed coil is about 8.52 kOe. The acceleration of the liner is carried out by 340 micro-F/40 kV MAGIC-280 Capacitor bank. The implosion velocity of the suitably designed liner is estimated to be about 0.317cm/micro-sec when the bank discharge current is about 2 MA. Flux is compressed as long as the effective implosion speed exceeds the flux diffusion speed. When the two velocities become equal the compressed field will go through its maximum. With the sub bank charging voltage= 3.1 kV, MAGIC charging voltage=25.2 kV, Triggered Spark gap voltage=25 kV, probe calibration = 0.33 kOe/mv, the signal obtained from the center multi-turn probe is as shown below. From the measurements carried out using multi-turn magnetic probe at the center of the liner, the initial

field has been estimated to be about 7.46 kOe, which is compressed to a maximum of about 40 kOe. Higher results are expected with better insulation design.



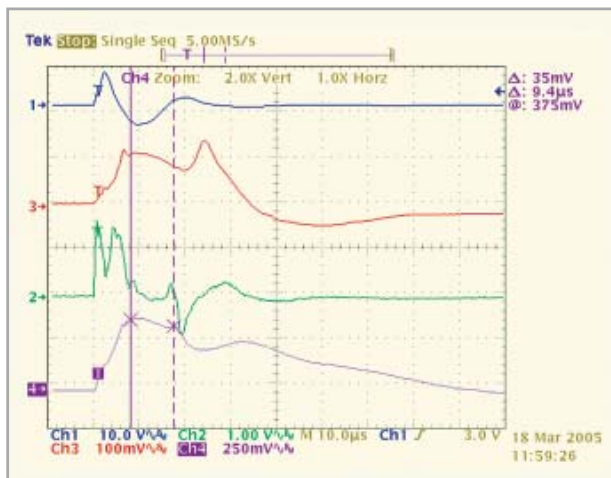
Center probe signal



Field Compression device before and after shot

**Field compression device in  $\theta$ -pinch configuration:**

In  $\theta$ -pinch configuration device, the MAGIC-280 capacitor bank is discharged through a thick single turn coil, with a thin liner placed co-axially. The liner (0.8 mm thick) is accelerated to maximum velocity of 0.7 cm/micro-sec, when the bank discharge current is about 1.07 MA. The maximum field obtained at the center is about 1.94 MOe, when the MAGIC charging voltage is about 16 kV and triggered spark gap voltage 25 kV. The signals obtained from the centrally placed 2-turn probe, are shown in figure.

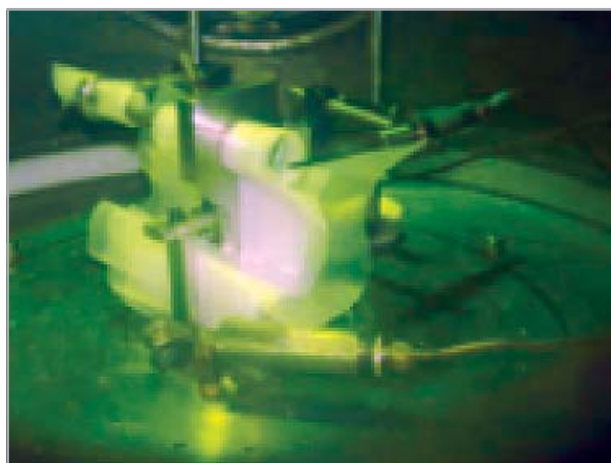


Center probe signal

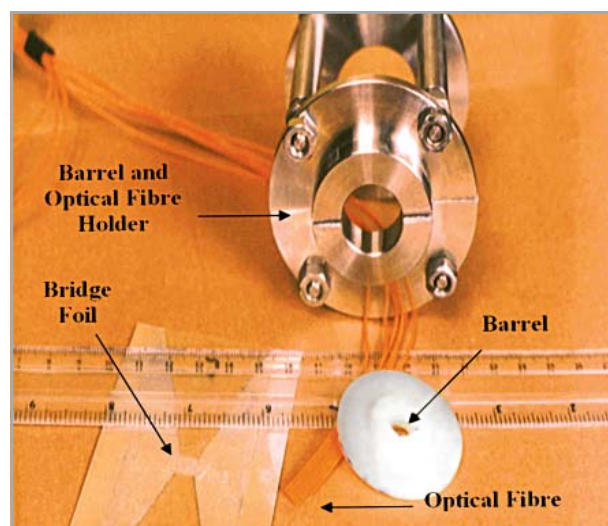
the Petzold-Gear BDF method with given initial data for  $y$  and  $y'$ . Neglecting the non-uniform deformation of the liner, which requires magneto hydrodynamic calculations, the center field obtained as per simulation is shown in the figure. The peak field at the center and the time to peak matches well with the published results.

T. C. Kaushik, *Advances in High Pressure Science & Technology*, A. K. Bandyopadhyay, D Varandani and K. Lal (eds.), (NPL, New Delhi, 2001) p. 137.

■ Exploding Foil Accelerator (Electric Gun) with Opening Switch Action



Field compression device connected to the load



Important Components of the EEF Experimental assembly

**Numerical analysis of electro-magnetically driven flux compression generator**

Electro-magnetically driven flux compression generators are single shot and destructive in nature. To carry out prior analysis, we have developed a numerical model in "1-dimension", considering the current distribution as a function of time. The circuit equation for axial current, azimuthal current, radius and inductance variation for each current, forms a set of ordinary differential equation. These first order differential-algebraic system of equations,  $g(t, y, y') = 0$ , are solved using

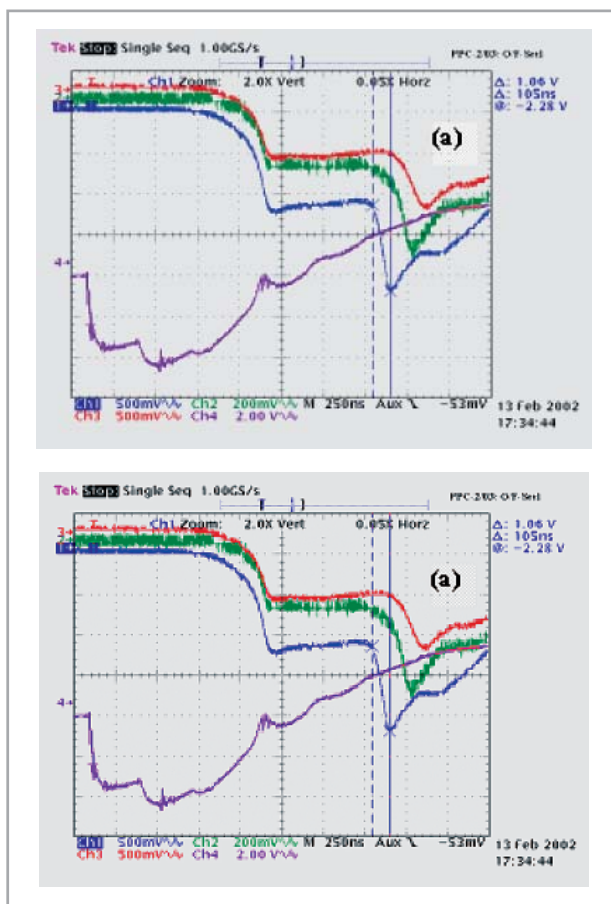
Exploding foil accelerator (Electric Gun) is based on the explosion of a thin metallic foil when subjected to rapid ohmic heating due to passage of high currents in short duration. A thin plastic sheet placed in front of the exploding foil is then punched out as the exploded foil plasma expands into "barrel". The velocity in such a system is highly sensitive to the rise time of the current. To experimentally demonstrate this fact and realize a higher velocity with the same capacitor bank system,

a concept of sharpening the current profile with an additional stage of exploding foil to act as an opening switch was adopted. A flyer velocity of 6.6 km/s, obtained with a single stage electric gun, was found to be enhanced to 7.4 km/s when additional stage was utilized. When properly optimized, it is expected to go up to twice the value using single stage. The flyer velocity was determined using a fast streak camera as well as a set of optical fibers.

As an extension of this work, an opening switch is being designed to generate MV/ sub- $\mu$ s pulses while the electric gun is being developed along with necessary diagnostics to characterize energetic materials, which cannot be employed in large quantities.

■ **A Compact Pulsed Neutron Source Based on Plasma Focus Device**

Recently, a few compact Plasma Focus (PF) devices have been developed and operated at Applied Physics Division to generate pulsed neutrons on a routine basis. The device is like a narrow co-axial plasma gun. The narrow PF tubes are of 5 cm in diameter and 15 to 20 cm in length (Fig.). The central anode and the outer cathode are made of stainless steel. Smooth and non-porous alumina ceramic sleeve is used as insulator at one end of the tube. Commercially available high purity alumina ceramic tubes are polished to make these tubes compatible to the PF operations. A capacitor bank (Fig.) made with a capacitor of 7.2  $\mu$ F is used as the energy source.

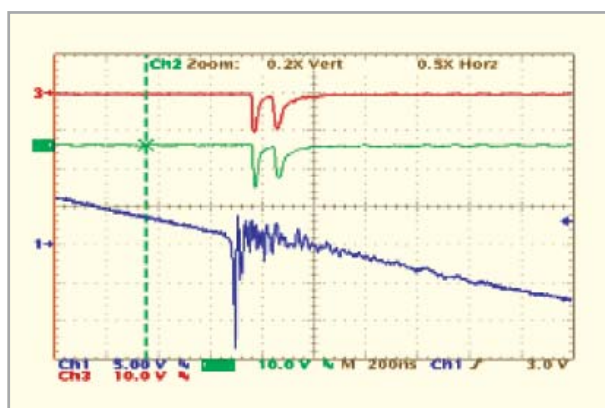


Signals from dI/dt loop and a set of 3 photodiodes (a) Single exploding foil and (b) two exploding foils.



PF device

Capacitor bank with PF device



Typical Signals from PF X-rays (top two) and neutrons current derivative (bottom).

T. C. Kaushik et al, IEEE Transaction in Plasma Science, 30(6), 2133

Conventional power supply and trigger units based on electricity supply were employed to charge and discharge the capacitor bank through the plasma focus device. But to make it portable type, for one of the plasma focus devices, the capacitor bank was charged to same voltage by a battery based power supply. The trigger unit of the spark gap used to discharge the capacitor through the PF device was also battery based.

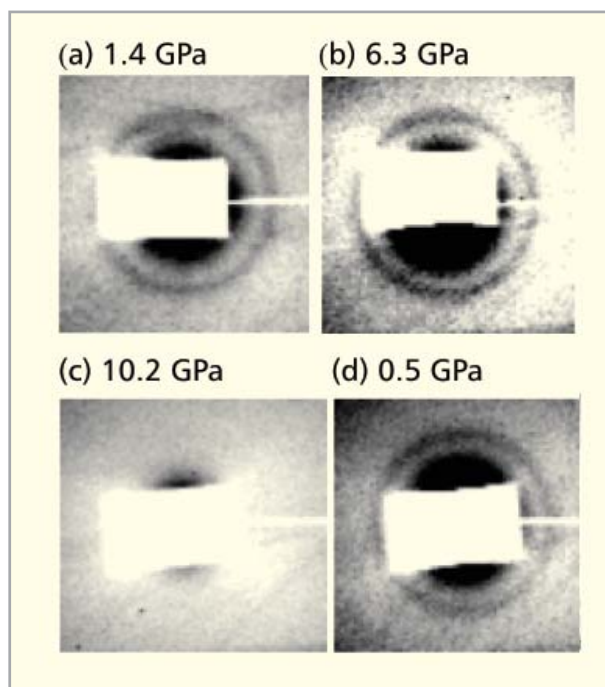
A calibrated silver activation detector and two plastic scintillator detectors are deployed for the measurements of emitted neutrons. The current derivative is monitored by a Rogowski loop. The device is normally operated at 25 kV at a deuterium filling pressure of 6 mb. Pulsed 2.45 MeV neutrons of  $\approx 10^7$  neutrons/pulse are generated due to D-D reaction. The pulse width of the neutron is 25 – 30 ns

With some modification and dimensional optimization of the plasma focus device it is expected to generate  $\approx 10^8$  neutrons/pulse for which work is in progress.

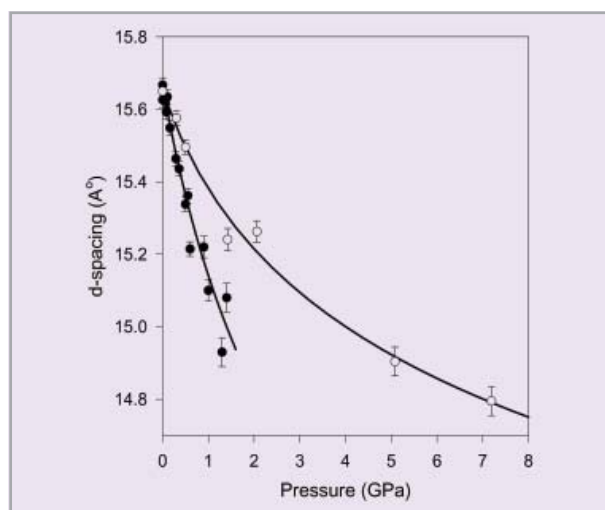
#### 2.4 MECHANICAL RESILIENCE OF SINGLE-WALLED CARBON NANOTUBES (SWNTS)

Single walled carbon nanotubes (SWNTs) are known to form two-dimensional triangular lattice by self-organizing into bundles. Our high pressure X-ray diffraction experiments, carried out with synchrotron X-rays, along with Raman measurements provide the understanding of the mechanical properties. X-ray diffraction studies on (11,11) SWNTs show that, under hydrostatic pressures, the radial strain is released prior to the reversible loss of lattice order in SWNTs.

Under non-hydrostatic pressures, the lattice order is found to vanish at  $\sim 2$  GPa, which becomes irreversible for compression beyond 6 GPa, in sharp contrast to our studies under hydrostatic conditions. Moreover, nanotubes are found to be much more compressible under non-hydrostatic conditions (bulk modulus (B)  $\sim 10$  GPa) than under hydrostatic pressures (B  $\sim 34$  GPa). However, the reappearance of the radial breathing modes (RBM) and tangential modes (TM) on release of pressure in the Raman measurements implies that the ordering of tubes in the pressure quenched SWNT bundles is marginally regained, with short coherence length, but not enough for the emergence of X-ray diffraction peaks.



Characteristic diffraction ring of the SWNTs at various hydrostatic pressures, (a-c) for increasing pressure and (d) for decreasing pressures [Pattern recorded at BL10XU beamline of SPring8 synchrotron].



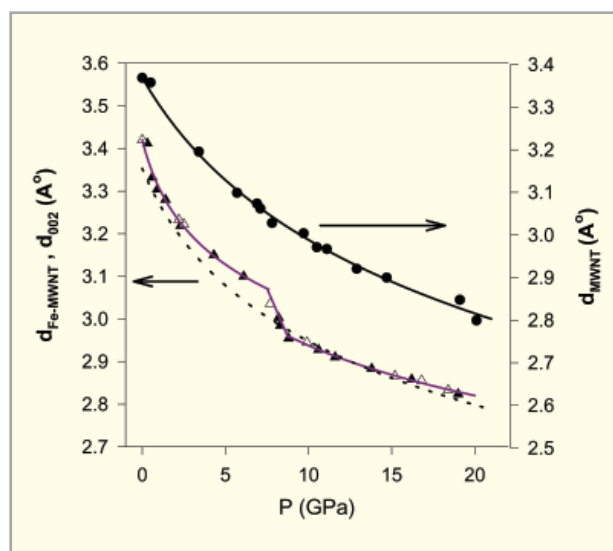
Variation of d-spacings under various non-hydrostatic (filled circles) and hydrostatic (open circles) pressures.

Surinder M. Sharma, S.Karmakar, S.K.Sikka, P.V.Teredesai, A.K. Sood, A.Govindraj, C.N.R.Rao, Phys. Rev. B 63 (2001) 205417  
S.Karmakar, Surinder M. Sharma, P.V.Teredesai, D.V.S. Muthu, A. Govindraj, S.K.Sikka, A.K.Sood, New J. Phys.5 (2003) 143.

## 2.5 STRUCTURAL AND MAGNETIC BEHAVIOUR ON Fe-FILLED MULTI-WALLED CARBON NANOTUBES (MWNTS)

High pressure angle dispersive X-ray diffraction experiments, were carried out up to  $\sim 20$  GPa, at the 5.2 R beamline of the Elettra synchrotron. Encapsulated iron inside nanotubes is found to be in the form of  $\alpha$ -Fe and  $\text{Fe}_3\text{C}$ . Unlike pristine MWNTs, the intertubular distances ( $d_o$ ) for the filled tubes undergo a sharp change at  $\sim 9$  GPa, as shown in Fig., possibly due to polygonization of the tubes. Mechanical properties of  $\alpha$ -Fe and  $\text{Fe}_3\text{C}$  are found to be very different (more compressible) from their bulk counterparts. The structural transition in MWNTs is coincident with an iso-structural phase transition in  $\text{Fe}_3\text{C}$  at  $\sim 9$  GPa, in sharp contrast to the absence of a transition in the bulk  $\text{Fe}_3\text{C}$  up to 70 GPa.

Magnetic behaviour of Fe-filled MWNTs has also been investigated with the *dc* magnetization measurements. Our results show that the encapsulated nanowires form one dimensional exchange coupled ferromagnetic system. Observed saturation magnetization,  $M_s$  ( $\sim 85$  emu/g), of the composite nanowires is found to be significantly less than the expected



Pressure variation of average intershell distance ( $d_o$ ) for filled tubes (triangles) and for pristine MWNT (solid circle). The  $d_{002}$  line of graphite is also plotted (dash line).

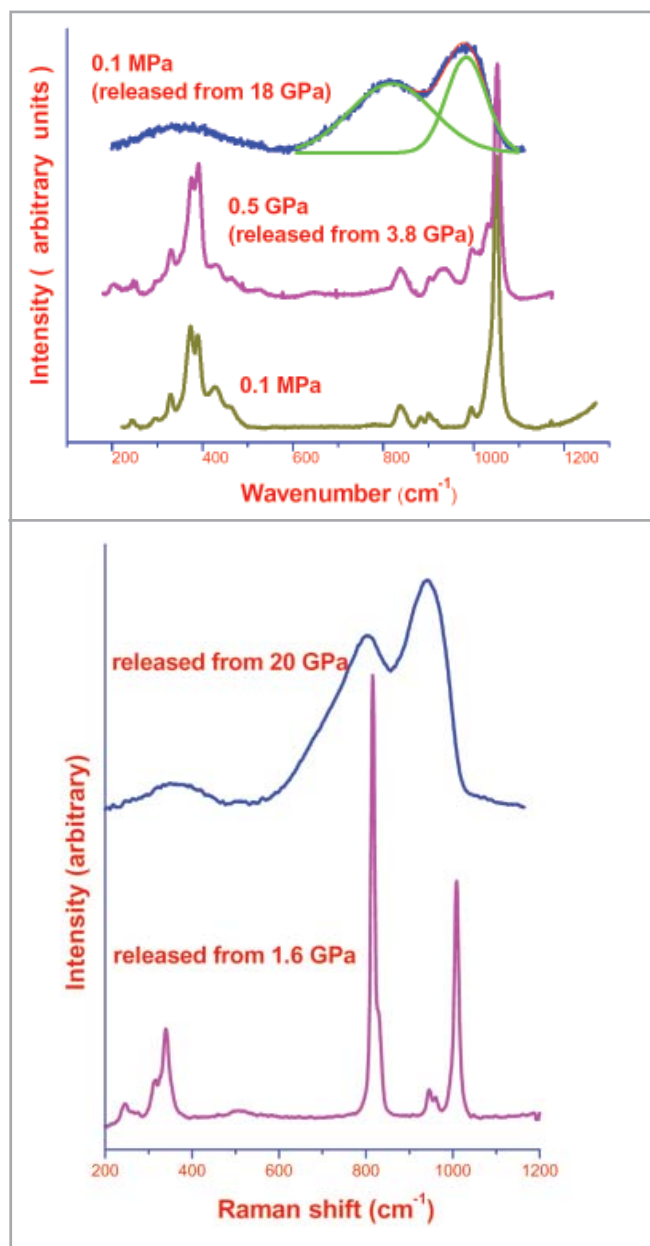
value. The observed low temperature hysteresis loop shift in the field cooled (FC) case, earlier explained in terms of the onset of antiferromagnetism in fcc Fe ( $\gamma$ -phase) at low temperature ( $< 50$  K) and its exchange coupling with the  $\alpha$ -Fe (assuming that  $\alpha$ -Fe and  $\gamma$ -Fe in the nanowire have a common interface). However, as our data shows the negligible abundance of  $\gamma$ -Fe, we feel that the hysteresis loop shift originates from the occurrence of exchange bias due to the disordered surface spins of the Fe nanowire.

S.Karmakar, Surinder M.Sharma, M.D. Mukadam, S.M.Yusuf, A.K. Sood, J. Appl. Phys. 97 (2005) 54306

S.Karmakar, Surindar M. Sharma, P.V. Teredesai and A. K. Sood, Phys. Rev. B 69, (2004) 65414.

## 2.6 IRREVERSIBLE AMORPHIZATION OF NEGATIVE THERMAL EXPANSION MATERIALS

Negative thermal expansion behavior (NTE) of the substances is useful in helping design materials with the appropriately tuned coefficient of thermal expansion. Some of the important NTE materials are zircon, zirconium tungstate,  $\text{A}_2(\text{MO}_4)_3$  compounds (where  $\text{A}=\text{Al}$ ,  $\text{Sc}$ ,  $\text{Lu}$ ,  $\text{Yb}$ ,  $\text{Tm}$ ,  $\text{Er}$ , and  $\text{Y}$  and  $\text{M}=\text{Mo}$ ,  $\text{W}$  etc.). We have studied the high pressure behavior of some of these compounds like  $\text{Y}_2(\text{WO}_4)_3$ ,  $\text{Al}_2(\text{WO}_4)_3$ ,  $\text{Sc}_2(\text{WO}_4)_3$  and a double molybdate  $\text{KSc}(\text{MoO}_4)_2$  using X-ray diffraction and Raman scattering techniques.  $\text{Y}_2(\text{WO}_4)_3$  is known to have the largest isotropic negative thermal expansion in this set of materials and our experiments show that it also has the largest NTE stability range. We have observed that  $\text{Al}_2(\text{WO}_4)_3$  and  $\text{Sc}_2(\text{WO}_4)_3$  show several phase transitions to lower symmetry structures prior to the transformation to a highly disordered state at  $\sim 7$  GPa, whereas  $\text{Y}_2(\text{WO}_4)_3$  amorphize directly at  $\sim 4$  GPa. In all these materials it was observed that the high pressure disordered phase is retained on release of pressure. Earlier studies had suggested that pressure induced amorphization in these materials maybe related to the softening of the transverse acoustic modes responsible for NTE. Even though, amorphization of yttrium tungstate supports this suggestion, the presence of precursor monoclinic phases prior to amorphization in  $\text{Sc}_2(\text{WO}_4)_3$  and  $\text{Al}_2(\text{WO}_4)_3$  raises a doubt on this relationship, as the monoclinic phases are known not to exhibit negative thermal expansion.

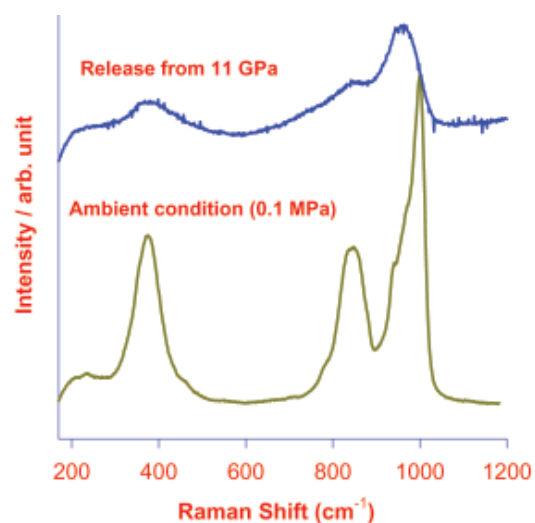


Raman measurements on  $\text{Al}_2(\text{WO}_4)_3$ ,  $\text{Sc}_2(\text{WO}_4)_3$ ,  $\text{Y}_2(\text{WO}_4)_3$  show that the amorphous phase is retained on release of pressure.

Nandini Garg, Chitra Murli, A.K. Tyagi and Surinder M.Sharma, Phys. Rev. B 72, (2005) 64106

S.Karmakar, S.K.Deb, A.K.Tyagi, Surinder M. Sharma, J.Solid State Chem 177 (2004) 4087

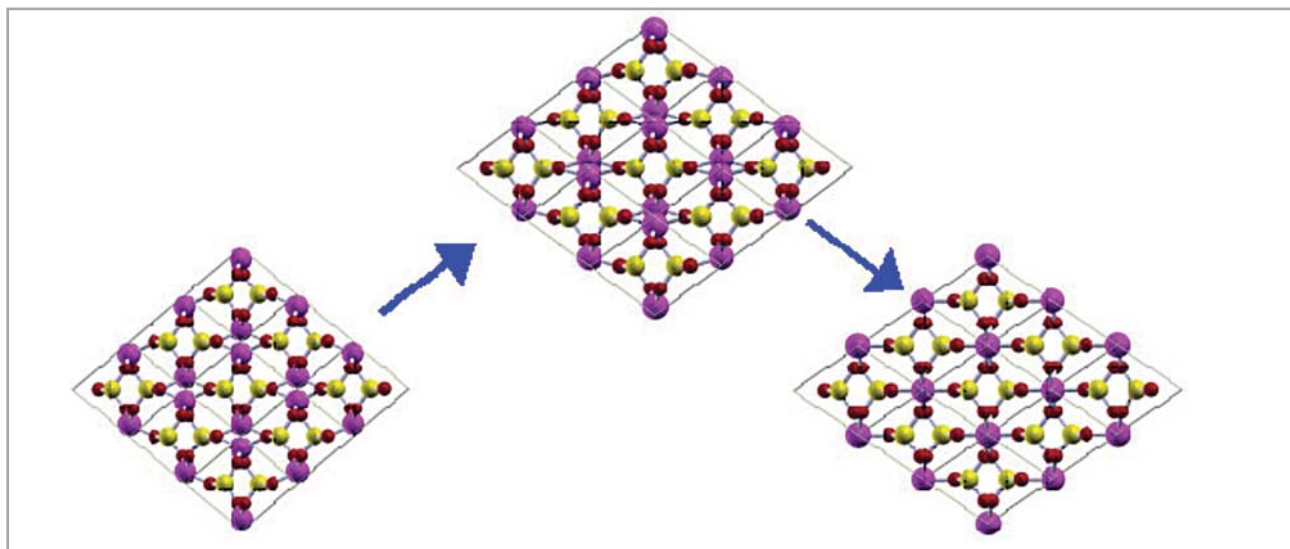
Nandini Garg, Vinod Panchal, A.K.Tyagi, Surinder M Sharma, J. Solid State Chem. 178 (2005) 998



## 2.7 STRUCTURAL CHANGES IN CRISTOBALITE- $\text{AlPO}_4$ UNDER HIGH PRESSURES

Several geologically important minerals of the earth's crust exist in the tetrahedral framework structures, made of corner linked tetrahedral units. The corner linkage acts as a flexible hinge between the tetrahedra, permitting the existence of several polymorphs. Therefore, it is expected that silica polymorphs like quartz, cristobalite etc. and the iso-structural materials like berlinite, orthorhombic  $\text{AlPO}_4$  etc. would show phase transitions. In particular, the pressure induced structural modifications of these materials provide important information for the modeling of the transition zone between upper and lower mantle of the earth. We have studied several of these compounds using experimental and theoretical techniques like X-ray diffraction, Raman spectroscopic studies, classical and first principle molecular dynamics.

Our recent Raman spectroscopic and X-ray diffraction studies have shown that cristobalite form of  $\text{AlPO}_4$  transforms to Cmc21 phase at 8.1 GPa under hydrostatic pressures. The new Cmc21 phase is found to be stable even at  $\sim 40$  GPa and  $310^\circ\text{C}$ . To understand the mechanism of this transformation, we have carried out classical molecular dynamical as well as the first principles structural relaxation calculations. Fig. shown delineates the path of this transformation.



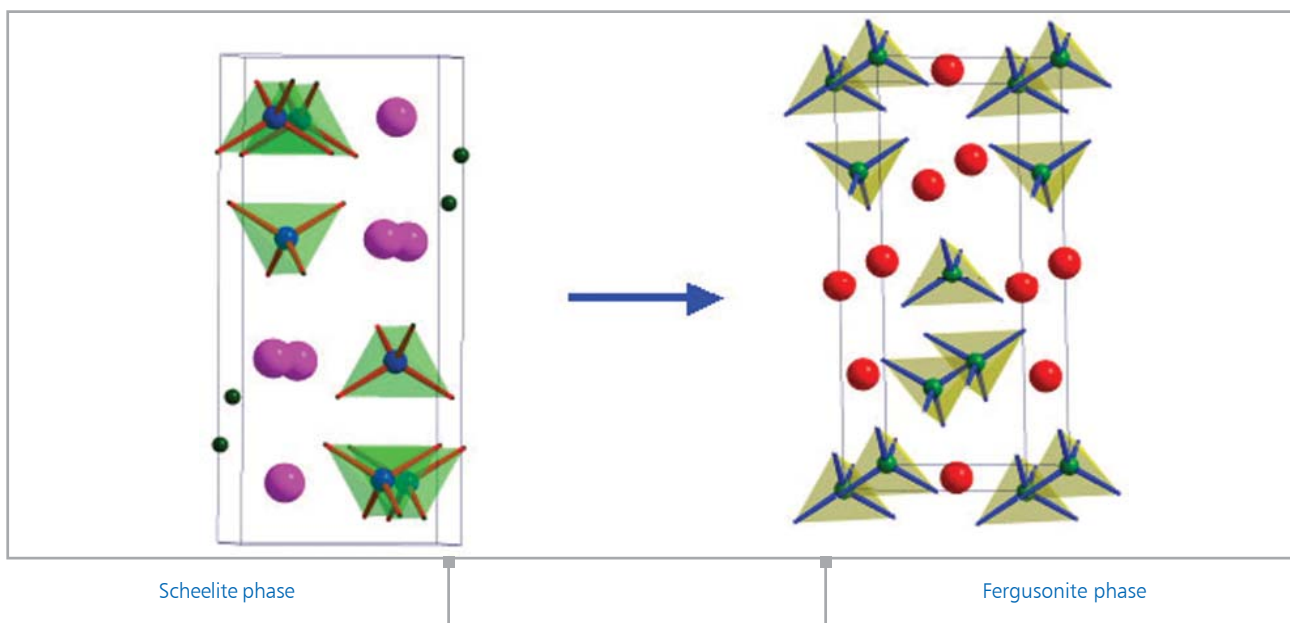
Snapshots of the transformation path of cristobalite  $AlPO_4$  to the  $Cmc2_1$  form at high pressure

H.K.Poswal, Nandini Garg, S. K. Kulshrestha and S. M. Sharma, Solid State Physics (India) 46, 59 (2003)

## 2.8 SCHEELITE STRUCTURED COMPOUNDS

Scheelite structured alkaline earth tungstates and molybdates are used as scintillators, cryogenic detectors of dark matter and are potential candidates for the laser host materials. Recently molybdates and tungstates have been the focus of high pressure studies to understand the structural stability in

these compounds. Some of the earlier studies on the scheelite compounds had suggested that due to the packing efficiency wolframite would be a preferred high pressure phase for these materials. However, some of the recent high pressure studies have shown that these compounds may not transform to this phase.



Scheelite phase

Fergusonite phase

We have carried out high pressure Raman and X-ray diffraction studies on  $\text{BaWO}_4$ ,  $\text{BaMoO}_4$  and  $\text{PbWO}_4$ . It is observed that all the three compounds undergo phase transitions to the lower symmetry phases at high pressures. The first transformation was at 7 GPa, 6 GPa and 7.5 GPa respectively. In barium tungstate and barium molybdate this high pressure phase is similar to a distorted scheelite structure (Fergusonite). Figure shows the two structures as determined by us. The second high pressure transition is at 14 GPa, 14 GPa and 10 GPa respectively. On release of pressure the high pressure phases transform back to the initial scheelite phase. From these studies it appears that the high pressure behavior of the molybdate and tungstate is similar. The temperature induced scheelite to fergusonite phase transition is known to be ferroelastic, associated with the phonon mode softening in the scheelite phase. The observed reversibility suggests similar mechanism for the high pressure behaviour.

Vinod Panchal, Nandini Garg, A.K. Chauhan, Sangeeta, Surinder M.Sharma, *Solid. State. Commun.*, 130, 203, 2004.

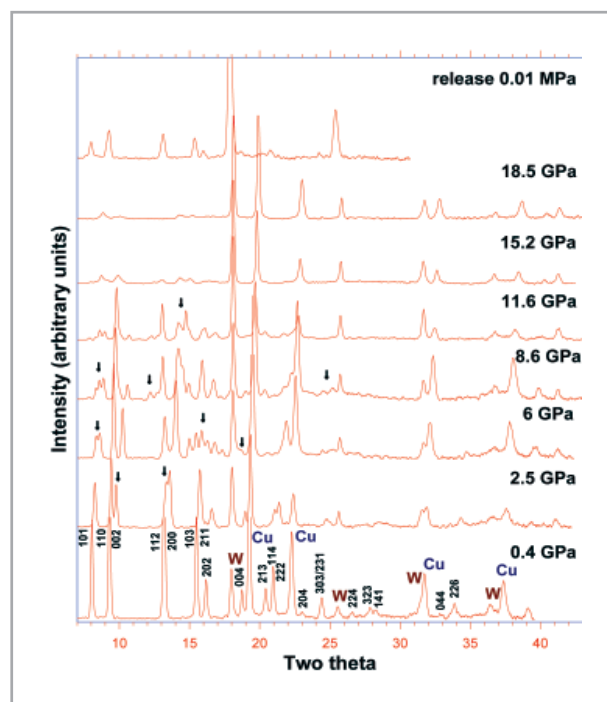
## 2.9 MOLECULAR SOLIDS UNDER HIGH PRESSURES

### ■ Pentaerythritol

Interatomic interactions in the molecular solids range from weak van der Waals to strong covalent or ionic type. Therefore, the high pressure studies of molecular solids are interesting, as the compression brings about a reduction in the intermolecular distances, causing significant variations in the interaction energies, which, could also lead to phase transformations. Several molecular solids like pentaerythritol, Amino acids, DL serine and alpha glycine have been studied with the help of Raman and X-ray diffraction studies. Some of these have shown changes in the strength of the hydrogen bond with pressure whereas pentaerythritol and DL serine have shown structural changes.

Specially Pentaerythritol  $(\text{C}(\text{CH}_2\text{OH})_4)$  which has a structure closely related to that of pentaerythritol nitrate (PEN) ( used as an initiating explosive, the explosive sensitivity of which seems to be related to its structural features) has been studied with the help of Raman and synchrotron based IR and X-ray diffraction measurements. Our results show that this compound

undergoes transformations to a lower symmetry phase between 5.2-5.9 GPa. It further undergoes phase transformations at  $\sim 8.5$  and  $\sim 11$  GPa; eventually evolving to a disordered phase beyond 14-15 GPa. All the structural changes are found to be reversible. The initial tetragonal phase was retrieved on Diffraction pattern of  $(\text{C}(\text{CH}_2\text{OH})_4)$  at different pressure release of pressure from 18.5 GPa.



X-ray diffraction patterns of  $(\text{C}(\text{CH}_2\text{OH})_4)$  recorded at different pressures.

Nandini Garg, Surindar M Sharma, S.K. Sikka, *Solid State Commun* 136 (2005) 56

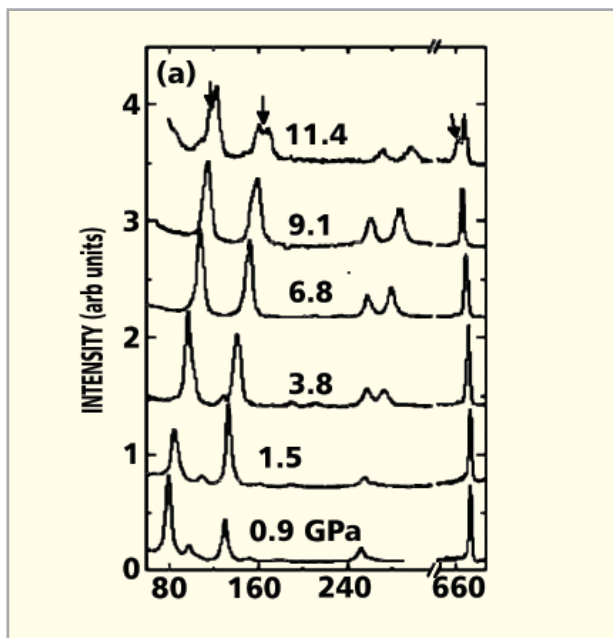
### ■ TCNE

High-pressure Raman scattering studies of the cubic and monoclinic polymorphs of tetracyanoethylene (TCNE) have been carried out. The evolution of the Raman spectrum with pressure suggests that the cubic form is stable up to about 8 GPa and the sample becomes opaque to visible light above 14 GPa. In the monoclinic phase, changes in the Raman spectrum indicate a subtle phase transition above 3.6 GPa and at higher pressure the sample progressively becomes black, similar to what has been observed in the cubic phase.

The Raman spectrum of the sample above 7 GPa is indicative of polymerization of TCNE. The spectrum of the pressure cycled opaque phase shows broad features characteristic of an

amorphous phase, which is understood as being due to random cross-linking of TCNE in the pressure reducing cycle.

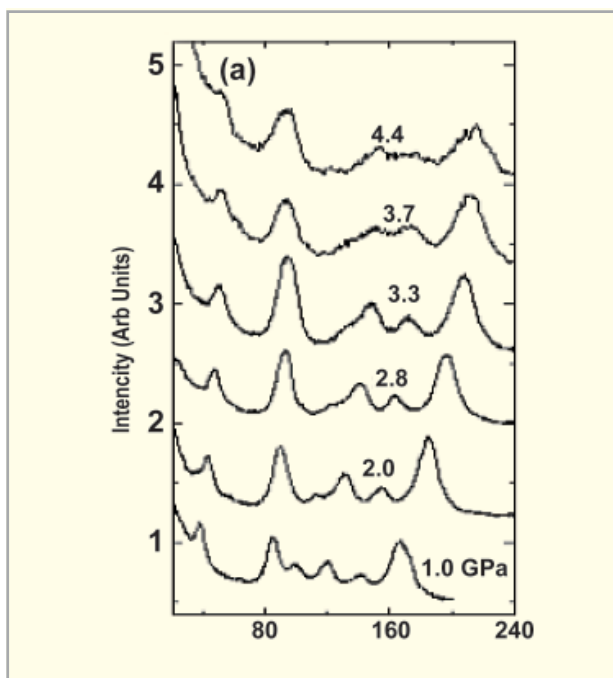
Rekha Rao, T.Sakuntala, S. K. Dab and R. Mukhopadhaya, J.Phys. Cond. Matter 17 (2005) 2633



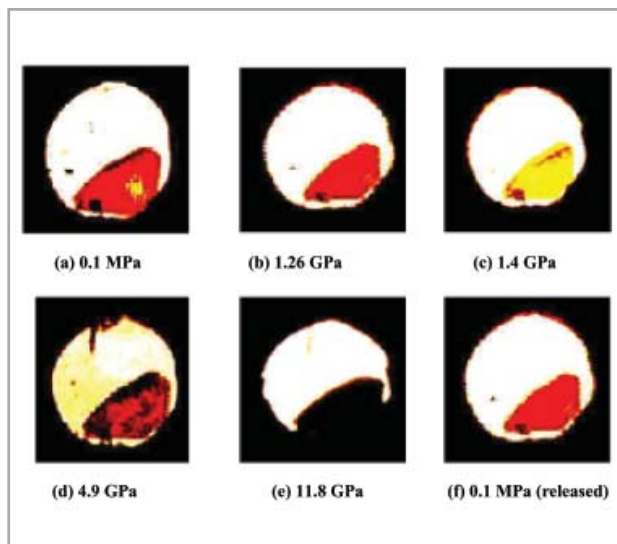
Raman spectra.

### 2.10 DEVELOPMENT OF HIGH PRESSURE OPTICAL ABSORPTION SET UP: STUDY ON RED-HgI<sub>2</sub>

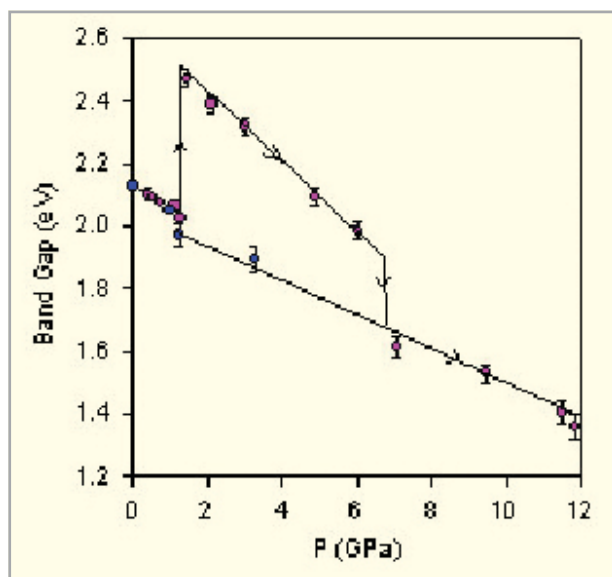
For the absorption studies under high pressures, a diamond anvil cell based high pressure optical absorption set up has been developed in the transmission geometry. This system can scan over 1.4 – 3.5 eV range. Using this , the band gaps can be determined with an accuracy of 0.005 eV. The sampling area for these measurement is ~10 micron (yellow spot on the sample, in Fig. (a)). The output signal is detected by lock-in technique which has been configured with the PC by the CVI software. Any visible change of the sample can also be recorded with the online viewing arrangement with the system.



Raman spectra



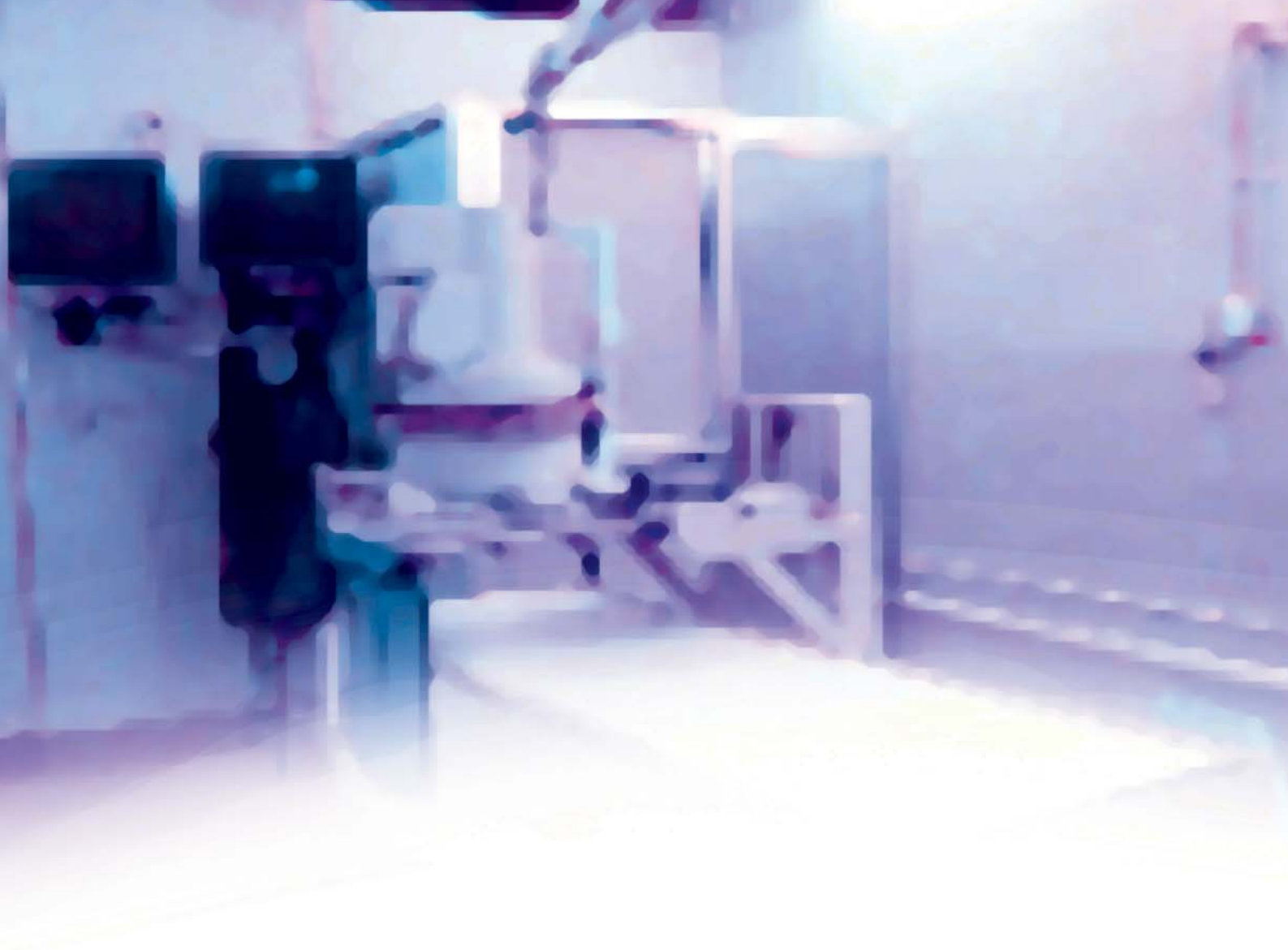
Microphotographs of red-mercuric iodide single crystal in the gasketed diamond anvil cell taken at different pressures. Yellow dot in (a) shows the focused spot.



Pressure dependence of the energy gap in  $\text{HgI}_2$ . Closed (open) circles are for increasing (decreasing) pressures

Using this technique, we have measured the pressure induced variations in the band gap of mercuric iodide. Our results show that it undergoes direct – direct – indirect gap transitions at 1.3 and 7 GPa respectively. The observed pressure dependence of the band gap suggests that, in the absence of any more phase transformations,  $\text{HgI}_2$  may metallize at  $\sim 40 \pm 6$  GPa. Combining with the compressibility results obtained from the X-ray diffraction measurements, it is found that in the tetragonal phase, intra-layer covalent bond deformation potential is much stronger than the van der Waals bond deformation potential and these are of opposite sign.

S.Karmakar, Surinder M Sharma, Solid State Communications 131, 473(2004)



### **3. RADIATION DETECTION AND IMAGING**

#### **INTRODUCTION**

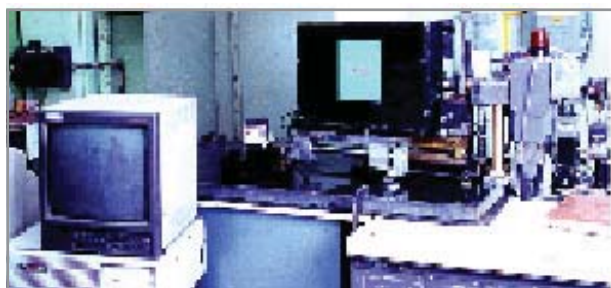
Radiation detection/imaging is the key to understanding the basic mechanism underlying several physical phenomena. X-rays have been used for imaging and detection for over a century starting with medical X-ray imaging to X-ray diffraction, tomography to the recent physical techniques such as EXFAS, X-ray holography. The detectors for X-rays have evolved from film to imaging plate, CCD and flat panel detectors. With the discovery of neutrons, new techniques were developed to detect and use them as imaging tool. New detectors for neutrons are required for ever-increasing application in the field of nuclear, defence and space industry. Applications are not only limited to detecting the intensities of such sources but also to determine their phase. This chapter deals with such new radiation detectors and imaging systems being developed at BARC.

### 3.1 RADIATION IMAGING – ADVANCED IMAGING WITH X-RAYS AND NEUTRONS

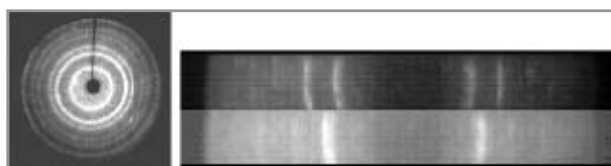
The radiation imaging section of High Pressure Physics Division has been engaged in a number of activities on basic and applied research using optical, X-ray and neutron sources as probe for imaging, which has direct relevance to the ongoing program of the department. A brief account of the basic research followed by review of spin-off technologies developed are mentioned briefly.

#### ■ X-Ray imaging for basic and applied research

**CCD Detector system for X-ray diffraction:** A novel ICCD (Intensified CCD) based detector system with high sensitivity for X-ray photons for the quick detection of phase transitions for materials under pressure has been developed. Several samples have been studied using this detector and new phase transitions have been detected under pressure. This detector system has now been supplemented by a cooled CCD coupled to a fibre optic taper for collection of high-resolution data with low noise.



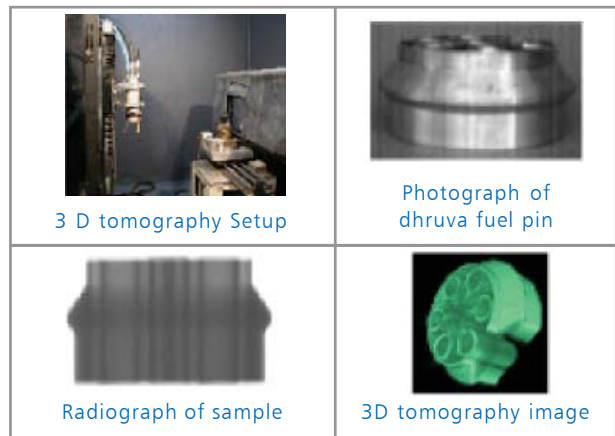
Photograph of X-ray diffraction set-up



Diffraction rings under ambient and High Pressure condition

**3D Cone Beam Tomography and digital X-ray imaging System:** We have developed a 3D X-ray cone beam tomography for the first time in the country. This technique

has strategic value in probing the interiors of large as well as small objects. We are being requested by HEMRL, Pune (a DRDO lab) and SAMEER, Mumbai to provide knowhow for developing such systems at high X-ray energy.



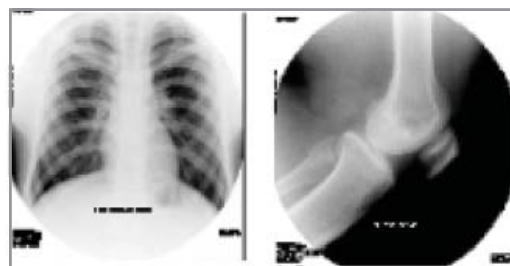
**Digital Medical imaging :** As a spin-off of basic research, We have developed a multifunctional digital medical imaging system for the first time within the country and which has been certified to be one order magnitude less dose compared to conventional film system and has function equal to or better than imported system of this type at a cost which is a fraction of imported cost. This system is under user trial at BARC Hospital.



Patient table along with Imaging Unit installed at BARC Hospital



Control Units

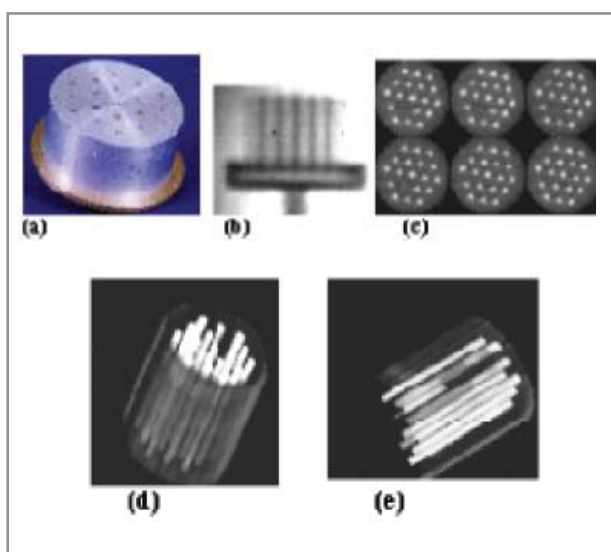


Radiography images of chest and knee

## ■ Neutron Imaging for basic and applied research

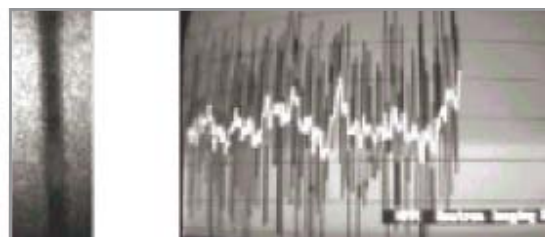
Our basic research work on neutron and X-ray imaging has several spin-off and most of them have found widespread applications and are of significant value to the programs of Department of Atomic Energy and for many other organizations such as HEMRL (DRDO), BHEL, NTPC, ECIL, BEL. Some of the applications and technologies developed are described below.

**Neutron Tomography (2D and 3D) :** We have developed a digital imaging technique for neutrons using CCD detectors. This was subsequently used in the development of neutron tomography at APSARA reactor. The entire reconstruction software and hardware was developed indigenously. This technique was extended for 3D tomography and volume visualization of the interior of the materials.



(a) photograph of object (b) radiograph (c) multiple tomographic slices (d) cutaway section

**Two Phase flow Visualization and analysis using real time neutron radiography:** We have developed two phase flow visualization inside metallic pipes and its quantitative analysis method using digital neutron imaging which has found direct application in AHWR program. This technique is also being used by BHEL in collaboration with NTPC for their coal gasification project and has provided very valuable input leading to change in design of nozzle by BHEL for their gasifier.



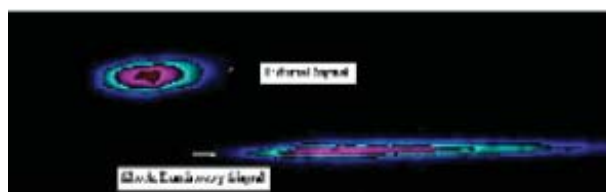
Single frame neutron image of water air flow inside metallic pipe and online plot of void fraction

## **Design of microtron based photo-neutron source:**

We have been engaged in utilization and application development using non-reactor based sources. In this direction, we have developed neutron radiography using Pu-Be neutron sources and 14 MeV neutron generator. We have successfully designed a neutron converter assembly on the microtron facility at Mangalore University with a source strength of  $2 \times 10^9$  n/s. We are also developing possible application areas for this neutron source including neutron radiography and elemental characterization for bulk sample analysis.

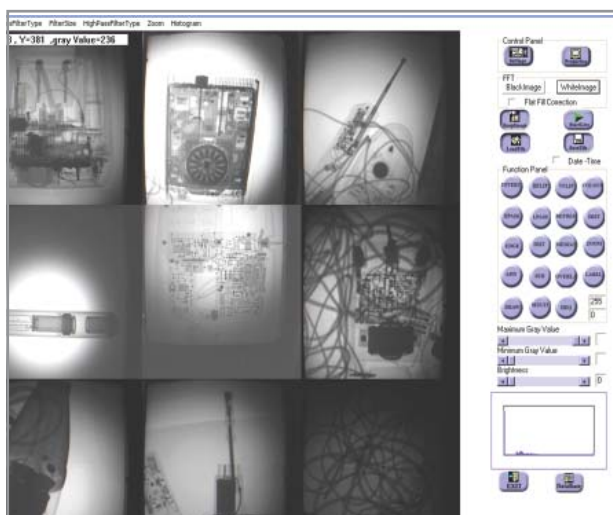
## **Laser induced shock studies using dynamic imaging technique:**

We have initiated a program of setting up of laser shock laboratory, which will be used to study material behavior under laser shock using dynamic imaging technique using a tunable laser oscillator of 300-800 ps and an amplifier chain. This laboratory will have the state-of-art dynamic imaging facilities such as optical and X-ray streak camera, framing cameras and multiple gated ICCD with 200 ps resolution, transient X-ray diffraction setup etc. The aim of this laboratory will be to study shock propagation inside transparent and opaque media using backlighting X-ray and dynamic X-ray radiography method, imaging of laser shock driven flyer plate motion, symmetry of shock using multiple ICCD, phase transition study using transient X-ray diffraction technique, study of instabilities etc. and to study laser shock induced physical phenomena in actinides.



Imaging of Laser Shock induced luminescence using streak camera

**Portable Baggage Inspection System:** In collaboration with ECIL, we have developed a portable battery-based baggage inspection system for inspection of unidentified objects at remote places. We are also collaborating with ECIL on developing imaging system for cargo scanning.



**Phase imaging:** With the emergence of coherent sources of X-ray such as synchrotron, which have both temporal and spatial coherence, and microfocus which has only spatial coherence, a new imaging modality called phase imaging has emerged. This technique which uses phase instead of attenuation to form image is very useful for imaging of soft tissues or soft materials such as carbon fibers. We are engaged in developing this imaging technique for both X-ray and neutron as follows.:

**a. X-ray Phase imaging at INDUS-II:** We are engaged in developing X-ray phase imaging technique and installing a phase imaging beam line at INDUS-II synchrotron for material characterization and medical imaging purpose. This beamline will cater to the needs of micro-tomography and micro-imaging using phase contrast and diffraction enhanced imaging.

**b. Neutron Phase Imaging Beam Line at CIRUS:**

The technique of phase contrast imaging using neutrons has also been initiated. This technique will be very useful in detection of minor defects and cracks and anomalies in materials, which are difficult to penetrate by X-rays. For this purpose a neutron beamline is being established at CIRUS reactor.

**c. X-ray holography:** This is a new method of determination of crystal structure and is based on measuring the interference of a known reference wave with an unknown object wave (containing information on atomic sites scattering the reference wave). We have developed algorithm for carrying out the simulation of such a phase sensitive technique.

P.S.Sarkar,A.Sinha, Y.kashyap, M.R.More, B.K.Godwal, Nucl. Instr. Meth. A 524, pp377-384 (2004)

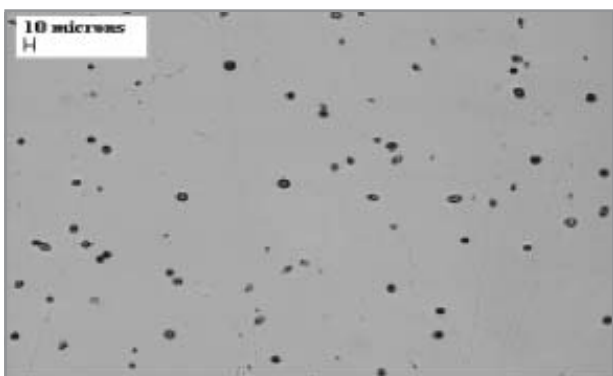
A.Sinha, P.S.Sarkar, Y.Kashyap, B.K.Godwal -Published in British NDT journal "INSIGHT", Jan 2003, vol (45) No.1

### 3.2 NEUTRON MEASUREMENTS USING SSNTD TECHNIQUE DURING PFBR & AHWR SHIELDING EXPERIMENTS

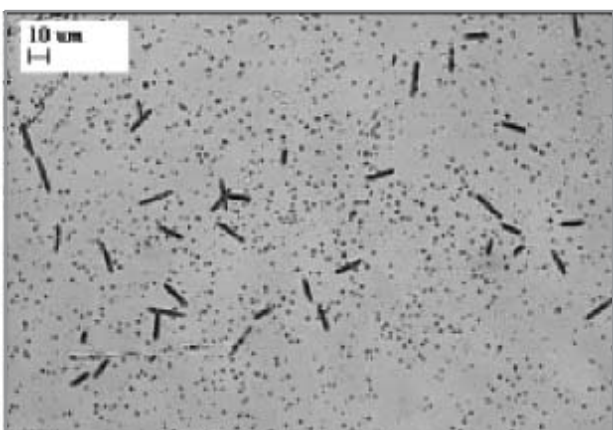
Solid State Nuclear Track Detectors (SSNTDs) in addition to activation detectors were used to optimize shield model configurations for Prototype Fast Breeder Reactor (PFBR) and in streaming experiments for Advanced Heavy Water Reactor. Lexan Polycarbonate track detector was used in combination with various fissionable nuclides such as Natural U, Th<sup>232</sup>, Np<sup>237</sup>, depleted U etc either in deposition form or foil form. The fission reaction rate per atom in various neutron energy regions were evaluated by counting the neutron induced fission tracks in Lexan detector. In addition, (n,α) reaction rate was also measured by keeping CR-39 in combination with Li<sub>2</sub>B<sub>4</sub>O<sub>7</sub> radiator in borated graphite & boron carbide models for PFBR. The photograph of shield model along with converter assembly for PFBR experiment is shown in first figure. The other two figures show the photographs of alpha and fission tracks revealed during experiments.



Shield models with holders and converter assembly.



Alpha tracks from (n, alpha) reaction in CR-39 + Lithium tetra borate (radiator).



Fission tracks in lexan by (n, fission) reaction.

V.B. Joshi, R.V. Kolekar and H.K. Dravid, Radiation Measurements 36 (2003) 741. R. Anuradha, Leena Joseph. D.B. Kulkarni, R. Nathuram, V.V. Shaha and D.N. Sharma, Appl. Radiation & Isotopes 62 (2005) 645.

### 3.3 STANDARDS AND CALIBRATION

The RSSD maintains the Primary and Secondary Standards of various parameters of radiation measurements. This is an apex laboratory in India, which ensures accurate radiological measurements. It is the recognized Regional Secondary Standards Dosimetry Laboratory (SSDL) of IAEA/WHO. The Division participated in the international intercomparison programmes on i) radioactivity measurement of several radioactive sources organized by BIPM and APMP, ii) in the postal dose Quality Audit conducted by IAEA for SSDLs in therapy level dosimetry.

#### ■ Neutron Standards and Radiological Standards

Various experiments were conducted for standardization of neutron sources and neutron fluence rate in reactors and accelerators as well as designing of shielding of reactors, accelerators and combat vehicles. Also, ISO recommended heavy water moderated  $^{252}\text{Cf}$  neutron source for the testing and calibration of neutron monitors used in reactors has been established.

A transfer standard for in situ standardization of neutron sources has been established using small cadmium covered high-density polythene sphere with gold foil. This standard was used for the standardization of neutron source output at Defense Lab., Jodhpur. Various experiments were conducted to establish the production of photo-neutrons from heavy water by hard gamma from  $^{208}\text{Tl}$  from an unirradiated thorium bundle. An experiment has been conducted to measure the neutron output of the Be sleeve, which will be used in a special reactor application when an Sb-124 source is loaded in the Zirconium alloy.

RSSD as a part of Secondary Standards Dosimetry Laboratory (SSDL) network of IAEA/WHO provides dosimetry support to more than three hundred radiotherapy centres in India, Sri Lanka, Myanmar and Nepal.

#### ■ Setting up of Calibration Lab.

A state-of-the-art laboratory that operates in the range of 200 mR/h to 20000 R/h for calibration of radiation measuring instruments has been established at Pune. The laboratory is

equipped with i) The 90 Ci Sentinel Cobalt Source Projector, ii) A CRC-2A camera loaded with 1 Ci Co-60 source, iii) Two distancing systems along with position indicators, iv) The various radiation measuring instruments, surveillance systems, data acquisition systems, a Gamma Zone Monitor and the electro magnetic lock and v) A computer based data management programme called "Calibration Manager".

#### ■ Theoretical Inputs

RSSD has been providing theoretical inputs pertaining to the shielding requirement and criticality safety of various existing facilities and for the upcoming projects of different Groups of BARC and DAE. Shielding requirement for the electron accelerators and 20 MeV proton accelerator were calculated as part of the safety evaluation of the facilities.

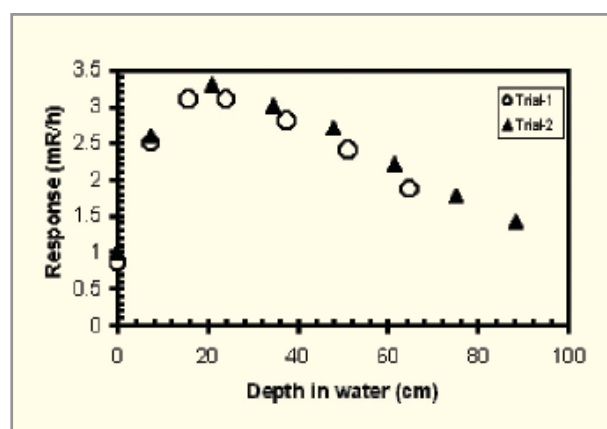
### 3.4 MEASUREMENT AND SIMULATION OF FLUENCE AND DOSE BUILD UP AT ELECTRON STORAGE RING INDUS-1

No radiation monitors are commercially available for a proper estimate of absorbed dose in a human torso, due to high energy photons generated in the electron storage rings, where dose build up is likely to be more than that in those radiation monitors. Therefore, a proper simulation for this dose is required.

Streaming of high energy photons has been observed through shield joints, penetrations, and at front ends of synchrotron radiation beam lines during the commissioning trials of the electron storage ring, INDUS-1, at the RRCAT, Indore. Experimental measurements are carried out in the streaming radiation field from a 450 MeV electron storage ring using radiation survey meters and water phantom to estimate the dose build up factor and the maximum dose depth to correct the instrument response for proper dose estimation. We have used a Victoreen make survey meter model 450P with water phantom to study the high energy response of the survey meter experimentally. Theoretical simulations using Monte-Carlo codes were also carried out to analyse and compare these with experimental results and were found to be in good

agreement. Further, we have measured bremsstrahlung photon spectrum using a 50.8 mm x 50.8 mm BGO detector in the direct and transmitted photon field through shields to evaluate the use of radiation monitors outside shielded enclosures.

The depth dose profiles measured at front end indicate that the maximum dose rate occurs at a depth of about 20 cm in water and the build up factor obtained was 3.3 with respect to the reading from the bare monitor (Fig). This indicates that the photon spectrum is harder at front end than at the bending magnet. The energy spectrum of direct photons through shield is extending beyond 12 MeV and indicates that the end point of the spectrum located beyond 100 MeV. On the other hand, the spectrum of transmitted photons indicates that the end point of the spectrum is around 12 MeV. However, due to the domination of low energy photons, the average energy of the transmitted spectrum is worked out to be 3.3 MeV only.



Depth dose profile in water

G.H. Haridas, K.K. Thakkar, S.D. Pradhan, A.R. Nayak and A.M. Bhagwat <[arnayak@barc.gov.in](mailto:arnayak@barc.gov.in)>

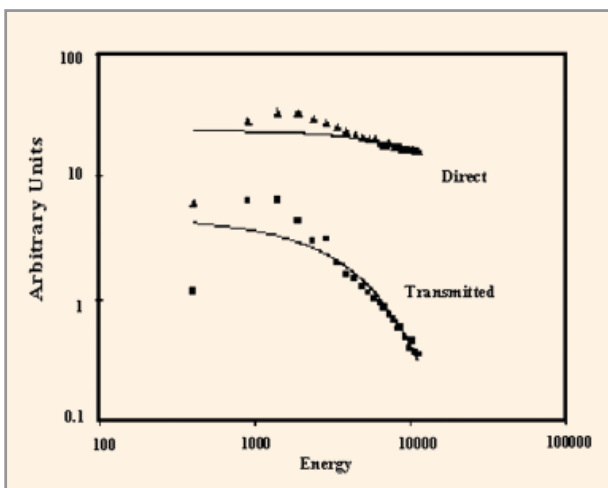
### 3.5 DEPTH DOSE PROFILE MEASURED IN WATER WITH VICTOREEN SURVEY METER 450P AT FRONT END

From theoretical simulations and experimental measurements the observations are summarized as:

The depth where maximum absorbed dose occurs and the build up factor vary at different locations around the storage

ring of Indus-1. The variation is due to spectral difference of the bremsstrahlung spectra at those locations. The harder the spectra, the higher the depth at which maximum absorbed dose occurs and the build up factor is more.

The measurements indicate that the maximum absorbed dose occurs within 30 cm water phantom and the build up factor corresponding to maximum absorbed dose at a depth of 30 cm in water (human body size) is found to be 6.4. For personnel radiation protection application within the shielded enclosures, in the streaming radiation field through front ends, shield penetrations and shield joints, if any from the storage ring a factor of 6 is recommended for correcting the monitor / survey meter response. Shown Fig. gives a comparison of direct and transmitted bremsstrahlung spectra through shields where the lines represent calculated results and symbols are the measured data.

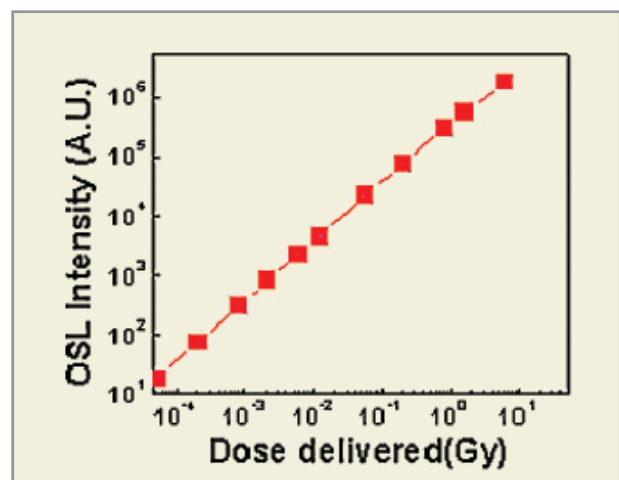


G.H. Haridas, M.K. Nayak, D.N. Sharma and M. C. Abani, BARC Report No. BARC/2003/I/001.

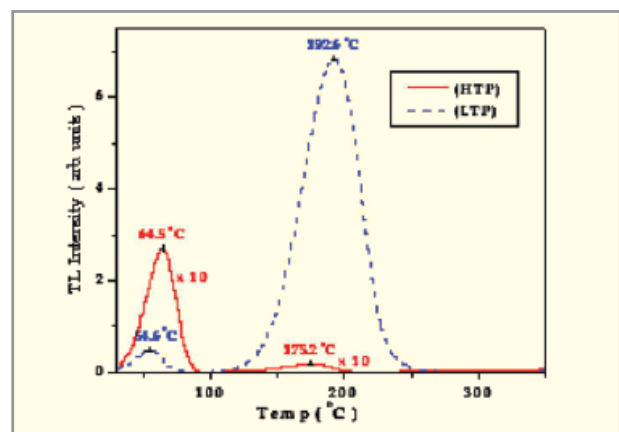
### 3.6 $\text{Al}_2\text{O}_3$ BASED PHOSPHORS FOR RADIATION DETECTION

Anion-deficient single crystal  $\alpha\text{-Al}_2\text{O}_3\text{:C}$  phosphor for dosimetry suitable for thermoluminescence (TL) and optically stimulated luminescence (OSL) techniques was developed. The material is 50 times more sensitive than TLD-100. A new technique called post-growth thermal impurification technique has been developed for preparation of material by diffusion of carbon

at low pressures and high temperatures. The technique yields conventional material (HTP) for dosimetry that has a peak at high temperature ( $\sim 190^\circ\text{C}$ ), as well as a new material (LTP) with enhanced (99% of total TL output) low temperature ( $\sim 60^\circ\text{C}$ ) TL peak. The OSL response of HTP material is found to be linear in  $50 \mu\text{Gy}$ - 1 Gy range, as shown in Fig. The new material is 200 times more sensitive than TLD-100 and has rapid fading off of the signal that can be utilized in passive and on-line radiation measurements using TL technique.



Dose linearity curve for conventional type material (HTP) used in OSL mode.



TL response of HTP and LTP materials. The curve for LTP material should be multiplied by a factor shown in figure and then compared.

M. S. Kulkarni, D. R. Mishra, K. P. Muthe, Ajay Singh, M. Roy, S. K. Gupta and S. Kannan, Radiation Measurements 39 (2005) 277.

### 3.7 DEVELOPMENT AND FABRICATION OF SEMICONDUCTOR RADIATION DETECTORS

Si charged-particle detectors have been fabricated for heavy ions (fission fragments), lithium-drifted Si(Li) and Ge(Li) detectors for betas and gamma-rays and lithium-6 coated Si detectors for neutrons. The process technologies such as semiconductor surface passivation, Li diffusion and metallization were standardized to produce low-leakage junction type of surface barrier detectors (Au/n-Si, Al/p-Si, Li/p-Si and Li/p-Ge) by fabricating suitable injecting and non-injecting contacts on single crystals. At present, the detector development and fabrication work is based on the high purity Si-single crystals and pursued with the objective of meeting some of the essential requirements of DAE.

In order to develop large area rugged detectors, a 30 keV ion implantation machine suitable for making shallow junctions over large area (up to 75mm dia.) is used. P+/n and n+/p type of silicon detectors are fabricated by implanting boron and phosphorous dopants and used for the measurement of energy as well as positions of charged-particles (Fig.). Position sensitive detectors were made by implanting a uniform

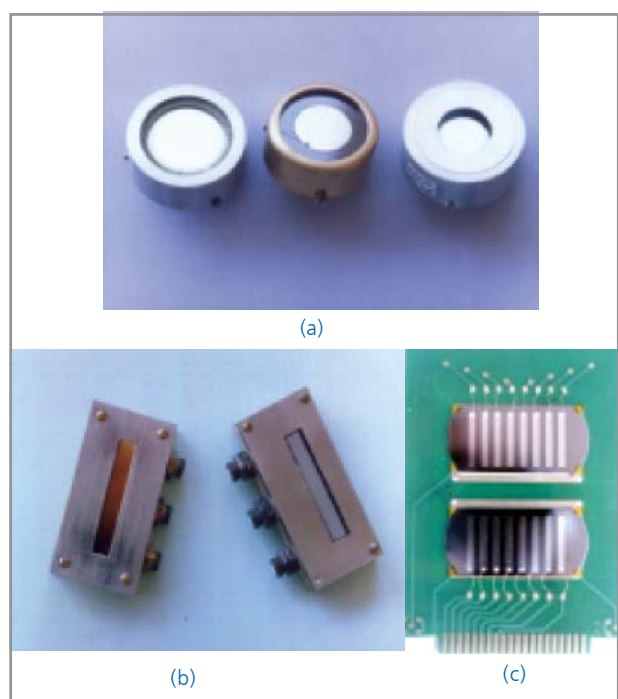
resistive layer at the back. Both partially depleted and fully depleted 8-element p+/n/n+ type Si detector arrays having 25 x 4 mm size elements with 0.5 mm spacing were fabricated, tested and used.

Development and fabrication of the state-of-the-art highly reliable silicon oxide passivated implanted silicon detectors have been taken up recently. A high temperature silicon oxidation facility has been set up. Oxide passivation carried out so far by using the chemicals and gases available in our country, has produced SiO<sub>2</sub>/Si interface with fixed charge density of less than 3x10<sup>11</sup>/cm<sup>2</sup>. A few oxide passivated detectors showing energy resolution of 25 keV for 5.48 MeV  $\alpha$  have been made by following the planar method of fabrication.

Charged-particle Si detectors which are routinely fabricated for in-house uses are: (1) E-type for energy measurement, with area of 25-300 mm<sup>2</sup>, sensitive depth of up to 300  $\mu$ m and energy resolution of 30-100 keV for 5.48 MeV  $\alpha$ ; (2)  $\Delta E$ -type for dE/dx (particle identification) measurement, with area of 25-50 mm<sup>2</sup> and thickness of 10-50  $\mu$ m; (3) Linear position sensitive detectors with dimension of 30-40  $\mu$ m x 5 mm and position resolution of 0.3-0.5 mm. 4) Si(Li) with area of 50 mm<sup>2</sup>, thickness of up to 3 mm and energy resolution of 40 keV for 1 MeV electron. Currently, these detectors are mostly used for either conducting nuclear experiments or  $\alpha$  monitoring in air.

R. Prasad, G.V.S.G. Acharyulu and D. Sahoo, DAE Nuclear Phys. Symp. 44B (2001) 402

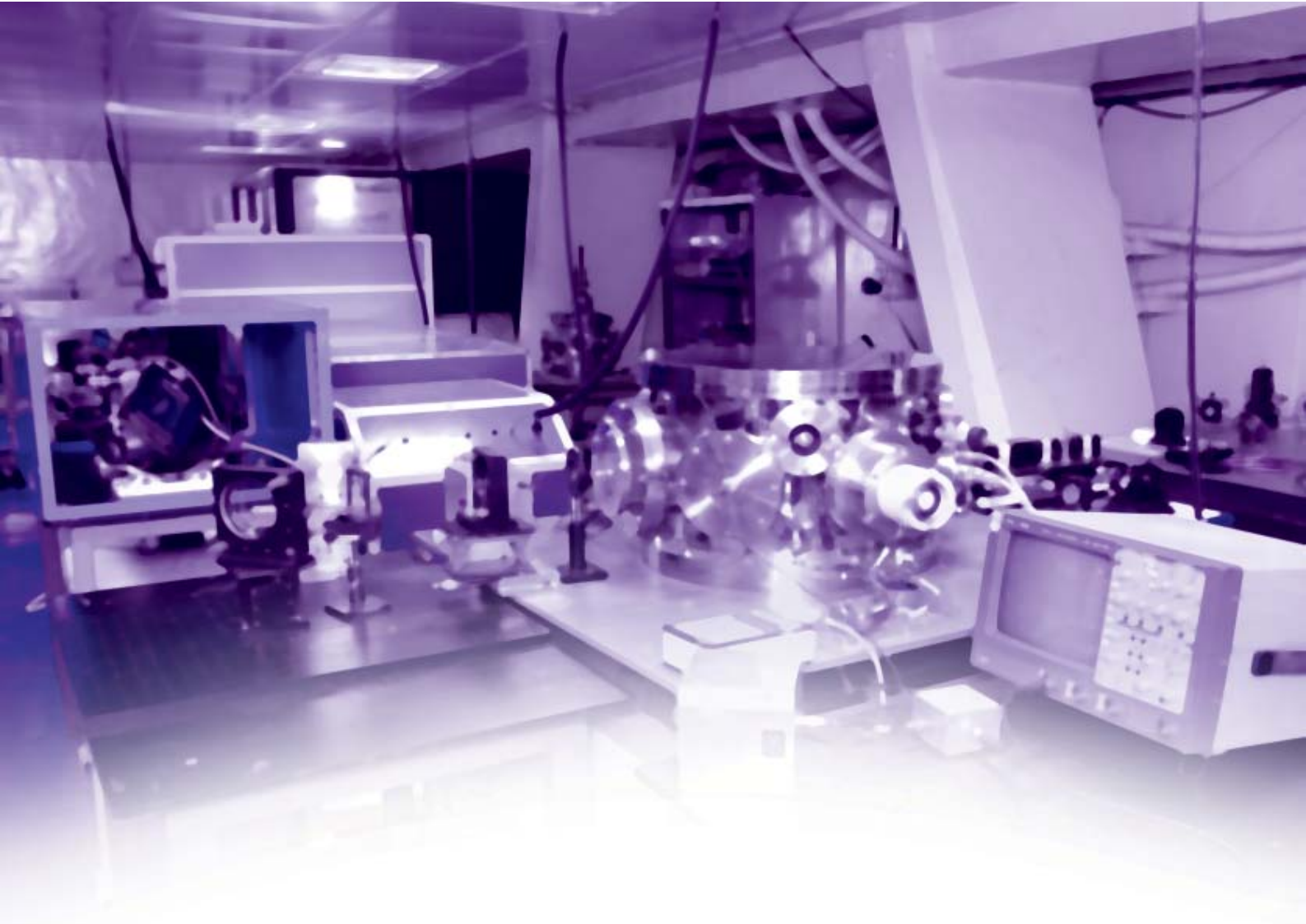
D. Sahoo, and R.Prasad, DAE Nuclear Phys. Symp 47B(2004) 500



Ion-implanted charged-particle detectors: (a) E-type; (b) Position sensitive; and (c) Array.

### 3.8 TLD BADGES FOR PERSONNEL MONITORING

The Department of Atomic Energy (DAE), since its inception has accorded high priority to safety on activities with radiation and radiation sources. TLD badges are used for Personnel Monitoring. They used to measure external individual doses from X, beta and gamma radiations. With increasing number of radiation workers, demand of TLD badges is also increasing. This has resulted in technology transfer of TLD badges to three private parties so far.



#### **4. LASERS AND PLASMA RELATED STUDIES**

##### **INTRODUCTION**

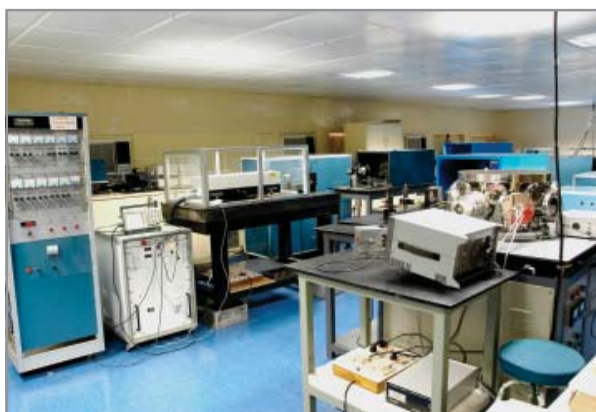
Laser system development and employing them for basic investigations and technological applications formed the major thrust area in BARC. Ultra short lasers and related diagnostics are being developed for shock wave studies. Single axial mode and solid state tunable dye lasers will spur new applications. Laser cooling of atoms in traps in 100 micro Kelvin opened new areas of studies. Laser produced plasmas by resonant ionization and using intense lasers are of practical importance. Laser-based instrumentation was developed for applications in nuclear fuel cycle. Deeper understanding of non-linear dynamics of the arc and the hydrodynamics of thermal plasma sources have helped in building reliable plasma torches with long lives.

**4.1 INTENSE PICOSECOND AND FEMTOSECOND Nd: GLASS LASERS TO GENERATE MULTI-MEGABAR SHOCKS AND STUDY INTENSE LASER MATTER INTERACTION**

Interaction of matter with ultra short and intense laser pulses offers the possibility of studying hydrodynamic phenomena at extremely high temperatures pressures and densities. Plasmas at millions of degrees with density few times the solid density are produced in extremely short time. Material Ablation velocity can reach upto 107 cms/sec resulting in an inward propagating shock wave. The shock pressure in such a situation can reach upto tens to hundreds of Megabars. Laser plasmas are sources of intense X-rays with duration of a few picoseconds to hundred picoseconds and also MeV electrons/ Ions. Conditions of these plasmas also favour fusion reactions giving rise to extremely short and intense burst of neutrons in addition to radiation at X-ray to gamma ray wavelength. Such intense X- ray, gamma ray and neutron sources are in the pico second to femtosecond time scales and are therefore ideally suited for several applications in material science where high temporal and spatial resolution are needed. These applications need laser systems with peak powers of Gigawatts to Terawatts.

The High Pressure Physics Division, has been developing two intense ( Picosecond and Femtosecond ) laser systems to generate focused laser intensities in the range of  $10^{13}$  -  $10^{16}$  Watts /  $cm^2$  that can be used to study intense laser-matter interaction.

■ **30 GW Nd:glass Picosecond Laser System**



Front end Master Oscillator of the High Power Laser system



Laser plasma interaction chamber fitted with various diagnostics

**Laser Parameters:**

- Energy per pulse – 10 Joules
- Pulse duration- 300 – 800 Picoseconds,
- Peak Power – 30 Gigawatts,
- Focused intensity-  $10^{12}$  -  $10^{14}$  Watts/ $cm^2$ ,
- Shock pressure generated - 10 -30 Mbar
- Plasma Temperature –  $10^5$  to  $10^6$  K

L.J.Dhareshwar,N.Gopi,B.S.Narayan,R.Vijayan,A.C.Shikalgar, BARC Report-BARC/2001/I/011,2001

· **Femtosecond Nd:glass laser system using Chirped Pulse Amplification technique**

A 1 Terawatt, 150 femtosecond Nd:Glass laser chain is currently under development. This laser system involves the revolutionary technique of Chirped Pulse Amplification. In this system the 100 femtosecond pulse has been successfully stretched to 2



Photograph of the 100 femtosecond Oscillator within a class 100 dust free structure

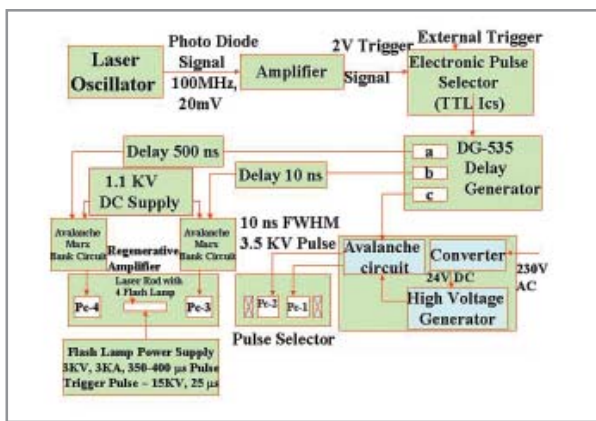
ina device called the stretcher that has been designed in this laboratory. This 2ns pulse will be further amplified in a regenerative amplifier (taking care that the spectral characteristics remain as close to the original as possible) and then further in a set of linear amplifiers before it is compressed to a 150 femtosecond pulse.

**Laser Parameters:**

- Laser pulse duration: 500 fs
- Peak pulse power:  $10^{12}$  Watt
- Wavelength: 1.06 micron
- Amplification medium: Nd:glass
- Focused Intensity: 10

■ Ultra fast, high resolution, Laser and Plasma Diagnostics

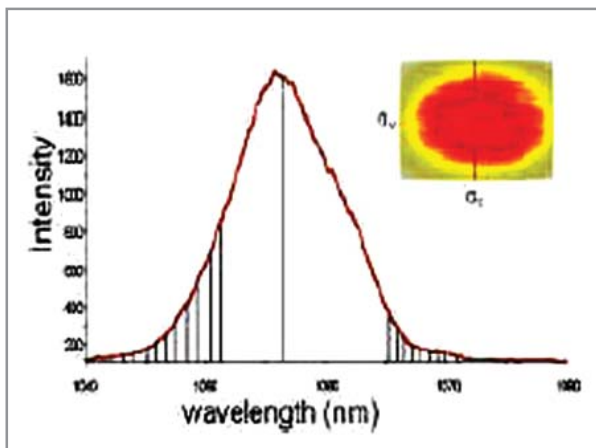
**Scanning Second Harmonic Autocorrelator:** An online pulse duration monitoring set up with a sub-picosecond temporal resolution has been developed.



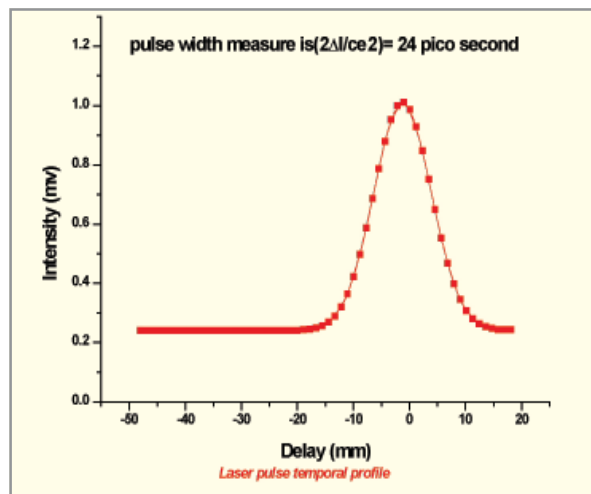
Fast switching electronics for the femtosecond laser system..



Second Harmonic Autocorrelator set up

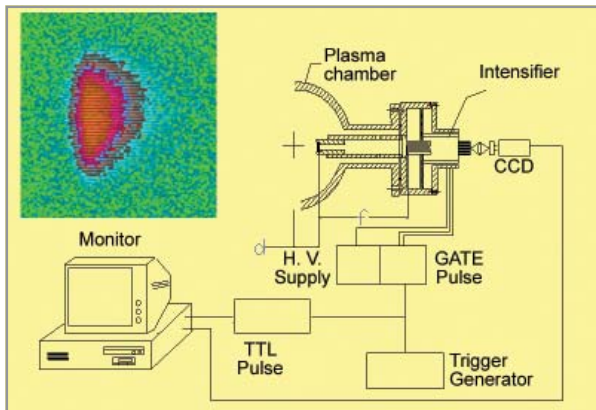


Spectrum of the chirped laser pulse and effect of frequency filtering within the pulse stretcher on the spatial profile of the laser beam.



Laser pulse temporal profile

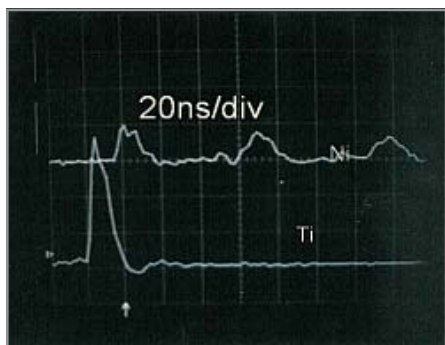
**X-ray diagnostics for laser plasma :** Several plasma diagnostics with high temporal and spatial resolution have been set up for laser-plasma interaction experiments. A Digital X-ray pin hole camera has been developed to image the spatial distribution of X-ray emission from laser plasma.



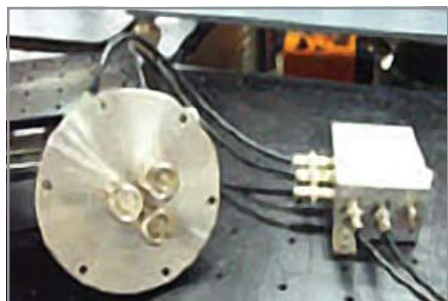
X-ray pinhole camera set-up and the recorded X-ray plume picture of the copper plasma

■ Measurement of X-ray emission scaling from Laser produced copper plasma

A three-channel, noise-resistant, PIN diode based detection system has been set up to measure X-ray emission from laser plasmas.

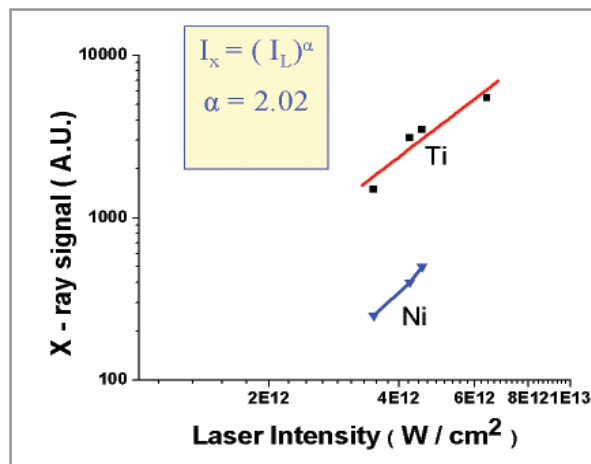


X-ray signals from copper plasma with Nickel and titanium foil filters



Three channel X-ray diode set up

Measurement of X-ray emission from a laser irradiated solid copper target and its scaling with laser intensity has been determined in the laser intensity range  $10^{12}$  to  $10^{13}$  W/cm<sup>2</sup>. X-ray diode diagnostic head was placed within the laser-plasma interaction vacuum chamber at a distance of 150 mm from the target at 45° with respect to the target normal. These double diffused silicon pin diodes have an active area of 100 mm<sup>2</sup>, depletion depth of 250 μm and rise time of 5 ns. Since the response of the detectors is slow as compared to the sub-nanosecond laser pulse duration, this set up records the integrated X-ray emission during the laser pulse. The X-ray filter foils were– 12 μm thick Titanium foil having an X-ray absorption K-edge at 4.96 KeV and a 5 μm thick Nickel foil with its K-edge at 8.32 KeV. Slope of the linear fit to both the graphs in Fig. shows a value of 2.02. X-ray emission intensity,  $I_x$  is thus observed to vary with laser intensity as  $(I_L)^{2.02}$ .



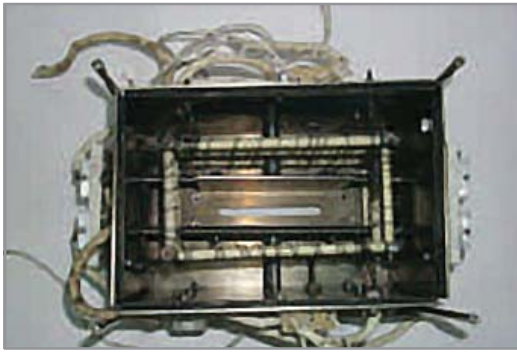
Scaling of X-ray emission with laser intensity in a laser produced copper plasma

L.J.Dhareshwar, S.Chaurasia, C.G.Murali, N.K.Gupta and B.K.Godwal Journal of Material Science, 2005.

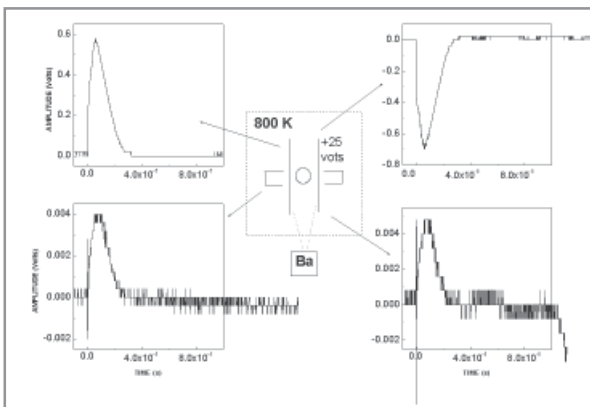
4.2 BARIUM PHOTOPLASMA STUDIES

Research is being carried out in studies of barium photoplasma in electric field. An efficient ion evolution process is required for laser-induced material processing of high purity materials. To achieve this goal the process has been experimentally simulated for which various hardware are made indigenously and applied physics experiments have been carried out with them. Fig. shows a photograph of a furnace assembly, kept on top of another furnace (not shown in the fig.), the

purpose of which is to heat a pair of parallel plate electrodes. By shining lasers on the atomic beam photoplasma is produced in between the parallel plates by multi-step resonant photoionization. The physics of ion motion of the plasma is studied in parallel plate geometry with hot electrodes and in presence of different potentials. Fig. shows typical ion signals on the anode, cathode and Faraday cups when +25 volts are applied on the anode. The motion of ions of this transient plasma at high density is primarily governed by space-charge dominated sheath physics whereas for low density it is determined by decreasing density of ion bunch. The role of re-evaporated atoms from electrodes is also considered in this study.



Assembly to study plasma evolution under electric field and high temperature. Electrodes are mounted on insulators kept outside the vapor zone while Faraday cups are located on opposite sides behind a hole in each electrode.



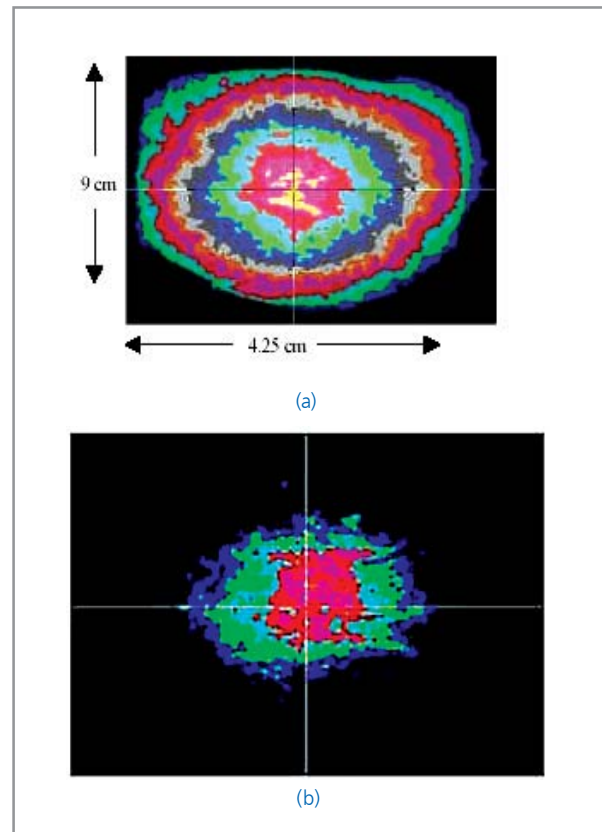
Signals on electrodes and faraday cup when 25Volts (7V/cm) is applied on anode.

A.Majumder, V.K.Mago, A.K.Ray, P.T.Kathar and A.K.Das., Appl. Phys. B, 2005

### 4.3 NOVEL SCHEME FOR SPATIAL FILTERING OF LASER BEAMS USING SATURABLE ABSORBER

Most basic experiments as well as, industrial, medical and military applications involving laser beams benefit enormously from use of laser beams having low divergences and a smooth spatial profile. The conventional technique of spatial filtering using a hard aperture, though simple in approach, requires very precise and stable positioning of an aperture of microscopic size at the focus of a lens, and is also susceptible to edge damages in case of alignment drift. A new technique has been developed for spatial filtering of laser beams based on a saturable absorber that is free of lateral positioning accuracy, can handle high average power lasers, and can be tailored by changing the absorber concentration and length, as well as the beam focusing parameters.

This technique has been successfully applied to reduce the divergence of laser beams from a high repetition rate Copper



Copper Vapor laser beam-spot at focal plane of lens ( $f=5m$ ) a) without and b) with saturable absorber

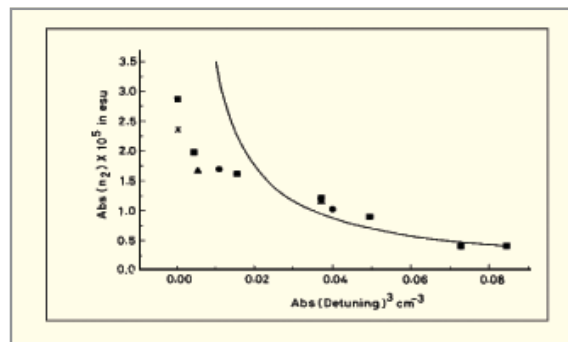
Vapour laser and a narrow band tunable dye laser, using circulating dye solution in a dye cell as a saturable absorber. In Fig. are shown typical spatial profiles (recorded at the focus of a lens of 5 m focal length), of (a) the unfiltered and (b) the spatially filtered Copper Vapour Laser beams, achieved using this technique.

#### 4.4 OPTICAL NONLINEARITY IN ATOMIC VAPOUR

An intense laser beam, while propagating through any transparent, homogeneous and isotropic medium, may undergo changes in its spatial, spectral and temporal characteristics (for pulsed lasers) due to an intensity dependent non-linear susceptibility exhibited by the medium. Such non-linear propagation phenomena are important in several areas ranging from development of high power lasers to applications in material processing, remote sensing and laser isotope separation. The nonlinear response of the medium, characterized by an intensity ( $I$ ) dependent refractive index,  $n_2 I$ , is strongly enhanced if the laser wavelength is tuned close to a spectral absorption feature in the medium.

Knowledge of  $n_2$  is important in estimating non-linear propagation effects. In a recent study, the resonant enhancement of  $n_2$  in atomic vapour was successfully investigated using the Z-scan technique, commonly employed for measuring  $n_2$  in condensed matter. This investigation was undertaken primarily, to assess the applicability of the Z-scan technique for measurement of optical nonlinearity in atomic vapour and to determine the frequency regime in which the dielectric response of atomic vapour to a near resonant laser can be formulated using the adiabatic following model. Our experimental data on atomic Sodium is the first report on use of the Z-scan technique for determining resonant nonlinearity in atomic vapour.

The measured absolute values of  $n_2$  as a function of cube of magnitude of detuning from the atomic transitions (589 nm and 589.6 nm) in sodium vapour are plotted in Fig.. According to the adiabatic following model,  $n_2 \propto \Delta\nu^{-3}$ , applicable at large frequency detuning ( $\Delta\nu = \nu - \nu_0$ ) from the atomic transition at  $\nu_0$ . Estimates for the dipole moment obtained from the value of optical nonlinearity measured by us were found to be in good quantitative agreement with reported data.

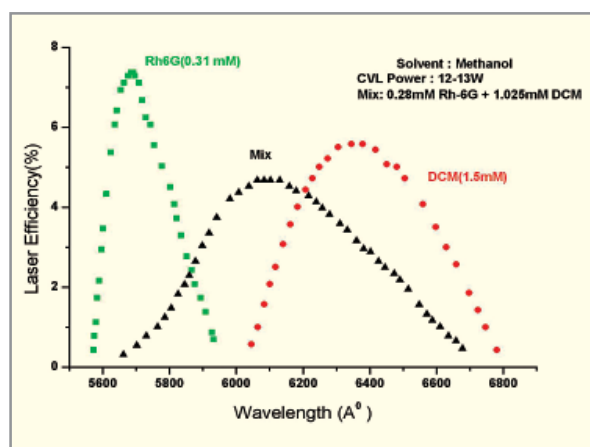


Measured values of  $n_2$  for different laser wavelengths, ■–Red detuned, and ●– blue detuned from D2 transition. ▲ – Red detuned from D1 transition. X - Reported measured value. The solid curve shows the expected dependence calculated using adiabatic following model.

Sucharita Sinha, G.K.Bhowmick, S.Kundu, S.Sasikumar, S.K.S.Nair, T.B.Pal, A.K.Ray, and K.Dasgupta, Optics Comm., 203(3-6), 427, (2002).

#### 4.5 EXTENDED TUNABILITY OF A BINARY DYE-MIXTURE LASER:

Performance of a dye laser based on a binary mixture of dyes (Rh6G and DCM), pumped by a Copper Vapour Laser, resulting in lasing over an extended frequency region has been demonstrated. Utilizing the two laser dyes Rh-6G and DCM dissolved in a common solvent, we have achieved improved



Tuning curves for a dye mixture laser, showing extended tunability in the dye mix as compared to that with each dye separately.

laser performance and a desired shifting of the laser tuning range as depicted in Fig. A rate equation model simulating the operation of such a laser has been developed providing: (a) an understanding of the dynamics of laser action in the mixture, and (b) theoretical estimates for optimum operating parameters for the system.

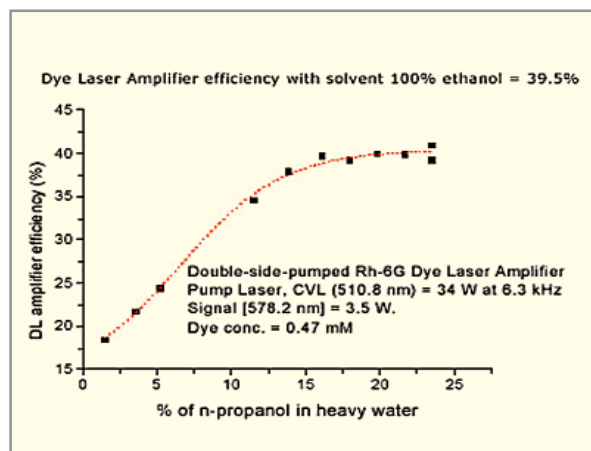
Sucharita Sinha, Alok K. Ray, Soumitra Kundu, Sasikumar, Tamal B. Pal, Sivagiriyaal K. S. Nair, Kamalesh Dasgupta, *Appl. Opt.* **41**, 7006 - 7011, 2002.

#### 4.6 SAFE AND SUPERIOR WATER AND HEAVY WATER BASED SOLVENTS FOR LASER DYES

The main obstacle in wide-spread use of liquid dye lasers in industrial environments is the safety restrictions associated with use of large quantities of rapidly circulating hazardous and toxic organic solvents. Detailed studies have been carried out in BARC on designing safer and superior solvents for applications of liquid dye lasers in the nuclear industry, based on binary mixtures of water with a suitable additive to prevent formation of non-fluorescent dimers of dye molecules in pure water. The water-based solvents for some commonly used laser dyes have not only shown efficiencies comparable with that obtained using conventional solvents such as ethanol, but have also reduced photo-chemical degradation, which is another limitation of dye lasers requiring regular change of dye solution.

For example, the rate of photo-degradation, characterized by a pump induced Quantum Yield of Photo-degradation, which is the probability that a dye molecule would undergo photo-degradation after absorbing a pump photon, was found to reduce from  $5.6 \times 10^{-6}$  in ethanolic solvent to  $2.9 \times 10^{-6}$  in a water/propanol solvent.

Compared to ethanol, the optical refractive index of Water, and especially Heavy Water, is much less sensitive to change in temperature, while it also possesses higher specific heat and density. As a result, localized and inhomogeneous energy deposition present in the dye laser gain region produces smaller optical gradients than in ethanol, making these solvents better suited for high average power laser operation. The results of a recent dye laser amplifier test with a mixture of heavy water and n-propanol is shown in Fig. that demonstrates achievement of amplifier efficiency comparable to that with pure ethanol.



Dye laser Amplifier efficiency  
with solvent 100% ethanol=39.5%

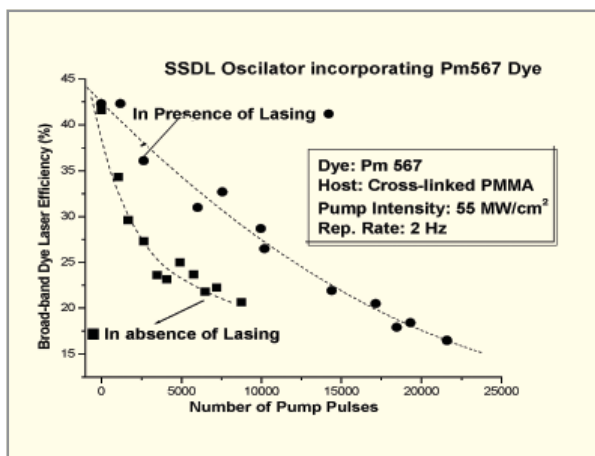
A.K. Ray, Sucharita Sinha, S. Kundu, S. Sasikumar, S.K.S. Nair, T.B. Pal, K. Dasgupta, *Applied Optics- LP 41*, 1704 - 1713, (2002).

#### 4.7 PHOTO-STABILITY OF LASER DYES – ROLE OF STIMULATED EMISSION

Reliable long-term operation of high power dye lasers is largely determined, among other factors, by the photo-stability of the lasing dye. Photo-stability of commonly used laser dyes belonging to Xanthene group, Rhodamine-6G, Rhodamine-B and Kiton –Red, dissolved in ethanol, have been evaluated under irradiation from a pulsed copper-vapour laser. Deterioration of laser performance on account of photo-degradation has also been simulated in terms of a time dependent rate equation model that brings out how the laser performance depends on degradation and possible losses due to the build-up of photodegraded products.

Since photo-chemical reactions proceed from the excited states of the dye molecule, it was anticipated that rate of photo-degradation would be reduced in presence of stimulated emission which would act as a competitive de-excitation channel. Investigating this role played by stimulated emission is difficult in liquid dye lasers as reduction in output power on account of photo-chemical degradation is slow due to rapid dispersion of the degraded molecules in the solvent volume. An experiment was therefore carried out with a solid-state dye doped laser medium where rapid reduction in output power

takes place due to dye degradation confined to the excited region. Fig. shows the reduction in output power of the dye laser, pumped by the second harmonic of a Q-Switched Nd:YAG laser, with and "without" lasing, confirming that rate of degradation is indeed slower in presence of stimulated emission. The data for "without lasing" condition was taken by releasing an intracavity shutter for a short time, to allow laser action to take place for measuring the output power.



Reduction in out put power of a solid state dye laser with and "without" lasing, as a function of the number of pump pulses.

Alok K Ray, Sasi Kumar, Sucharita Sinha, S. Chattopadhyaya, K. Dasgupta, National Laser Symposium, Jan 2005, BARC, Mumbai.

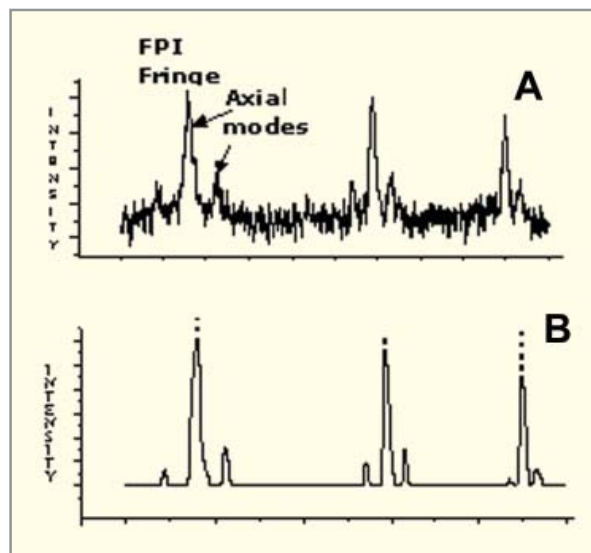
**4.8 DIFFERENTIAL WAVELENGTH METER: AN IMPROVED TECHNIQUE**

A differential wavelength-meter, is an instrument that was developed in BARC for precisely determining small changes in the wavelength of a highly monochromatic radiation source, such as a frequency tunable laser, whose output frequency may vary with time, either on its own or by design. It can also be used to analyse the spectral components of a light source, for example, between the axial modes of a laser. In order to make precision measurements one uses a Fabry-Perot Interferometer (FPI).

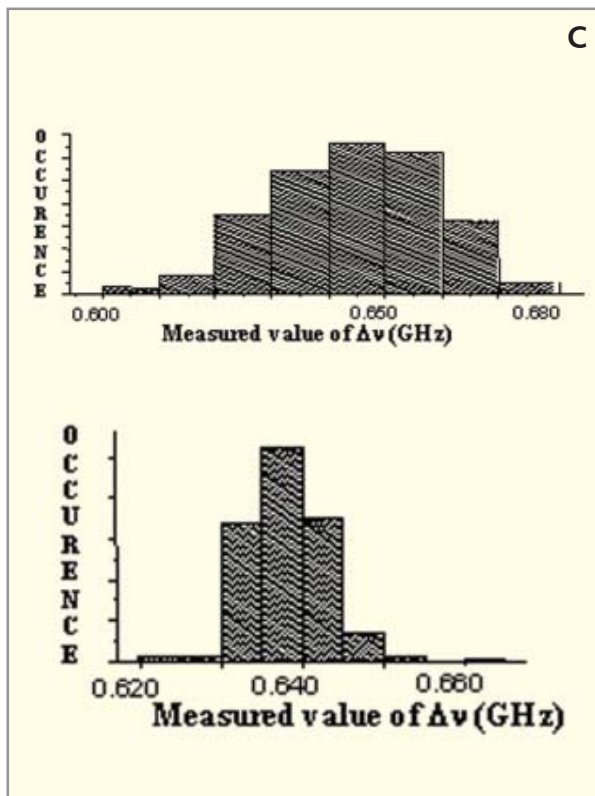
In earlier designs, it was necessary to accommodate a complete circular fringe pattern, formed with a FPI and a short focal length lens, in the CCD camera, in order to determine the fringe radii of different orders that were used to compute the

change in wavelength. In that case, for very sharp spectral lines analysed by a high resolution FPI, the fringe width becomes comparable to the CCD camera pixel size, thereby limiting the accuracy of the system. To overcome this resolution limit, a new technique has been developed, in which, large diameter FP fringes with proportionally large fringe-widths are produced by using a long focal length lens. The CCD camera now accommodates only a part of the fringes. However, the radii of the fringes can still be determined from a measurement of the fringe separations, which is possible because of a special functional relationship between the diameters of the fringes formed by a FPI.

The results of a test measurement of the separation ( $\Delta v$ ) between the axial modes of a He-Neon laser are shown in the figures below. Fig. A shows the raw video signal across the FPI fringes. Each fringe shows the He-Ne laser spectrum with decreasing resolution from the fringe center (not seen in fig.). A digital FFT based noise filter applied on the video line signal brings out the laser spectrum clearly (Fig.B), from which the mode separation is computed. Fig. C shows the results of a large number of measurements, confirming a narrower spread in data obtained, and a hence a higher accuracy using the new technique.

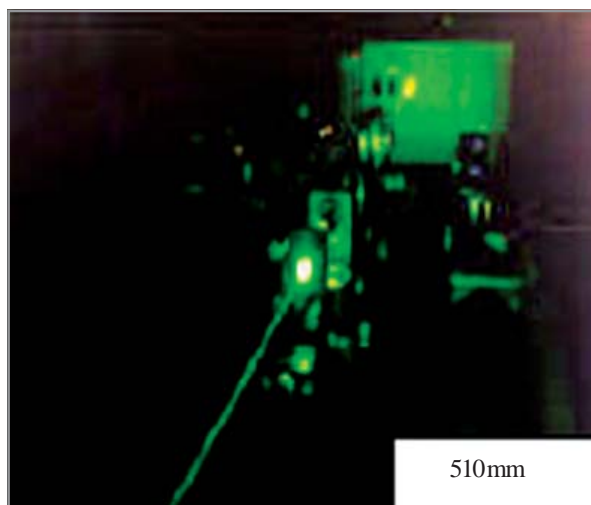


Raw video signal (A) and filtered video signal (B) of FPI fringes recorded with a CCD camera and acquired through a Digital Storage Oscilloscope in the PC, showing axial modes in He-Ne laser spectrum.



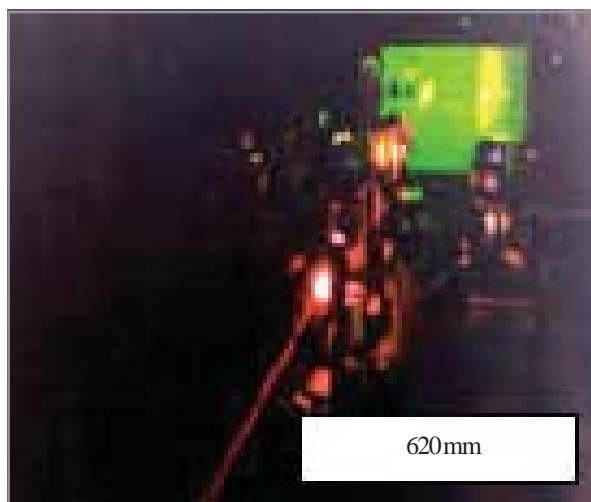
Distribution in values of  $D_n$ , measured with FP Interferometer fringes formed with a 20 cm focal length lens (Left) and a 100 cm focal length lens (Right). Std. deviation in latter case is  $\sim 5$  MHz.

The wide wavelength tunability of the OPO was utilized to excite uranyl nitrate solution at  $\sim 430$  nm and the resulting fluorescence (Fig. B) spectrum was recorded showing the signature peaks of uranyl ion (Fig. C). In comparison to the conventional approach of using Nitrogen laser in uranium trace detection, use of wavelength tunable radiation will substantially improve the sensitivity and selectivity in ultra trace detection of several elements, including uranium, in process streams and effluents.

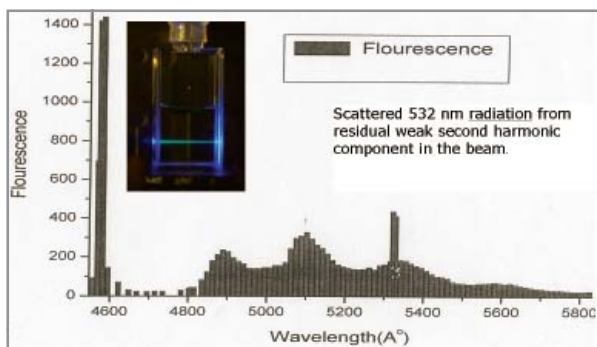


#### 4.9 OPTICAL PARAMETRIC OSCILLATORS

As part of BARC's ongoing efforts to develop advanced tunable lasers, L&PTD had embarked upon a programme for design and development of Optical Parametric Oscillators, which are solid state coherent beam sources with widely tunable output wavelength, and with several advantages over commonly used tunable laser sources such as dye lasers. Fig. A shows an OPO set-up in BARC in operation at two widely different wavelengths. Several techniques for reduction of threshold pump power requirement in OPOs have been investigated, including a new technique based on injection of an external, spectrally uniform dye laser beam into the OPO that resulted in  $\sim 33\%$  reduction in the input power threshold. Threshold reduction would facilitate development of high repetition rate narrowband OPOs, one of the aims of this activity.



Optical parametric oscillator pumped by the 355 nm output from a frequency tripled Nd:YAG laser.



Fluorescence spectrum. Inset shows Fluorescence in Uranyl Nitrate solution excited by an OPO output beam of 430 nm

R.C.Bapna, and K.Dasgupta, J. Modern Optics 49(3), 391-396, (2002).

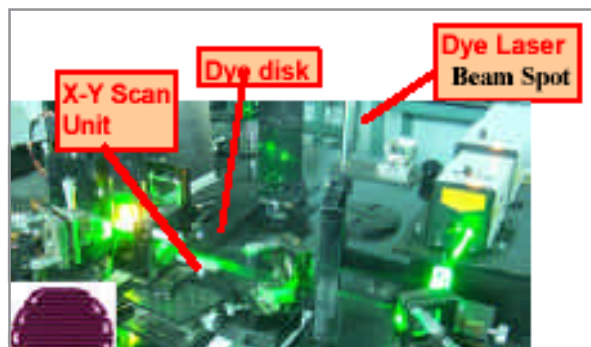
#### 4.10 SOLID STATE DYE LASER

Optically excited solid-state dye lasers are emerging as superior alternatives to liquid dye lasers for many applications in spectroscopic investigations and analysis. The main limitation in solid state dye lasers, in which the dye molecules are dispersed in a polymeric or composite transparent solid material, is rapid photo-degradation of the active medium. In a collaborative effort between L&PTD, BOD and UICT, dye-doped polymeric materials using both physical and chemical doping are being developed at BARC. The major thrust is to improve heat dissipation, suitable laser disk preparation and special laser designs for prolonging the operation life of the disks. MPMMA, co-polymers P(MMA : HEMA) and covalently linked dye monomers were developed. These samples are tested in laser amplifier and oscillator configurations. Fig. shows some of the dye doped polymer disks, after sectioning and optical polishing, fabricated in collaboration with UICT. An indigenously developed polymeric (MPMMA) disc doped with (0.5 mM) Rh6G dye was longitudinally pumped with the 2<sup>nd</sup> harmonic of YAG laser. Lasing efficiency of 10% was obtained with 24 nm spectral width at 558 nm as central wavelength.

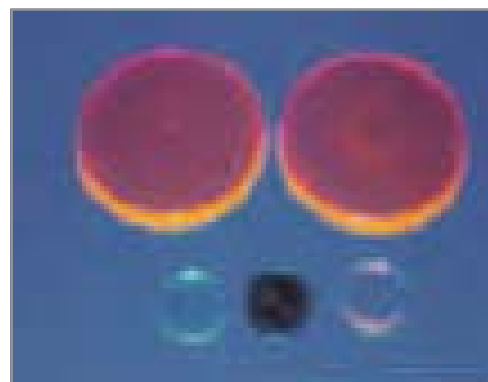
When excited by the second harmonic of a pulsed Nd:YAG laser at 10 Hz pulse repetition frequency at a single spot, a Pyromethene dye doped cross-linked PMMA disk exhibited 39% optical efficiency as a laser amplifier, with only a 4% drop in efficiency after 1 hr operation. With motorized area scanning,

to utilize a larger volume, more than 7 hrs of operation of Rhodamine 6G dye doped modified PMMA disk in a laser oscillator has been achieved without any noticeable drop in efficiency.

To improve the photo-stability of dye doped solid host, work on synthesizing covalently linked rhodamine B dye monomer (chemical doping) with MMA was initiated. The dye derivative capable of forming covalent crosslinkage with the monomers has been prepared and tested. This will enhance the heat dissipation of the dye through backbones of polymer macromolecule and lead to long operational lifetime of the solid-state dye laser. This search for new materials will pave the way for a final solid state dye material and laser configuration useful for laser spectroscopy and related work.



10Hz Solid-state dye laser. The inset shows the scan pattern of the pump beam on the disk obtained with the scanning disk.



Indigenously developed samples dye doped polymer (Rhodamine 6G in MPMMA)

S.Singh, V.R.Kanetkar, G.Shridhar et al, Journal of Luminescence, Vol 101, p285, March 2003.

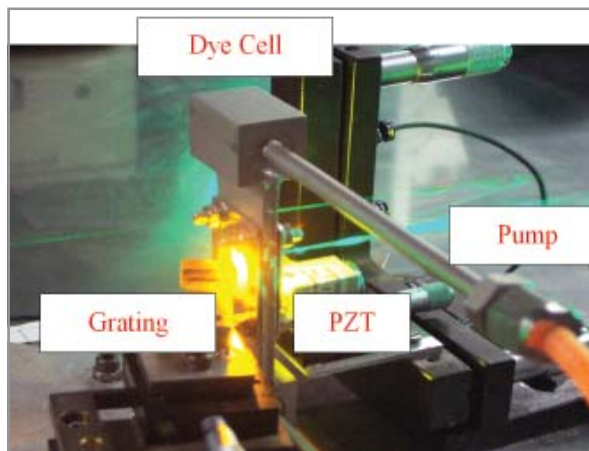
J.Thomas, Sasi Kumar, Alok Ray, K.Dasgupta, NLS-4 (2005), BARC, Mumbai

#### 4.11 DEVELOPMENT OF A SINGLE LONGITUDINAL MODE (SLM) DYE OSCILLATOR - PRE-AMPLIFIER SYSTEM PUMPED BY COPPER VAPOR LASER

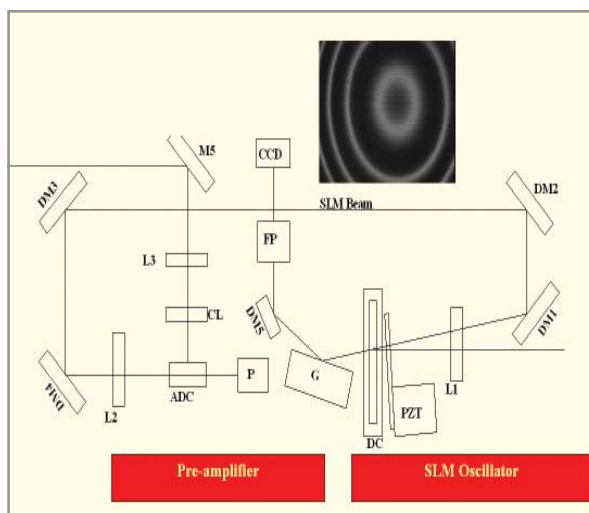
Narrow band single longitudinal mode (SLM) dye lasers are used in the selective excitation/photoionization of atoms with low isotopic shifts. A Single Longitudinal Mode (SLM) pulsed dye laser in the Littrow configuration with a narrow time averaged linewidth  $\sim 600\text{MHz}$ , an excellent spatial mode (near TEM<sub>00</sub>), a broad tuning range (564 - 600nm), negligible Amplified Spontaneous Emission (ASE) and efficiency of 5% has been demonstrated. The low output power from the (SLM) oscillator which has a good spectral and spatial content was boosted up in a pre-amplifier transversely pumped by the green beam of the Copper Vapor Laser with an extraction efficiency of 11%. The laser oscillator (cavity length = 3cm) consists of a diffraction grating (3300 lines/mm) in the Littrow configuration, a demountable flow through dye cell and an output coupler ( $\sim 4\%$  R) mounted on a PZT actuator. The short cavity results in an extremely low value of background Amplified Spontaneous Emission (ASE). The green wavelength of the CVL operating at a PRF of 6KHz. pumps the dye laser in a longitudinal resonator configuration.

In the preamplifier, the laser beam from the SLM oscillator is focused in a reflected beam geometry into the amplifier dye cell which is transversely pumped by CVL (510.6 nm, 6 kHz). The input signal beam is spatially and temporally overlapped with the amplifier gain (0.8 mM Rhodamine 6G in ethanol). The dye flows through an indigenously developed demountable dye cell at a high flow speed of 15 m/sec.

The schematic and a photograph of the laser are shown in figures. The mode drift and fluctuations in the SLM output were reduced by employing both passive and active frequency stabilization techniques. Active frequency stabilization was established by using an active stabilization control loop which is based on PID control logic.



Photograph of SLM Dye Laser



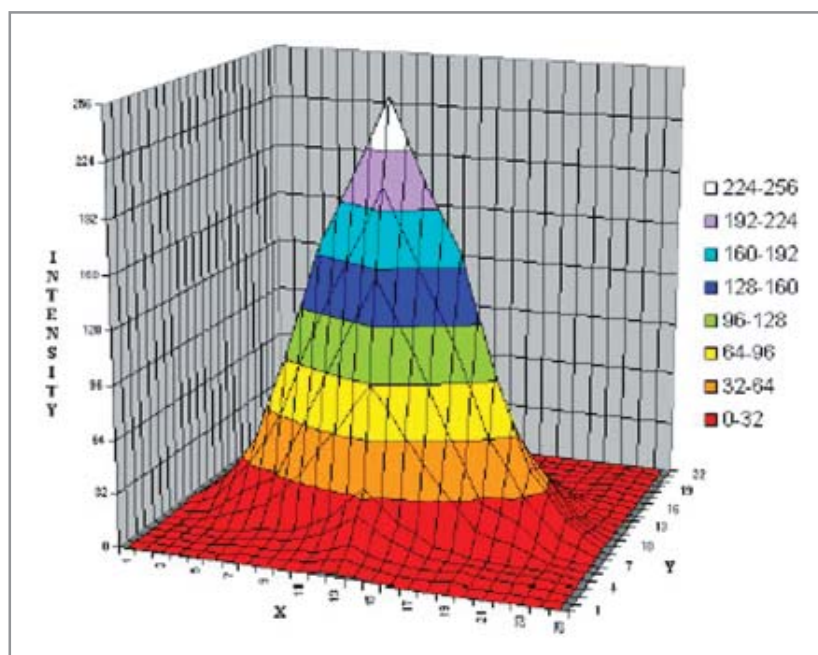
Schematic of SLM Oscillator- Pre amplifier

V.S.Rawat, G.Sridhar, K.G.Manohar, Sunita Singh, NLS-2003

#### 4.12 A PRE-PROTOTYPE DIGITAL BEAM PROFILER FOR INFRARED LASERS

A pre-prototype digital beam profiler has been developed in the Laser and Plasma Technology Division for measurement of intensity profiles and other parameters of infrared lasers. The profiler is simple, inexpensive, made from all indigenously available materials and easy to operate. It uses an array of thermocouples as the sensor element, which can handle even highly intense laser beams like focused beam of pulsed carbon-di-oxide laser.

A Cartesian Positioner has been developed which has three controlled stepper motors for accurate positioning of the sensors at any chosen spatial position in the laser beam. The whole beam can be scanned under the control of the software and the data collected can be processed for various computations. The software can also present the data



A typical profile for a carbon-di-oxide laser

graphically, in the form of 2-D or 3-D intensity profiles. It also provides the information regarding various beam parameters like the best Gaussian fit, divergence, beam diameter, focusability to required size, irradiance etc. The figure shows a typical profile for a carbon di-oxide laser beam, obtained using the profiler.

A.S.Dongare, V.Parthasarathy, S.S.Thattey, S.K.Sarkar. BARC Report: BARC/2003/E/002

#### 4.13 KINETICS OF ISOTOPE-SELECTIVE MULTI-STEP PHOTOIONIZATION FOR LASER SPECTROSCOPY AND TRACE ANALYSIS

Resonance ionization mass spectrometry (RIMS) technique, having exceptionally high selectivity (both isotopic and isobaric)

and high sensitivity, is potentially useful for applications in environmental monitoring, nuclear industry, geophysics, trace analysis and isotope separation. Trace analysis problems range from detection of radioisotopes in the environment to measurements of solar neutrino flux and studies of nuclear structure at on-line mass separator facilities. These problems

require extremely high selectivity. The use of narrowband lasers in RIMS is one of the ways by which it is possible to obtain the large optical isotopic selectivity and is recently applied to the measurements of rare calcium isotopes, which can have a number of applications. For instance, the rare, long-lived radioisotope  $^{41}\text{Ca}$  has applications for radiochemical dating, determination of cosmic ray flux and medical tracer. The rare isotope  $^{43}\text{Ca}$  is potentially usable as an ion qubit in quantum logic experiments. However, useful measurements in these applications require isotopic selectivity in the range of  $10^{10} - 10^{16}$  against the predominant stable isotope  $^{40}\text{Ca}$ . Achieving this high selectivity and still maintaining high efficiency requires careful selection of the resonance excitation steps of a multi-step photoionization

process.

The kinetics of multi-step photoionization of atoms with narrowband lasers is described most accurately by the Density Matrix (DM) method which incorporates the coherences established between the atomic states of the laser fields. This approach is a comprehensive one, involving complicated computational procedure. However, its development is necessary for investigating atomic excitations with narrowband lasers. We have obtained the equations of motions for the time evolution of the DM elements for multi-step photoionization of atoms and developed the computer code to solve the DM equations numerically for real atomic beams having finite angular divergence and velocity distribution. We have validated the code against the reported data for calcium. The results are presented in Table. We have also incorporated the finite laser linewidth in the code. The DM code thus developed is useful for laser isotope separation and trace analysis of lanthanides and actinides.

Isotope	Isotopic selectivity		
	Our value from DM method	Reported experimental value (Bushaw et al., Spectrochim. Acta B 54, 321, 1999)	Reported value from DM method (Bushaw et al., Spectrochim. Acta B 54, 321, 1999)
<sup>41</sup> Ca	$3.3 \times 10^5$	$2.0 \times 10^5$	$2.5 \times 10^5$
<sup>42</sup> Ca	$1.3 \times 10^7$	-	$1.3 \times 10^7$
<sup>43</sup> Ca	$6.1 \times 10^7$	-	$5.3 \times 10^7$
<sup>44</sup> Ca	$2.0 \times 10^8$	-	$1.9 \times 10^8$
<sup>46</sup> Ca	$9.6 \times 10^8$	-	$9.0 \times 10^8$
<sup>48</sup> Ca	$2.7 \times 10^9$	-	$2.5 \times 10^9$

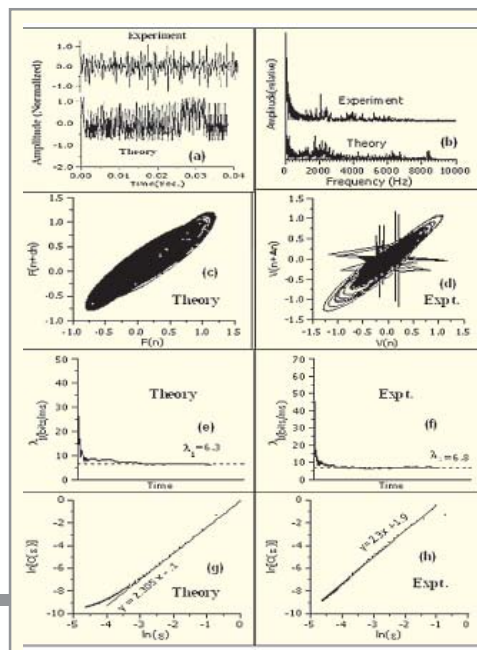
Optical isotopic selectivity of minor calcium isotopes against the major isotope <sup>40</sup>Ca in the 4s2 1S0 – 4s4p 1P1 – 4s4d 1D2 three-step photoionization scheme.

G.P.Gupta, A.K.Pulhani, B.M.Suri, Journal of optical society of America B, Vol.21, 436(2004)

#### 4.14 NON-LINEAR DYNAMIC STUDY OF ARC ROOT DYNAMICS

High power thermal plasma systems are being used for a large number of advanced materials processing applications. Recent studies have shown the device performance and process efficiency to be critically dependent on understanding and controlling the arc dynamic characteristics. Until this time, arc physicists had been looking either at the static characteristics or at the dominant frequencies in the fluctuation power spectra to characterize electrode erosion or process degradation. An entirely new approach to analysis of experimental data and analytical prediction in arc instabilities have been initiated at BARC that went beyond frequency spectra or time series to look at the fluctuation data from the point of view of nonlinear dynamics. For the first time, atmospheric arc devices were shown to be exhibiting chaotic transitions with current and gas flow as the chaos controlling parameters. It has been possible to characterize the dynamic stability of the plasma system through the phase portrait, the Liyapunov exponent and the fractal dimension. This was supplemented through a generalized predictive theory for characterizing the dynamics of the arc root. The theory attempts to solve the nonlinear amplitude equation for the fluctuations in plasma field parameters near the instability threshold as function of operating conditions. It has been able to identify the local temperature and electrode metal vapor concentration gradients at the arc root to be the major control parameters for generation of unstable modes and predict conditions for

generation of catastrophic conditions leading to arc extinction. The figure shows a comparison between predictions and experimental data. This nonlinear dynamic approach has the potential to predict instabilities and control procedures in complex dynamic systems through their signatures in phase space. This approach has yielded good results in an arc assisted Nanomaterials generator.

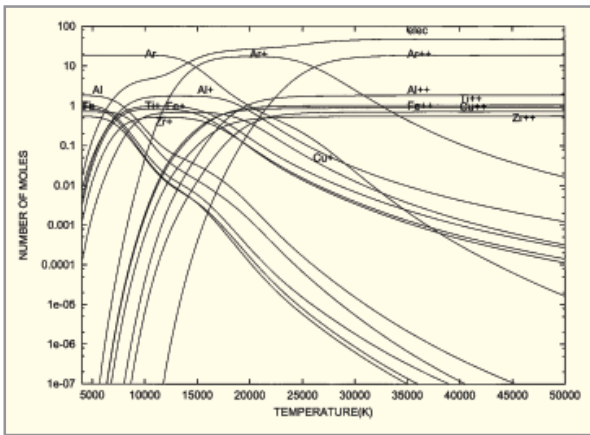


Experiment and theory for an atmospheric plasma arc with  $I=200A$ : (a) time series (b) Power spectra (c) & (d) Phase portraits (e) & (f) Evolution of Lyapunov exponents; (g) & (h) dimension computations

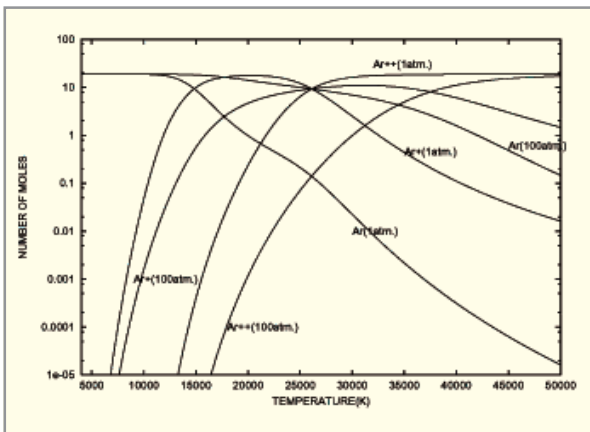
S.Ghorui and A.K. Das, Origin of fluctuation in arc plasma devices, Physical Review E, vol.- 69,(2004), pp.-026408

**4.15 THERMO PHYSICAL PROPERTIES OF THERMAL PLASMAS**

Generation of thermo physical properties of arc plasmas for different plasma generating gases is a basic necessity for process characterization and device design. A major problem in computation of high temperature thermo physical properties is the availability of elemental free energy data at extremely high temperatures (>30,000 K). A code to compute composition and other thermo physical properties of arc plasmas has been developed using the partition function approach. Figures show a few results of computation with a typical plasma gas namely argon.



Composition of plasma consisting of (Ar(75% by weight)+Fe(5% by weight)+Al(5% by weight)+Cu(5% by weight)+Ti(5% by weight)+Zr(5% by weight) at pressure of 1 atm and temperatures varying from 4000-50,000K



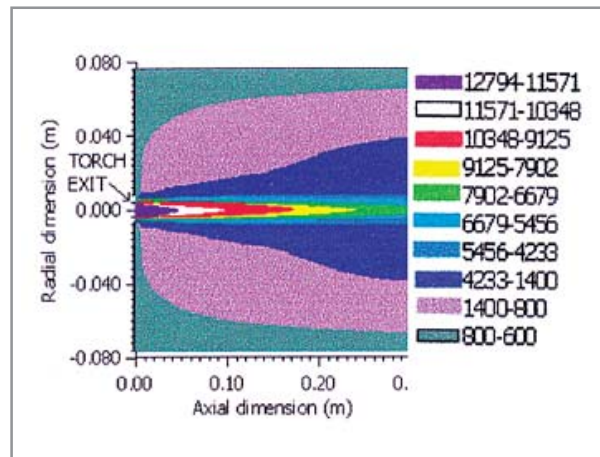
Effect of pressure on ionization in argon plasma

Indrani Banerjee, S.V.Bhoraskar and A.K.Das, Proceedings of the Symposium on Power Beam and Material Processing, 25-28, Sept.2002, BARC, Mumbai, India, pp.313-317

**4.16 COMPUTATIONAL FLUID DYNAMICS (CFD) OF THERMAL PLASMAS**

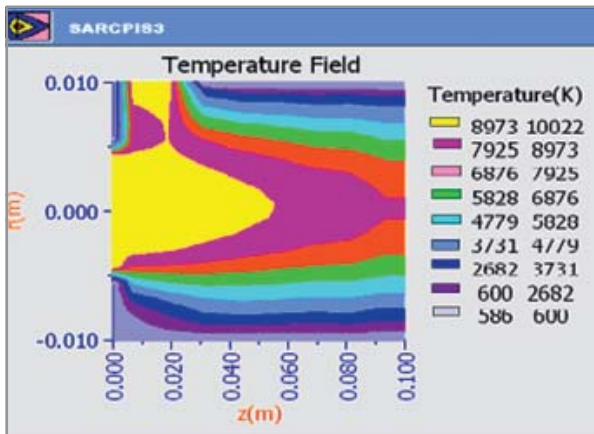
Thermal plasma jets and current carrying arc columns interacting with materials present extremely complex problems of electro-fluid dynamics. The presence of sharply varying material properties, turbulence, arc spot etc need specialized CFD simulation codes for device design and enhancement of process performance. L & PT Division has developed 2D (SARCIS2-Simulation of ARC Plasma In Steady State in 2 D) and 3D (SARCIS3-Simulation of ARC Plasma In Steady State in 3 D) CFD codes for simulating thermal plasma flows in plasma chemical reactors.

SARCIS2 is a 2D finite volume FORTRAN solver of electromagnetic NS equation for simulation of arc discharge. The solver can simulate arc discharge with variable material



Temperature distribution inside a reaction chamber of radius 3 inch for a 20 kW nontransferred plasma torch.

properties as well as input plasma parameters and geometry. Once the simulation is completed, graphics files showing potential distribution, current, distribution, enthalpy distribution, flow velocity in radial and axial direction, isotherm contours and stream lines get automatically created. A typical



A sample output from SARCPI33 giving asymmetric distribution of temperature in the nozzle region of a plasma torch

output in simulation of a reaction chamber is given in Fig. Owing to inherent asymmetry in most of the arc plasma systems due to attachment of arc root at a particular position or the typical geometries of the plasma reactors, 2D simulation becomes inadequate and 3D solver is the only option for accurate prediction of plasma field quantities. SARCPI33 is a FORTRAN code for numerical simulation of arc plasma jet in 3D in laminar as well as turbulent modes. The code uses finite volume technique, cylindrical coordinate system and SIMPLE algorithm for solution. A sample simulation result of the nozzle region of a plasma torch is displayed.

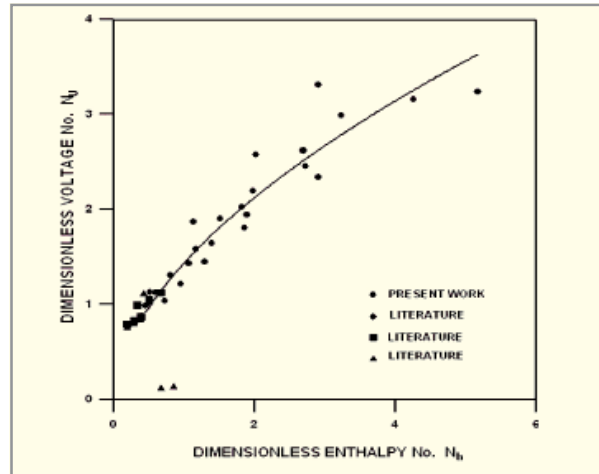
S. Ghorui, A.K. Das and N. Venkatramani, Plasma Sources Science and Technology, 9, 1-8, (2000)

A.K. Tiwari, C.S.R. Prasad, V.K. Kansal, S. Ghorui and A.K. Das, Proceedings of the 18th National Symposium on Plasma Science & Technology, Dec, 8-11, 2003, Ranchi, pp.21

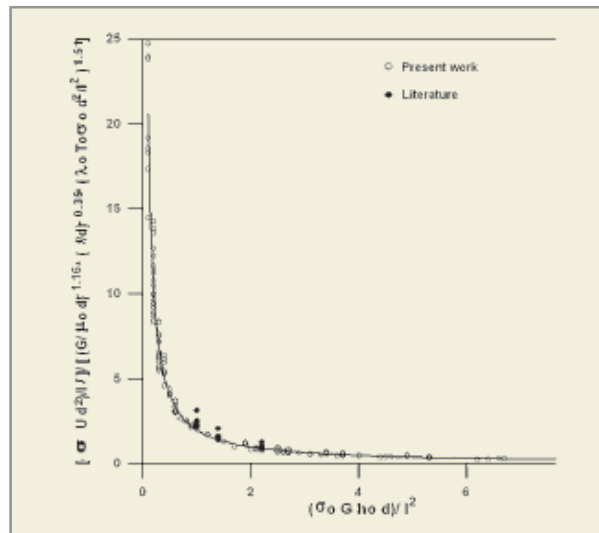
#### 4.17 SIMILARITY ANALYSIS FOR PLASMA TORCHES AND JETS

Dimensional analysis is methodology of representing the overall effects of complex phenomena of plasma beams in terms of dynamic similarity in the form of generalised functions, expressed in terms of generalised arguments in the form of dimensionless numbers, corresponding coefficients and constants. The various non-dimensional numbers for a flowing plasma with electromagnetic fields are derived from the conservation equations of mass, charge, momentum and

energy. The similarity expressions provide design data for large systems based on data generated on small systems. Work done at L & PT Division, BARC has been able to generate generalized relation for gas stabilized plasma torches. Figures illustrate the data generated and comparison with data published.



Plot of non-dimensional Current voltage Characteristics (CVC) using Enthalpy number and Voltage numbers (5.26%). The plot also includes the experimental points observed in literature.

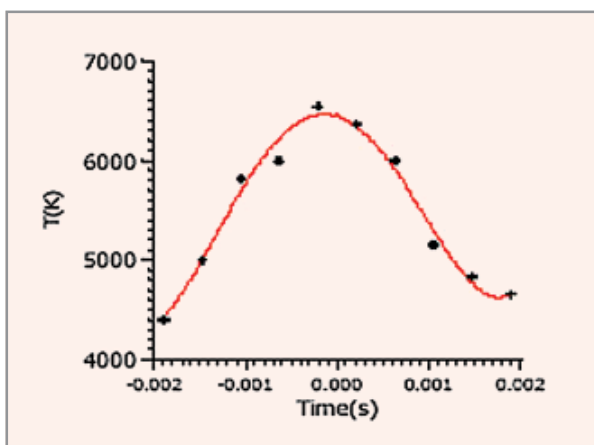
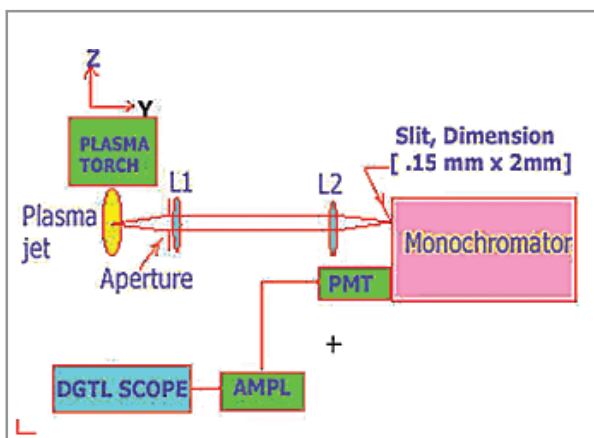


Generalized Current Voltage Characteristic (CVC) relationship of a transferred arc plasma melter torch with experimental points in literature (6.5-9.3%)

A. M. Paingankar, A. K. Das, V. S. Shirodkar, K. P. Shree Kumar, and N. Venkatramani, Plasma Sources, Science and Technology, 8, 100.

**4.18 INNOVATIVE DIAGNOSTICS: TIME RESOLVED TEMPERATURE MEASUREMENT IN A SPRAY PLASMA JET**

It has long been observed that plasma spray process is beset with problems associated with partially melted or unmelted powders that is responsible for severe degradation of process efficiency. The problem is being looked at both from the point of view of arc instabilities as well as fluctuations in the power supply. An attempt was made by us to measure the temperature fluctuations in plasma jet caused by ripple in DC power supply through an innovative use of the atomic Boltzmann plot method. It was found that temperature of the plasma jet fluctuates widely, from 4400 K to 6500 K during each ripple period of 6.67 mS. Due to this; the spray powder is non-uniformly heated, degrading the spray coating. This



Experimental arrangement for measurement of temperature fluctuation and a sample temperature profile

measurement was given a pointer to determine the correct power level for getting low porosity spray coatings. Figure shows the measurement system and the temperature variation.

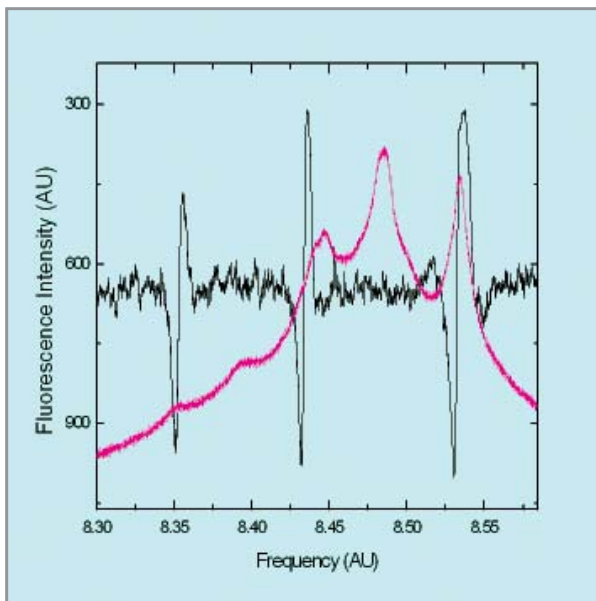
S. N. Sahasrabudhe, N. V. Kulkarni, S. Ghorui, D. N. Barve, N. K. Joshi and S. V. Bhoraskar, Proceedings of the Symposium on Power Beam and Material Processing, 25-28, Sept.2002, BARC, Mumbai, India, pp.323

**4.19 LASER COOLING OF ATOMS**

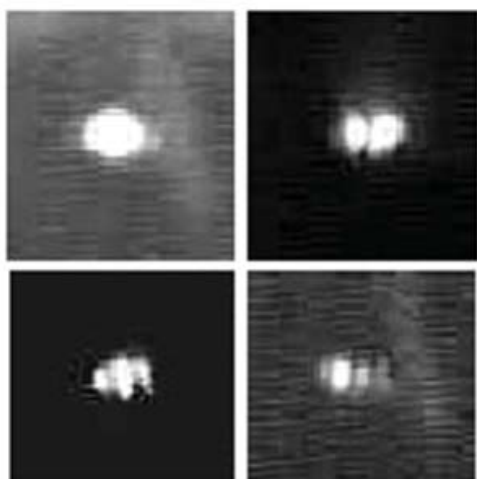
The field of laser cooling of atoms is one of the prime and frontier areas of research in contemporary physics today. BARC is one of the few laboratories in India, which undertook work in laser cooling and was first to demonstrate laser cooling of cesium atoms. Notably, this has been achieved using local expertise and technology. The efforts have realized a state-of-the-art facility, for laser cooling of atoms, consisting of Magneto-Optical Traps (MOT), dark trap, sophisticated diagnostic techniques for temperature and number density of cold cloud etc. The facility has been routinely used for generating cold samples of Cs (~100 μK) and Rb (~200 μK) for a variety of investigations, which include precision spectroscopy, collision physics and quantum optics. The long-term vision in this programme includes Bose condensation and development of advanced devices such as atomic clocks, gradiometers and futuristic quantum computation.



A view of the Laser Cooling Laboratory at Laser & Plasma Technology Division showing a magneto-optical trap (MOT) for cold cesium atoms and relevant diagnostic set-up.



Studies in Ultra-Cold Collisions: Experimental result on control of cold collisions in a sample of lasercooled cesium atoms. A control laser is swept across the cesium resonance  $6S_{1/2} F=4 \rightarrow 6P_{3/2} F=3,4,5$ , which results in enhancement and de-enhancement of the number of trapped atoms in a MOT. The frequency scale is provided by the saturated absorption spectrum.



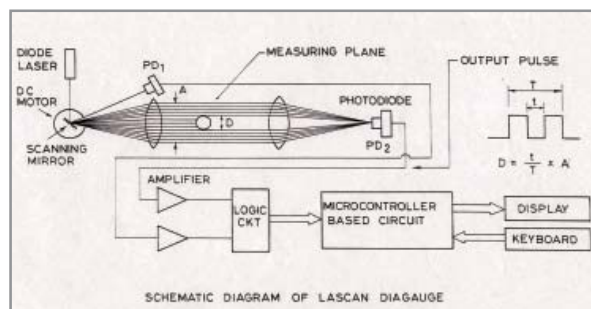
Cold and Spin Polarised Cesium Atoms: Trapping of cold atoms in multiple potential wells formed in a single MOT. Fluorescence images show multiple clouds signifying a transition from a single well to four well trapping potential.

K.G. Manohar and B.N. Jagatap, Frontiers in Atomic, Molecular and Optical Physics, **3**, 219 (2003).

#### 4.20 LASER BASED INSTRUMENTS FOR DIAMETER MEASUREMENT AND REBOUND VELOCITY MEASUREMENT

**Lascan Dia-Gauge:** It is a laser-based diameter measuring instrument using beam scanning technique. Here a fine beam of visible light from diode laser scans a measuring plane using a rotating mirror and collimating optics. An object kept in the measuring plane obstructs the scanning beam for the time proportional to its dimension. The parallel beams are then focused by a receiving optics on a photodiode to generate a shadow pulse of object, which is electronically processed to give the dimension of the object. It can measure diameters in the range of 1 mm to 25 mm with an accuracy of  $\pm 5 \mu\text{m}$ .

**Rebound velocity Meter:** A laser based rebound velocity measuring instrument has been developed which can measure falling as well as rebound velocity of a spherical object with an accuracy of better than 2%. It is based on time-of-flight principle. A horizontal sheet of uniform intensity laser light is generated and the time taken by the object to pass through the sheet is measured to calculate its velocity. User can select through keyboard to display the ratio of rebound velocity to falling velocity.



Lascan Dia-Gauge

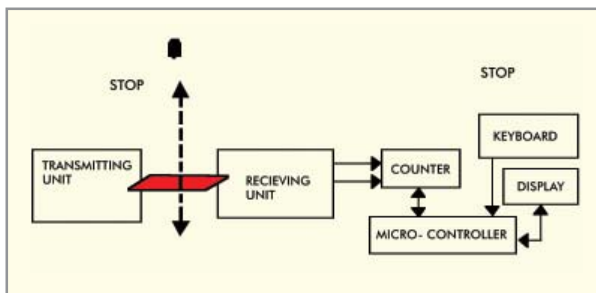


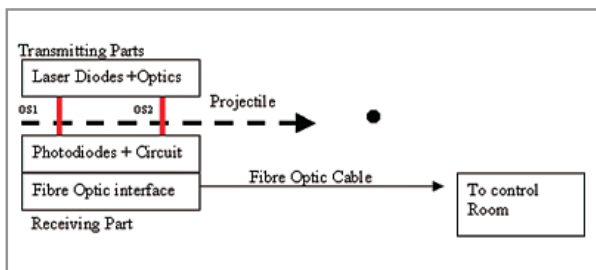
Diagram of the Rebound Velocity Meter

Aseem Singh Rawat, U C Bhartiya, R C Khattar; LAMI 1997, IGCAR, Kalpakkam  
 Aseem Singh Rawat ; INCON 2004, PIET Pune

**4.21 LASER BASED INSTRUMENT FOR PROJECTILE SPEED MEASUREMENT**

**Projectile Speed monitor:** supplied to DMRL Hyderabad to measure the velocity of a projectile fired from gas gun, has been upgraded as per user requirement and is separated into two units. (1) Sensor unit, carrying Laser, photo-detector and pulse generating ckt, (2) Monitor unit, carrying microcontroller based circuit to calculate and display the velocity based on signal received from the sensor unit. The velocity of projectile is calculated by measuring the time taken by the projectile to cover the distance between two optical screens OS1 and OS2 of sensor unit, separated by known distance.

The monitor unit is in the control room and the sensor unit is near the target , separated by a distance of 50 meters and connected through a fiber optic cable to avoid EMI. The upgraded model has been supplied to DMRL, Hyderabad and so far has been successfully tested upto the projectile speed of 2600 m/sec.



Schematic diagram of SENSOR UNIT



Photograph of the Sensor Unit

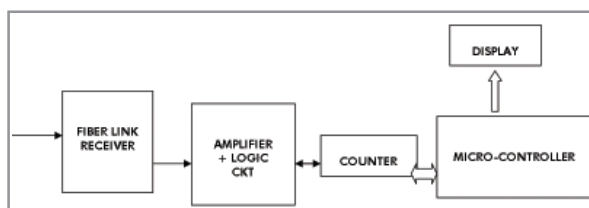
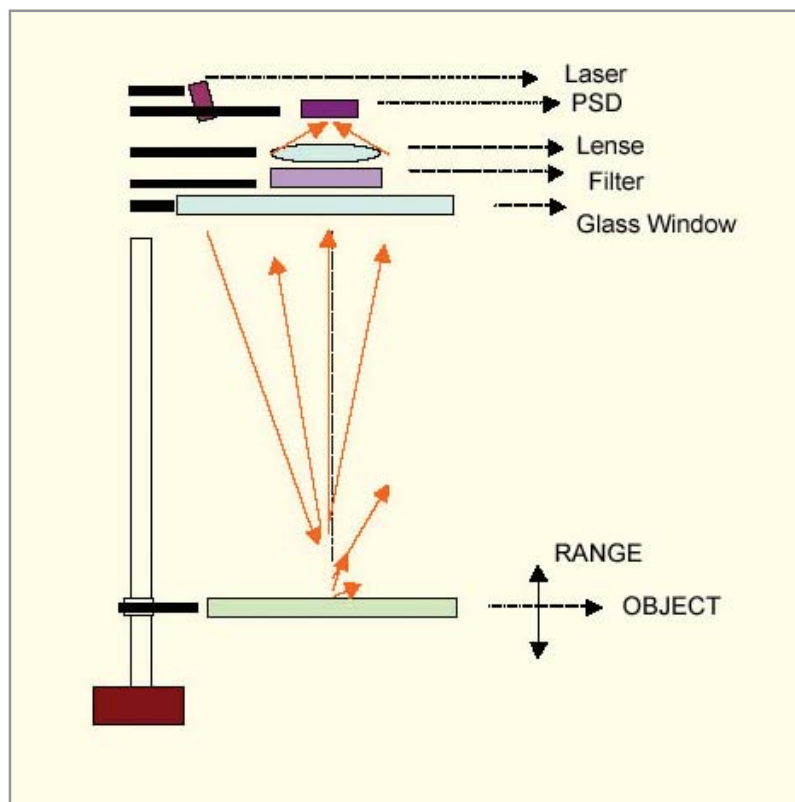


Diagram of the Monitor unit

Aseem Singh Rawat, Nitin Kawade, S L Makker, Vembu Ananthraj ; ICLAOM 2003, IIT Delhi  
 Aseem Singh Rawat, Nitin O. Kawade ; BARC Newsletter, Sept. 2004

**4.22 LASER BASED INSTRUMENT FOR FREE SURFACE LEVEL MEASUREMENT OF LIQUID METAL**

Laser based Optical Triangulation technique is most suitable where noncontact and remote measurement of a surface level or object distance is required. One of such application is in a nuclear experiment, where it is required to measure the free surface level of liquid metal from a height of 1 meter with an accuracy of  $\pm 1$  mm. A Diode Laser based instrument, using optical triangulation technique, is under development for liquid metal level measurement. In Optical Triangulation technique, a triangle is formed between the light source (LASER), point of reflection/scattering (free surface) and the detector. Using the geometry of a triangle, any variation in the free surface level is determined by measuring the variation of focused spot on the photo-detector (fig). Linear Position sensitive detector (PSD) is used as photo detector. The sensor-object distance is calculated trigonometrically and accuracies of better than 0.5% are the norm. Measurement time could be as low as 10 ms, allowing real-time study of moving or vibrating objects.



Schematic of liquid level sensor

#### 4.23 CCRF DISCHARGE STUDIES AND DEVELOPMENT OF A 40 MHz, 5 kW RF POWER SUPPLY FOR A DIFFUSION COOLED SLOW FLOW SLAB TYPE CO<sub>2</sub> LASER

Radio frequency excitation of CO<sub>2</sub> laser is preferred to DC because it offers advantages such as high power density, low operating voltage, no need for electrical ballasting, better stability, easy power modulation, area scalability and compact rugged all metal modular structure. A 5 kW, 40 MHz rugged and reliable RF power supply has been designed and developed to power the capacitively coupled RF excited CO<sub>2</sub> laser. It consists of a class- C amplifier based on a VHF power tetrode (4CX 5000A), driven by solid state MOSFET and BJT amplifier stages with a 40 MHz crystal oscillator at the first stage. The matching circuits between various amplifier stages of the RF power supply were developed and optimized for maximum power transfer, negligible reflected power and good electrical stability. The RF power amplifier has been successfully tested

up to 2 kW of output power level using a 50 ohms water-cooled RF load.

An all metal, slow flow diffusion cooled slab type CO<sub>2</sub> laser head with free space resonator as shown in the Fig. has been fabricated. The discharge channel consists of a pair of aluminum electrodes separated by ceramic spacers. It is one meter long with 7 mm height and 15 mm or 40 mm width. The gas mixture (He: N<sub>2</sub>: CO<sub>2</sub>, 68: 26:6) flow rate was varied from 1 to 4 SLPM and the discharge pressure varied from 5-40 Torr. The two main problems associated with RF excitation, namely the problem of optimum power transfer from RF supply to discharge (i.e. impedance matching) and problem of uniformity of longitudinal voltage distribution have been studied extensively. Using proper impedance matching network, the RF reflected power has been reduced below 1% of the forward power. By using terminating inductors at electrode ends, the standing wave voltage on the electrode measured was uniform within 15 % and did not contain any harmonics.



Slab type RF excited Carbon dioxide laser system

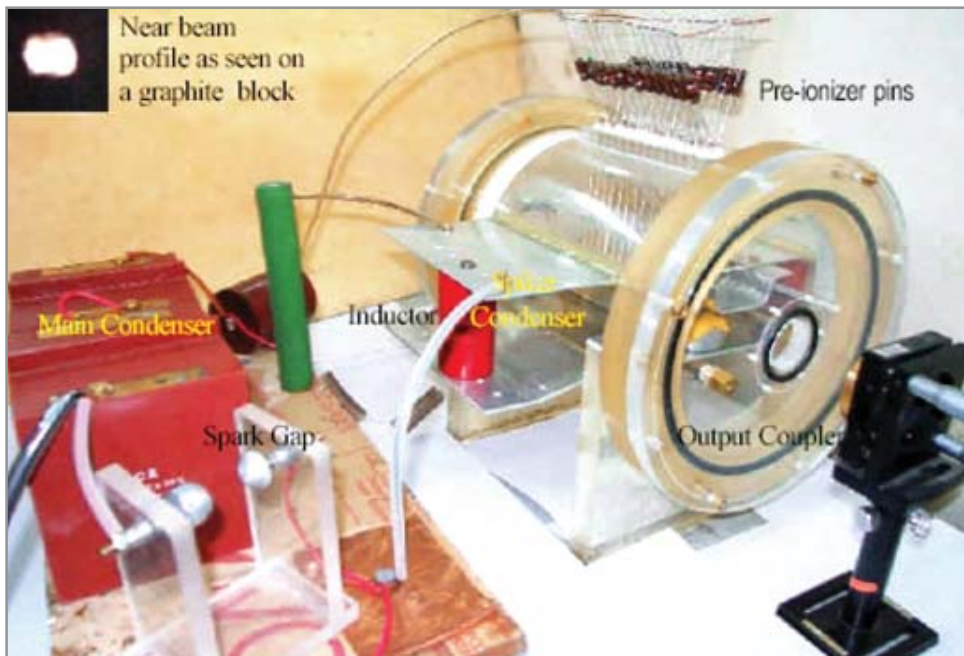
N. K. Joshi, D. P. Chakravarthy and M. Madanmohan. Proc. Nat. Laser Symposium- 2003, p.179-180, IIT Kharagpur, Dec. 22-24,2003

and facilitate the occurrence of an arc free discharge. We have, in our laboratory, achieved helium-free operation of a conventional TEA-CO<sub>2</sub> laser under a wide range of operating conditions. This was rendered possible by integrating the spiker and sustainer-like actions in to a single pulser network by making use of a coupling inductance. This, in addition to delaying the spiker with respect to the preionisation, also decided the rate of rise of voltage across the electrodes and therefore, tailored the sustainer pulse such that arc-free operation at atmospheric pressure in a helium-less gas mixture became possible. The fact that expensive and scarce helium is not a constituent of the laser gas mixture makes it an ideal system for high repetition rate operation as the gas recirculatory loop consisting of the heat exchanger and the catalytic re-converter can be readily dispensed with here.

#### 4.24 OPERATION OF A HELIUM-FREE TEA CO<sub>2</sub> LASER

The major role of the expensive and scarce helium gas that constitutes majority of the gas mixture in a pulsed Transversely Excited Atmospheric pressure (TEA) CO<sub>2</sub> laser, is to stabilise

D. J. Biswas, J. P. Nilaya, and A. Kumar, **Opt Commun** **248**, 521 (2005)  
 D. J. Biswas, J. P. Nilaya, and A. Kumar, **US PATENT (Granted)**,  
 Publication date: 01-06-2005, Publication No: 2005-0002432A1



Laser head and the pulsar system. Inset shows the laser beam



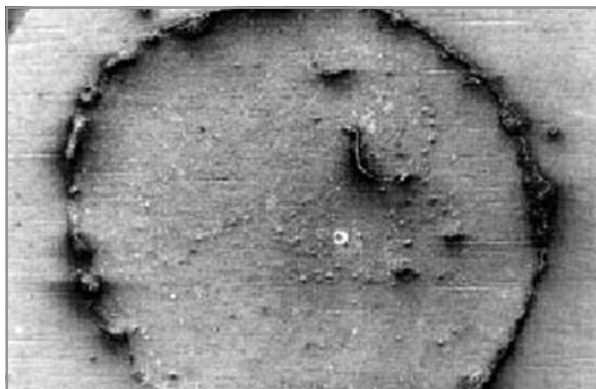
## **5. MATERIALS IN DEVICE APPLICATIONS**

### **INTRODUCTION**

A sustained effort is being made for research in advanced functional materials for fabrication of components for nuclear reactors, synchrotron sources, lasers and other applications. In addition, new materials are being investigated for emerging device applications. Cylinders of high temperature superconductors have been fabricated and characterized for application to superconducting motors. Thin films and multiplayer coatings have been prepared for laser resonators, optical components for synchrotrons and analytical instruments as well as study of physical properties of materials. Single crystals, glasses and glass-ceramics for application in nuclear particle detectors, lasers, hermetic seals and vacuum components are being routinely prepared and used in devices. In addition, fundamental studies on superconducting and colossal magneto-resistive materials have been carried out and will be described in this chapter.

### 5.1 LASER DECONTAMINATION AND ANALYSIS OF ZIRCALOY CLAD SURFACE

MOX fuel elements are fabricated inside leak tight glove boxes and this process results in loose contamination on the tube surface and ends. The advantages of laser assisted decontamination are that it is a dry process generating very little secondary waste and it is a non-contact process. By making use of an indigenous TEA CO<sub>2</sub> laser capable of generating ~1 J/pulse of 1 ms duration we have achieved high decontamination factor on commonly used clad surfaces e.g., Stainless Steel, Zircaloy. The effect of laser assisted radioactive decontamination on the surface morphology of autoclaved zircaloy, the clad material for a variety of nuclear reactors, has been studied by making use of a scanning electron microscope



SEM photomicrograph of the contaminated Zircaloy surface after showing the presence of the particulates (50X)



SEM photomicrograph of the same clad surface after exposure to a single pulse of the laser (50X)

for a range of laser fluences. It is found that there exists a definite window of laser parameters for which satisfactory decontamination of autoclaved zircaloy substrate is possible without altering its surface property.

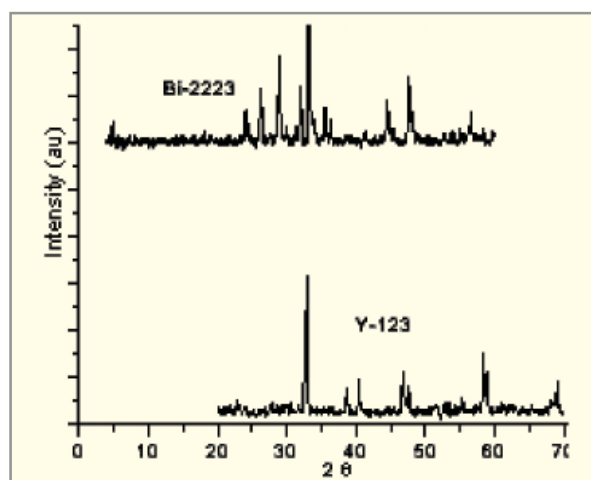
J.P.Nilaya, M.B. Sai Prasad, P. Raote, A. Kumar, D. N. Sah, and D. J. Biswas, National Laser Symposium, BARC, Mumbai 2005.

M.B.Sai Prasad, J.P.Nilaya, A. Kumar and D. J. Biswas. National Laser Symposium, BARC, Mumbai 2005.

### 5.2 FABRICATION OF HOLLOW CYLINDER OF HIGH TEMPERATURE OXIDE SUPERCONDUCTORS

Since the advent of high temperature superconductivity, several families of superconducting compounds have been discovered. Of these compounds, YBa<sub>2</sub> Cu<sub>3</sub> O<sub>7</sub> (Y-123) and Bi<sub>2</sub> Sr<sub>2</sub> Ca<sub>2</sub> Cu<sub>3</sub> O<sub>10</sub> (Bi-2223) continue to show the most promise for bulk applications, especially levitators and as rotors of different shapes in hysteresis electrical motors. These devices operate due to the demagnetization process in bulk high temperature superconductor elements. It has been shown that the torque varies linearly with the total hysteresis losses in high temperature superconductor rotor.

Y-123 and Bi-2223 powders were synthesized by nitrate decomposition route. The calcined powders were characterized by X-ray diffraction to determine their phase purity.



XRD pattern of Bi-2223 and Y-123 powders.



Sintered HTSC oxide cylinders.

Hollow cylindrical shapes of approximate dimensions O.D – 55mm, I.D – 45mm and length 50 mm have been fabricated by cold isostatic pressing and subsequent sintering.

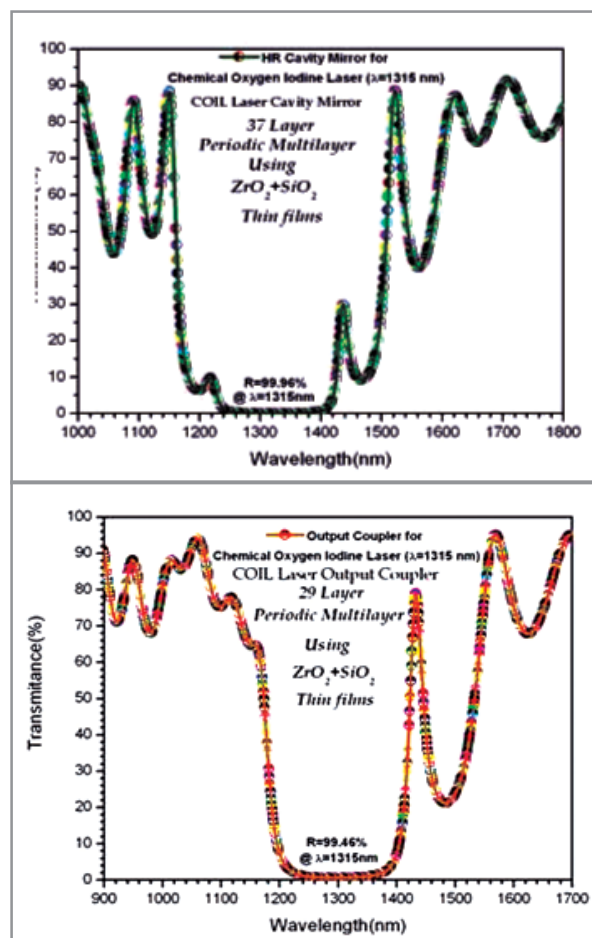
The transition temperatures ( $T_c$ ) in these components were found to be 86 K and 102 K for Y-123 and Bi-2223 respectively. The development of these components is being carried out in collaboration with the designers.  $J_c$  of the Bi2223 cylinder has been found to be in the range of 400 mA/cm<sup>2</sup>.

M.R. Gonal, K. Adhikari, A. Gulnar, N.C. Soni, Ram Prasad and S.K. Malik, Pcoeed. DAE Solid State Physics Symp. 34C, 269.

### 5.3 DEVELOPMENT OF MULTILAYER COATINGS FOR THE RESONATORS OF CHEMICAL OXYGEN IODINE LASER

The chemical oxygen iodine laser is a chemical laser that converts energy derived from chemical reactions into laser photons. The feedback resonator mirrors are the two essential components that constitute the laser cavity. The atomic iodine is energized to form an optical gain region and power is extracted with these optical resonators at the wavelength of 1315 nm. There are stringent requirements with respect to the specifications of multilayer optical coatings for the resonators which include both ultra low-loss as well as high damage threshold at this near infrared lasing wavelength. Keeping

view of these criteria we have successfully designed developed these multilayer dielectric mirrors using refractory ZrO<sub>2</sub> and SiO<sub>2</sub> thin film optical materials and adopting a process control reactive electron beam deposition technique.



High reflecting resonating mirror for chemical oxygen iodine laser system lasing at 1315 nm and Output Coupler for chemical oxygen iodine laser system lasing at same wavelength of 1315 nm.

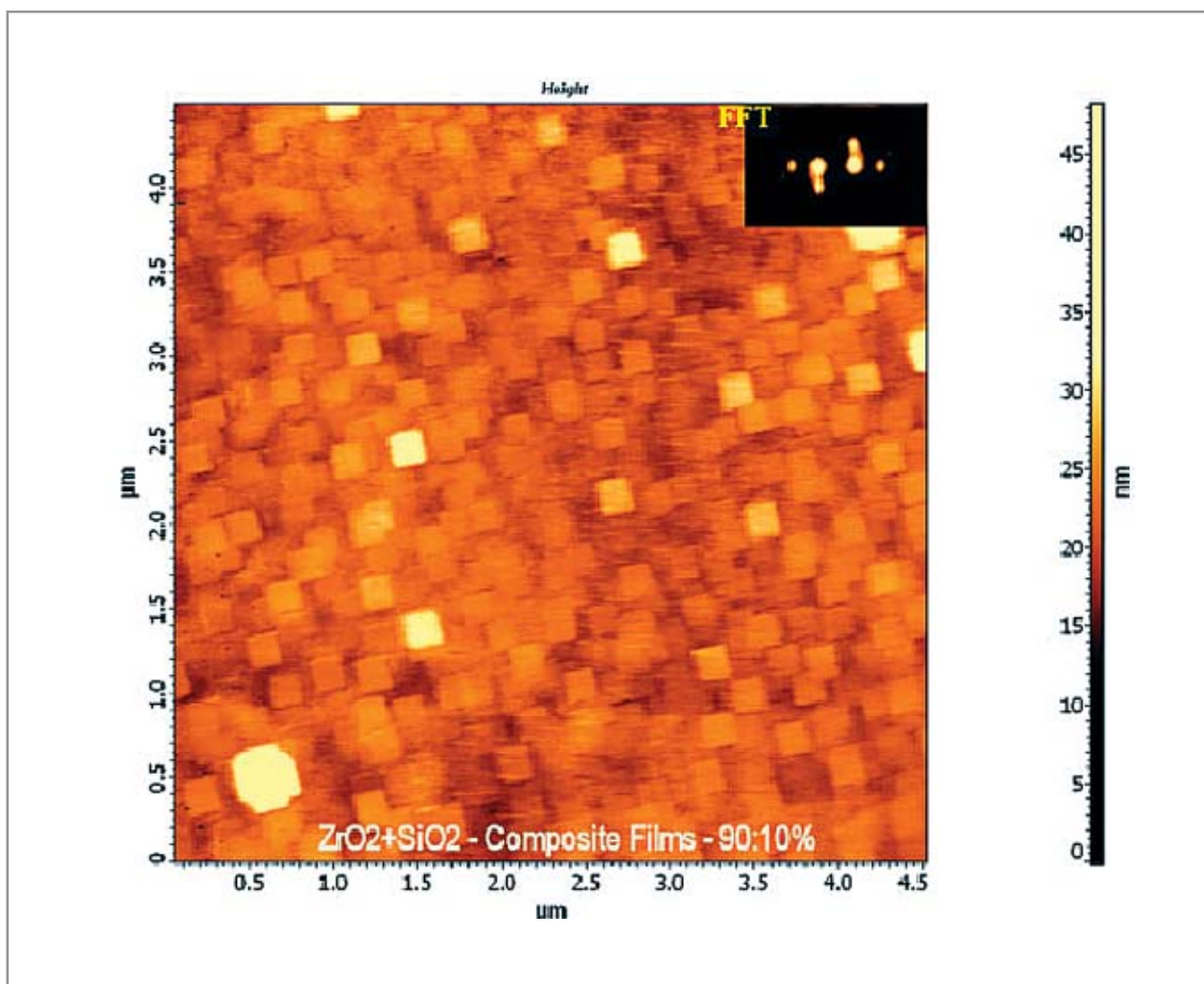
For high reflecting feed back mirrors, a reflectivity value of 99.96% has been achieved by adopting a periodic 37-layer quarterwave design as shown in the figure. A 29-layer periodic quarter wave design has been adopted to develop the output couplers that carry an optimized reflectivity value of 99.46% at the COIL wavelength.

N. K. Sahoo, S. Thakur, M. Senthikumar, D. Bhattacharyya, N. C. Das, Thin Solid Films, 440, 155, (2003)

#### 5.4 ACHIEVEMENT OF ORDERED 3D ISLAND STRUCTURES IN ZIRCONIA FILMS BY STABILIZING WITH SILICA

Order structures in thin films have been closely associated with stress and strain factors that ultimately decide the stability of the multilayer device. Ordered 3D-island growth mostly is an outcome of a resultant thin film strain field resulting into such

self-organization process. With our continued research on co-deposition technique, we have successfully achieved such ordered structures in  $ZrO_2$  thin films being stabilized by the  $SiO_2$  through a reactive electron beam multi source deposition process. The fast Fourier transform of the topography measured through the Atomic Force Microscopic (AFM) technique has revealed a strong two-fold symmetry.



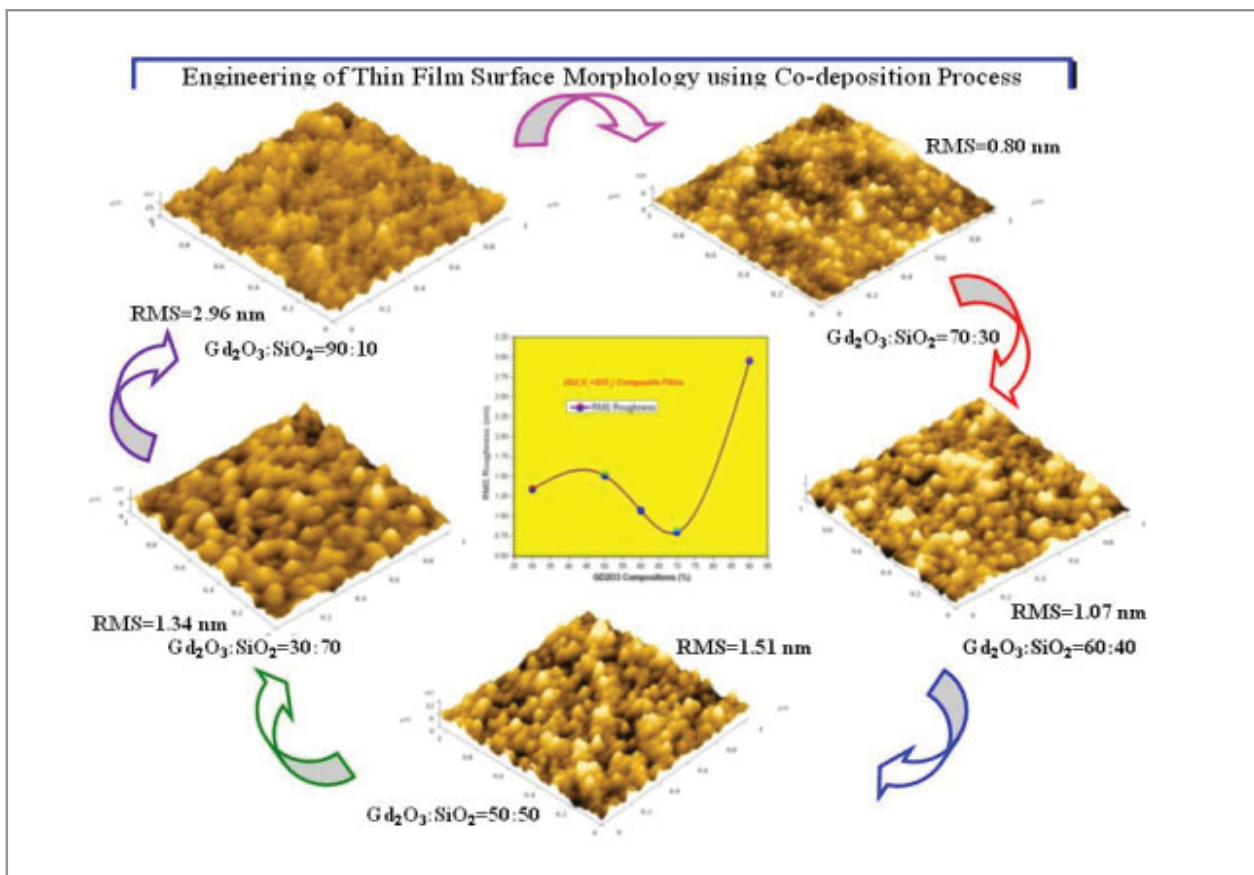
Generation of ordered 3D Island structures in silica stabilized zirconia thin films. The inset figure demonstrates the FFT analysis of the topography.

N. K. Sahoo, S. Thakur, M. Senthilkumar, R. B. Tokas and N. C. Das, Vacuum, 77, issue 1, 87, (2004)

**5.5 ENGINEERING MORPHOLOGICAL CONTROL OVER THIN FILM SURFACE FOR THE DEVELOPMENT OF LOW-SCATTER DEEP ULTRAVIOLET COATINGS**

The quality of optical components used in complex applications such as lasers, synchrotrons, analytical instruments and lithography systems is critically influenced by surface morphology and associated optical losses. Such losses also become more highlighted as the application wavelengths go below the ultraviolet spectral regions. One possible way to improve the efficiency and performance of such devices is to minimize the RMS roughness as well as to gain the control over the topography through advanced deposition techniques.

Process control multi-component co-deposition technique is one such approach that can be utilized to manipulated morphological features on the composite thin film surfaces. Using such a methodology we have successfully demonstrated superior morphology in certain composite gadolinia-silica ( $Gd_2O_3-SiO_2$ ) thin films depicts experimental results on the tuning of the morphology of such composite coatings characterized through a multi-mode atomic force microscopic technique. It can be seen form these figures that composite films with different mixtures of  $Gd_2O_3$  and  $SiO_2$  components have shown wide ranges in RMS roughness values. The best morphology and minimum RMS roughness parameters have been achieved for a composite film that carries a 70/30 composition ratio of  $Gd_2O_3:SiO_2$ .



Engineering of composite thin film morphology for developing low-scatter multilayer devices.

S. Thakur, N. K. Sahoo, M. Senthilkumar, and R. B. Tokas, Optical Materials, 27, issue 8, 1402, (2005)

## 5.6 STRUCTURE AND FUNCTION OF CLASS-B BACTERIAL NON-SPECIFIC ACID PHOSPHATASE OF *S. TYPHIMURIUM*: Lys154

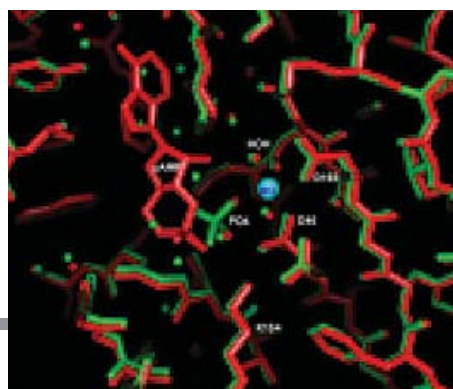
AphA protein, member of class-B bacterial non-specific acid phosphatases, dephosphorylates disparate organophosphates and exhibits phosphotransferase activity. *aphA* gene of *Salmonella enterica* sv. Typhimurium (*S. typhimurium*) codes for a 237 amino-acid polypeptide, 23 of which function as signal peptide for periplasmic localization.

The AphA protein of *S. typhimurium* was purified to homogeneity using genetic engineering and column chromatography methods. The protein was crystallized by the vapour-diffusion sitting-drop method using crystallization screens prepared in-house. The crystal structure of phosphate tethered recombinant AphA by the molecular replacement method and that of AphA-cAMP complex, were solved and refined to crystallographic R-factor of 16.5% and 15.9% using diffraction data to 2.0 and 2.3 Å resolution, respectively. The diffraction intensity data were collected using MAR345dtb imaging plate system and Cu K $\alpha$  radiation. The functionally active AphA, in the crystals, exists as a homo tetramer (Fig.). The central (core) domain of AphA monomer adopts  $\alpha/\beta$  structure. The Mg<sup>2+</sup> ion, in the active site, is coordinated by three protein ligands (Asp46, Asp48 and Asp169 residues), a phosphoryl oxygen and two solvents. The crystal structure of AphA-cAMP reveals the local environment of the inhibitor and the basis of structural diversity of AphA substrates with disparate organic moieties. Further, some mechanistic details of the phosphatase activity could be constructed using bioinformatic approaches and comparison with the members of the HAD superfamily, which suggested functional role of an invariant Lys154 residue also.

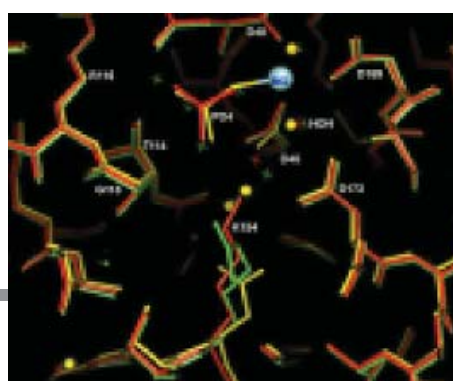
The Lys154Asn and Lys154Arg mutants of AphA were synthesized *in situ* using site directed mutagenesis and were purified. The mutant proteins display dramatic changes in the Michaelis-Menten kinetic parameters. The crystal structures of the mutant proteins were elucidated at 2.25 and 2.1 Å resolution (R-factors 15.9 and 16.7%, respectively) (Fig.). The structures explain the dramatic changes in the kinetic properties of these mutants, and establish unequivocally the functional role of Lys154.



Cartoon showing the structure of active AphA. The subunits are shown in different colors. The Mg<sup>2+</sup> (cyan) in the active site of each monomer is marked.



Superposition of active site residues in the structures of phosphate tethered AphA (red) and AphA-cAMP (green) showing partial overlap of cAMP with phosphate.



Superposition of the active site residues of native AphA (red), K154N-AphA (yellow) and K154R-AphA (green).

R.D. Makde, Vinay Kumar, G.D.Gupta, J. Jasti, T.P. Singh and S.K. Mahajan. Acta Cryst. D59, 1849-1852,(2003).

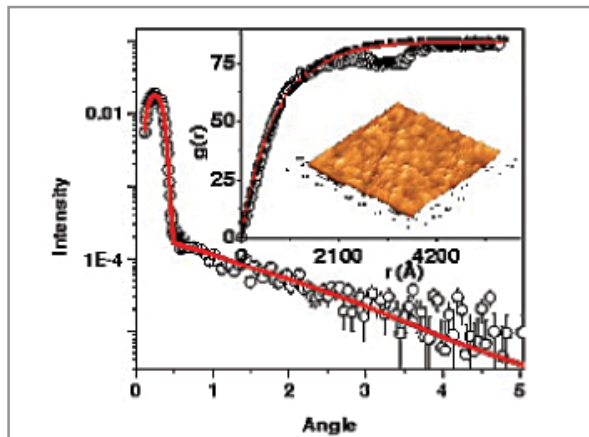
### 5.7 AN IDEAL TOOL FOR ROUGHNESS CHARACTERIZATION: NEUTRON REFLECTOMETRY

We encounter rough surfaces in various walks of our daily life. In many applications it is important to characterize the “roughness” of a surface. Scattering of light from the screen in a movie theatre highlights the fact that a rough surface, unlike a mirror, causes diffuse reflection of light. This elucidates the fact that scattering of a suitable radiation can be fruitfully utilized to characterize “roughness” of a surface at various length scales. In this regard specular and diffuse reflectivity are ideal tools to characterize “roughness” at microscopic length scales in thin films. Detailed morphology of a rough surface is given by an in-plane height-height correlation function on the surface. Neutrons have an edge over other radiations in their capability to penetrate deep inside a medium and sample buried interfaces. Fourier transform of the in-plane height-height correlation function dictates the intensity of Diffuse Neutron Reflectivity (DNR). We determined the morphology of a Ni film using DNR. Such experiments are performed routinely on our Polarized Neutron Reflectometer (PNR) at Dhruva guide hall. Photograph of this instrument is shown in figure. The open circles are the diffuse scattering data around the specular peak at an incident angle of 15 arc minutes. Best fit to this data (continuous line) gives the details of the morphology of interfaces of the film. AFM image of the exposed surface of the sample is shown in the top inset of figure. The in-plane correlation function for the exposed surface obtained from the best fit to DNR (continuous line) as well as from AFM data (dots) have also been shown in this



Polarized Neutron Reflectometer at Dhruva

inset. They match quite well over the entire length scale. This example demonstrates the strength of DNR as a non-destructive technique in determining morphology of interfaces.

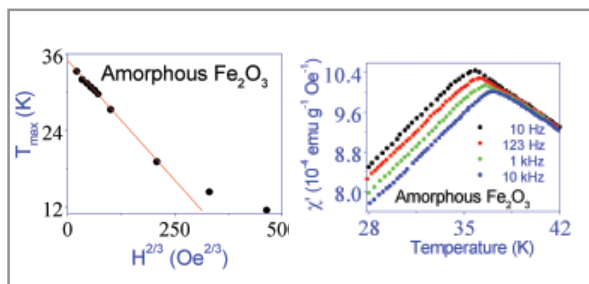


Diffuse (Off-specular) Neutron Reflectivity data (see text) from Ni film. Top inset shows the AFM image of the air-film interface as well as height-height correlation function obtained from AFM and DNR.

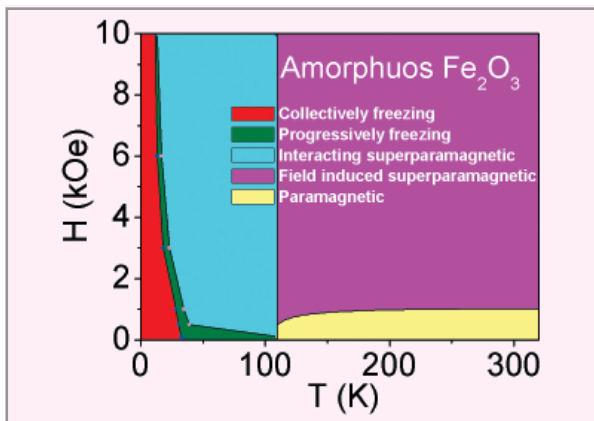
Saibal Basu and Surendra Singh, J. Neutron Research, (under publication)

### 5.8 STUDY OF MAGNETIC NANOPARTICLES

The unique magnetic properties of nano-sized magnetic particles/ clusters have made them potentially useful from both technological and theoretical points of view. The conflicting results of the magnetic behaviour reported in the literature for the “X-ray amorphous” Fe<sub>2</sub>O<sub>3</sub> prompted us to carry out a detailed magnetization study on this important material. The presence of field induced spin-clusters with mean diameter of spin cluster ~ 30 Å has been found. The de Almeida-Thouless type phase boundary  $T_g(H) \propto H^{2/3}$  for these clusters has also been seen [Figure].



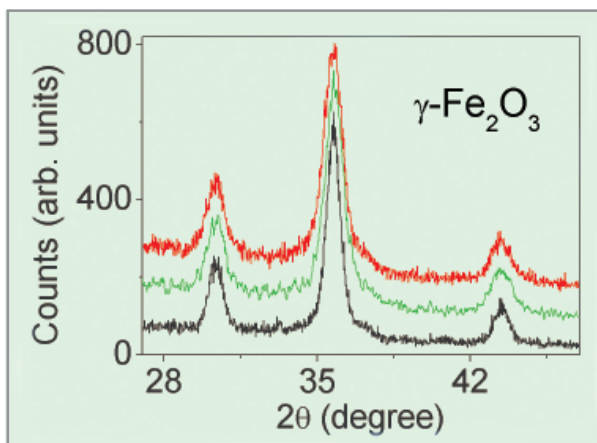
Left: Almeida-Thouless phase diagram, Right: Real part of the ac susceptibility



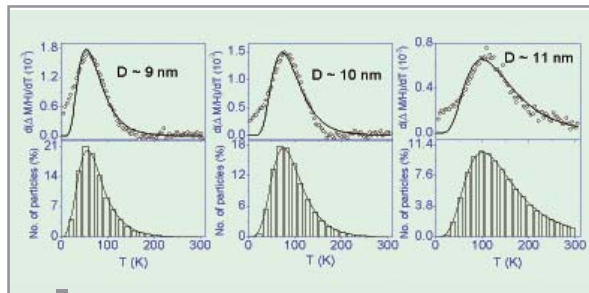
H-T phase diagram of amorphous Fe<sub>2</sub>O<sub>3</sub>.

The dynamic magnetic properties of this system has been studied by frequency dependent ac susceptibility. We have given a phase diagram in the *H-T* plane (figure) for this technologically important magnetic material and answered the reasons for the conflicting reports in the literature.

The dependence of magnetic properties of Y-Fe<sub>2</sub>O<sub>3</sub> nanoparticles with its particle size with average particle diameter of ~ 9, 10 and 11 nm has been studied using the dc magnetization technique. A lognormal distribution function, for the superparamagnetic blocking temperature has been found.



X-ray diffraction patterns at RT for the  $\gamma$ -Fe<sub>2</sub>O<sub>3</sub> samples annealed at 200, 250 and 350 °C (from top to bottom) giving the average diameter of 9, 10 and 11 nm, respectively



Upper: The temperature derivative of the difference between the ZFC and FC dc susceptibility curves  $d(\Delta M/H)/dT$  vs *T* fitted with the Lognormal distribution function. Lower: Blocking temperature histograms.

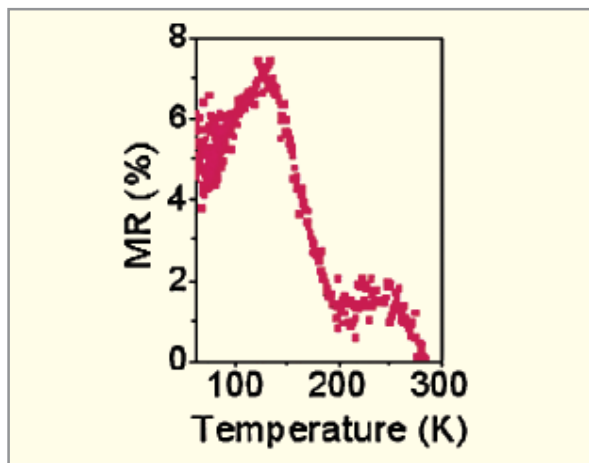
Magnetic properties of Co<sup>2+</sup> exchanged NaY zeolite (Fig.) have been investigated. A Langevin function behaviour with a saturation moment of 3.2 μ<sub>B</sub> per Co<sup>2+</sup> ion and a cluster moment of 6.66 μ<sub>B</sub> has been found. Magnetic correlation between Co clusters below 5 K builds up.

M. D. Mukadam et al. *J. Magn. Mater.* 272-276 (2004) 1401

M. D. Mukadam et. al, *J. Magn. Mater.* 269 (2004) 317

### 5.9 CMR/HTSC THIN FILMS AND MULTILAYERS

Thin films of colossal magnetoresistive material La<sub>1-x</sub>Pb<sub>x</sub>MnO<sub>3</sub> (LPMO) were prepared on SrTiO<sub>3</sub> substrates with different



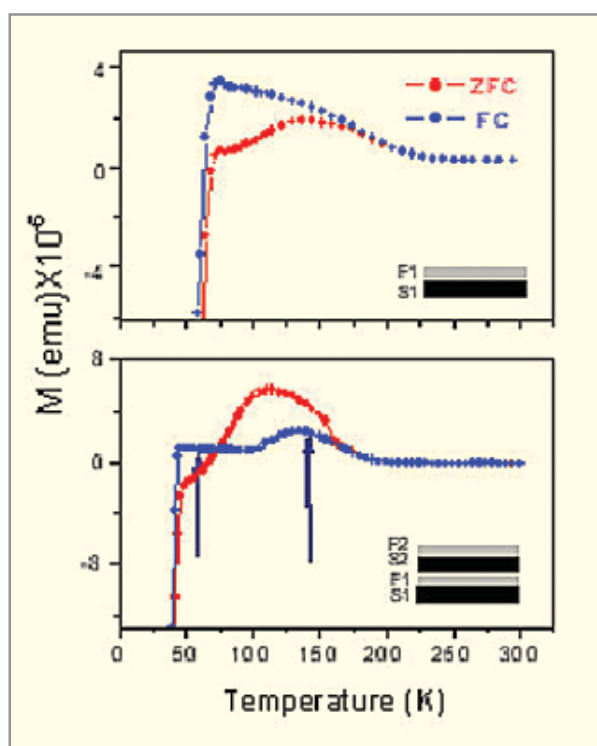
Temperature dependence of magneto-resistance for a four layer structure (100 nm YBCO/50 nm LPMO)<sub>2</sub>. A peak at 140 K is attributed to AF coupling between LPMO layers.

microstructure i.e. nanocrystalline, polycrystalline and single crystalline. Nanocrystalline films were found to yield a very high magnetoresistance of >100% at 1T field which is attributed to tunnel barriers at grain boundaries. Ferromagnetic resonance studies of these films showed that grain boundaries have spin glass character.

Multilayers of High Temperature Superconductor (HTS), and Colossal Magneto Resistive (CMR) materials are of interest as CMR materials contain spin-polarized carriers and in HTS carriers are paired. These multilayers are ideal for study of interplay between superconductivity and magnetism. Epitaxial

transition of single CMR layer. Comparison of Field Cooled (FC) and Zero Field Cooled (ZFC) magnetization in two and four layer structures showed that the peak at 140 K originates from anti-ferromagnetic (AF) coupling between two CMR layers (Fig.). The origin of this AF coupling, observed for the first time, is not yet understood, but its temperature is seen to coincide with the thermo- dynamic fluctuations induced cooper pairs in YBCO.

Ajay Singh, D.K. Aswal, L.C. Gupta, S. K. Gupta, J.V. Yakhmi and V.C. Sahni, Supercond. Sci. Technol 17 (2004) 342.



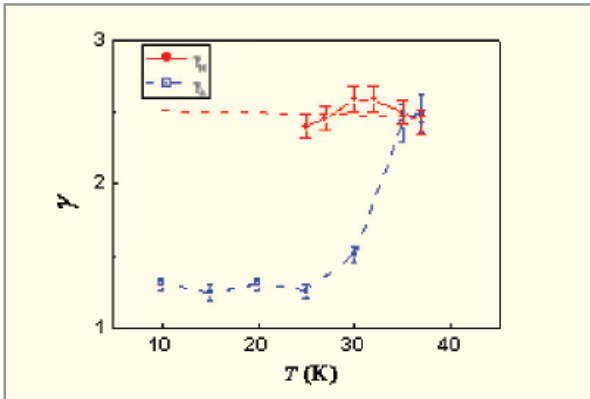
Zero-field-cooled (ZFC) and Field-cooled (FC) magnetization as function of temperature for a two-layer and a four-layer structure with 50 nm LPMO and 100 nm YBCO layers. Insets show schematics of hetero-structures.

multilayers of LPMO and  $\text{YBa}_2\text{Cu}_3\text{O}_x$  (YBCO) have been (in-situ) prepared on single crystal  $\text{SrTiO}_3$  substrates by laser ablation technique. Four layer structures were found to show two peaks in magneto-resistance at 235 K and 140 K, respectively (Fig.). The peak at 235 K is attributed to insulator to metal

## 5.10 STUDIES ON $\text{MgB}_2$ SUPERCONDUCTOR

Polycrystalline samples of new superconductor  $\text{MgB}_2$  with high  $J_c$  were synthesized at atmospheric pressure in argon. Several studies were carried out to understand the properties of this material. These include (a) studies by XPS and XRD showed that it interacts with atmosphere to yield  $\text{Mg}(\text{OH})_2$ ,  $\text{MgCO}_3$  and  $\text{B}_2\text{O}_3$  etc, (b) positron annihilation studies showed that charge density fluctuations in boron layer are associated with superconductivity, (c) Andreev reflection studies on  $\text{MgB}_2/\text{Ag}$  planar contacts showed possibility of two energy gaps in the material and (d) microwave absorption studies showed dissipation due to vortex motion and were used to determine  $H_{c1}$ .

In addition several studies were carried out on  $\text{MgB}_2$  thin films and single crystals in collaboration with Pohang University of Science & Technology, South Korea. These include, (a) field and angular dependence of  $I$ - $V$  characteristics to show universal behaviour of vortex glass transition, (b) angular dependence of critical current show that properties of  $\text{MgB}_2$  are in accordance with anisotropic GL model, (c) a new method based on scaling of critical current density developed to determine penetration depth anisotropy as function of temperature for the first time (Fig.), (d) mechanism of Peak Effect (PE) studied to show that PE arises due to a transition from elastic vortex lattice to plastically deformed structure followed by melting transition and (e) a new Dynamic Disordering (DD) transition with noise increasing at higher currents was found.



Penetration depth ( $\gamma_\lambda$ ) and  $H_{c2}$  ( $\gamma_H$ ) anisotropies for  $MgB_2$  determined by scaling of critical current density and resistivity measurements, respectively.

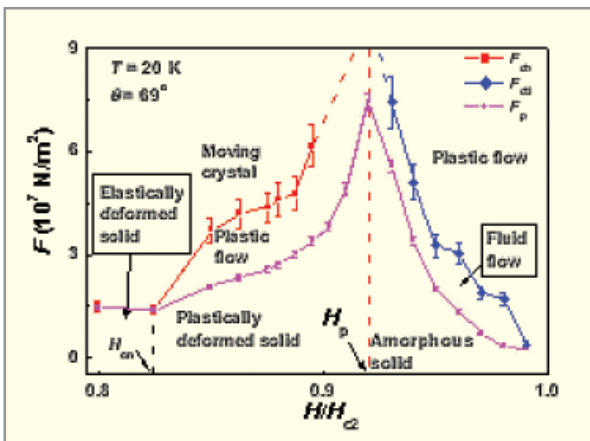
### 5.11 GROWTH OF SINGLE CRYSTALS BY CZOCHRALSKI TECHNIQUE



The automated Czochochowski crystal pullers at CTL, TPPED.



Some of the crystals that have been grown using crystal pullers.



Dynamic phase diagram of  $MgB_2$  single crystals.

It is software-controlled and fully automated crystal growth system capable of growing a wide variety of materials.

#### Features of crystal pullers:

1. Diameter and size of grown crystals: User defined
2. Diameter Control accuracy: within 1 mm to the set value
3. Crystal weighing accuracy: 0.1 gram
4. Method of heating: Induction
5. Maximum Temperature: upto 2000 °C
6. Temperature control accuracy 0.1 °C
7. Growth atmosphere can be selected/controlled
8. Provision to fill/mix three different gases at a time in controlled composition
9. Growth rates 1 mm/hr to 10 mm/hr.

**Capability:** All Czochochowski growable crystals with melting point lower than 2000 °C.

S. K. Gupta, Shashwati Sen, Ajay Singh, D.K. Aswal, J.V. Yakhmi, Eun-Mi Choi, Hyun-Jung Kim, Kijoon H. P. Kim, Seungje Choi, Hyun-Sook Lee, W. N. Kang and Sung-Ik Lee, Phys. Rev. B 66 (2002) 104525.

A.K. Chauhan, Crystal Growth & Design 4/1(2004) 135 A.K. Chauhan, PhD thesis, University of Mumbai (2005)

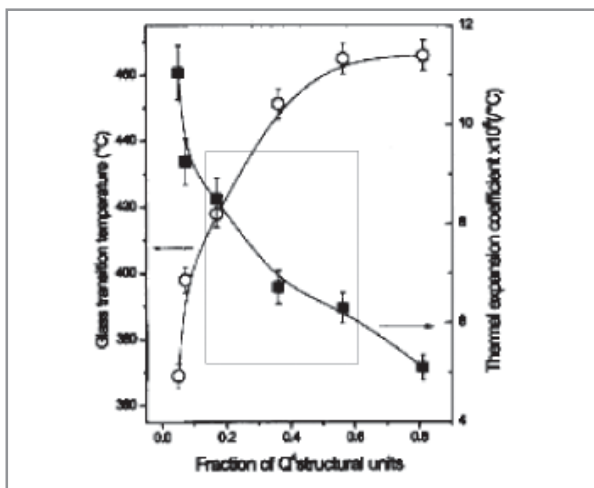
5.12 B<sub>2</sub>O<sub>3</sub> SUBSTITUTED (PbO)<sub>0.5</sub>(SiO<sub>2</sub>)<sub>0.5</sub> GLASSES

PbO-SiO<sub>2</sub> based glasses are technologically important and have got applications in making ultrasonic delay cables, electron multipliers, TV picture tubes, glass-to-metal seals etc. Thermal expansion coefficient, glass transition temperature (T<sub>g</sub>) and micro hardness depend on the composition and nature of different types of linkages present in the glass network. We have studied <sup>29</sup>Si MAS NMR and micro hardness on lead silicate



Photograph of 7- pin GM Seal

glasses with varying mole ratios of SiO<sub>2</sub> to PbO and having different amounts of alkali / alkaline earth metal oxides. A composition with SiO<sub>2</sub> to PbO mole ratio ~6.9 and having oxides of Na, K and Ba was found suitable for making compression type glass to metal (GM) seals. A large number



Variation of average TEC and T<sub>g</sub> as a function of the mole fraction of Q<sup>4</sup> structural units of silicon for (PbO)<sub>0.5-x</sub>(SiO<sub>2</sub>)<sub>0.5</sub>(B<sub>2</sub>O<sub>3</sub>)<sub>x</sub> glasses with 0.0 ≤ x ≤ 0.4.

of such GM seals were fabricated using this glass for Heavy Water Plants of DAE.

Structural aspects of two series of glasses namely, (PbO)<sub>0.5-x</sub>(SiO<sub>2</sub>)<sub>0.5</sub>(B<sub>2</sub>O<sub>3</sub>)<sub>x</sub> and (PbO)<sub>0.5</sub>(SiO<sub>2</sub>)<sub>0.5-y</sub>(B<sub>2</sub>O<sub>3</sub>)<sub>y</sub> were studied by using both <sup>11</sup>B and <sup>29</sup>Si MAS NMR and correlated with TEC and T<sub>g</sub> (Fig.). The significant decrease in the average linear thermal expansion coefficient and increase in T<sub>g</sub> for glasses having lower lead concentration have been attributed to the increased number of Si-O-B linkages and the formation of Q<sup>4</sup> - type Si configurations which lead to enhanced rigidity in the structure. The effect is less pronounced for (PbO)<sub>0.5</sub>(SiO<sub>2</sub>)<sub>0.5-y</sub>(B<sub>2</sub>O<sub>3</sub>)<sub>y</sub> glasses, basically due to the fact that B<sub>2</sub>O<sub>3</sub> plays the role of a glass former.

V.K. Shrikhande, V. Sudarsan, G.P. Kothiyal, and S.K. Kulshreshtha, J. Non Cryst. Solids 283 (2001) 18.

V. Sudarsan, V.K. Shrikhande, G.P. Kothiyal, and S.K. Kulshreshtha, J. Phys.: Condens. Matter 14 (2002) 6553.

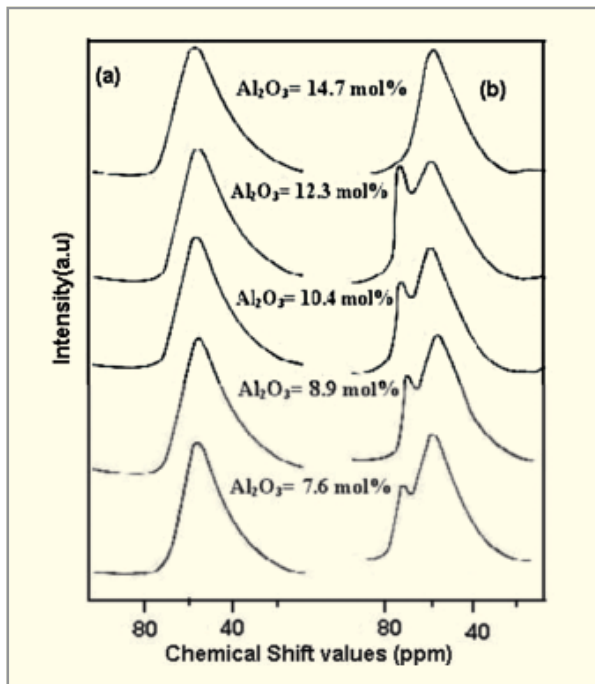
5.13 STRUCTURAL PROPERTIES OF MACHINEABLE MAGNESIUM ALUMINO-SILICATE GLASSES AND THEIR GLASS-CERAMICS

Magnesium Alumino-Silicate (MAS) glass-ceramics have wide applications in the field of high voltage and high vacuum. We have studied the effect of MgF<sub>2</sub> concentration on the thermal, mechanical and other physico-chemical properties of these glass-ceramics, in order to improve the machineability, high



Some of components fabricated from machineable MAS glass-ceramics.

voltage break down strength, outgassing and other physico-chemical properties. Significant improvement has been achieved in the machineable quality of this material.



<sup>27</sup>Al MAS NMR patterns for (a) glass (b) glass-ceramic samples with varying concentration of alumina.

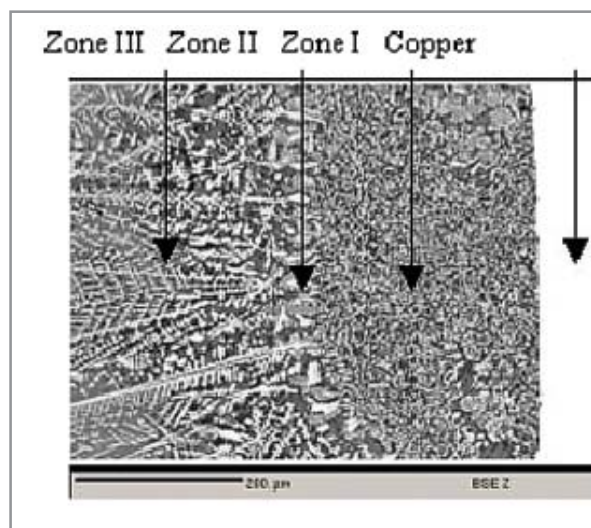
Structural properties with varying concentration of Al<sub>2</sub>O<sub>3</sub> were investigated in detail using <sup>29</sup>Si and <sup>27</sup>Al MAS NMR. For glass sample, <sup>29</sup>Si NMR studies show that with increasing Al<sub>2</sub>O<sub>3</sub> contents, the Q<sup>2</sup> and Q<sup>4</sup> structural units are partially transformed to Q<sup>3</sup> structural units and for higher concentration of Al<sub>2</sub>O<sub>3</sub>, the phase separation occurs and crystalline Mg<sub>2</sub>SiO<sub>4</sub> phase with δ ≈ -61.5 ppm, is formed. In case of glass ceramic samples, characteristic peaks of fluorophlogopite phase responsible for machineable quality have been clearly identified.

<sup>27</sup>Al NMR spectra of glass samples (Fig. a), shows that all Al<sup>3+</sup> are part of the glass network structure and have tetrahedral coordination with oxygen, whereas for glass-ceramics samples, Al<sup>3+</sup> are present at tetrahedral sites in fluorophlogopite phase (additional peak at δ ≈ -71, (Fig. b). However, at higher Al<sub>2</sub>O<sub>3</sub> concentration (14.7 mol %), absence of this peak indicates the presence of all Al<sup>3+</sup> as part of the glass network and as such fluorophlogopite phase is absent, consistent with XRD data.

M. Goswami, A. Sarkar, T. Mirza, V.K. Shrikhande, Sangeeta, K.R. Gurumurthy and G.P. Kothiyal, Ceram. Int. 28 (2002) 585.

### 5.14 INTERFACE STUDY OF LITHIUM ZINC SILICATE (LZS) GLASS-CERAMICS TO COPPER AND SS-321 HERMETIC SEALS

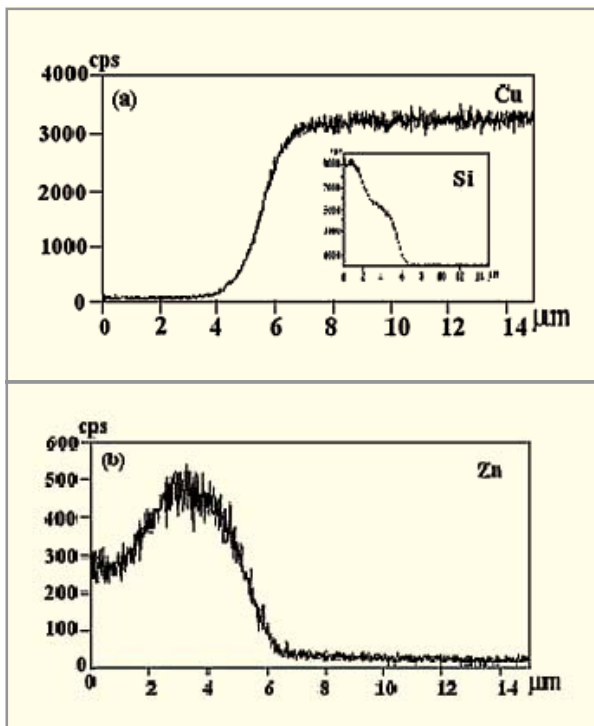
LZS glass-ceramics have potential applications in the field of sealing technology because their tunable thermal expansion characteristics. We have prepared LZS glass-ceramics suitable for hermetic seal with Cu and SS-321. A comprehensive study on the microstructure and elemental inter-diffusion across the interface of LZS glass-ceramics to copper as well as SS-321 alloy seals was undertaken to understand the mechanism of seal formation. Samples were prepared by melt-quenched technique followed by controlled crystallization and match typed hermetic seals were fabricated using both Cu metal as well as SS-321 alloy as outer housing. These seals were found to withstand a vacuum of 10<sup>-6</sup> torr with helium leak rate of 10<sup>-9</sup> Torr l/s.



Microstructure of LZS glass-ceramic to Cu interface.

BSE image of the microstructure of a representative LZS glass-ceramics to copper seal, close to interface. Globally, two types of microstructure, bright and dark are observed close to the interface (zone I and zone II). The dark structure is found to be rich in Si and bright structure is depleted in Si and rich in Zn.

Microstructure in zone III towards core shows the development of dendritic crystal growth.



Microprobe elemental line scans across the LZS glass-ceramic to Cu interface.

Microanalytical line scans taken at the copper and zone-1 interface for LZS glass-ceramics to Cu seal, show inter-diffusion of Cu, Zn and Si across the LZS glass-ceramic to Cu interface, which is responsible for making hermetic seal.

G.P. Kothiyal, B.I. Sharma V.K. Shrikhande, M. Goswami, J.V. Yakhmi. Key Engg. Mater. 280-283 (2005) 947

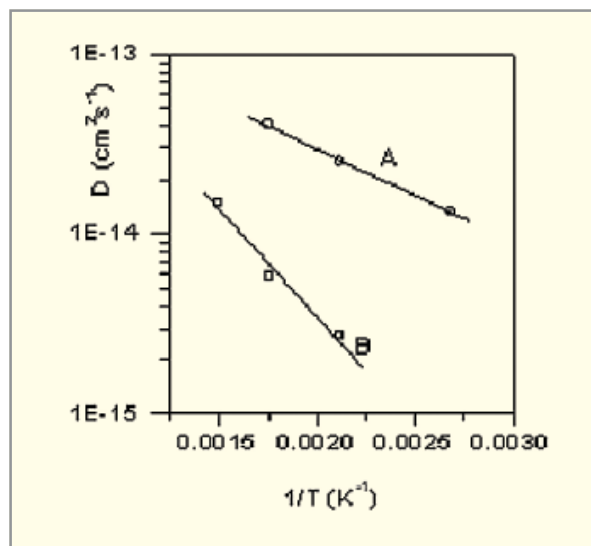
B.I. Sharma, M.Goswami, P.Sengupta,V.K. Shrikhande, G.B.Kale, G.P.Kothiyal. Material Letters 58 (2004) 2423

### 5.15 SOME STUDIES ON Cs DIFFUSION AND CORROSION IN BOROSILICATE GLASSES

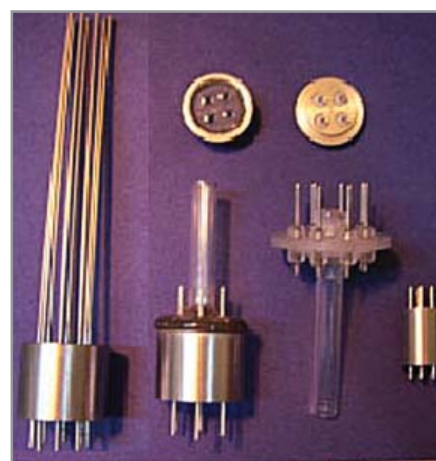
Borosilicate glass is considered to be one of the most suitable matrices for immobilization of High Level radioactive Waste (HLW). For environmental safety concern, it is necessary to know the diffusion rates of different actinides and fission products, such as <sup>137</sup>Cs, <sup>90</sup>Sr, <sup>99</sup>Tc, <sup>129</sup>I, <sup>241</sup>Am <sup>244</sup>Pu etc. in the glass matrix. This glass has potential applications in the

fabrication of matched type glass-to-metal (GM) seals. The study on the corrosion behaviour of the glass is important from the point of view of hermeticity of GM seals. We have determined diffusion coefficients of Cs in borosilicate glasses having compositions with varying amounts of SiO<sub>2</sub>, N<sub>2</sub>O, B<sub>2</sub>O<sub>3</sub>, K<sub>2</sub>O and Al<sub>2</sub>O<sub>3</sub> at different temperatures by employing Heavy Ion Rutherford Backscattering Spectrometry (HIRBS) at the 14 UD BARC-TIFR Pelletron accelerator facility at Mumbai.

From the plot of diffusion coefficient vs. 1/T activation energies for diffusion of Cs are found to be 4.3 and 22 kJ/mol for two samples A and B with different compositions.



Plot of diffusion coefficient as a function of 1/T.



GM seals using glass composition (B).

The results suggest that the borosilicate glass containing high Na<sub>2</sub>O content (sample A) allows more diffusion of Cs. Hence it is not suitable for immobilization of HLW. Corrosion studies in both alkali and acid media at different temperatures have shown that the degradation rate of those glasses in alkaline medium is much higher (46.77 mg /cm<sup>2</sup>) than in acid medium (5.80 mg /cm<sup>2</sup>) at 90°C. A large number of various types of GM seals (Fig.) have been fabricated using these glasses for use in high vacuum equipment.

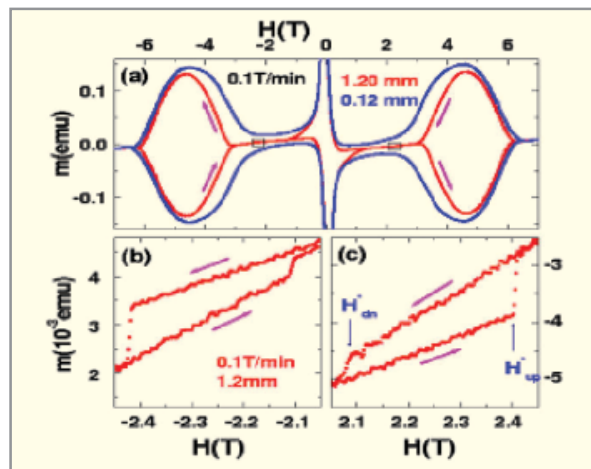
B.S. Tomar, Sumit Kumar, V.K. Shrikhande and G.P. Kothiyal, Nuclear Instrum. Methods in Phys. Res. B 227 (2004) 391.

### 5.16 ORDER-DISORDER TRANSITION IN VORTEX MATTER

Phenomenon of peak effect in weakly pinned superconductors represents an order-disorder transition in vortex matter. It occurs in the regime where inter-vortex interaction is comparable to pinning interaction. Using magnetization measurements on 2H-NbSe<sub>2</sub> single crystals, this transition was shown to be of first order in nature. Vortex matter exhibits pronounced metastability near this transition. Recently we demonstrated the absence of thermal relaxation of the metastable states, suggesting that the relevant energy barriers are much larger than thermal energy.

We studied the equilibrium magnetization of single crystalline V<sub>3</sub>Si spheres of different pinning strengths in the vicinity of peak effect. At the onset of the peak effect we observe a “first-order” like magnetization step (see Fig.), which is hysteretic with respect to the direction of field and temperature scans. The step is observed only for fields oriented away from high symmetry directions like [110] and [100]. Accompanying the magnetization step is an abrupt reorientation of the vortex lattice by tilting towards a high crystal symmetry direction. Coupling between vortex lattice and the underlying crystal lattice is suggested as a possible mechanism for the reorientation.

Heavy-fermion superconductor UPt<sub>3</sub> (T<sub>c</sub> ~ 0.55K) also exhibits peak effect. Mixed phase diagram of UPt<sub>3</sub> crystal, indicating ordered and disordered vortex phases, is constructed using AC susceptibility measurements. In addition, normal state

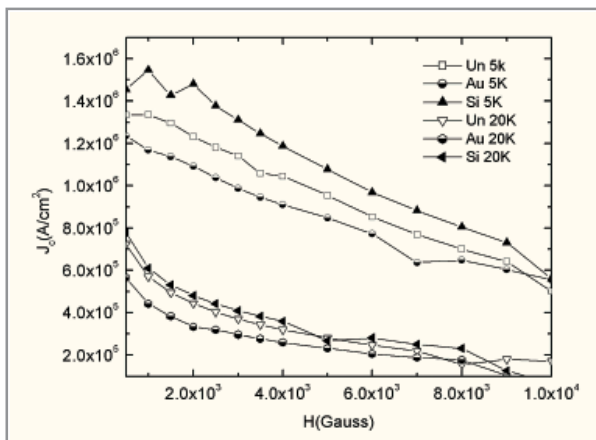


(a) four quadrant Hysteresis loop. The two boxes marked around ±2 T are magnified in (b) and (c) which depicts the magnetization step feature.

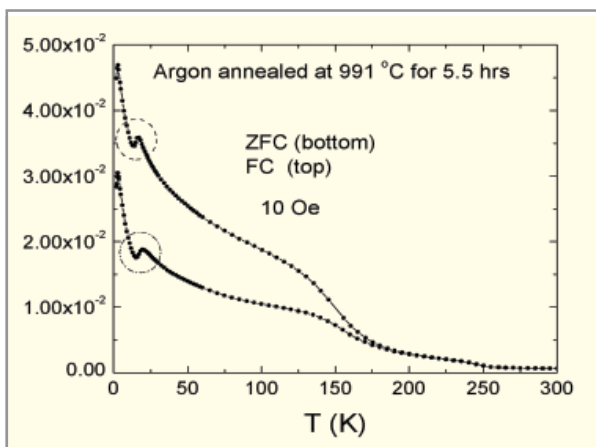
paramagnetic region displays Curie-Weiss behavior with  $i_{\text{eff}} = 2.64 i_B / U$  - atom. Moreover,  $M_{\text{FC}}(T)$  and  $M_{\text{ZFC}}(T)$  curves diverge at low temperatures, indicating a spin-freezing phenomenon.

### 5.17 MAGNETIC RESPONSE OF SUPERCONDUCTORS

Heavy ion irradiation enhances magnetization hysteresis in high T<sub>c</sub> materials significantly. Critical current density vs field data obtained from hysteresis measurements on irradiated MgB<sub>2</sub> films is plotted in Fig. We observed an enhancement in the critical current density of MgB<sub>2</sub> thin films on irradiation by 100 MeV Si<sup>+8</sup> ions. On the contrary, irradiation by 200 MeV Au<sup>+15</sup> ions leads to decrease in the pinning strength. This is understood in terms of the parameters for irradiation - induced defect structure.



Open symbols correspond to  $J_c$  of unirradiated samples. Si ion irradiation enhances  $J_c$  (Filled triangles) while Au irradiation reduces  $J_c$  (half filled circles).



Meissner signal is indicated by a sharp decrease in the paramagnetic signal around 16 K (shown in dotted circle)

We recently initiated studies on superconducting nanoparticles of lead prepared by reducing a lead salt in aqueous solution by gamma ray irradiation. Magnetization of particles of average size 75 nm thus formed has been measured using SQUID magnetometer. We observed a significant enhancement (by a factor of 3-4) in critical fields although critical temperature is equal to that in bulk lead. The enhancement in critical field and the detailed shape of the magnetization curve are described using Ginzburg-Landau theory.

The response of a hard superconducting disc subjected to a slowly rotating magnetic field is studied by applying the minimum flux change criterion. Magnetization and field profiles obtained under different magnetic histories compare favorably with published experimental results. We also calculated non-linear AC susceptibility tensor for superconducting cylinders of arbitrary cross-section with field applied in different directions to explain several experimental results. The effect of geometric anisotropy and AC field amplitude on the fundamental and higher harmonics is also studied.

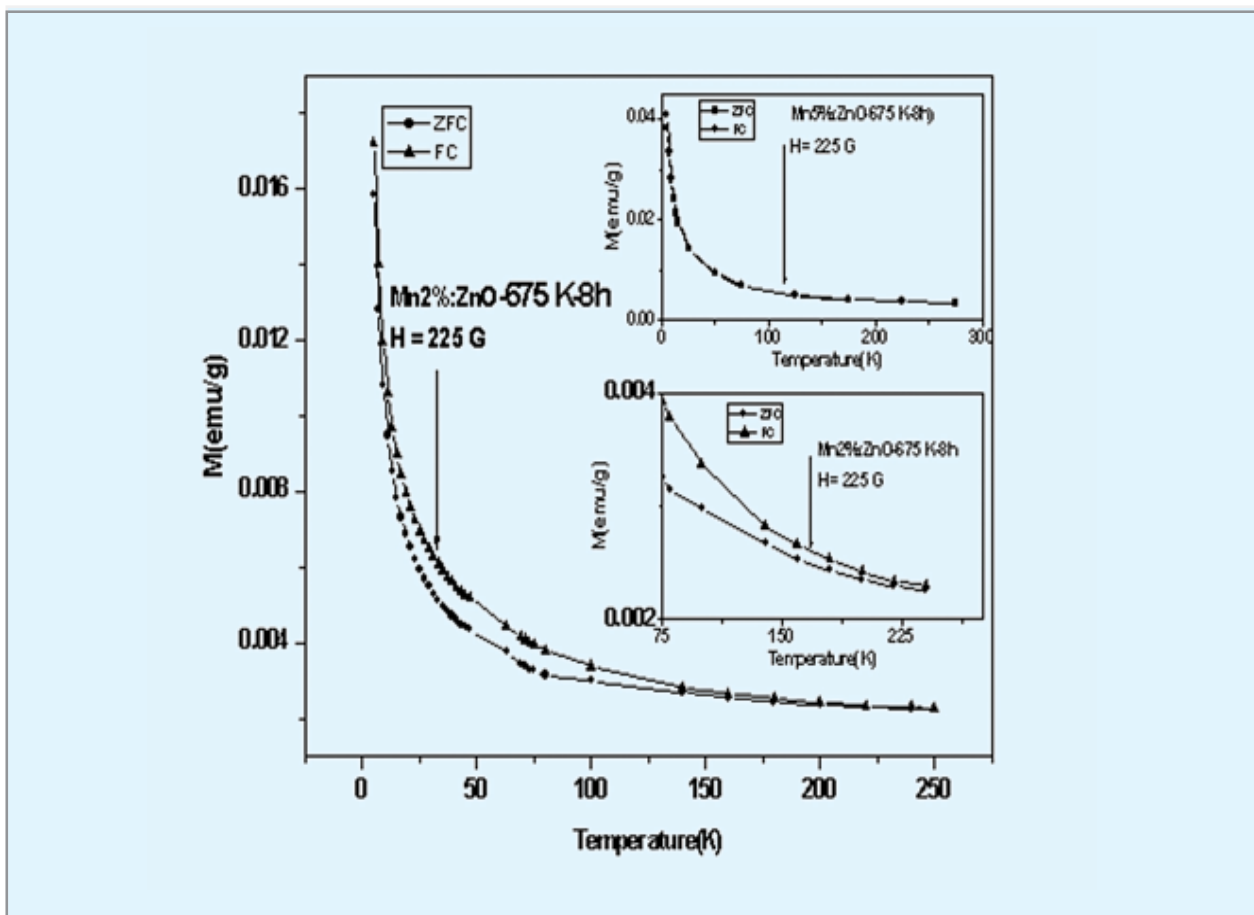
Recently discovered magnetic superconductor  $\text{RuSr}_2\text{GdCu}_2\text{O}_{8-d}$  (Ru1212) exhibits superconductivity below 16 K. However, the nature of the magnetic interaction is controversial. Doubts on the presence of bulk superconductivity exist due to the lack of clear evidence of Meissner effect. Our measurements showed a clear evidence of Meissner effect in an oxygen-reduced  $\text{RuSr}_2\text{GdCu}_2\text{O}_{8-d}$  (Ru1212) both in field cooled and zero field cooled histories (Fig.) in spite of a strong low temperature paramagnetic background from the  $\text{Gd}^{3+}$ -sublattice.

### 5.18 MAGNETIC SEMICONDUCTORS

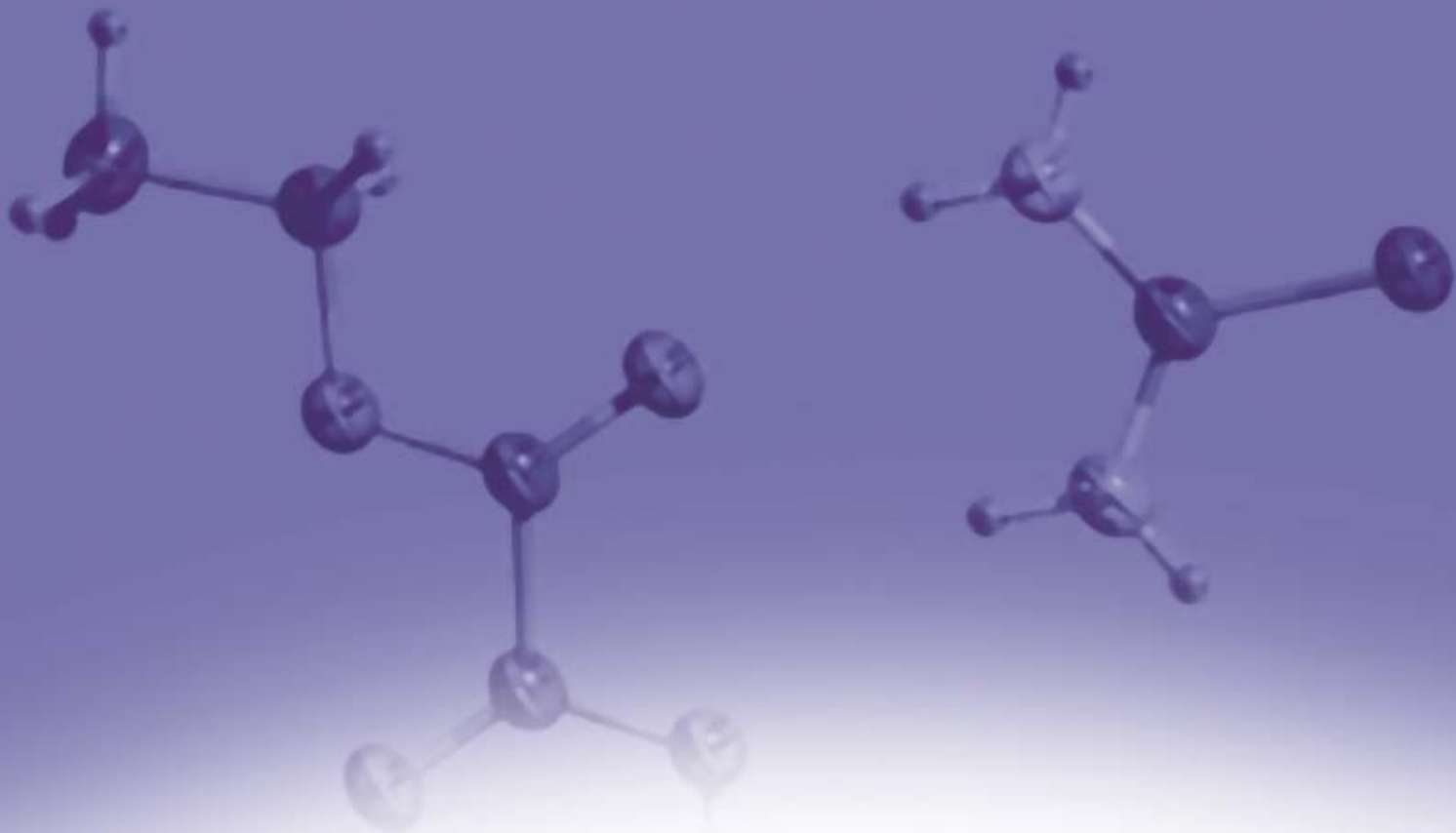
Development of semiconductors, which exhibit ferromagnetism at room temperature are essential for spintronic applications. One of the approaches we have chosen is to implant Co ions into n-GaN epitaxial films. We have carried out detailed magnetization measurements on these samples. At 7% of Co, these films showed ferromagnetic order at  $\sim 270$  K.

The presence of 3d-valence band in the large gap semiconductor ZnO makes it possible to dope it with 3d-transition metals. Several samples of ZnO doped with different Mn concentration (2% and 5%) were prepared by a variety of dry & wet routes such as co-precipitation, solid-state reaction, reverse micelles and mixing-grinding. The materials were subsequently annealed at temperatures ranging from 200°C to 1000°C for 6 to 24 hrs, to ascertain material homogeneity and avoid multiple phase formation. X-ray investigations revealed Wurtzite structure and the average particle size is about 50 nm. EPR and XPS data reveal 3+ valence state for Mn. Blocking temperature in the range 200-275 K is inferred from

magnetization measurements, suggests the possibility of ferromagnetism in the bulk.



ZFC-FC measurement on ZnO (2% Mn) at 225 G. The deviation between ZFC-FC denote blocking temperature around 225 K.



## 6. CRYSTAL STRUCTURE AND LATTICE

### INTRODUCTION

Structure and dynamics are two key attributes that characterize materials and determine their properties. In the following chapter, a variety of interesting structural investigations have been highlighted that include magnetic moment arrangements in novel manganites and molecular magnets by neutron scattering, metal clusters by first principles calculations, and protein structures in solution and hydration in cements by small-angle neutron scattering. Dynamics studies by neutron scattering are used to understand phase transitions in important silicate minerals of geophysical interest, phenomena of negative thermal expansion and variety of molecular motions in liquid crystals. Rich physical insights have been achieved by exploiting combination of experimental and theoretical techniques.

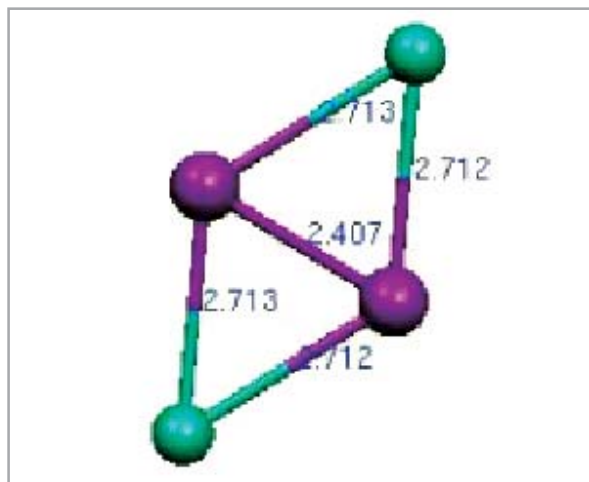
## 6.1 METAL CLUSTERS

The quantum confinement of electrons in the finite size systems is called the quantum size effect. It is the reason, which causes clusters of any materials to show properties that are quite different as compared to their respective bulk behaviors. Therefore, from the fundamental point of view, these materials offer detail understanding of the atomic structures, which leads to different physical and chemical properties of macroscopic phases from their embryonic stages.

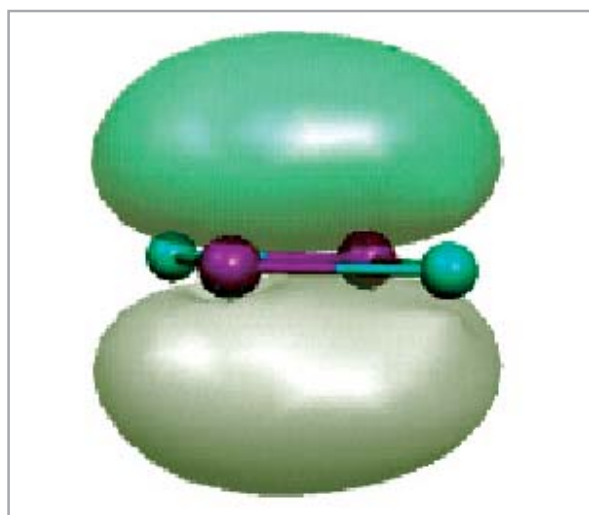
In order to illustrate these aspects we have worked out the electronic structure calculations for clusters and small molecules to understand the chemical binding and other physical properties. The theoretical work demands much less expenditure as compared to the experiments and therefore can suitably be further used to design new materials with tailoring properties for advanced technologies.

In a recent work we carried out the neutral and charged silicon clusters upto  $n = 13$  atom using the *ab-initio* molecular orbital theory. It has been found that although the geometrical arrangements remained similar for the neutral and charged systems, the electronic structures are significantly different which has further been reflected in their relative stabilities. These results are in excellent agreement with the observed experimental mass abundance spectrum. Among other works we have predicted the FCC cage structure of III-IV mixed clusters with significantly large energy gaps. Aromaticity in metal clusters is one aspect, which has been worked out and showed that a large number of tetramer clusters having iso-electronic configurations (14 valence electrons) show similar behavior. Hydrogen storage in light metal alloys is one of the most important aspects in today's world. We have worked for the interaction of hydrogen atoms on small clusters. For this purpose the electronic and geometric structures of  $\text{Li}_n\text{Al}_n\text{H}_n$  clusters have been carried out.

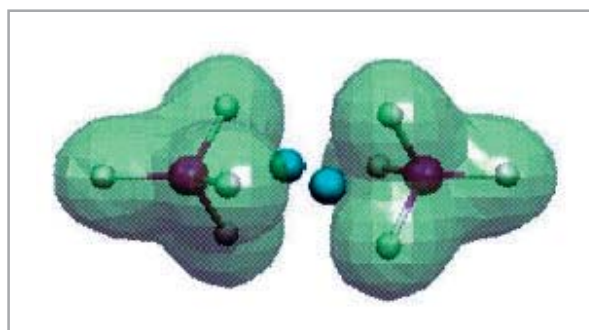
Chirajeeb Majumdar and S.K. Kulshreshtha, Phys. Rev. B 70 (2004) 125441-6



Geometry of  $\text{Li}_2\text{Al}_2$  cluster



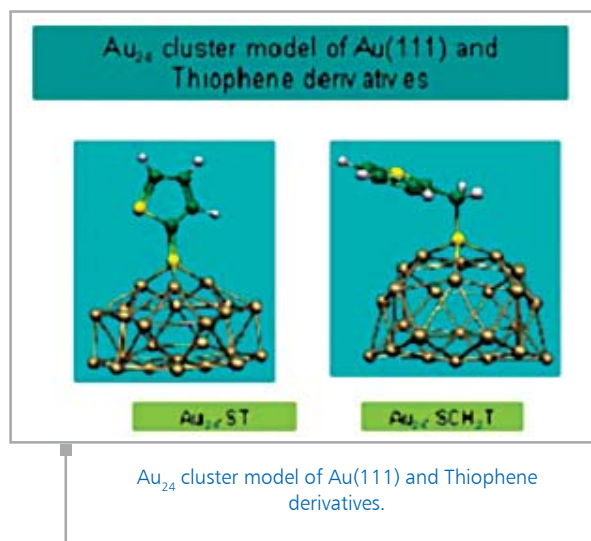
Molecular orbital plots for  $\text{Li}_2\text{Al}_2$



Its hydride  $\text{Li}_2\text{Al}_2\text{H}_8$ .

## 6.2 MOLECULAR ELECTRONICS

Nanoelectronics- a developing field in which electronic devices are composed of nanometer size components- is one topic that has attracted a lot of interest due to its immense potential in the electronic industry. It is widely believed that in a decade or so, silicon based devices will be shrunk to its physical limit and therefore, the search would be on for alternative materials from which nanoscale devices can be constructed. Organic molecules with  $\pi$ -electrons delocalized over the whole molecule are materials of great interest because of their unique electronic transport properties. Molecular scale electronics promises to utilize single molecules as the basic operational elements to design molecular wires, rectifiers, two terminal diode switches and assembling them into more complicated electronic devices like molecular logic gates. In order to understand the molecular properties at the fundamental level we have started theoretical investigation of the geometrical and electronic structures of conjugated organic molecules substituted with different donor and acceptor groups. This work is required to primarily screen some of the suitable molecules which could be most promising candidates to show device properties at very lost cost. To measure electrical properties experimentally, the molecule has to be attached with a non-interacting metallic electrode. Therefore, it is required to understand the interface structure of the metal-molecule junction. We have carried out theoretical investigations on the electronic and structural aspects of the metal-molecule interface considering gold as an electrode and thiophene as a potential organic molecule. In order to understand the molecular properties at the fundamental level we have carried out theoretical investigation of the geometrical and electronic structures of conjugated organic molecules substituted with different donor and acceptor groups. This work is required to primarily screen some of the suitable molecules which could be most promising candidates to show device properties at very lost cost. To measure electrical properties experimentally, the molecule has to be attached with a non-interacting metallic electrode. Therefore, it is required to understand the interface structure of the metal-molecule junction. We have carried out theoretical investigations on the electronic and structural aspects of the metal-molecule interface considering gold as an electrode and thiophene as a potential organic molecule. A typical result for the adsorption geometry of thiophene thiol and thiophene methyl thiol molecules on the  $Au_{24}$  cluster is shown in figure.



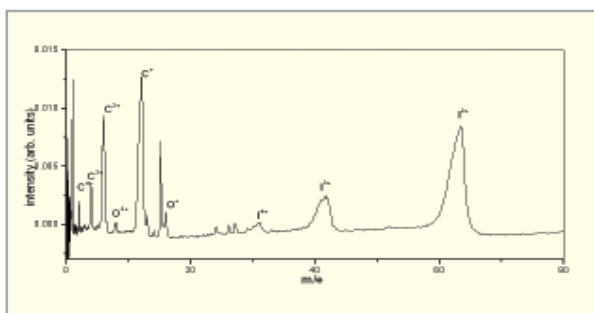
Chiranjeeb Majumdar et al. J. Chem. Phys. 118(2003) 9809

## 6.3 COULOMB EXPLOSION IN METHYL IODIDE CLUSTERS

Coulomb explosion occurs when the intense laser field ( $10^{14}$ - $10^{15}$  W/cm<sup>2</sup>) interacts with the molecule/clusters, which is generally achieved using picosecond or femtosecond lasers. The electric field associated with the laser pulse is sufficient enough to remove several electrons, causing the components of the molecule/cluster to become highly charged. When the repulsive energy of like charges, known as coulomb repulsion, overcomes the total cohesive energy, the cluster/molecule disintegrates into multiple charged fragments with large kinetic energy. There are very few reports of coulomb explosion using nanosecond laser pulses.

Recently, we have observed nanosecond laser-induced coulomb explosion process in methyl iodide clusters by dye laser pulses ( $\lambda=557$ - 568 nm, pulse width 7-8 ns), leading to generation of multiple charged  $C^{+p}$  ( $p=4$ ) and  $I^{+q}$  ( $q=4$ ) species with large kinetic energy as shown below. Under these conditions, the laser intensity in the focus region is  $\sim 10^9$  W/cm<sup>2</sup>. Formation of such multiply charged species requires absorption of large number of photons i.e.  $\sim 30$  for  $C^{4+}$  (I.P = 64.49 eV) and  $\sim 20$  photons for  $I^{4+}$  (I.P = 44.01 eV) in 557- 568 wavelength region. Absorption of 30 photons, which are nonresonant with the molecular states, is extremely improbable and the

actual mechanism by which several visible photons can be absorbed is being looked into. Additional experiments such as wavelength dependence and cluster size effects, which could help in understanding the absorption mechanism, are being carried out currently.

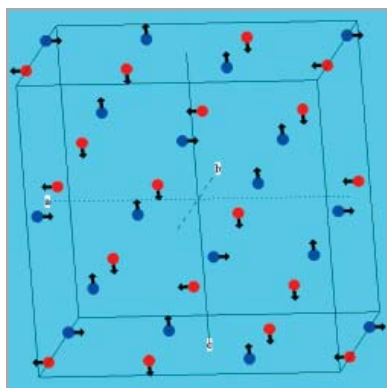


Time of Flight Mass Spectra of Methyl Iodide cluster

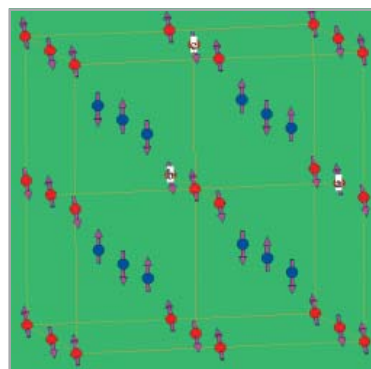
P. Sharma, R.K. Vatsa, B.N. Rajasekhar, N.C. Das, T.K. Ghanty and S.K. Kulshreshtha, Rapid Commun. Mass Spectr. 19 (2005) 1522.

### 6.4 MAGNETIC STRUCTURES IN $\text{La}_{1-x}\text{Ca}_x\text{MnO}_3$ (X = 0.4, 0.5, 0.6)

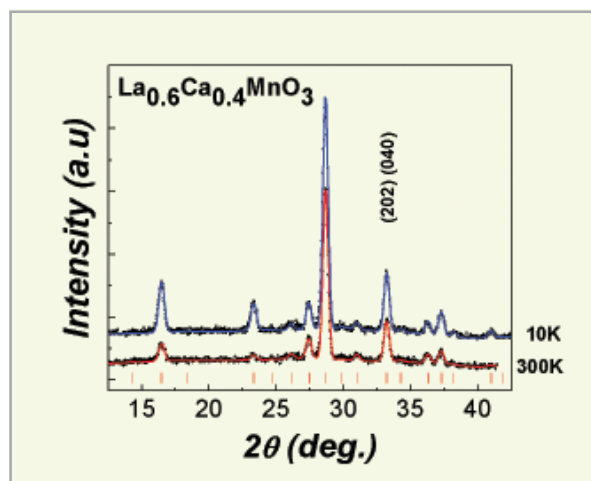
The magnetic phase diagram of  $\text{La}_{1-x}\text{Ca}_x\text{MnO}_3$  exhibits a complex ordering processes in the region of  $x=0.5$ . The compositions in the vicinity of  $x=0.5$  exhibits metal-insulator, Ferro Magnetic (FM), Charge-Ordering (CO), and Anti-Ferro Magnetic (AFM) ordering. We have studied the magnetic structure of the compounds with  $x = 0.4, 0.5,$  and  $0.6$ . The samples were prepared using standard ceramic technique. Neutron diffraction patterns were recorded on the powder neutron diffractometer ( $\lambda = 1.094 \text{ \AA}$ ) in Dhruva.



Magnetic structure of  $\text{La}_{0.4}\text{Ca}_{0.6}\text{MnO}_3$



Magnetic structure of  $\text{La}_{0.5}\text{Ca}_{0.5}\text{MnO}_3$



Neutron diffraction pattern of  $\text{La}_{0.6}\text{Ca}_{0.4}\text{MnO}_3$  at 300 K and 10 K.

The compositions are isostructural and crystallize in the  $O'$ -orthorhombic ( $b/v2 < a \leq c$ ) symmetry (Space Group  $Pnma$ ). Figure shows a section of the neutron diffraction pattern of  $x=0.4$  at 300 K and 10 K. An increase in the intensity of the low angle fundamental reflection at 10 K indicates ferromagnetic ordering. There is no signature of antiferromagnetic ordering. The total refined magnetic moment on the Mn site at 10 K was obtained as  $3.1\mu_B$  which is in reasonable agreement with the expected average moment ( $3.4\mu_B$ ) of mixed  $\text{Mn}^{3+}/\text{Mn}^{4+}$  matrix. Evidence of tilting of the  $\text{MnO}_6$  octahedra accompanying the magnetic transition is found in this compound.

The compound  $x=0.5$  exhibits ferromagnetic ( $T_C \sim 240\text{K}$ ), antiferromagnetic ( $T_N \sim 170\text{K}$ ) and charge ordering ( $T_{CO} \sim T_N$ ) transitions. On cooling below  $T_N$ , the lattice parameter  $a$  and

c increase (~1.2%) while b decreases (~1.6%). This anomalous behavior in the cell parameters originates from the orbital ordering of the  $d_{z^2}$  orbital in  $Mn^{3+}$  along the a-c plane. The AFM ordering in presence of charge ordering is of CE type. In this case  $Mn^{3+}$  and  $Mn^{4+}$  are located at two different sites. The refinement were carried out in the space group  $P2_1/m$  with  $2a \times b \times 2c$  cell. The magnetic structure for the two sublattice are treated with the propagation vector  $[\frac{1}{2} \ 0 \ \frac{1}{2}]$  for  $Mn^{4+}$  and  $[0 \ 0 \ \frac{1}{2}]$  for  $Mn^{3+}$ . The moment obtained for  $Mn^{3+}$  is  $1.5 \mu_B$  in the a-c plane and  $1 \mu_B$  for  $Mn^{4+}$  along c – axis.

The compound  $x=0.6$  exhibits antiferromagnetic ordering below 260 K. The magnetic structure (figure) is different from that observed for  $x = 0.5$ . The magnetic reflections could be indexed with  $3a \times b \times 2c$  cell. The profile refinement is carried out in the space group Pm. The refined magnetic moment obtained is  $1.5 \mu_B$  oriented along the a-axis at one site and along the c-axis on the other site. The structure is similar to that reported for  $x = 0.67$

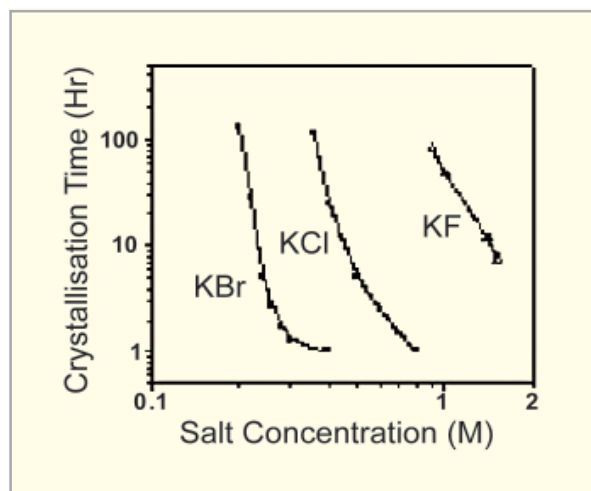
- P. Schiffer et al., Phys. Rev. Lett. 75 336 (1995).  
 A. Das et al., J. Magn. Magn. Mater. 237 41 (2001).  
 E.O. Wollan and W.C. Kohler, Phys. Rev. 100 545.  
 P.D. Babu et al., Solid State Commun. 118 91 (2001).  
 A. Das et al. Phys. Rev. B 70, 22404 (2004).  
 P.G. Radaelli et al., Phys. Rev. B 59, 14440 (1999).

## 6.5 STRUCTURE AND INTERACTION IN PROTEIN SOLUTIONS AS STUDIED BY SMALL-ANGLE NEUTRON SCATTERING

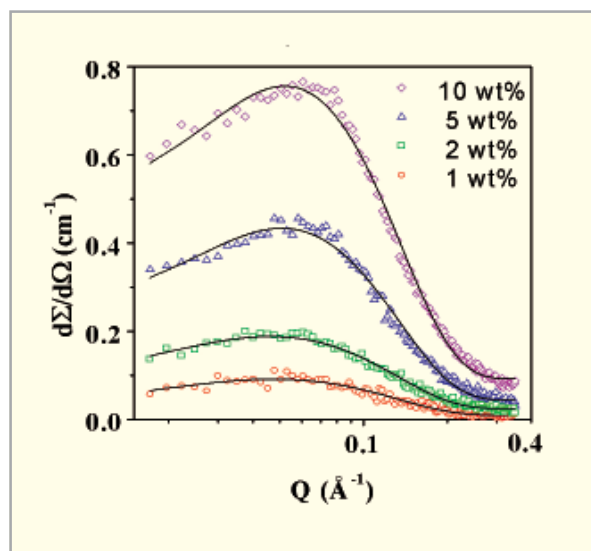
Understanding the mechanism of protein crystallization is of both biological and scientific interest. The structure and interaction amongst the protein macromolecules control the onset of different protein phases, which are governed by the mechanism of molecular approach, reorientation and incorporation. Small-Angle Neutron Scattering (SANS) is a powerful tool to determine the structure and interaction in protein solution. We have used SANS to characterize protein solution to compare the effect of the salts KF, KCl and KBr on protein crystallization.

The phase diagram of the crystallization of lysozyme as a function of concentration of salts KF, KCl and KBr. It is found

that the propensity of the salt to crystallize protein follows the Hoffmeister series (KF<KCl<KBr) with the marked differences in the effect of these salts.



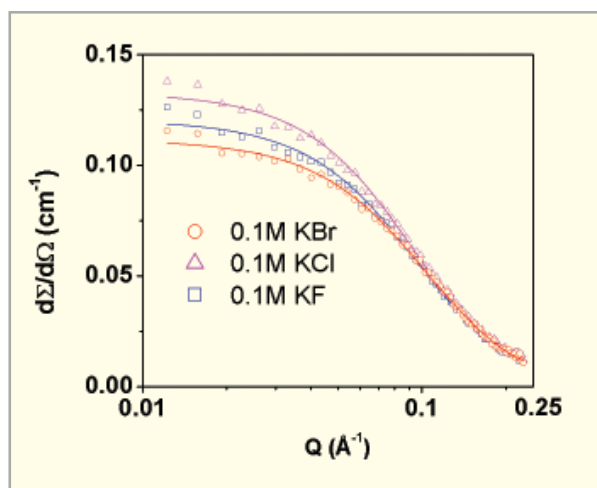
Effect of varying concentration of different salts on crystallization of lysozyme.



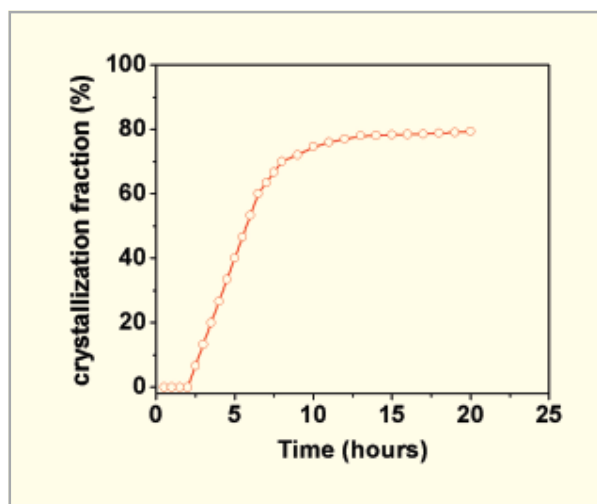
SANS data on aqueous solution of lysozyme at different concentrations.

The analysis shows that the lysozyme macromolecules are prolate ellipsoidal with dimensions semi-major and semi-minor axes as  $22 \pm 1$  and  $13.5 \pm 0.5 \text{ \AA}$ , respectively. It is also found that the effective (structural + counterion) charge on the

protein as obtained by taking into account screened Coulomb interaction between the protein macromolecules is much smaller than the structural charge suggesting increase of counterion condensation with the increase in concentration.



SANS data on 1 wt% lysozyme in presence of 0.1 M concentration of salts KF, KCl and KBr.



Time evolution of crystallization of 1 wt% lysozyme

SANS data were performed at different salt concentrations of the phase diagram (Fig.) to understand the changes in structure and interaction towards the crystallization. Fig. shows the

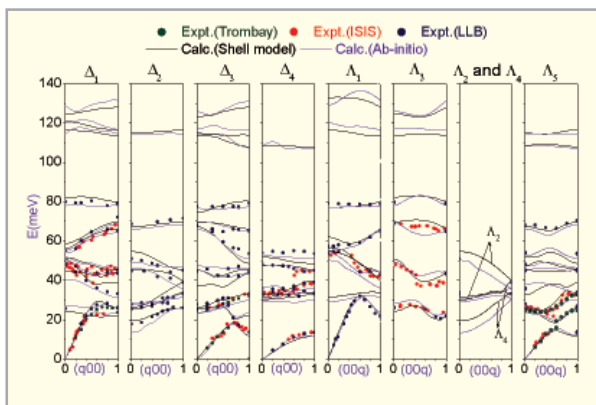
SANS data for 1 wt% lysozyme in presence of 0.1 M concentration of salts KF, KCl and KBr. The counterion condensation seems to be responsible for the differences in effect of different salts. This leads to the formation of dimers and the comparative effect of different salts follow the Hoffmeister series.

Time evolved measurements prior to crystallization show that the protein solution mostly consists of monomes and dimers. Interestingly, higher-mers are not observed in these measurements as perhaps they are formed for short times towards the process that leads to the crystallization. Fig. shows the rate of crystallization in one of the protein/salt solutions (1 wt% lysozyme + 0.4 M KBr) as measured in an interval of every half an hour for 20 hours. It is seen even after some time (1-2 hours) of that when crystallization has started ( $\sim 1$  hour), the crystal concentration is very small. Further, as the time progresses, crystallization increases linearly and the formation of crystals almost saturates at longer times.

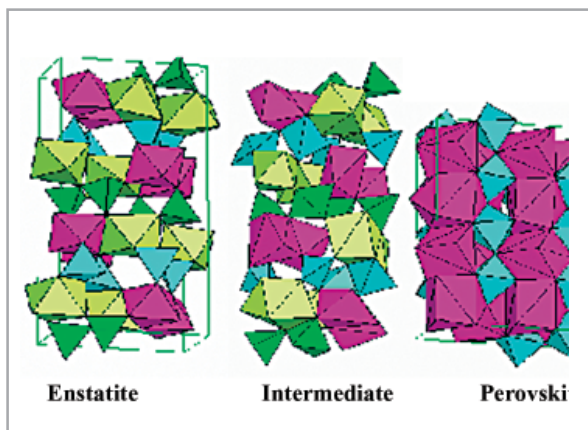
D.I. Svergun et al., Rep. Prog. Phys. 66, 1735 (2003)  
S. Chodankar and V.K. Aswal, Phys Rev. E (under publication)

### 6.6 PHYSICS OF THE EARTH'S INTERIOR: NEUTRON INELASTIC SCATTERING, LATTICE DYNAMICS AND MOLECULAR DYNAMICS SIMULATION

The Earth's mantle comprises of rock forming silicates of magnesium, iron, calcium, aluminium, etc. The crystal structure and the elastic and vibrational properties of these minerals have an important bearing on their high pressure-temperature thermodynamic properties and phase transitions. Using the inelastic neutron scattering technique, we have measured the vibrational properties of several geophysically important minerals, namely  $\text{Mg}_2\text{SiO}_4$ ,  $\text{MgSiO}_3$ ,  $\text{Al}_2\text{SiO}_5$ ,  $\text{ZrSiO}_4$  and  $\text{MnCO}_3$ . These minerals have complex crystal structures and the interpretation of the inelastic neutron scattering data (Fig.) involves extensive lattice dynamics calculations. The neutron data provide a stringent test of the interatomic potentials used and provide the vital inputs necessary for the prediction of the thermodynamic properties.



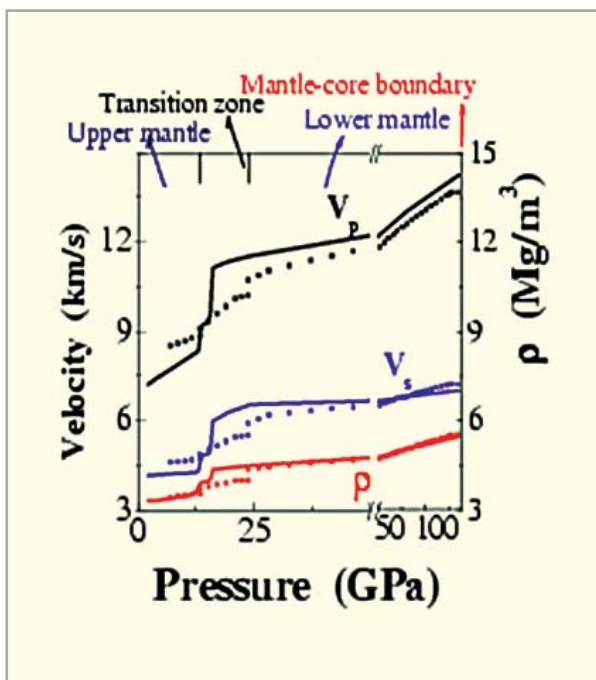
Molecular dynamics simulations (performed on the BARC parallel computer ANUPAM) using transferable potentials over a large pressure-temperature range in the Earth's mantle starting from the upper mantle phase enstatite  $MgSiO_3$  show several phase transitions which result in discontinuities in the simulated seismic velocities and densities (Fig.). With increasing pressure, enstatite transforms first to a new novel five-coordinated silicon phase, and then to the lower mantle perovskite phase involving six-coordinated silicon atoms. The new intermediate phase is crystalline but orientationally disordered. These studies suggest that the major discontinuities between the upper mantle, transition zone and lower mantle could arise due to changes in silicon coordination.



The simulated (full line) longitudinal ( $V_p$ ) and transverse ( $V_s$ ) wave velocities and density compared with published seismic data. The discontinuities represent the phase transitions. The corresponding crystal structures starting with the upper mantle phase enstatite  $MgSiO_3$  are also shown.

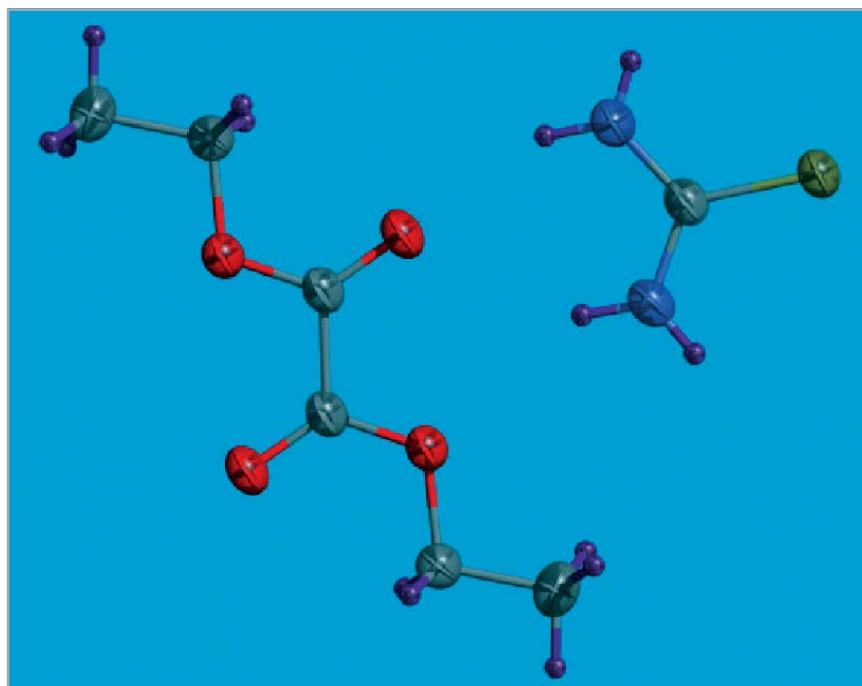
S.L. Chaplot and N. Choudhury; American Mineralogist 86 (2001) 752-761

S. L. Chaplot, N. Choudhury, S. Ghose, M. N. Rao, R. Mittal and K. N. Prabhatarsee; European Journal of Mineralogy 14 (2002) 291-329



### 6.7 HYDROGEN BONDING IN THIOUREA: DIETHYL OXALATE COMPLEX IN 2:1 RATIO

The crystal structure of thiourea:diethyl oxalate in 2:1 ratio is the first of its kind where diethyl oxalate exists as solid which otherwise is a liquid at room temperature when complexed with thiourea. Diethyl oxalate is the next simplest molecule in the series of symmetric diesters after dimethyl oxalate. Unlike dimethyl oxalate, it is a liquid at room temperature. The complex crystallizes in triclinic centrosymmetric space group  $P-1$  with the following unit cell dimensions  $a = 7.1870(7) \text{ \AA}$ ,  $b = 7.4890(8) \text{ \AA}$ ,  $c = 8.3637(7) \text{ \AA}$ ,  $\alpha = 63.783(7)^\circ$ ,  $\beta = 67.41(1)^\circ$ ,  $\gamma = 64.933(7)^\circ$ . The R-factor = 0.0386 for  $1850 \text{ Fo} > 4\sigma(\text{Fo})$  and 0.0417 for all 2020 data. There is a center of inversion at the center of the C-C bond of diethyl oxalate. This system is stabilized by N-H...S and N-H...O hydrogen bonds. The thiourea moiety is planar, but non-planarity exists in diethyl oxalate moiety unlike the case of dimethyl oxalate. The terminal methyl group in ethyl ester is insulated by an intermediate methylene group



Hydrogen bonding in Thiourea: Diethyl oxalate complex in 2:1 ratio.

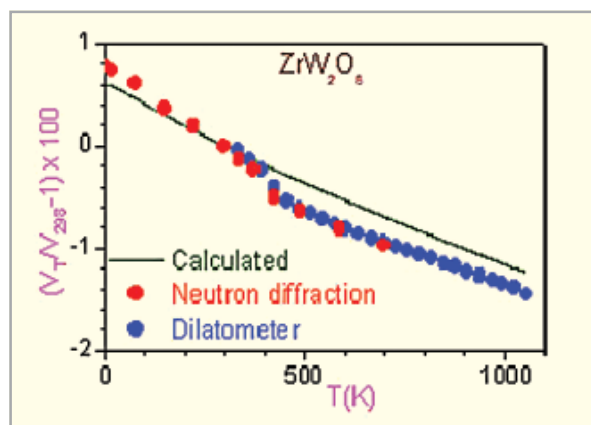
hence no C-H...O bonds are observed in this complex. This makes the hydrogen of the terminal CH<sub>3</sub> of ethyl group less polarizable to the external dipoles of thiourea. And hence it can be concluded that the formation of complex of thiourea: diethyl oxalate is basically the result of the N-H...O hydrogen bond interactions.

R.Chitra, Amit Das, R. R. Choudhury, M. Ramanadham, S. Lakshmi, M. A. Sridhar and J. Shashidar Prasad, J. Chemical Crystallography (under publication)

### 6.8 ORIGIN OF NEGATIVE THERMAL EXPANSION IN CUBIC ZrW<sub>2</sub>O<sub>8</sub>, HfW<sub>2</sub>O<sub>8</sub> AND ZrMo<sub>2</sub>O<sub>8</sub> AS REVEALED BY NEUTRON INELASTIC SCATTERING AT HIGH PRESSURES

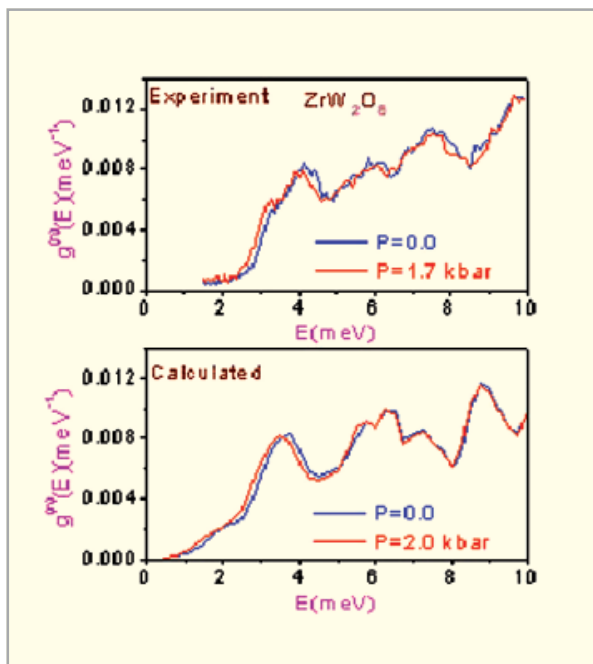
Large and isotropic negative thermal expansion is found in cubic AX<sub>2</sub>O<sub>8</sub> (A=Zr, Hf; X=W, Mo) (Figure) up to high temperatures. The compounds can be used for the preparation of controlled thermal expansion composites where the NTE

material to some extent compensates for the positive thermal expansion of the other components.



The experimental and calculated relative volume thermal expansion for cubic ZrW<sub>2</sub>O<sub>8</sub>,  $(V_T/V_{298}-1) \times 100\%$ ,  $V$  and  $V_T$  being the cell volumes at temperature  $T$  and 300 K respectively.

The AX<sub>2</sub>O<sub>8</sub> compounds have a framework structure consisting of corner linked AO<sub>6</sub> octahedral and XO<sub>4</sub> tetrahedral units. The analysis of the observed NTE, specific heat and phonon density of states measurements in ZrW<sub>2</sub>O<sub>8</sub> and HfW<sub>2</sub>O<sub>8</sub>



The comparison between the calculated and experimental inelastic neutron scattering spectra for cubic  $ZrW_2O_8$ .

The experimental data for cubic  $ZrW_2O_8$  are at 160 K and at pressures of 0.0 and 1.7 kbar.

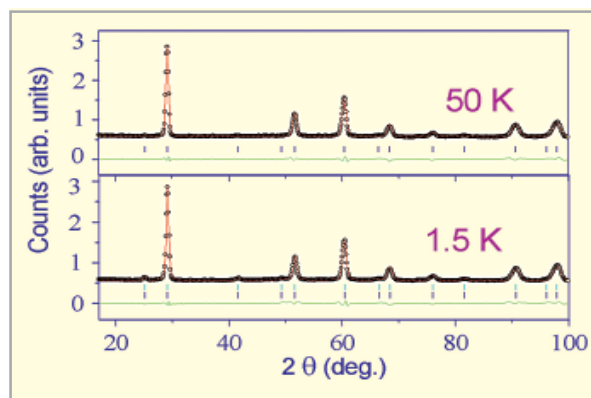
The experimental spectra at  $P=0.3$  kbar and 1.0 kbar fall in between those of  $P=0$  and 1.7 kbar, and have not been shown here for the clarity.

suggested that low energy phonon modes play an important role for the understanding of the NTE behaviour. Our lattice dynamical calculations for  $ZrW_2O_8$  and  $HfW_2O_8$  reproduce the observed anomalous thermal expansion in these compounds. The unusually dominant contributions of the transverse acoustic and optic modes below 8 meV lead to a large NTE. The calculations of phonon spectra for cubic  $ZrW_2O_8$  predicted (figure) softening at  $P=2.0$  kbar compared to that at ambient pressure, by about 0.1-0.2 meV for phonons of energy below 8 meV. High-pressure inelastic neutron scattering experiments conducted by us on cubic  $ZrW_2O_8$  and  $ZrMo_2O_8$  confirm phonon softening (figure). The thermal expansion as derived from the phonon measurements is found in good agreement with that obtained from diffraction data.

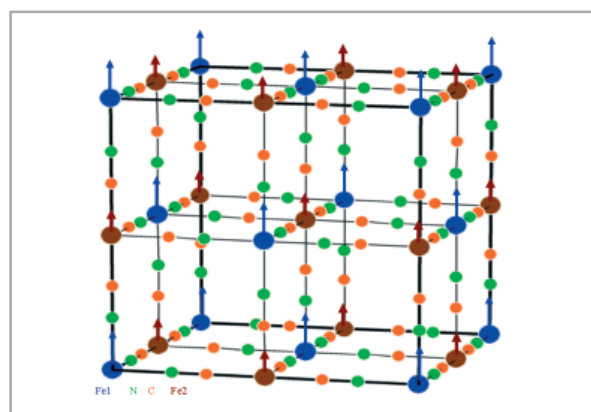
S. L. Chaplot and R. Mittal, Phys. Rev. Lett. **86**, 4976 (2001)  
R. Mittal, S. L. Chaplot, A. I. Kolesnikov, C. -K. Loong and T. A. Mary, Phys. Rev. B **68**, 54302 (2003).

## 6.9 STRUCTURAL AND MAGNETIC PROPERTIES OF HEXA-CYANOMETALLATE BASED MOLECULAR MAGNETS

Molecular magnetic materials are the subjects of an active research in recent years because of their possible applications in future information processing and storing devices. Hexacyanometallates, represented by the general formula,  $A_n[B(CN)_6]_m \cdot xH_2O$  where A and B are transition metals, are one of the most promising candidates in this regard. Ferri-ferricyanide forms one of the basic compounds in molecular based hexacyanometallates category. We have carried out structural and magnetic studies of ferri-ferricyanide,  $Fe[Fe(CN)_6]_4 \cdot 4H_2O$  by using DC magnetization, Mössbauer spectroscopy and Neutron diffraction techniques.

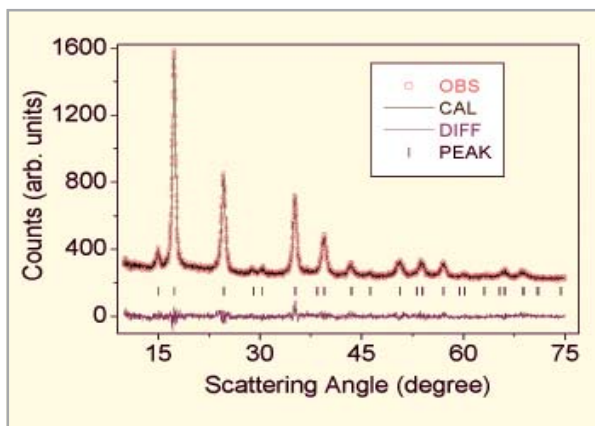


Neutron diffraction patterns of  $Fe[Fe(CN)_6]_4 \cdot 4H_2O$ .

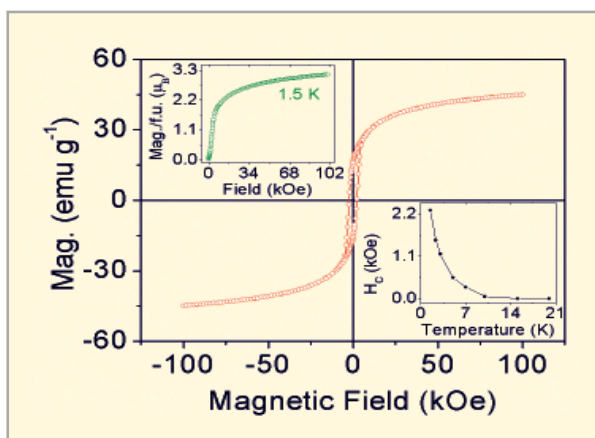


Chemical and magnetic unit cell of  $Fe[Fe(CN)_6]_4 \cdot 4H_2O$ . Blue ( $S=5/2$ ) and brown ( $S=1/2$ ) arrows show the alignment of spins in the magnetic unit cell.

Our neutron diffraction study has shown that this compound crystallizes in fcc structure (space group Fm3m) with two Fe sites [Fe1 at (0,0,0) and Fe2 at (1/2, 1/2, 1/2)] (Figs.). It orders ferromagnetically below 17.4 K with a collinear arrangement of high spin ( $S = 5/2$ ) and low spin ( $S = 1/2$ )  $\text{Fe}^{3+}$  ions at (0,0,0) and (1/2, 1/2, 1/2) sites, respectively.



X-ray diffraction pattern of  $\text{Co}_{0.75}\text{Ni}_{0.75}[\text{Fe}(\text{CN})_6] \cdot 6.8\text{H}_2\text{O}$ .



Hysteresis curve at 1.5 K for  $\text{Co}_{0.75}\text{Ni}_{0.75}[\text{Fe}(\text{CN})_6] \cdot 6.8\text{H}_2\text{O}$ .  
Top inset shows the virgin magnetization curve.  
Bottom inset shows the temperature dependence of coercive field.

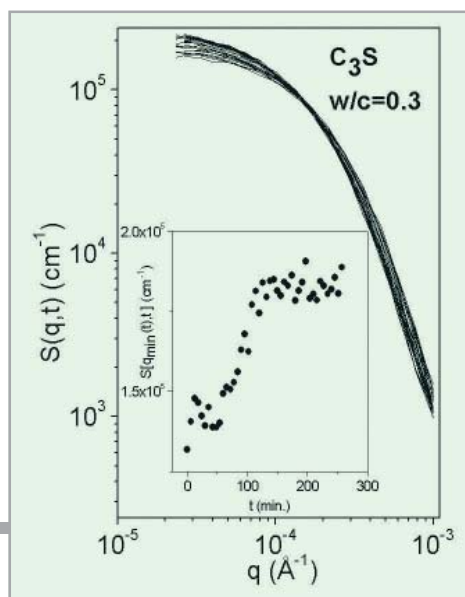
We have also studied  $\text{Co}_{0.75}\text{Ni}_{0.75}[\text{Fe}(\text{CN})_6] \cdot 6.8\text{H}_2\text{O}$ , with an aim to study the effect of substituting Co in  $\text{Ni}_{1.5}[\text{Fe}(\text{CN})_6] \cdot x\text{H}_2\text{O}$  on magnetic properties of this compound. We have used X-ray diffraction (Fig.), DC magnetization (Fig.), neutron diffraction, IR and Mössbauer spectroscopy techniques. Our studies have shown that substitution of Co in the parent

compound,  $\text{Ni}_{1.5}[\text{Fe}(\text{CN})_6] \cdot x\text{H}_2\text{O}$  induces disorder and spin glass behavior in the compound. It lowers the magnetic ordering temperature from 23.6 to 15.9 K, however, without any significant change in the coercive field.  $\text{Co}^{II}$  ion is found to possess the low spin state with  $S = 1/2$ .

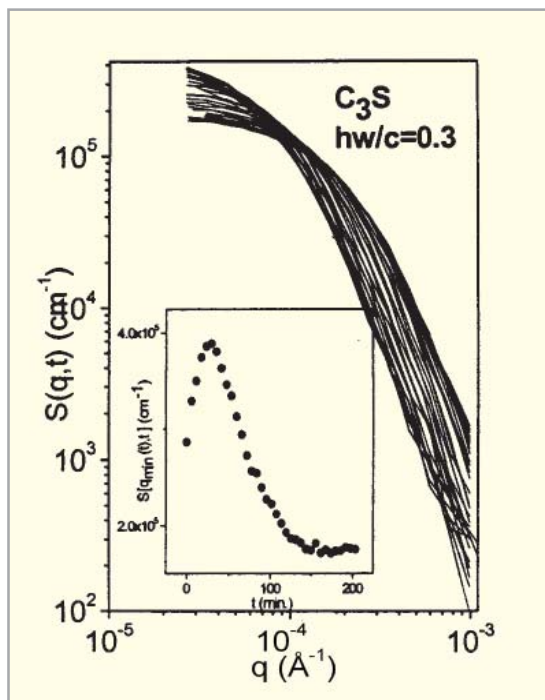
A. Kumar, S. M. Yusuf and L. Keller, Phys. Rev. B 71 (2005) 054414  
A. Kumar and S. M. Yusuf, Physica B, 2005.

### 6.10 TEMPORAL EVOLUTION OF MESOSCOPIC STRUCTURE AND DYNAMICAL SCALING OF STRUCTURE FACTOR FOR SOME NON-EUCLIDEAN SYSTEMS

Real time hydration of calcium silicates with light and heavy water has been investigated in mesoscopic length scale. The scattering data could not be interpreted in terms of linear theory of new phase formation. Predictions of non-linear theories on the dynamics of new phase formation have been



Time evolution of scattering function  $S(q,t)$  for light water hydrating calcium tri silicates ( $\text{C}_3\text{S}$ ) with  $w/c=0.3$ . The inset shows the time evolution of  $S(q_{\min}(t), t)$  where  $q_{\min}$  is the lowest attained  $q$  value for a particular measurement.  $q_{\min}$  varies slightly from one measurement to the other and is represented time dependent.



Time evolution of scattering function  $S(q,t)$  for heavy water hydrating calcium tri silicates ( $C_3S$ ) with  $w/c = 0.3$ . The inset shows the time evolution of  $S(q_{\min}(t), t)$  where  $q_{\min}$  is the lowest attained  $q$  value for a particular measurement.  $q_{\min}$  varies slightly from one measurement to the other and is represented time dependent.

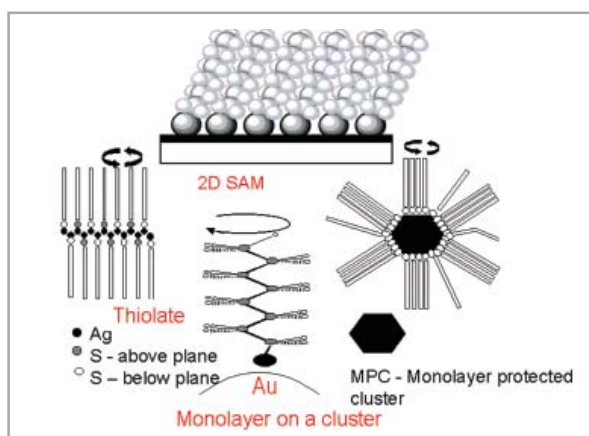
examined for the hydration of calcium silicates with light water and heavy water. The validity of the dynamical scaling hypothesis for new phase formation has also been examined. In the case of hydration with light water, reasonable agreement has been observed with dynamical scaling hypothesis with a new measure of the characteristic length. The characteristic length does not follow a power law relation with time. It increases with time and reaches a plateau. Mesoscopic structure of the hydrating pastes cannot be described in terms of a classical porous medium with a well-defined specific inner surface. Hydrating mass is found to be mass fractal throughout hydration, with mass fractal dimension increasing with time and reaching a plateau. But, in the case of hydration with heavy water, no agreement has been observed with the scaling hypothesis. Hydrating mass undergoes transition from mass fractal to surface fractal and finally again to mass fractal. The qualitative features of the kinetics of hydration, as measured in small-angle scattering experiments, are strikingly different for hydration with light water and heavy water.

S. Mitra, V.S.S. Sastry, K. Venu and R. Mukhopadhyay, Chem. Phys. Lett. 406 (2005) 263.

S. Mitra, K.Venu, I. Tsukushi, S. Ikeda and R. Mukhopadhyay, Phys. Rev. E, 69 (2004) 061709

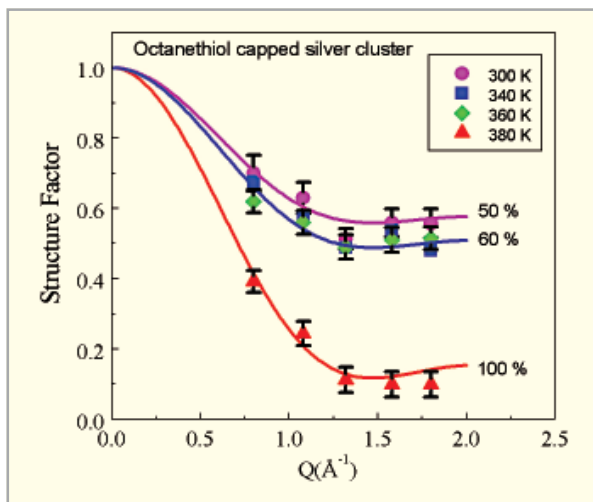
## 6.11 DYNAMICS IN MONOLAYER PROTECTED METAL-NANO CLUSTERS

Monolayers of thiols on noble metal surfaces have been the simplest of systems in which many of the fundamental properties such as friction, lubrication, etc. could be investigated. Monolayer-Protected metal Clusters (MPCs) where about 60% of the metal cluster surface was covered, are important in technology not only by giving a higher number density of molecules at the surface but also by preserving the nanodimension of the cluster. Each molecule of MPC has a compact, crystalline metal core. This metallic core of 1-4 nanometer diameter is encapsulated within a shell of tightly packed hydrocarbon chains linked to the core via sulfur atoms. The surface alkyl chains diverge as they move away from the core, resulting in the interpenetration of the monolayers of adjacent clusters in the solid state. Such interactions between isolated monolayer chains or bundles of chains lead to the formation of superlattice (Fig.). It is found that when the core is of gold atoms the superlattice formation does not take place. The present study was undertaken with



Schematic representation of the systems under investigation.

The 2D SAM represents an assembly of monolayers on a thin metal film deposited on a suitable substrate. This resembles the thiolates. A schematic representation of an MPC is also shown. Uniaxial rotational motion of the chain is shown



Variation of Structure factor with  $Q$  The percentage of mobile Alkyl Chains are indicated at different temperatures

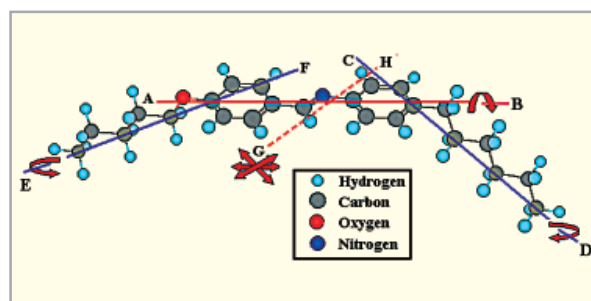
the objective of understanding the dynamics of alkyl chains in the isolated MPCs (gold based) and metal cluster superlattices (silver based), especially when they go through a phase transition. The results have been compared with a layered silver thiolate also, chosen to represent a planar two-dimensional monolayer.

In the cluster superlattice, QENS broadening was observed even at room temperature and below the chain melting temperature ( $T_{cm}$ ) whereas for the isolated cluster it was seen only above  $T_{cm}$ . In the layered silver thiolate, it was observed above the melting point. Data pertain to the rotational motions of the alkyl chains and can be best described by jump diffusion among  $N$  equivalent sites or continuous rotation about the molecular axis. At room temperature, the observed dynamics in Ag-MPC correspond only to the noninterdigitized molecular chains which amount to about 50% of the total (Fig.). Above 340 K, contribution from the interdigitized chains manifest and at 380 K, close to the superlattice melting temperature ( $\sim 392$  K), all the chains become dynamic. It is clearly established that the temperature required for the dynamics to manifest increases from the isolated cluster to the superlattice to the thiolate, suggesting a gradual increase in intermolecular interactions. Reorientation times for all these systems have been obtained at each temperature. Our work is the only example where microscopic information on the phase transitions in the MPC systems related to the alkyl chain motions has been obtained using QENS technique.

S. Mitra et al, J. Phys. Chem. B, 106 (2002) 3960;  
R. Mukhopadhyay et al, J. Chem. Phys., 118 (2003) 4614;  
T. Pradeep et al, J. Phys. Chem. B, 108 (2004) 7012

## 6.12 MOLECULAR REORIENTATION IN NO.M TYPE LIQUID CRYSTAL

Liquid crystals usually exhibit several mesophases differing by the degree of ordering of the molecules and the dynamics of these molecules is influenced by the transition from one phase to the other. Molecules undergo several kinds of motions leading to complicated trajectories of protons in molecular fluids. Internal molecular vibrations, translational and rotational diffusion, etc., are such possible motions. Molecular reorientational motions in undeuterated PentyloxyBenzylidene HexylAnilene (PBHA) and ButyloxyBenzylidene OctylAnilene (BBOA) are studied by the QuasiElastic Neutron Scattering (QENS) technique in their different mesophases. Molecular conformation in PBHA liquid crystal is shown in figure. It is found that there exist simultaneous reorientational motions of the chain group and the reorientational motions of the whole molecule around its molecular axis in the smectic-G, smectic-B, and smectic-C phases (figure). In smectic-A and



Molecular conformation in PBHA liquid crystal

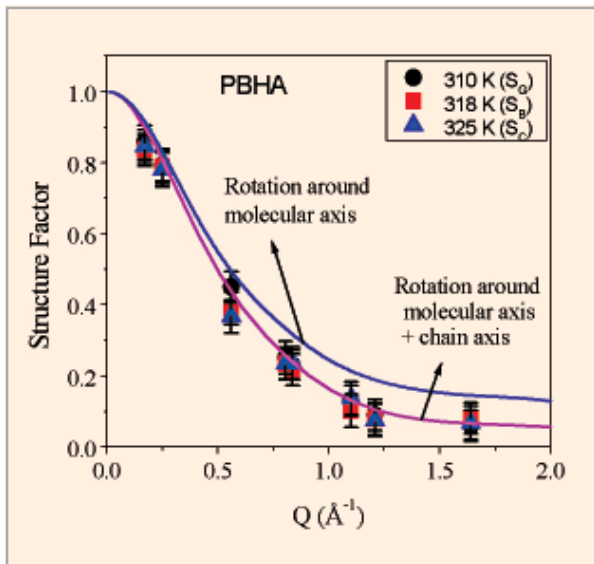
nematic phases, additional body axis fluctuations are found to exist in both PBHA (figure). Similar models describe the data for BBOA system also. The average amplitude of body axis fluctuations is found to be  $15^\circ$  and  $25^\circ$ , respectively, in the smectic-A and nematic phases of PBHA, and  $14^\circ$  and  $29^\circ$ , respectively, in BBOA. This is a demonstration that it is possible to separate the different dynamical contributions from different parts of a molecule in a same experiment by suitable modeling. Generally one uses partially deuterated samples which are

usually very expensive or not easily available contributions from different parts of a molecule in a same experiment by suitable modeling

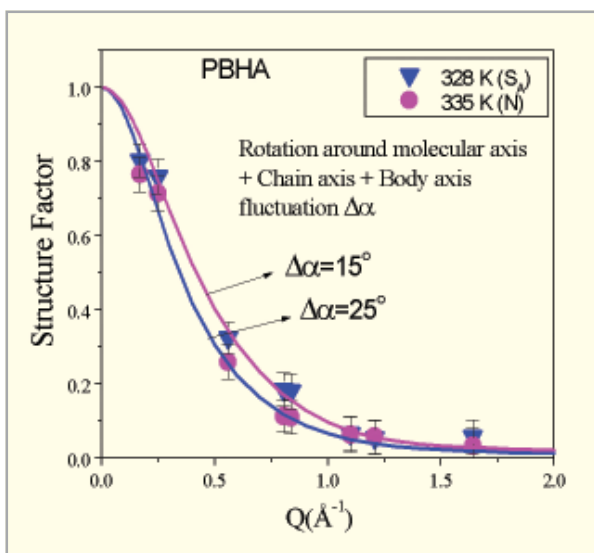
S. Mitra, V.S.S. Sastry, K. Venu and R. Mukhopadhyay, Chem. Phys. Lett. **406** (2005) 263.

S. Mitra, K.Venu, I. Tsukushi, S. Ikeda and R. Mukhopadhyay, Phys. Rev. E, **69** (2004) 061709.

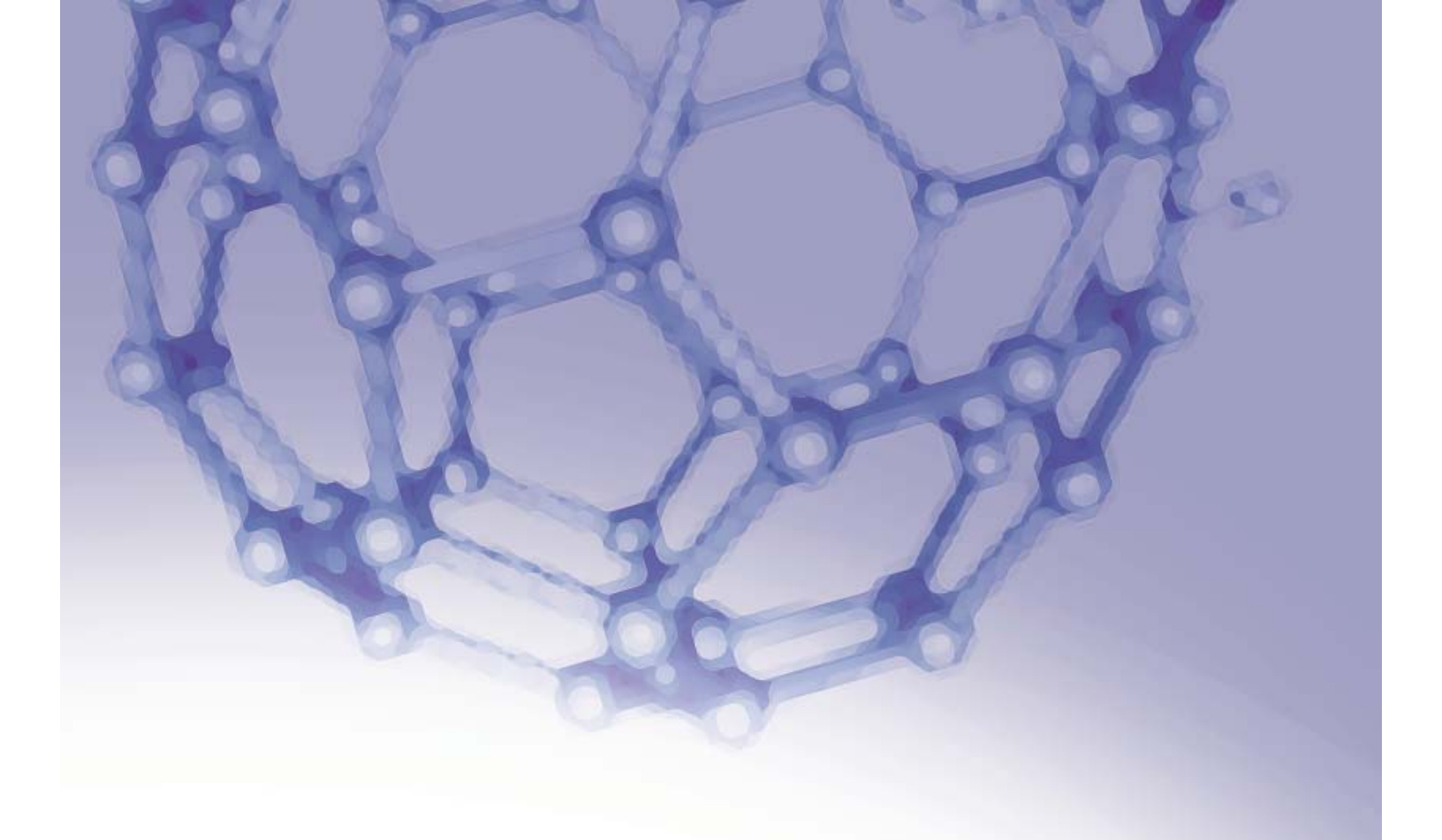
S. Mitra, R. Mukhopadhyay and K. Venu, Chem. Phys. **261** (2000) 149.



Variation of structure factor with  $Q$ . The solid lines are the calculated model function



Variation of structure factor with  $Q$ . The solid lines are the model function



## 7. THEORETICAL STUDIES AND SIMULATIONS

### INTRODUCTION

The chapter deals with the first principle calculations based on electronic structure and molecular dynamic methods that are carried out for systems such as, complex materials, doped fullerenes, disordered systems of liquid Germania, etc. The study leads to finding new material with high temperature superconductivity. The EOS of actinides has been studied using theories beyond DFT, namely, Dynamical Mean Field Theory with Local Density and Generalized Gradient Approximation.

Theoretical models and robust numerical algorithms for simulations of radiation hydrodynamic phenomena and particle transport for the design and analysis of ICF configurations have been developed. These are supplemented with models for evaluating material databases, such as EOS data, radiation opacity, etc.

Theoretical models have been developed for simulations of Nuclear Electromagnetic pulse, Virtual Cathode Oscillators and 3-D electron beams. Characteristics of atomic vapor free jet, expanding in vacuum are predicted using a 3-D Direct Simulation Monte-Carlo code. A 2-D time-dependent rate equation model has been used for simulation of dye-laser oscillators.

Computational tools, DYNATOOL and DYNADIM, have been developed for efficient Dimensional Analysis of a Dynamical System. Finally, a secure-symmetric-key algorithm using the chaotic Lorenz system for encryption/decryption of text messages has also been implemented.

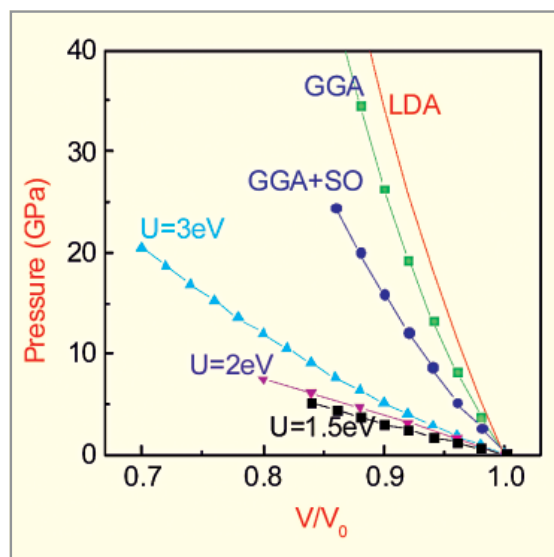
## 7.1 COMPUTATIONAL PHYSICS- EQUATION OF STATE: ACTINIDES

We carry out first principles calculations and use them to predict new phenomena, resolve the anomalies in the experimental data, and generate Equation Of State (EOS) tables for materials. We have recently predicted that hole-doped  $\text{MgB}_2\text{C}_2$  (which belongs to the  $\text{MgB}_2$ -family) is a strong candidate for high temperature superconductivity with transition temperature ( $T_c$ ) in the range of 50°K to 80°K for different hole dopants and that  $\text{Th}_3\text{Ni}_2\text{B}_2\text{N}_3$  enhances  $T_c$  to 30°K (compared to 13°K in  $\text{La}_3\text{Ni}_2\text{B}_2\text{N}_3$ ). We also calculate *ab initio* phonon frequencies with harmonic approximation, energy bands at non-zero temperature and electron-phonon coupling constants. EOS efforts are for static pressure and dynamic shock conditions and are mainly aimed at actinides using theories beyond Density Functional Theories (DFT), namely the Dynamical Mean Field Theory (DMFT). Our EOS (along with opacity of materials) is needed for coupled radiation hydrodynamic simulations.

For an accurate prediction of EOS it is necessary to predict high pressure phase transitions based on the first principles electronic structure, and Molecular Dynamics (MD) simulations. Our earlier work on thorium showed for the first time that contribution of  $5f$ -states through hybridization is essential for its structural stability at ambient condition. We parallelized the electronic structure and MD computer programs on the BARC parallel processors for use in large scale simulations, which is important for some of the strategically significant actinides which occur in many phases, some of which have more than 30 atoms per unit cell. The intriguing properties of plutonium come from the fact that it lies at the delocalized-localized transition region and hence its electronic structure studies in different phases have proved extremely difficult. The low temperature phase of Pu is the so-called  $\alpha$  phase and the conventional wisdom about it has been that correlation effects are not very important, and hence the usual band structure studies are adequate. Exploiting a recent finding that a structure with 2 atoms per unit cell well-approximates  $\alpha$ -Pu, we have carried out electronic structure and total energy calculations of this pseudo-alpha-phase. An interesting finding of our work is

that Local Density Approximation (LDA) and Generalized Gradient Approximation (GGA) fail to reproduce the experimental equilibrium volume and bulk modulus even when phonon and electronic thermal contributions to free energy are considered, leading us to conclude that, contrary to the accepted view, correlation is important in  $\alpha$ -Pu as well.

We have also studied both  $\gamma$ -Pu (see Fig.) and  $\delta$ -Pu, and find that DFT is unable to reproduce the experimental data on these phases. As the discrepancies are due to the inability of DFT to treat electronic correlation, we invoke a Hubbard  $U$  interaction energy for the  $5f$  electrons (LDA+ $U$  method). To improve further, we are developing a combination of LDA and Dynamical Mean Field Theory (LDA+DMFT), which is technically more sound and expected to give better results. Accurate EOS of Pu is very important for reliable strategic stockpile stewardship and management.



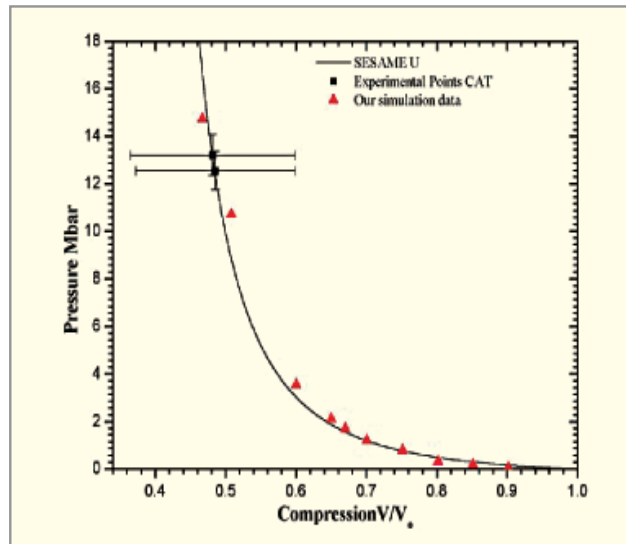
$\gamma$ -Pu EOS: LDA, GGA, GGA+SO, & LDA+ $U$ . Optimum  $U$  gives bulk modulus of about 30 GPa. [in-between that of  $\alpha$ -Pu (40-66 GPa) and Pu (30-35 GPa), as expected]

A.K. Verma, D.M. Gaitonde, R.S. Rao and B.K. Godwal., J. Phys. Condens. Matter (under publication)

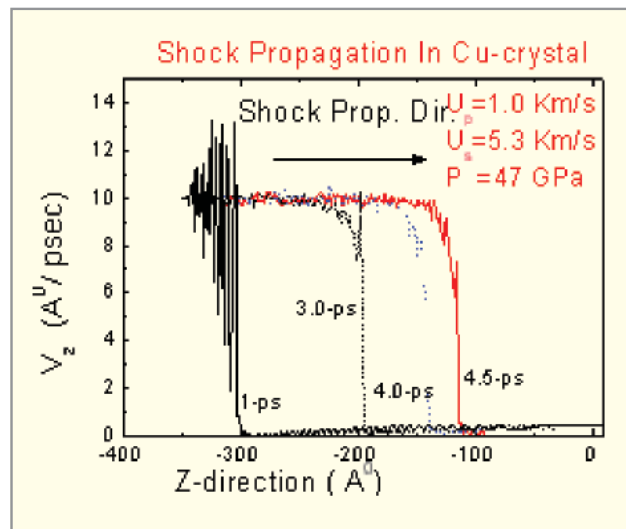
**7.2 SHOCK SIMULATIONS BY MOLECULAR DYNAMICS**

Theoretical studies of materials at arbitrary temperatures and matter densities have been pursued to support the experimental groups on laser-matter interaction and related phenomena. Using first principles total energy results, we have developed routines to calculate shock Hugoniots and these calculations were carried out for copper and uranium, to corroborate with the laser shock data obtained at RRCAT.

We also developed a routine to obtain the embedded atom (glue) type potentials for metals using our *ab initio* results. The fitting of the parameters of the interatomic glue potentials has been carried out to reproduce the total energies obtained by first principles calculations for various structures and compressions. This fitting can also be extended to match the forces on the atoms. These quasi *ab-initio* potentials are useful for large scale molecular dynamics (MD) simulations – including high pressure melting studies by 2-phase method, shock simulation, etc., both of which have been carried out by us with these potentials. Our shock simulation studies with quasi *ab-initio* potentials are intended to predict the rapid physical phenomena occurring in the high density – high energy regime, for a better planning of the laser shock experiments in our laboratory. As the computational code is parallelized in the 18-node parallel processor installed at Purnima complex, sampling of millions of atoms is feasible. 250,000-atom sample has already been tried in sequential as well as parallel form for shock simulations and thus multimillion-atom sample-size is feasible with the 128-node machine available at the computer center. Results of a sample simulation with 76,800 atoms in shown in Figure. As can be seen initially the shock front is elastic but later it is overtaken by the plastic front.



Shock Pressure vs  $V/V_0$  for natural uranium. ( $V_0$  denotes the equilibrium volume under ambient conditions).



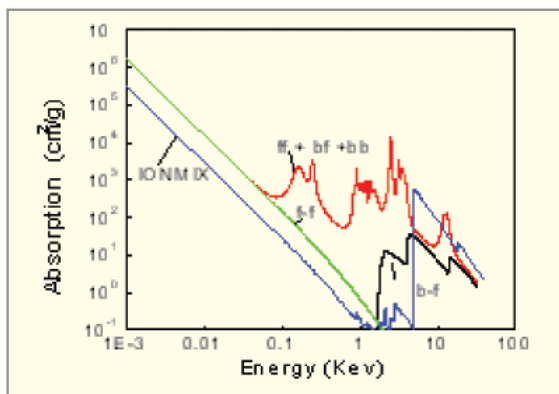
Shock front in Cu crystal at different time intervals from the initial shock impact.  $U_p$  and  $U_s$  are particle and shock velocities, respectively, and denotes the pressure in the shocked side of the front.

B.K. Godwal et al., Laser and Particles Beam, 21, 523-528 (2003).

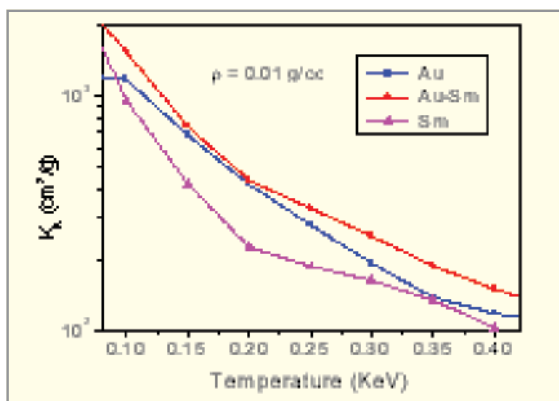
A.K. Verma, R.S. Rao and B.K. Godwal, J. Phys. Chem. Solids, 2006.

### 7.3 NON-LTE MODEL FOR RADIATION HYDRODYNAMICS

We have developed LTE and non-LTE models for radiation hydrodynamics. Radiation opacities and emissivities are essential data for any high density high temperature plasma simulations and we have developed computational model for them. First figure shows results for gold from our non-LTE model. Model has been tested against a number of benchmark and experimental results. For high Z elements non-LTE simulations show a marked improvement over LTE results. We used this model to investigate the opacities of composite targets. It is shown that the mixing of two high Z materials can lead to an enhancement in the Rosseland means (figure) which is of direct interest in indirect-drive inertial confinement fusion. For Au-Cu mix targets, these

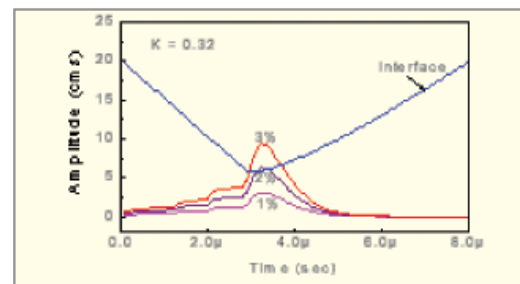


Opacity of gold. Model includes Bound-bound, bound-free, free-free, scattering and plasma oscillation contribution.

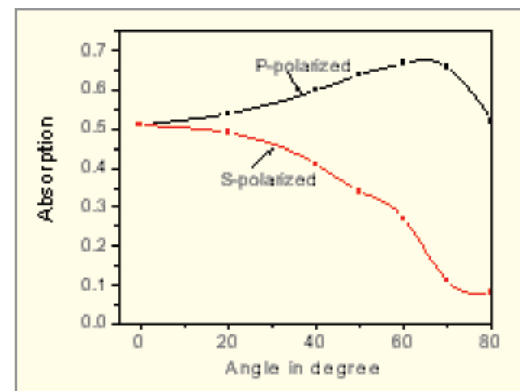


Enhancement in opacity of composite target as compared to pure gold.

predictions have been verified experimentally. In Inertial Confinement Fusion (ICF), the growth of Rayleigh – Taylor (RT) instability is a matter of concern. We have developed a semi analytical model to analyze the growth of RT instability. We studied the growth of RT instability when a heavy flyer impacts a target. We obtained the maximum tolerance for initial non-uniformities at the flyer target interface (figure). We have also developed a model for the interaction of ultra short high intensity laser with high-density plasma. The model can calculate the absorption of laser light for s and p polarized wave incident at any angle.



Growth of initial perturbation of 1, 2 & 3%. Maximum tolerance of 2% predicted. Movement of interface is also shown.



Calculated absorption of ultra short lasers on Al. Results agree with other published experiments.

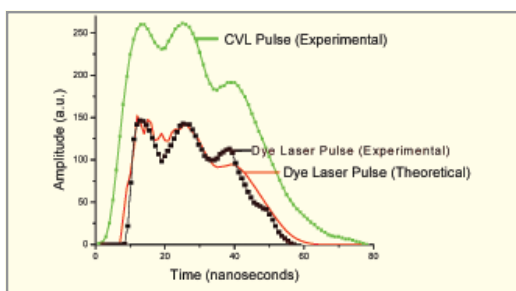
N. K. Gupta and B. K. Godwal, Laser and Particle Beams, 19, 259 (2001).

J. A. Chakera et al., Appl. Phys. Lett. 83, 27 (2003).

N. K. Gupta and S. V. Lawande, Laser and Particle Beams, 7, 27 (1989).

#### 7.4 THEORETICAL MODELING OF TRANSVERSELY PUMPED PULSED DYE LASERS

The spatio-temporal evolution of the output from a transversely-pumped, pulsed, narrowband, dye laser oscillators has been explained using a two-dimensional time-dependent rate-equation model that takes into consideration the coupled orthogonal propagation of the pump and dye laser radiation within the absorbing and amplifying medium, as well as, the time dependent diffraction loss in the oscillator cavity. The model successfully predicts the evolution of the dye laser oscillator out pulse, the intra-pulse change in output divergence and the intensity distribution across the output beam of dye laser amplifiers. Fig. shows an oscillator output pulse generated by the numerical model as compared to the corresponding experimentally measured pulse.

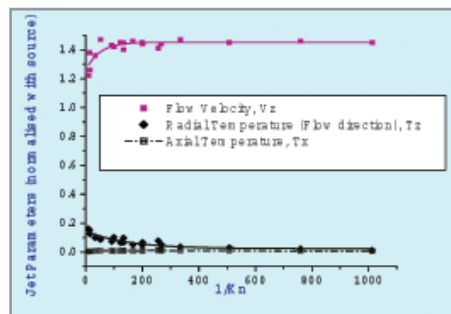


Experimental and theoretical pulse waveforms of the output of a copper vapour laser pumped dye laser.

#### 7.5 DIRECT SIMULATION MONTE-CARLO CODE DEVELOPMENT

A 3-D Direct Simulation Monte-Carlo (DSMC) code has been developed to predict the characteristics of atomic vapour free jet expanding in vacuum. Since DSMC is a probabilistic method, the statistical accuracy has been ensured by developing a parallel simulation code, which allows larger number of simulation particles by using the distributed memory architecture. For post processing, the data are collected from the nodes directly, instead of storing them in master, which helps in efficient management of time and memory. The model parameters have been optimized with extensive trials. The code has been verified using established reported results in literature and validated with in-house experimental data of atomic vapour jet expansion.

The code will help to arrive at the process operating conditions to ensure purity of the desired product in a laser based isotope purification process. The computational experimental study zone over three orders of magnitude of Knudsen number (from 0.001 to 0.1).

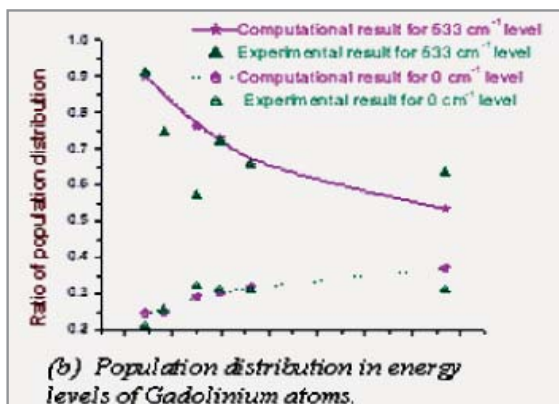
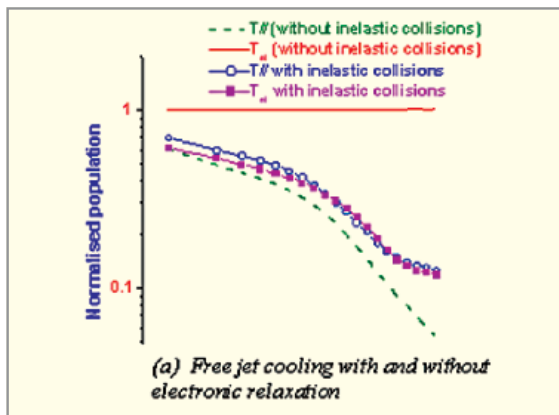


Vapor jet characteristics as a function of Knudsen Number

Jaya Mukherjee, Ph. D. Thesis, 2004, Mumbai University

#### 7.6 ELECTRONIC RELAXATION IN ATOMIC VAPOUR JETS

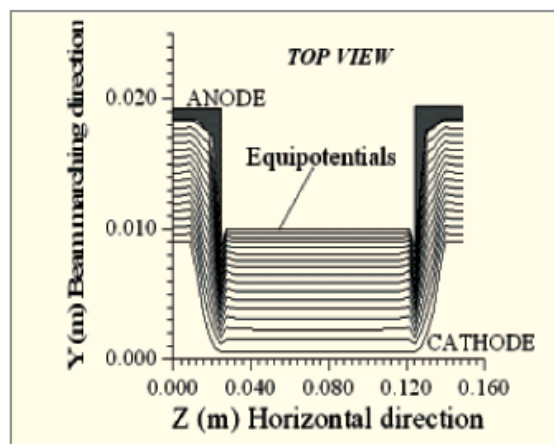
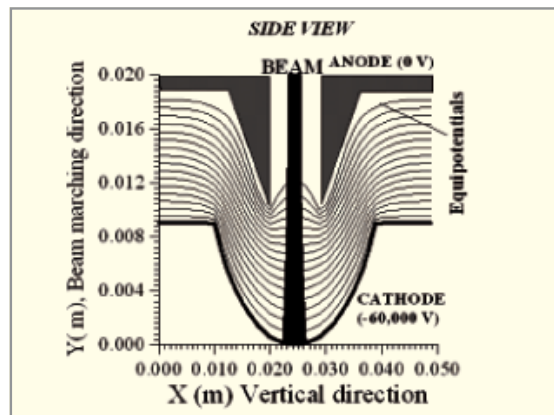
The laser-based purification method uses laser photons which is the costliest component of the process. To make the process economic, the atoms addressed by the lasers should be available in the lowest electronic level. This could be achieved by efficient electronic relaxation of the atoms generated at high temperature. A probabilistic Direct Simulation Monte Carlo (DSMC) computational code has been developed to study the behaviour of the free jet under different operational conditions and optimize the parameters to achieve the desired electronic relaxation. The code has been verified with theoretical and experimental data reported in literature and then used to study the free jet expansion of desired metal vapour. The result indicates that a suitably tailored beam can provide desired number of collisions between atoms in different electronic states and bring down the major population to ground and lowest metastable state. Fig. A shows that reduction in electronic temperature of the atomic vapour due to electronic relaxation of atoms as a result of inelastic collision. Fig.B indicates the population distribution of gadolinium atoms as a function of Knudsen number.



Jaya Mukherjee, Ph. D. Thesis, 2004, Mumbai University

## 7.7 BEST (BASIC ELECTRON-BEAM SIMULATION IN THREE DIMENSION)

In applications involving electron beam assisted melting and evaporation, it becomes necessary to correctly simulate the trajectory of the electrons emitted from the electron gun and transported to the work. Though commercial codes for achieving this objective do exist, each code has its own limitations while being applied to various gun and chamber geometry. In this context, BEST is a finite difference FORTRAN code structured to plot the trajectory of the electron beam for the experimental evaporation system under development at BARC. It generates a 3-D simulation of electron beam under applied as well as self-consistent electromagnetic field. A typical beam profile from the code is given in the figure.



Side view of the beam and the equipotential lines generated from the code in a strip beam gun.

S. Ghorui, A.K. Das, BARC report-BARC/2001/E/021, 2001.

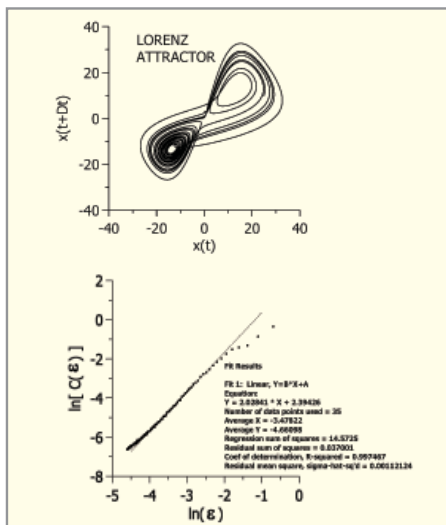
## 7.8 ANALYSIS OF DYNAMICAL SYSTEMS

A host of computational tools have been developed for analyzing complex nonlinear dynamic systems that exhibit periodic, quasi-periodic, chaotic or random behavior under different operating conditions.

### ■ DYNADIM (Dimensional Analysis of A Dynamical system)

Dimension of non linear dynamic systems provides an important measure for easy characterization of dynamics of

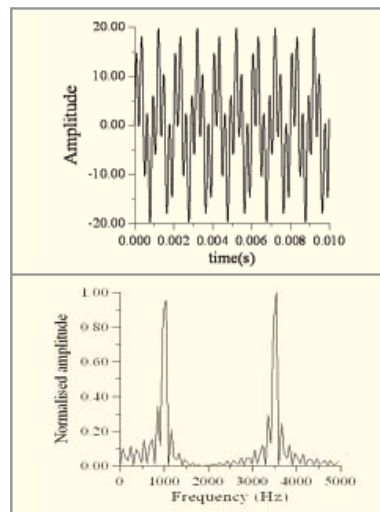
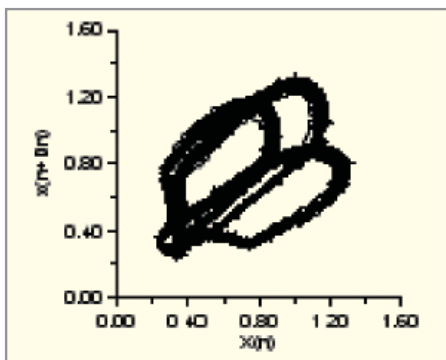
the systems. The code DYNADIM uses a unique indexing technique of hypercubes that provides a clever means to drastically reduce the requirement of storage.



A Lorenz attractor [left] of dimension 2.05 and determination of its dimension from the slope of the linear region of the plot in DYNADIM [right]. Computed value 2.02 is very close to the theoretical estimate 2.05.

### ■ DYNATOOL (Tool Kits for Dynamical Analysis)

This includes a number of tools for dynamical analysis such as reconstruction of phase space diagrams using different delays, different state space dimensions and power spectrum. Fig. shows a phase space diagram of a signal constructed using DYNATOOL in a plasma experiment. The time series and the power spectra are shown alongside.



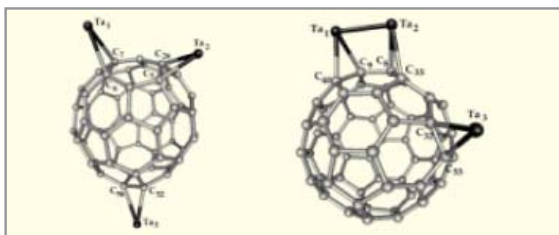
2D projection of a phase space diagram constructed by DYNATOOL in 4 dimensional state space using delay coordinate

S. Ghorui, S.N. Sahasrabudhe, P.S.S. Murthy, A.K. Das and N.Venkatramani" PRAMANA, Journal of Physics, 59, 1, 143, 2002.

## 7.9 QUANTUM SIMULATIONS

A programme of first-principles (Car-Parrinello) studies, including both molecular dynamics and optimization, of physical and chemical systems is being carried out. Using our in-house parallel computing facility and with the aim of providing theoretical support and guidance to our broad-based experimental programme, a variety of complex systems are being investigated. Some of the problems that have been studied include the high-pressure behaviour of a complex material (berlinite  $AlPO_4$ ), doped fullerenes, optical properties of organic molecules (DIP, Alq), ion solvation of alkali metal (K/Na) ions in water/water clusters, quantum dots, etc..

Motivated by unusual experimental results, the interaction of transition metal atoms (Ta) with  $C_{60}$  was studied. Among several novel insights obtained, an interesting feature was the high mobility of (three) Ta atoms on the cluster surface, leading to dimerisation. The correlated nature of their motion was characterized and contrasted with the behaviour of a single dopant Ta atom.



Correlated motion of Ta atoms on the fullerene surface

Ad-atom behaviour on surfaces as described above is of vital importance to processes such as adsorption, desorption, surface chemical reactions and crystal growth. The first direct evidence of the motion of a single alkali-metal (K and Na) hetero-atom on a fullerene surface was obtained. Several regimes of behaviour of the hetero-atom were identified, ranging from diffusive to orbital motion.

L. M. Ramaniah, S. M. Sharma, K. Kunc, N. Garg and M. Laghate, Phys. Rev. B68, 14119 (2003)

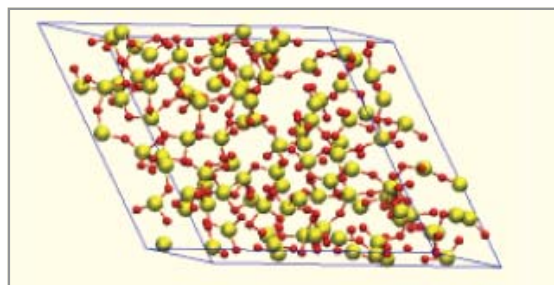
L. M. Ramaniah, M. Boero and M. Laghate, Phys. Rev. B70, 35411 (2004).

## 7.10 CLASSICAL SIMULATIONS: DISORDERED SYSTEMS (LIQUID AND AMORPHOUS)

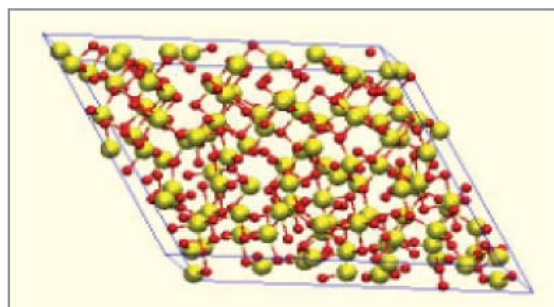
Pressure induced structural changes in Germania are known to be similar to the geologically important material silica but at much lower values. High pressure properties of crystalline  $\alpha$ -quartz,  $\beta$ -quartz, glass and liquid structures of  $\text{GeO}_2$  were investigated by means of classical molecular dynamics simulations at various temperatures using 4374 atoms. Following are the significant results.

Upon heating,  $\beta$ -quartz structure transforms to  $\alpha$ -quartz structure around 1000 K and subsequently melts to form randomly connected tetrahedral liquid at about 1550 K. The  $\beta$ -quartz as well as  $\alpha$ -quartz structure is shown to transform to a dense octahedral phase upon compression to 5 GPa and 9 GPa respectively. For vitreous  $\text{GeO}_2$  the compression brings about only gradual changes in the Ge-O coordination and also the density. Upon release of pressure this state reverts back to initial structure with a

sudden change in density around 3-4 GPa. Except at temperatures higher than 2500 K, the liquid was observed to undergo a first order phase transition to a denser 6 coordinated structure as in the crystalline case with an increasing transition pressure with temperature. Detailed analysis of the transition suggests it to be liquid to solid rather than liquid to liquid phase transition, unlike what the recent experimental results claim. The liquid  $\text{GeO}_2$  (1650 K, 0.1 MPa) and its high pressure form (1650 K, 15 GPa).



$\text{GeO}_2$  at 1650 K, 0.1 MPa



$\text{GeO}_2$  at 1650 K, 15 GPa

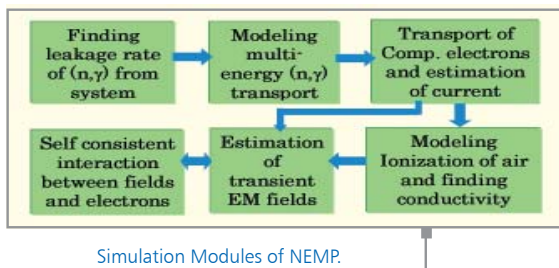
Shanavas K.V., Nandini Garg, and Surinder M. Sharma, Solid State Physics (India) 49 (2004) 392

## 7.11 NUCLEAR ELECTROMAGNETIC PULSE

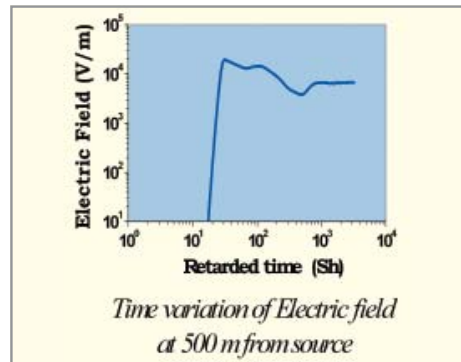
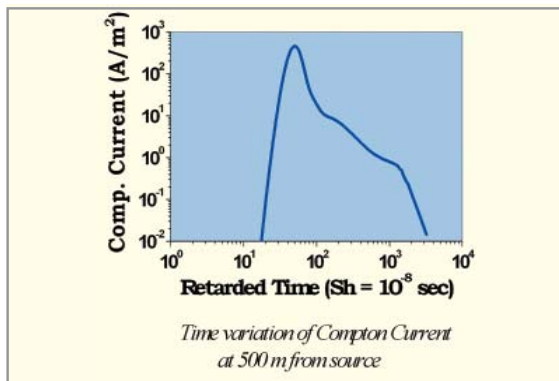
Nuclear Electromagnetic Pulse (NEMP) is a high intensity Electromagnetic Pulse originating from a nuclear event. Theoretical Physics Division has made significant progress in understanding this multi-physics process involving coupled neutron-gamma-electron transport, plasma physics, air chemistry and Electromagnetics. The major achievements lie in theoretical modeling and numerical

simulation of the generation and propagation of NEMP fields through atmosphere.

It is known that any nuclear event produces large number of neutrons and gammas. Neutrons, while traveling, undergo either inelastic scattering or capture with the atoms of the ground or air to produce the secondary gammas. The gammas interact with air molecules to generate Compton electrons, which then move forward leaving behind the positive ions. This partial charge separation creates a radial electric field. The electrons deposit their energy by ionization, thereby producing highly conducting plasma around the source. For low altitude nuclear event, the air-ground interface causes asymmetry in current distribution, leading to a net upward current and hence a radiated EMP. Fig. shows the modules involved in a NEMP simulation.



Figures show the time variation of Compton current and electric field at 500 m from a typical  $(n, \gamma)$  source. A noticeable fact of both the current and field waveform is their long time duration with magnitudes sufficient to induce very strong electric current and voltage surges that can cause severe damage to electronic equipment.



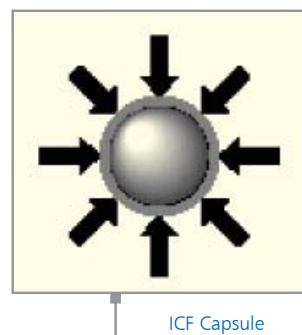
G. Kondayya and Aditi Ray, Nucl. Sci. & Engg. (under publication).

Aditi Ray and G. Kondayya, IEEE Trans. Ant. Prop. (under publication).

G. Kondayya and Aditi Ray, Annals of Nucl. Engg. (under publication).

## 7.12 HYDRODYNAMIC PHENOMENA

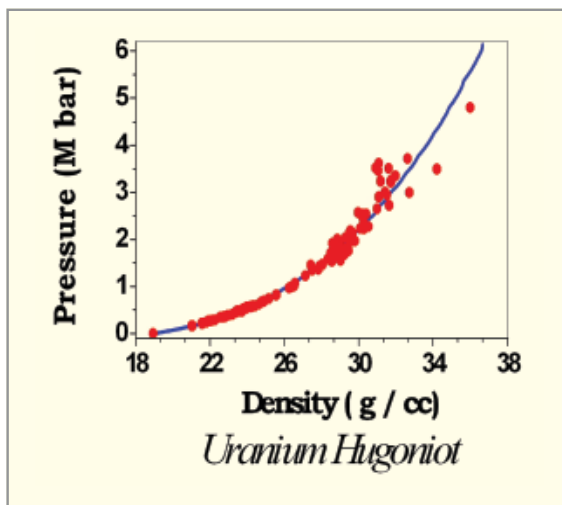
Hydrodynamics is an inevitable ingredient of many fields of science and technology, e.g., astrophysics, Inertial Confinement Fusion (ICF), etc. In directly driven ICF, lasers generate an intense shock wave to implode a fuel capsule to conditions appropriate for thermonuclear fusion, see Fig. The resulting hydrodynamic motion of the capsule is also coupled to other processes like radiative transfer, particle  $(n, \gamma, \alpha)$  transport, fission and fusion physics, nuclear



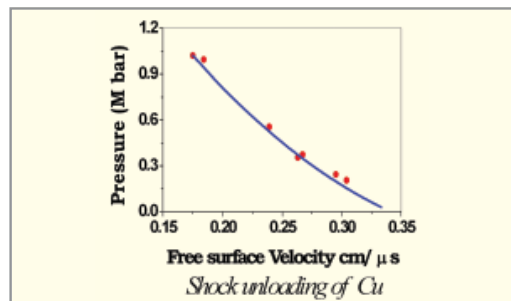
transmutation, etc. Theoretical modeling of ICF systems needs, in addition to robust numerical hydrodynamic algorithms, databases like Equation Of State (EOS), radiative opacity, particle interaction cross-sections and material properties. Theoretical Physics Division is engaged in

developing mathematical models amenable to detailed simulations of hydrodynamic phenomena for the design and analysis of ICF configurations.

Pressure gradients in a medium induce macroscopic motion thereby changing its density which, in turn, affects the pressure distribution in a self-consistent manner. The resulting hydrodynamics, characterized by four variables: macroscopic velocity, density, pressure and internal energy, is described by three conservation equations of mass, momentum and energy, and an EOS formally expressing pressure as a function of energy and density. For ICF simulations, EOS databases are needed over a wide range of density ( $10^{-4}$  -  $10^4$  gm/cc) and temperature ( $\sim 10$  -  $10^9$  K) for different elements, compounds and alloys. We recently developed a global EOS model for solids using Thomas-Fermi theory for electrons and Cowan's model for ions together with formulations to account for degenerate compression at zero temperature. We also extended the EOS model to include solid-solid as well as liquid-gas phase transitions. A simple scheme for dissociation of diatomic molecules like  $D_2$  was also incorporated. These models have been tested extensively against experimentally measured shock Hugoniot data, shock unloading data and critical point data for a variety of materials. Fig. shows a comparison of theoretical and experimental Hugoniot for uranium. Another comparison shows shock unloading pressure against free-surface velocity in copper.



Uranium Hugoniot.



Shock unloading of Cu.

We have developed 1-D & 2-D hydrodynamic codes, using Euler and Lagrange numerical schemes and the new EOS data. Many shockwave problems encountered in ICF have become amenable to accurate analyses with these developments.

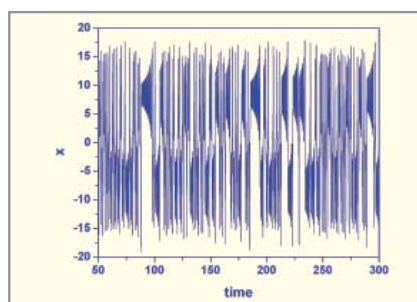
M.K. Srivastava, Aditi Ray, G. Kondayya and S.V.G. Menon, BARC Report (2005), (under publication).

Aditi Ray, M.K.Srivastava, G.Kondayya and S.V.G. Menon, Laser and Particle beams (under publication).

### 7.13 CHAOS BASED CRYPTOGRAPHY

Cryptography is the science of protecting privacy and authenticity of information under hostile conditions. Modern cryptography is now routinely employed for large scale information exchange using networking schemes.

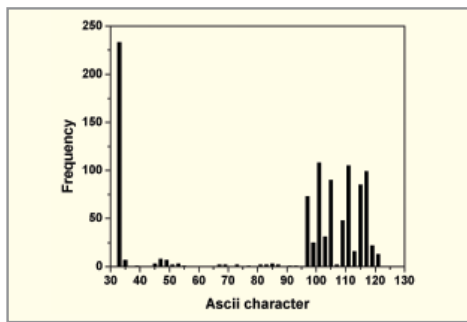
Apparent randomness (Fig.) ensuing in chaotic systems can be effectively deployed to encrypt and decrypt secure messages. Defining features of chaos, viz, sensitivity to initial conditions, ergodicity and mixing are exploited.



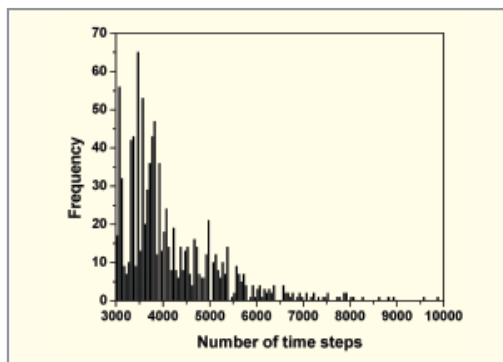
Time series  $x(t)$  for chaotic Lorenz parameters.

A software based approach is preferred for digital communications. Security related software is highly relevant to DAE environment and its constituent institutions. A secure symmetric key algorithm based on proposed Baptista's scheme has been developed using chaotic Lorenz system for encryption/decryption of textual messages. The number of time steps defining the trajectory constitutes the cipher representing each character in the message. The cipher text of the message is an ensemble of such integers. The system used provides parameters forming a large key space. The encryption keys selected are based on different concepts thereby making them independent and diverse. The algorithm has been tested for local communications via e-mail transfers of the cipher texts.

Frequency distributions of standard English text message and its encrypted version are shown in Fig. B. Different plaintext messages based on 256 Ascii characters exhibit similar statistical features for their cipher texts indicating the necessary security.



Standard English text message.



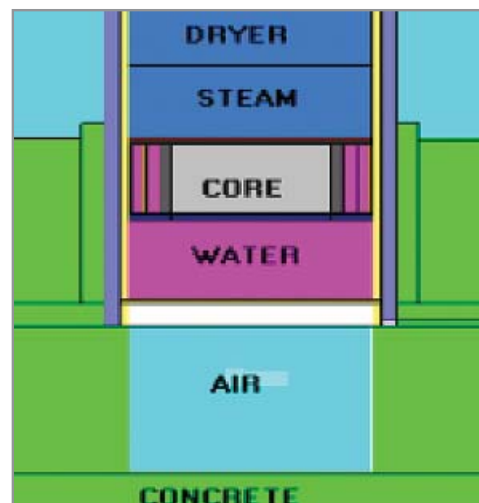
Encrypted English text message.

B.R Ivan, S.D. Dhodapkar and Q.V. Lawande, National Workshop on Cryptology, Amrta Vishwavidhyalaya Peetham, Kerala (2004).

Q.V. Lawande, B.R.Ivans, and S.D. Dhodapkar, BARC Newsletter 258 (July 2005)

### 7.14 NEUTRON-GAMMA TRANSPORT FOR NUCLEAR SCIENCE APPLICATIONS

The particle transport is an extremely important topic since it arises in a wide variety of physical phenomena. The process can involve a variety of particles such as neutrons, gas molecules, ions, electrons and quanta (photons, phonons) moving through various background media such as components of nuclear reactor core, stellar or planetary atmosphere, gases and plasmas. The particle transport theory refers to the mathematical description of transport of particles through a host medium. The particles stream between random interaction events such as scattering, absorption etc. The problem is to evaluate the "expected" or average distribution of particles in the phase-space. This distribution function obeys a linear form of the well-known Boltzmann transport equation. This is an integro-differential equation with the position, energy and direction of particle and possibly time as independent variables. Discretisation of all the variables leads to a massive set of coupled linear equations which are solved by sophisticated iterative techniques.



Schematic diagram showing complex internals of a reactor.

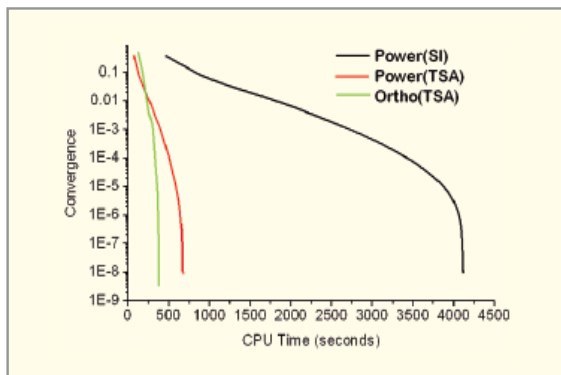


Figure showing the effectiveness of two techniques

The work on transport theory involves in-house development of efficient computer codes and multi-group cross-section libraries. During last few years, two neutron-gamma transport codes ONEDTRAN and ATRAN (1-D and 2-D) have been developed which can solve steady state and pulse-decay problems. They were used to evaluate the neutron-gamma distribution in atmosphere resulting from a localized source upto a distance of few kilometers. In another application, the 2-D code was used to evaluate the cumulative neutron fluence received by TAPS-BWR pressure vessel during its lifetime to estimate the radiation damage. This requires simulation of the complex internals of the reactor (Fig). Recently, a 3-D neutron-gamma transport code ATE3 has been developed in Cartesian XYZ geometry for criticality and external source problems. This code can use conventional methods of solution as well as some advanced techniques based on Krylov sub-space methods. Fig. shows the effectiveness of two techniques based on Krylov methods to solve the K-eigenvalue problem for a Light Water Reactor test case. Transport problems often require too large memory and CPU time. It is planned to attempt parallelisation on the distributed memory parallel computer systems being developed at BARC.

Anurag Gupta and R.S. Modak, *Annals of Nuclear Energy*, 31 (2004) 2113.

Anuradha Sharma, NSRP-15, BARC, Mumbai, (2003)

R.S. Modak, Vinod Kumar, S.V.G. Menon and Anurag Gupta, *BARC / 2005 / E / o21* (2005)

## 7.15 VIRCATOR MODELLING AND SIMULATION

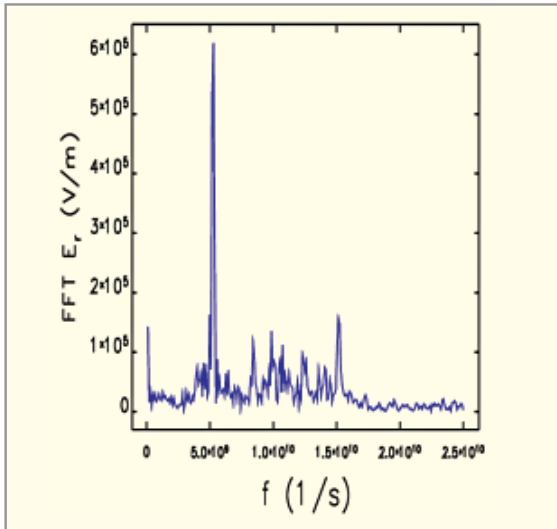
The Virtual Cathode Oscillator (VIRCATOR) is a source of high power microwave pulse. It consists of a diode and a drift tube. At high current densities, a virtual cathode is formed in the drift region whose position oscillates with time. The virtual cathode also gives rise to an oscillation of electrons between the cathode and virtual cathode. In BARC, the KALI series of Vircators has been built by Accelerator and Pulse Power Division. The modeling and simulation of the KALI series is in part the aim of this study.

As a first step in modeling the VIRCATOR, we considered a 1-dimensional model of the drift space and found that contrary to previous simulations which indicated that electron oscillation frequency is proportional to the current density, the electron oscillation frequency is in fact proportional to the square root of the current density as borne out in experiments.

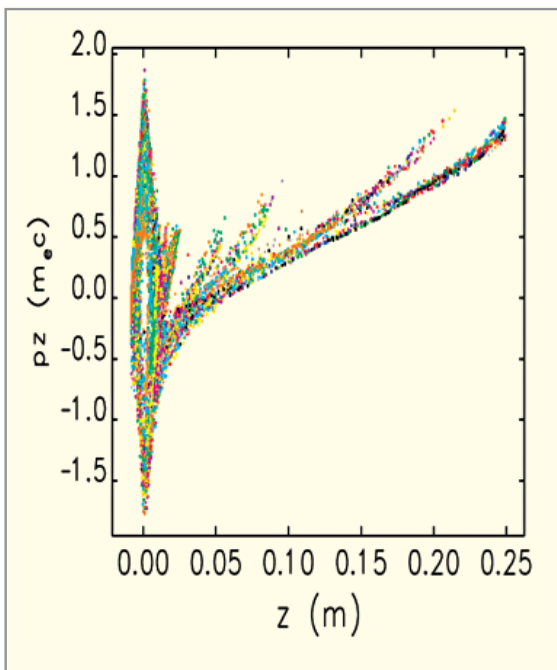
An integral part of the VIRCATOR is a high power diode that accelerates electrons. The space charge effect limits the maximum current that can flow across the diode. Its value is generally taken to be the Child-Langmuir expression for infinite parallel plates. We have demonstrated that in closed diodes, the space charge limited current may exist only in an asymptotic sense. Further, the Child-Langmuir law has been generalized for non-zero injection velocity of electrons.

Diodes in high power applications are open to electromagnetic radiation due to the presence of insulators. We have found that the Child-Langmuir law is grossly inadequate in situations where electromagnetic radiation escapes from the diode as this leads to an increased repulsion between the electrons and hence a drop in current. We have incorporated the loss mechanism within the Child-Langmuir formalism and shown that our predictions agree with numerical simulations.

A realistic VIRCATOR simulation was carried out using the Particle-In-Cell code, SPIFFE, which we modified to include absorbing boundaries. Using the current and voltage recorded for the KALI-1000 VIRCATOR, the simulation correctly predicted the microwave frequency and output power. Work is under way to simulate the VIRCATOR using only the time profile of the voltage pulse.



The simulated frequency spectrum of KALI-1000.

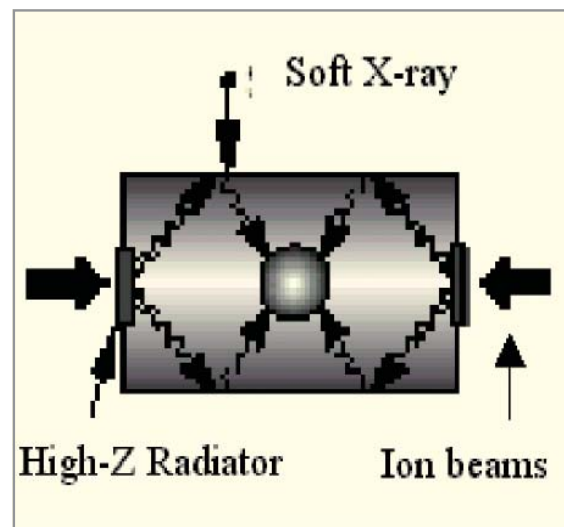


A typical phase-space plot in KALI-1000.

D. Biswas, R. Kumar and R.R. Puri, Phys. Plasmas 10 (2003) 4521.  
R.Kumar, R.R. Puri and D Biswas, Phys. Plasmas, 11 (2004) 324  
R.R. Puri, D.Biswas and R.Kumar Phys. Plasmas, 11 (2004) 1178  
D.Biswas R.Kumar and R.R. Puri Phys. Plasmas, 12 (2005) 93102

## 7.16 RADIATIVE TRANSFER

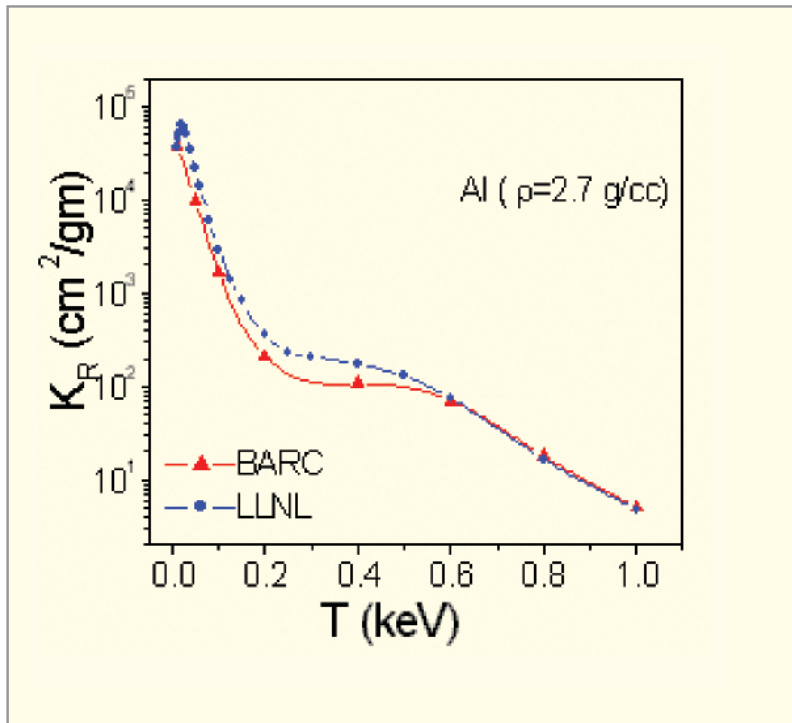
Radiative transfer is an important phenomenon in many scientific disciplines, e.g., astrophysics, Inertial Confinement Fusion (ICF), atmospheric science, etc. Radiations emitted by astrophysical or laboratory plasmas have been used traditionally as a reliable diagnostic tool. In an indirectly driven ICF, lasers or ion beams generate an intense source of thermal X-rays at temperature  $\sim 10^7$  K in a cavity called hohlraum. On absorption of this radiation, a fusion capsule placed at the centre of the hohlraum is imploded to



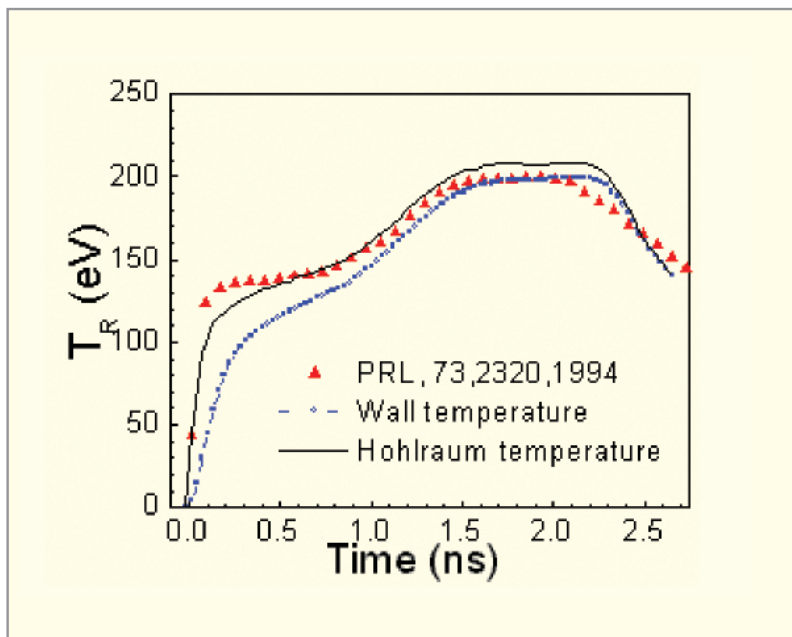
ICF Hohlraum

conditions appropriate for thermonuclear fusion. By the same process, milligrams of a fissile capsule can also be made super critical momentarily. These are some examples of systems involving radiative transfer. Theoretical Physics Division has been developing mathematical models for simulations of radiative transfer phenomena.

At very high temperature, atoms of any material not only acquire kinetic energy but also get internally excited and ionized. On de-excitation, these atoms release photons. The resulting radiative transfer via continued absorption and reemission process induces hydrodynamic motion in materials in the hohlraum. An important part of the work involves developing opacity models over a wide range of



Rosseland opacity.



Hohlraum Temperature.

density, temperature and ionization state of ions. Many factors like distribution of ion species, their excitation spectrum, lowering of ionization continuum, screening effect on bound energy levels, energy level splitting, broadening of energy levels, etc., are required to be incorporated in the basic atomic physics models for opacity. Shown Fig. is a typical plot of temperature dependence of Rosseland opacity for aluminum and its comparison with research results reported in a LLNL publication.

Using opacity databases, we have also developed 2-D codes for modeling ICF hohlraum physics. Fig. shows the temperature-time profile in a hohlraum driven by laser beams and its comparison with experiment. As seen from Fig., improvements in several details of physics packages for opacity are needed. These developments together with applications to indirectly driven ICF experiments are our plans for immediate future.

Vinod Kumar, S.V.G. Menon, BARC/ThPD/570/2003

M.K. Srivastava, Vinod Kumar and S.V.G. Menon, BARC/2001/I/023

M.K.Srivastava, Vinod Kumar, and S.V.G. Menon, Phys. Plasmas, 7 (2000) 2616



## 8. ASTRONOMY AND ASTROPHYSICS

### INTRODUCTION

Research activities in astronomy and astrophysics at BARC are aimed at understanding the non-thermal processes in the Universe using Very High Energy gamma-ray astronomy as a diagnostic tool. These activities are also intimately connected with the quest to unveil the sources of high energy cosmic radiation and understand the processes which enable charged particles to be accelerated to energies of upto 1020 eV and beyond. The fact that a significant fraction of the energy density of the Universe is contained in the non-thermal component illustrates the astonishing efficiency of such Cosmic accelerators as well as the importance of this component in the evolution of the Universe.

## 8.1 VHE ASTRONOMY AND ASTROPHYSICS

Research activities in Very High Energy gamma ray astronomy (VHE  $\geq 10^{12}$  eV), which were pursued at the High Altitude Research Laboratory, Gulmarg (34.1°N, 74.2°E, 2743 m asl), using the 6 element first generation atmospheric Cerenkov telescope have been consolidated with the setting up of the country's first imaging gamma ray telescope **TACTIC** (TeV Atmospheric Cerenkov Telescope with Imaging Camera) at Mt. Abu (24.6°N, 72.7°E, 1400m asl). The imaging element and the indigenously developed signal processing unit are shown in figure. The TACTIC imaging element deploys a 9.5 m<sup>2</sup> tracking light collector for collecting the Cerenkov photons produced following the interaction of cosmic VHE gamma rays with the Earth's atmosphere. The indigenously developed telescope which deploys a 349 pixel photomultiplier tube based camera with a pixel resolution of 0.31° uses a number of novel concepts like programmable topological trigger generation, single channel rate stabilization and multi-processor distributed data acquisition. Operating at an energy threshold of about 1 TeV, it has successfully detected gamma ray flaring activity



TACTIC imaging element

from two extragalactic sources Mkn 421 and Mkn 501. The telescope has also picked up steady gamma ray emission from the Crab Nebula with a statistical significance of  $> 11\sigma$  in 104 hours of on-source observations. The energy spectrum of the Nebula in the 1-16 TeV energy range derived from this data collected during the 2003-04 observation season matches very well the spectra determined by the other telescopes. Three additional Cerenkov telescopes have also been deployed in a triangular configuration of 20m side around the imaging element for studying the local intensity fluctuations in the Cerenkov light pools produced by  $\gamma$ -rays and hadrons. These elements which deploy 16 pixel cameras of 0.9° resolution have a potential of improving the sensitivity of the telescope for gamma ray detection.



Indigenously developed signal processing instrumentation of the TACTIC telescope.

## 8.2 GeV ASTRONOMY AND ASTROPHYSICS

As part of the worldwide efforts to open up the hitherto unexplored gamma ray window of 10-100 GeV (1GeV=10<sup>9</sup>eV) energy range, the centre has embarked on an ambitious programme for setting up a 21m aperture gamma ray telescope at the high altitude astronomical site at Hanle (32.7°N, 78°.9°E, 4200m asl) in the Ladakh region of North India. This state-of-the-art telescope **MACE** (Major Atmospheric Cerenkov Experiment) will deploy a 832 pixel photomultiplier tube based imaging camera with a pixel resolution of 0.1°. The advantage offered by the high altitude is equivalent to increasing the light collector area by a factor of about 2.5, however, a number of technical challenges posed by the large size of the telescope

and the low temperature desert conditions at Hanle have to be overcome. The preliminary simulation studies of the telescope suggest an on-axis gamma ray energy threshold of less than 20 GeV. When operational by 2010 the MACE telescope is likely to be the highest altitude and lowest energy threshold telescope in the world. With an energy range overlapping with the next generation satellite experiments being presently developed, the telescope will play an important role in enhancing our understanding of the high energy processes in the Universe.

### 8.3 LOW ENERGY COSMIC RAY NEUTRON MONITOR

At the Gulmarg Observatory a 21 detectors low energy cosmic ray Neutron Monitor (NM) is being operated continuously to study the variation of the low energy cosmic neutron background in the atmosphere. A major Forbush decrease of about 16% detected on 29.10.2003 was correlated to one of the largest solar flares in recent times of class X17.2. In addition to recording all the features of the decrease as monitored by the world-wide network of NM, important neutron multiplicity data during the course of this event has also been recorded by the Gulmarg NM. The fully automated NM also has a provision of monitoring neutrons produced in atmospheric lightning discharges. The NM is presently being upgraded and like other such experiments operating round the globe its data will also be available on the Internet soon.

### 8.4 THEORETICAL ASTROPHYSICS

Theoretical astrophysics studies has been conducted for understanding some interesting satellite observations on Active Galactic Nuclei (AGN) and X-ray binary systems involving a Neutron Star or a Black Hole as the primary component. Recent observations by the Chandra X-ray satellite have shown that radio/optical knots usually found in kilo-parsec scale jets of AGNs also emit X-rays. A typical knot has been modeled as an expanding spherical plasma cloud fed continuously by a non-thermal electron population and the spectrum of the radiation emitted from the knots as also the time dependent electron distribution in them has been calculated. The broad band spectral

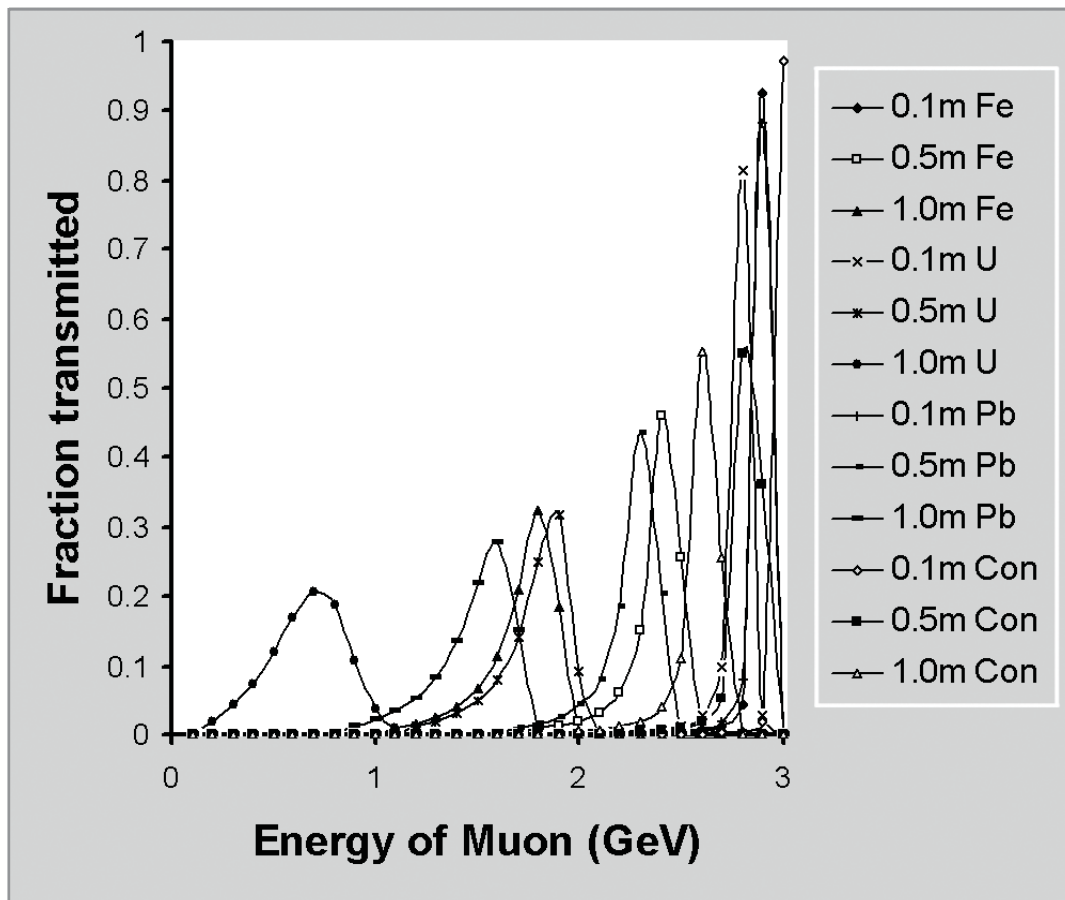
features are fairly well reproduced in our model, however, additional data on these sources will be required to fully validate the model. Our work also predicts the presence of a broad spectral feature around 1-10 MeV in the radiation spectrum of Black Hole X-ray Binaries which may be observed by future sensitive satellite experiments.

### 8.5 SCATTERING OF COSMIC MUONS TRANSMITTED THROUGH SLABS OF CONCRETE, IRON, LEAD AND URANIUM

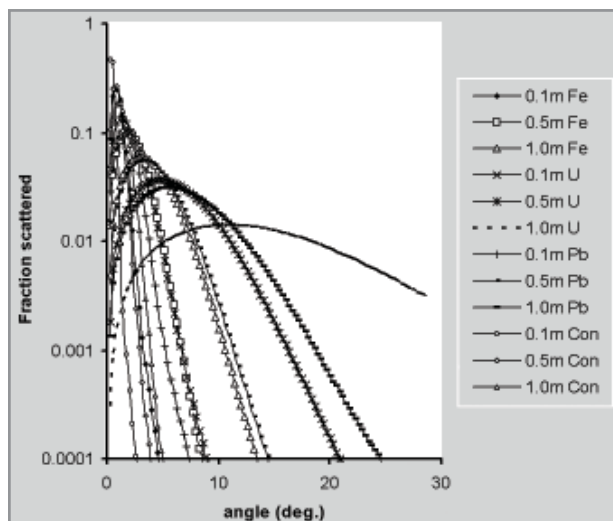
In a recently developed technique cosmic ray muons are used for image reconstruction and material Z discrimination. Experimental results and theoretical simulations have demonstrated the ability to reconstruct complex objects and to detect materials of high atomic number hidden in a much larger volume of low atomic number using cosmic ray muons. This method is anticipated to be very useful in surveillance for cross-border transport of nuclear and other heavy materials.

In order to facilitate this study we have carried out Monte Carlo simulations using Muon Simulation Code (MUSIC) to estimate the energy and angular distribution of transmitted muons through slabs of different materials. Muons of different energies in the range 0.5 GeV to 5 GeV incident normally on the slabs have been considered. The processes of muon interaction with matter, such as bremsstrahlung, pair production and inelastic scattering are treated as stochastic processes for muon energy loss  $>1$  MeV. Ionisation and knock-on electron production are simulated using Landau distribution. The angular deviation and lateral displacement of muons due to multiple scattering, as well as bremsstrahlung, pair production and inelastic scattering are taken into account. Scattering of muons due to inelastic scattering was treated using the double differential cross-section.

The calculated results of differential energy distribution of 3 GeV normally incident muons transmitted through slabs of concrete, iron, lead and uranium of 10 cm, 50 cm and 100 cm thickness are presented in left Fig. and the angular distribution of these transmitted muons.



Energy distribution of 3 GeV muons transmitted through slabs of different materials.



Angular distribution of 3 GeV muons transmitted through slabs of different materials

The angular distribution was fitted with an empirical distribution. A correlation between the peak positions of the angular distribution and energy distribution is established.

M. Sengupta-Mitra, P.K. Sarkar and V.A. Kudryavtsev, Proc. DAE Nuclear Phys. Symp. 47B (2004).



## 9. INSTRUMENTATION IN PHYSICAL SCIENCES

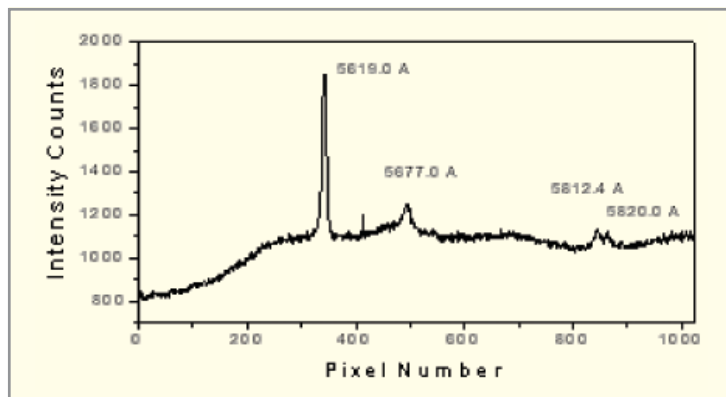
### INTRODUCTION

Development of dedicated instruments meeting stringent requirements of research in physical sciences and needs of Department of Atomic Energy has been an integral part of developmental activities at BARC. Recent developments of multi-channel Raman spectrometer for analysis of microparticles, scanning monochromator for isotopic analysis and electron spectrometers meet some of the increasing demands for improved analysis of materials. An optical periscope has been specially designed for video recording of objects with a resolution of 0.7 mm in the core of Fast Breeder Test Reactor. Instruments for sensing of toxic gases are being developed and a notable development is room temperature operating sensors based on Te and conducting polymer thin films.

## 9.1 DESIGN & DEVELOPMENT OF A MULTICHANNEL SPECTROGRAPH USING CCD AS A DETECTOR

We have designed and developed a multichannel spectrograph to study the Raman spectra of micro samples of materials which may be inorganic or organic in nature. In this kind of study, micro-particles of the sample are irradiated by an intense monochromatic beam of laser light. The light scattered by micro particles consists of the unshifted Rayleigh components as well as the Raman components shifted in frequency from the excitation line. Since the Raman-scattered light is very weak as compared to Rayleigh-scattered light, the instrument developed by us has high light collection efficiency.

The spectrograph is based on Czerny-Turner type of optical configuration having a plane grating of frequency 1200 grooves/mm as a dispersing element, concave spherical mirror of focal length 0.523 m as a collimating element and a concave spherical mirror of focal length 0.5 m as a focusing element. The reciprocal linear dispersion of the spectrograph varies in the range of 14.32 Å/mm to 15.27 Å/mm over the spectral range of 454 nm to 657 nm on the image plane. The image plane consists of C.C.D. array of pixels 1024 x 256. The pixel size



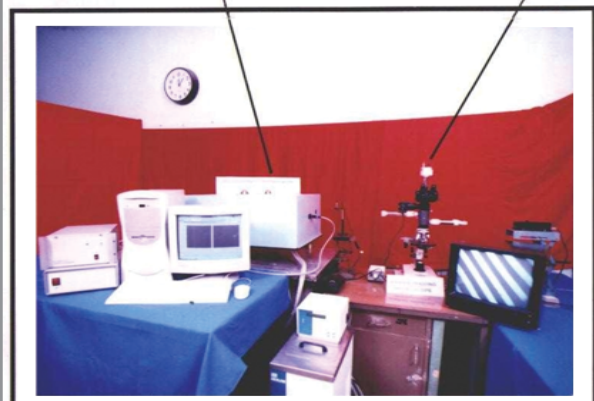
Benzene spectrum recorded in the multichannel spectrograph using CCD as a detector

is 26 x 26 micron. A spectrum of band 400 Å in one span can be recorded by the C.C.D. coupled with a PC-based data acquisition and image processing system. A sine drive assembly has been incorporated for linearizing the wavelength scale. The instrument covers a wavelength range of 4000 Å to 7000 Å. The practical value of the resolution is 1.5 Å. Raman spectrum is recorded on the C.C.D. camera by illuminating the material with an intense beam of a diode pumped green laser ( $\lambda = 532$  nm) of power of 200 mW. It is absolutely essential to introduce a notch filter before the entrance slit for blocking the entry of Rayleigh scattered light of wavelength  $\lambda = 532$  nm into spectrograph and admitting only Raman scattered light into the spectrograph. The notch filter has been developed indigenously by depositing alternate layers of  $\text{TiO}_2$  and  $\text{SiO}_2$  on the glass substrate using a non-quarter wave coating design. Following figures show the photograph of the instrument and Raman spectrum of benzene recorded using the spectrograph.

R.P. Shukla, Sanjiva Kumar, A.K. Sinha, Manika Mallick, S. Thakur, N.K. Sahoo and N.C. Das, *Journal of Optics* 33, No. 2, Page 87 – 107 (2004)

### Multichannel Spectrograph

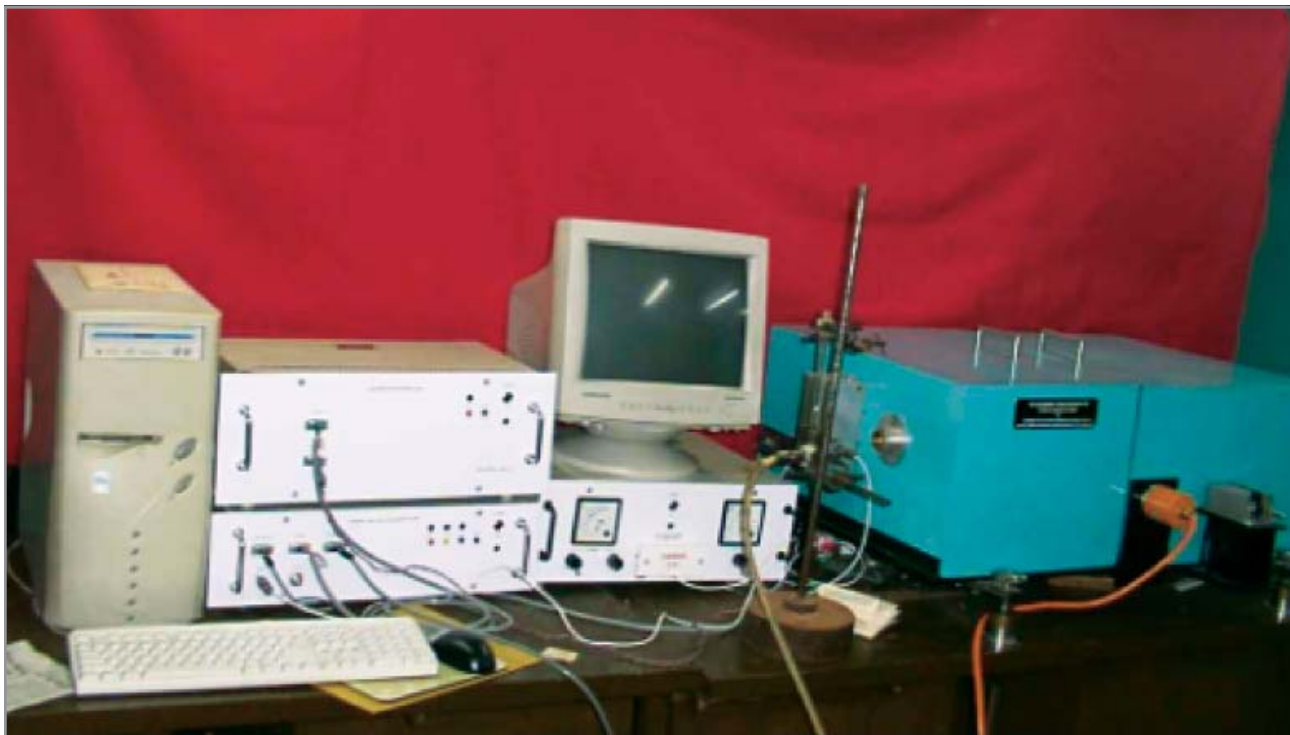
### Raman Imaging Microscope



Photograph of the Multichannel Spectrograph Coupled with the Raman Imaging Microscope

## 9.2 SCANNING MONOCHROMATORS (0.5 m) FOR ISOTOPIC ANALYSIS OF MOLECULES SUCH AS $^{15}\text{N}$ - $^{14}\text{N}$ IN NITROGEN GAS

A 0.5 m Czerny-Turner scanning monochromator has been designed and developed indigenously for isotopic analysis



Photograph of the complete system for isotopic analysis using the monochromator

of gas molecules such as nitrogen (Fig.). The monochromator uses a plane holographic grating of groove density of 2400 lines/mm for wavelength dispersion and has a wavelength range of 2000-5000 Å. The wavelength resolution of the monochromator is 0.4 Å using a minimum slit width of 50 µm. Scanning of the wavelength is done by rotating the grating using a stepper motor. A sine drive mechanism is used for linearizing the wavelength scale. For the quantitative determination of percentage concentration of  $^{15}\text{N}$  in the sample of nitrogen gas, the (2-0) band of the second positive ( $\text{C}^3\Pi_u - \text{B}^3\Pi_g$ ) system has been chosen since the band heads corresponding to the isotopic species  $^{14}\text{N}^{14}\text{N}$  and  $^{15}\text{N}^{14}\text{N}$  have a isotopic shift of 6.1 Å. The abundance of  $^{15}\text{N}$  isotope in air as calculated from the intensities of the bands is 0.35 %.

R. P. Shukla, D.V. Udupa, Manika Mallick, Sanjay Somkuwar, B. J. Shetty, A.K. Sinha and V.C. Sahni, BARC Newsletter, (July 2005)

### 9.3 NUCLEAR OPTICAL INSTRUMENT

An optical periscope, shown in Fig., has been designed and fabricated indigenously for viewing / photography and video recording the objects in the core of Fast Breeder Test Reactor (FBTR). The periscope consists of a scanning prism mechanism, zoom lens objective, a system of relay lenses and an eyepiece sub-assembly for viewing the objects. The objective of the periscope is a zoom lens system for obtaining a continuously varying magnification from 2X to 5X. Zoom lens objective system has a variable focal length from 100 mm to 250 mm with an aperture varying from 10 mm to 25 mm respectively. This covers a semi-field angle of  $3^\circ$  for the objective lens of focal length of 250 mm and  $4^\circ$  for the objective of focal length of 100 mm. Two prisms of  $45^\circ\text{-}90^\circ\text{-}45^\circ$  types are used for scanning the object space in vertical direction. One prism is fixed, whereas the prism facing the object can be rotated about the horizontal axis through an angle of  $110^\circ$ . The rotation of the entire periscope assembly along the vertical axis scans the object space on the horizontal plane. The combination of these two rotations is used to scan the field of interest. Linear resolution of the instrument is 0.7 mm.

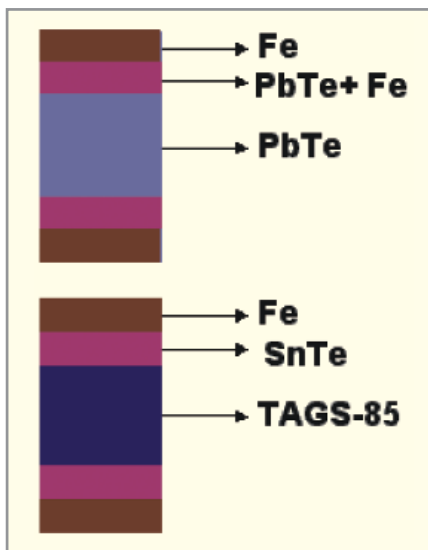


A periscope 5.3 meter in length fabricated for remote controlled Fast Breeder Test reactor (FBTR). Lenses  $L_{1A}$ ,  $L_{1B}$  and  $L_{1C}$  form the zoom lens objective of the periscope.

N.C. Das, Sanjiva Kumar, D.V. Udupa, R.P. Shukla, A.M. Kadu and R.K. Modi,  
Report No. : BARC/2004-E-17

#### 9.4 DEVELOPMENT OF THERMOELECTRIC GENERATORS

The development of thermoelectric generators has been taken up for generation of electricity from Compact High



Schematic diagram of PbTe and TAGS-85 alloy thermoelements.

Temperature Reactor (CHTR). For this purpose, n-type PbTe and p-type  $(AgSbTe_{2/0.15})(GeTe)_{0.85}$  (TAGS-85) alloys has been prepared. The room temperature electrical conductivities ( $\sigma$ ) and the thermo-emfs ( $S$ ) of these materials were in the range of 1000-1600 mho  $cm^{-1}$  and 150- 200  $\mu V/K$ , respectively.

Low resistivity contacts with iron at both ends have been fabricated by vacuum hot pressing. To overcome the problem of thermal expansion mismatch between the thermoelectric alloy and the iron, intermediate layers of PbTe+Fe for the n-type PbTe and SnTe for the p-type TAGS-85 were used. Device modules consisting of a pair of



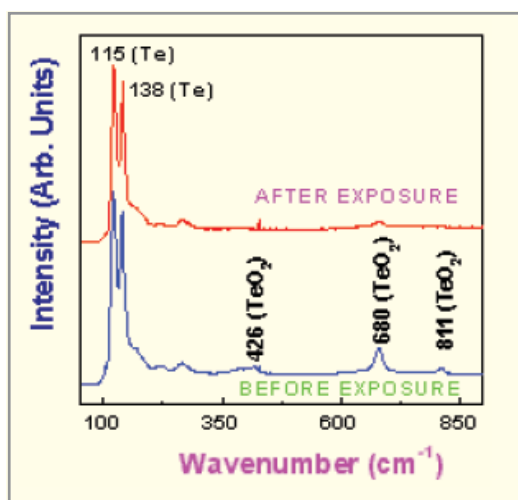
A device consisting of a pair of thermo-elements with a power output of 750 mW.

thermo-elements were fabricated using silver strips for contacts. For a temperature difference of 300 °C, the device produced an electrical power of ~750 mW with voltage of ~30 mV and current of 25 Amp.

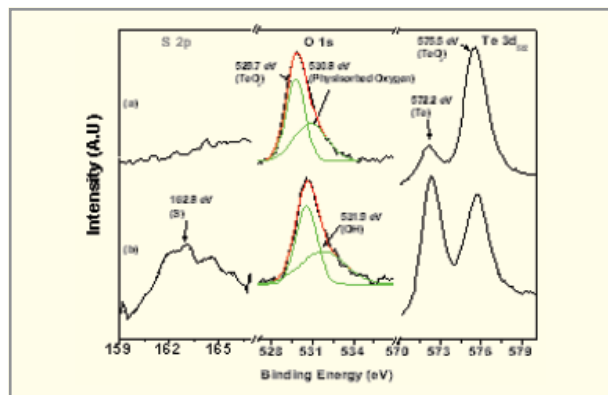
Ajay Singh, C. Thinaharan, S. Bhattacharya, P. Sengupta, K. Bhanumurthy, D.K. Aswal and S.K. Gupta, DAE-Solid State Physics Symp. 2004.

## 9.5 ROOM TEMPERATURE OPERATING GAS SENSORS

Room temperature operating sensors for reducing ( $H_2S$  and  $NH_3$ ) and oxidizing ( $NO_2$ ) gases have been developed using vacuum evaporated Te thin films. Gas sensing mechanism of these films was investigated by XPS, Raman and impedance spectroscopy techniques ( Figs.). On interaction with reducing gases, adsorbed oxygen on the surface on Tellurium films was removed and the change in resistance was mainly contributed by intra-grain region of the films. Based on these results, we propose the following detection mechanism. Te is known to be a lone pair (p-type) semiconductor, where lone pair electrons form the upper part of the valence band. Oxygen atoms adsorbed on the surface act as acceptors and traps lone pair electrons, leading to an increase in carrier concentration and conductivity in the intra-grain region. On removal of adsorbed oxygen, hole density decreases, thereby



Raman spectra of Tellurium thin films before and after exposure to  $H_2S$  gas. Peaks corresponding to  $TeO_2$  are reduced on exposure to  $H_2S$ .



XPS spectra of Te films before and after exposure to  $H_2S$  gas in the S-2p, O-1s and Te-3d region.  $H_2S$  exposure leads to reduction in adsorbed oxygen.

increasing the resistivity of the films. Decrease in film resistance on exposure to oxidizing gases is similarly explained.

Shashwati Sen, K. P. Muthe, Niraj Joshi, S. C. Gadkari, S. K. Gupta, Jagannath, M. Roy, S. K. Deshpande and J. V. Yakmi, Sensors & Actuators B 98 (2004) 154.

Manmeet Kaur, S. K. Gupta, C. A. Betty, Vibha Saxena, V. R. Katti, S. C. Gadkari, and J. V. Yakhmi, Sensors & Actuators, B 107 (2005) 360.

## 9.6 CONDUCTING POLYMERS BASED SENSORS AND ACTUATORS

A reversible change in the chemical, physical and/or mechanical properties of conducting polymers in response to a given stimulation can be explored in sensors as well as low power electromechanical actuators. We have developed Ammonia gas sensors, uric acid biosensor and actuators using polycarbazole, polyaniline and polypyrrole (PPy) films respectively.

Polycarbazole thin films for ammonia sensors were prepared by LB technique using a mixture of dimethylsulfoxide (DMSO) and chloroform as spreading solution. The ammonia sensors based on these films operated at room temperature showed linear response to ammonia in 0-200 ppm range.

For the development of actuator, free-standing films of polypyrrole doped with dodecyl benzene sulfonate (PPy-DBS)



Photographs of actuator action, (a) before application of voltage and on application of (b) +2 V and (c) -2V voltage.

were prepared by galvano-static electrochemical polymerization of pyrrole. One side of the films was coated with thin gold layer. The actuators were tested in a 1 M LiClO<sub>4</sub> aqueous solution by passing current between the actuator strip and SS wire as counter electrode. The bending movement of about 90° on both sides was observed on application of positive and negative voltages.

Vibha Saxena, Sipra Choudhury, S. C. Gadkari, S. K. Gupta and J. V. Yakhmi, *Sensors & Actuators B* 107(2005) 277.

### 9.7 HIGH RESOLUTION ELECTRON SPECTROMETER

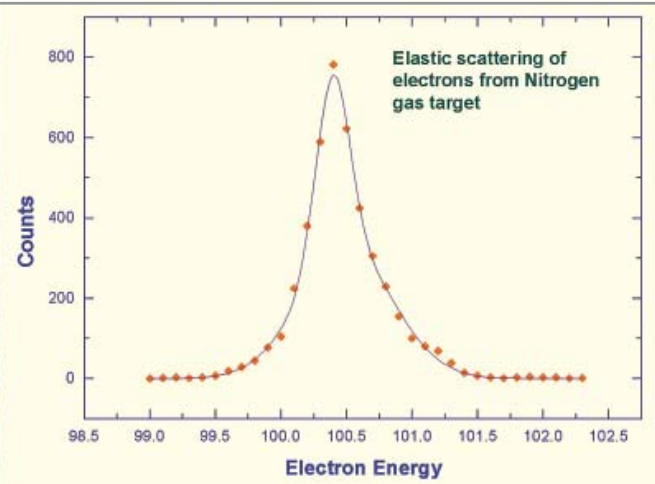
Electron–molecule collision reactions form the primary basis for a stable plasma state, which is the core process in many natural phenomena such as fusion, planetary atmospheres, inter-stellar physics and magneto-hydrodynamic reactions.

An electron–molecule collision spectrometer has been setup to measure differential cross sections of various molecules. It has an electron gun, two identical hemispherical energy analyzers, a Faraday cup and a gas inlet system. The electron gun fitted with thoria-coated tungsten cartridge filament that produces a nearly mono-energetic beam of electrons over a broad energy range (10 eV – 1500 eV) and currents upto 10 μA. The hemispherical analyzers coupled with 5-element electrostatic zoom lenses are mounted on rotary turntables and image the scattering volume. The outgoing electrons arising out of a scattering reaction are analyzed for both energy and momenta. A channeltron detector is used to detect the analyzed electrons. The entire spectrometer is kept in a vacuum chamber, pumped by a 500 l/s turbomolecular pump giving a residual pressure of about 5 x 10<sup>-8</sup> Torr.

The detection electronics is based on fast pre-amplifiers coupled to the channeltron detectors. Finally, the accumulated data is displayed online as a spectrum containing the energy of the incident electrons and number of counts accumulated from the scattering reaction.



High Resolution Electron-Optic Spectrometer and test spectrum recorded for  $N_2$ . The FWHM is  $\sim 0.5$  eV.



K.G. Bhushan, K.C. Rao, S.C. Gadkari, Asian J Phys. (under publication).

cathode, which enhances the pumping by inducing the production of larger numbers of energetic neutral getter atoms. This also results in obtaining higher pumping speed for inert gases like argon and helium.

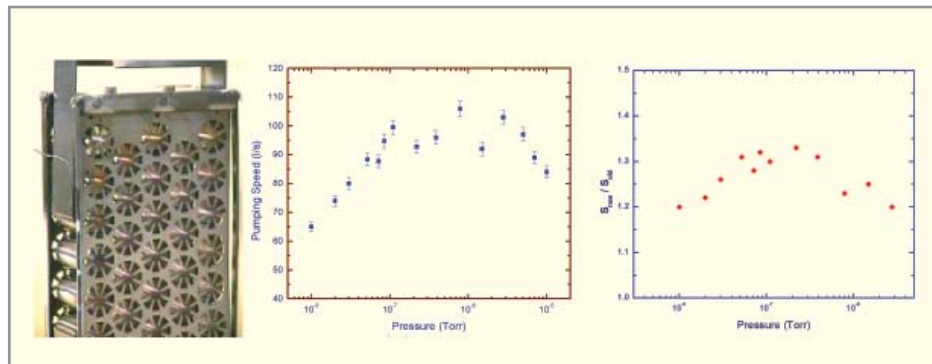
## 9.8 NEW ELECTRODE DESIGN FOR TRIODE SPUTTER ION PUMP

High-energy particle accelerators, synchrotron radiation sources, surface analytical instrumentation systems etc., require ultra-high vacuum conditions, they also require good pumping characteristics for non-getterable gases (i.e., Ar, He,  $CH_4$ ).

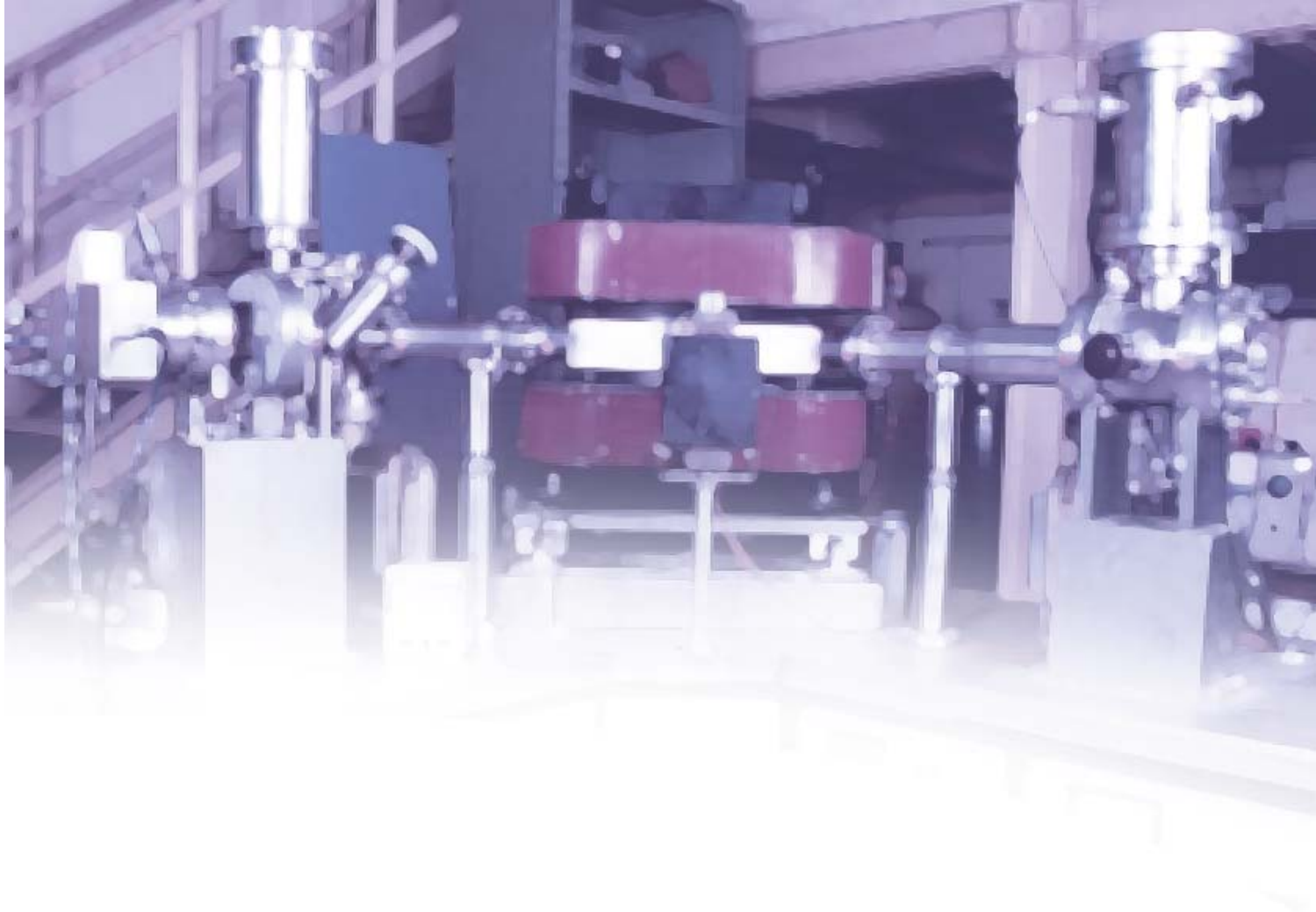
The pumping speed was measured for the new pumping element with Nitrogen gas. The modified element demonstrates a remarkable trend at high pressures indicating high throughput capacity. Results compared with standard SIP element for nitrogen gas show a 30% increase in the pumping speed.

Higher pumping speed for non-getterable gases and hydrogen is usually obtained by using a combination of pumps, like TSIP and sublimation pump or turbomolecular pump and cryo-pump. A new pumping element has been developed for the triode sputter ion pump based on electromagnetic field simulations of a penning cell. The new element gives a higher pumping speed for the same volume as compared to the standard element based on titanium strips. This is attributed to the different geometrical structure of the

K.G. Bhushan, S.C. Gadkari and J.V. Yakhmi, IVS Bulletin 7 (4) (2004) 3.



The new electrode element and the plots showing the pumping speeds of the newly developed TSIP and its comparison with an earlier pump.



## 10. MASS SPECTROMETRY

### INTRODUCTION

Mass Spectrometry is a crucial analytical tool for a number of DAE programs that require isotopic ratio measurements of samples of hydrogen, lithium, boron, uranium, plutonium etc. Moreover, monitoring of deuterium, lithium-6 and uranium-235 in various enrichment processes as well as determining the overall tritium and plutonium produced in nuclear reactors are extremely important for DAE. Realizing the importance of mass spectrometric techniques in nuclear areas, BARC, since its inception in 1954, took up the development of technologies towards the underlying instrumentation programme in a major way.

BARC has developed expertise in areas like HV/UHV technology, precision mechanical engineering and fabrication, magnet technology, ion optics, sensitive and stable analog and digital electronics, data systems that are important to develop sophisticated mass spectrometers. These include the Isotopic Ratio Mass Spectrometers (IRMS) for (a) isotopic ratio measurements for hydrogen, lithium, boron, nitrogen, potassium, rubidium/strontium, uranium, and plutonium, (b) Inductively Coupled Plasma source Mass Spectrometer (ICPMS) for elemental analysis, (c) Quadrupole Mass Spectrometer (QMS), and (d) double focusing mass spectrometer with a resolving power of about 6000. The chapter also deals with the recent development of state-of-the-art instrument based on time-of-flight and electrostatic ion-trap mass spectrometry.



The process gas mass spectrometer

### 10.1 MASS SPECTROMETERS FOR RMP, MYSORE

Process Gas mass spectrometers are used at RMP, Mysore to measure the isotopic abundance of masses 329, 330 and 333 (isotopes of UF<sub>5</sub> corresponding to Uranium 234, 235 and 238) in natural, enriched and depleted UF<sub>6</sub> samples and also to measure precisely the isotopic ratios of mass 330 and mass 333. The fabrication and testing of fourth such mass spectrometer PGMS-4 has been completed, delivered, installed and commissioned at RMP, Mysore.

In addition to this, new and upgraded electronics for earlier two mass spectrometers has been designed, fabricated, tested and delivered to RMP, Mysore.

M.M. Gulhane, R. Datta, T.K. Saha, C.K. Nazare, K. Joshi, B. Reddy and V.K. Handu, ISMAS, Silver Jubilee Symposium on Mass Spectroscopy, (2003).

R.B. Ingole, M.M. Gulhane, Kuldeep Joshi, Rabi Datta, T.K.Saha, C.K. Nazare, V.K.Handu and V.C. Sahni, ISMAS, Silver Jubilee Symposium on Mass Spectroscopy, (2003).

### 10.2 THERMAL IONIZATION MASS SPECTROMETER TIMS

TIMS-type mass spectrometers are frequently used to determine the isotopic abundances of Li, B, U and Pu isotopes in solid samples. Two such mass spectrometers were delivered earlier to Chemical Engineering Division for Li and B isotopic analysis while three similar instruments, but with different geometry, have been delivered to RMP Mysore (TIMS-1), AFFF Tarapur (TIMS-2), and KARP Kalpakkam (TIMS-3). TIMS-1 at RMP, Mysore has been upgraded recently for better sensitivity and precision.

Recently, design and fabrication of an advanced version of TIMS mass spectrometer for U and Pu analysis was undertaken. Design and fabrication work of different parts and associated electronics have been completed and assembly is in progress.



Thermal Ionization Mass Spectrometer

S.N. Bindal, K.V. Kurup, K.A. Sayed, R.G. Ochani, A.R. Parkar, V.B. Reddy, P. Raju, T.K. Saha, N.V. Rao, V.K. Handu, S.R. Halbe and V.V.K. Rama Rao, 8th National Symposium on Mass Spectrometry, (1999)

P.Abhichadani, et. al 8<sup>th</sup> National Symposium on Mass Spectrometry, IICT Hyderabad (1999)

### 10.3 QUADRUPOLE MASS SPECTROMETERS (QMS)

Development of QMS has been undertaken as an R & D effort owing to its applications in faster isotopic and elemental analysis. The source of ions can be either electron bombardment type ion source for gas sample analysis or an inductively coupled plasma ion source for trace element analysis. Over the last few months, quadrupole mass spectrometer, which analyzes masses up to 300 amu, has been successfully completed and tested. Analysis of samples like  $\text{CF}_2\text{HCL}$ , used for  $\text{C}_{13}$  enrichment, from L&PT Division has been successfully carried out. We have also been able to

resolve  $\text{O}_{16}$  and  $\text{O}_{18}$  isotopes in  $\text{CO}_2$  gas and measure the abundance of  $\text{O}_{18}$ .

Recently, further improvements have been carried out on this QMS. The imported RF and DC supplies have been replaced by in-house developed supplies.

The imported QMA & its power supply used in the in-house developed Inductively Coupled Plasma Ion Source Mass Spectrometer (ICPMS) has also been replaced by in-house developed QMS. This ICP-MS has reached a sensitivity level of 1 ppb.

A collaborative programme has also been taken up with CCCM, Hyderabad for the development of RIMS for rare isotope analysis. Design and fabrication of a new quadrupole mass spectrometer has been taken up for this application. All the fabricated parts have been received and assembly and testing have been initiated.



P. Maithi, S.K. Sarkar, V. Parthasarthy, V. Natraju, K.A. Jadhav and V.K. Handu, BARC Report (2204)/E/006.

M.Pande, M.Gulhane, V.Natraju, D.Ramanathan, V.K.Handu, M.K.V.Rao and V.C.Sahni, National Symposium on Electromagnetic compatibility, EMC-2000, Chennai (2001)

has been undertaken. Design of such a system has been completed and required components are procured and assembly of the same is undertaken.

#### 10.4 MASS SPECTROMETERS FOR HEAVY WATER ANALYSIS

More than twelve mass spectrometers for D/H analysis have been fabricated and installed at various DAE units. This equipment is frequently used for testing of distillation column used for heavy water up-gradation, performance testing of catalyst used for hydrogen water exchange and other R & D activities in the Heavy Water Division.

This mass spectrometer gives a precision of about 2 ppm at natural level (153 ppm) in the isotopic ratio measurement of mass3 and mass2 dispersed ion beams. To improve this, development of a new and automated sample inlet system



Mass Spectrometer for heavy water analysis

M.S. Murthy, B.S. Prahallad Rao, V.K. Handu and J.V. Satam, BARC Report 1026.

### 10.5 MASS SPECTROMETERS FOR HEAVY WATER BOARD

Development of TIMS, QMS, and ICP mass spectrometers has been undertaken for the Heavy Water Board. TIMS mass spectrometer, with a twin ion source for solid and gaseous samples is being developed for analyzing Boron 10 / 11 in the form of sodium metaborate as well as Oxygen 16 / 18 in the form of carbon dioxide gas respectively. QMS mass spectrometer is being developed for Oxygen 16 / 18 in the form of Carbon dioxide gas and ICP mass spectrometer is being developed to analyze Boron 10 / 11 as well as trace impurities present in Boric Acid, Boron Metal and Boron Carbide.

Components required for these mass spectrometers have been procured. Fabrication of various sub-systems has been completed. Assembly of these sub-systems has been initiated.

### 10.6 INDIGENOUSLY DEVELOPED MATRIX ASSISTED LASER DESORPTION TIME OF FLIGHT MASS SPECTROMETRY (MALDI-TOFMS)

Recently, matrix-assisted laser desorption/ionization time-of-flight mass spectrometry (MALDI-TOFMS) has been widely used as an analytical tool for biological research. This technique generates intact biomolecular ions without fragmentation whose molecular weight can be precisely determined by a time-of-flight mass spectrometer. This technique has found wide application in various fields such as proteomics, genomics, drug synthesis etc. We have indigenously designed, fabricated and tested MALDI-TOFMS for biological research as shown in Figure. This spectrometer consists of an octagonal interaction chamber and a linear time of flight mass spectrometer. Biomolecules are co-crystallized in an organic matrix and deposited on a sample holder. A nitrogen laser of 337.1 nm wavelength was used to desorb / ionize the biomolecules. The biomolecular ions generated are mass analyzed by a time-of-flight mass spectrometer and the signal is detected through secondary electron multiplier. The detector output is monitored on an oscilloscope and is interfaced with a computer for further processing. Initial testing was carried out with organic

matrices such as dihydroxybenzoic acid (DHB), sinapinic acid and nicotinic acid for mass spectrum. Subsequently, MALDI experiments were performed with various proteins such as lysozyme, cytochrome-C, substance-P, insulin, angiotensin in different matrices. We could detect few femto moles of the analyte molecules of molecular weight ranging from 1Da to 100 KDa. This project work is in progress and experiments are currently on for improving the sensitivity and the resolution of the spectrometer.



Matrix assisted laser desorption ionization time of flight mass spectrometer.

M. A. N. Razvi, BARC Report (2005)

### 10.7 ELECTROSTATIC ION TRAP

An ion trap has been designed which traps ions using purely electrostatic fields. The ion trap works like an optical resonator. Two electrostatic ion mirrors are placed collinearly and ions are injected into the trap (Fig.). During injection the voltages on the entrance mirror are reduced to zero and the exit mirror acts like a reflector with a focusing effect. As the ions get reflected from the exit mirror, the voltages on the entrance mirror are switched ON fast enough so that the ions are now trapped between two reflecting mirrors.



Details of Ion Trap



Beamline connected to Electrostatic Ion Trap

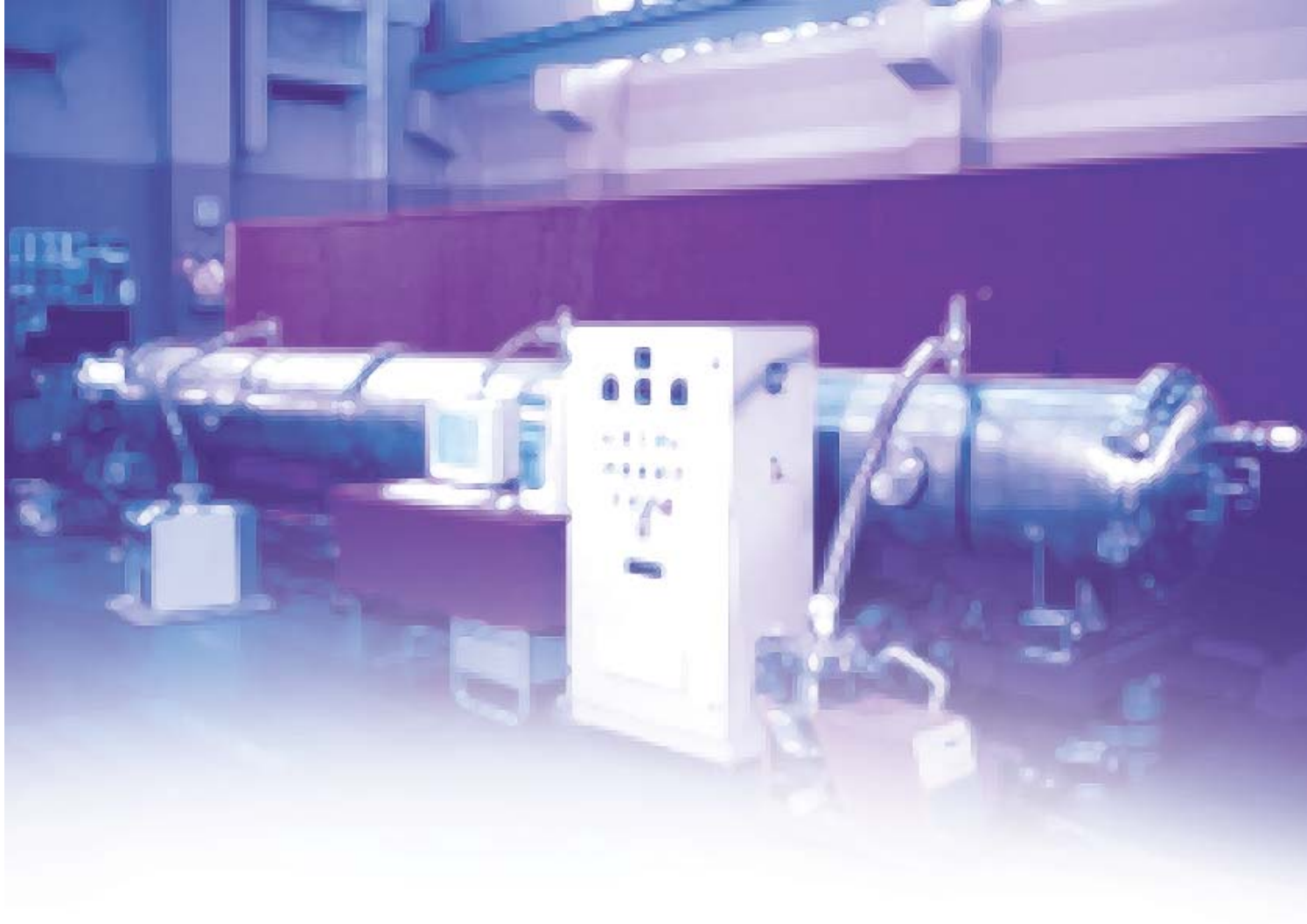
Ions that are trapped in the ion trap can be detected by an image charge detection setup. The motion of the ions inside the trap can then be analyzed by performing Fast Fourier Transform operation on the oscillatory signal from the image charge detector. The resulting frequency spectrum is a direct indication of the mass of the ions trapped in the ion trap. It can be seen that the larger the number of oscillations analyzed, the higher will be mass resolution.

#### 10.8 HIGH RESOLUTION REFLECTRON TIME-OF-FLIGHT MASS SPECTROMETER

The spectrometer consists of a broad high current (mA) ion source (Kauffmann type) that works on the principle of magnetron wherein the electrons are trapped in a specific volume within a steady magnetic field effecting multiple collision ionization of gaseous and/or low vapor pressure liquid/solid samples. The ions in the plasma within the volume are then extracted by applying opposite potentials and then channeled into the special ion optics to accelerate them perpendicularly into the drift space and subsequently to the reflectron through a symmetric lens system.

The reflectron has a gridless design. Ions are detected using a hybrid ion detector consisting of a combination





## 11. SYNCHROTRON BEAMLINE INSTRUMENTATION

### INTRODUCTION

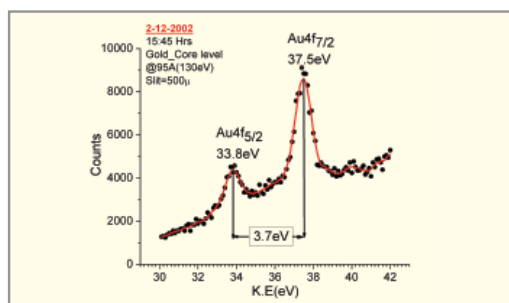
BARC has been involved in the development of various beamlines on synchrotron radiation sources at Raja Ramanna Center for Advanced Technology, Indore. This chapter describes development of some of these beamlines. The Photophysics beamline on INDUS-1 is operational since March 2003 and is meant for photoabsorption and fluorescence studies in the VUV (500–3000Å) range. The Angle Resolved PhotoElectron Spectroscopy (ARPES) beamline works in the 40–1000 Å range and has been used to study photo-emission spectroscopy for probing electronic states in atoms, molecules and solid surfaces. High resolution VUV beamline, commissioned in 2005, has been employed in high resolution studies in the range 700–2000 Å. The Photoabsorption Spectroscopy Study beamline is under installation process and it will be used for near-to-absorption edge (17–225 Å) spectrum analysis in terms of local electronic structure. PhotoElectron Spectroscopy (PES) beamline will use X-rays in the energy range from 0.8 keV to 15 keV. The heart of the beamline is a double crystal monochromator and its development has been largely an indigenous effort. An Extended X-ray Absorption Fine Structure (EXAFS) beam line for X-ray absorption studies using energy dispersive geometry is ready for installation. The energy range for this beamline will be 5-20 keV with a resolution of  $10^{-4}$  (bandwidth of 1 keV at 10keV).

### 11.1 ANGLE RESOLVED PHOTOELECTRON SPECTROSCOPY BEAMLINE AT INDUS-1

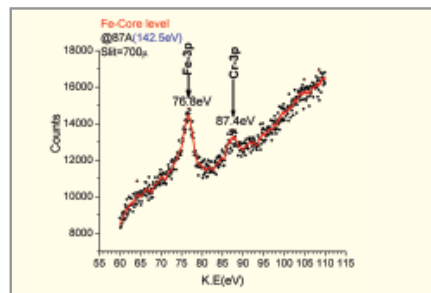
Photoemission spectroscopy is the most powerful technique to probe the state of electrons in atoms, molecules, solids and surfaces. In a photoemission process, an electron is excited from its ground state by the absorption of a photon for increasing its energy so that it can free itself from the system to which it is bound. Once in vacuum, this freed electron, called photoelectron, can be collected and analysed and its ground state properties can be retrieved from this analysis. Moreover, measurement of the angular distribution of photoelectrons from oriented crystals provides information on the wave vector of electron states. The technique, therefore, named as Angle Resolved PhotoElectron Spectroscopy (ARPES) is a unique tool to map the energy dispersion curves of electrons in solids. This beamline is being used to investigate the ground state, electronic states for valence electrons in chemisorbed or physisorbed atoms or molecules in the spectral region of  $40 \text{ \AA}^0$  to  $1000 \text{ \AA}^0$ . These states correspond to the chemical bond between adsorbed species and substrate and give the most direct picture of the chemisorption bonding process.



ARPES beamline at INDUS-1.



Core level photoelectron spectrum of gold



Photoelectron spectrum of stainless steel sample.

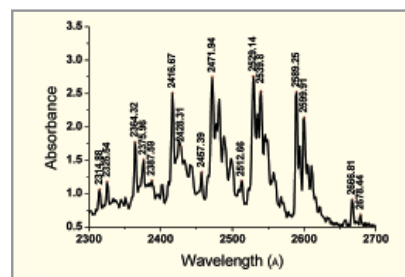
P. Pal, M.K. Dalai, B. R. Sekhar, S. N. Jha, S.V.N. Bhaskara Rao, N.C. Das C. Martin and f. Studer, J. Phys. :Condense Matter 17, 2993 (2005)

### 11.2 PHOTOPHYSICS BEAMLINE AT INDUS-1

The photophysics beamline is a medium resolution ( $1 \text{ \AA}$ ) beamline using Seya-Namioka Monochromator and operating in the VUV region of  $500 \text{ \AA}$  to  $2000 \text{ \AA}$ . Using this beamline a variety of atomic, molecular and condensed matter experiments will be carried out in the gas phase and



Seya-Namioka monochromator in photophysics beamline.



Absorption spectra of benzene at 50-mbar pressure.

solid state. In the gas phase, the experiments are being carried out for photoabsorption and photofragmentation spectroscopy of atomic and molecular species contained in an absorption cell.

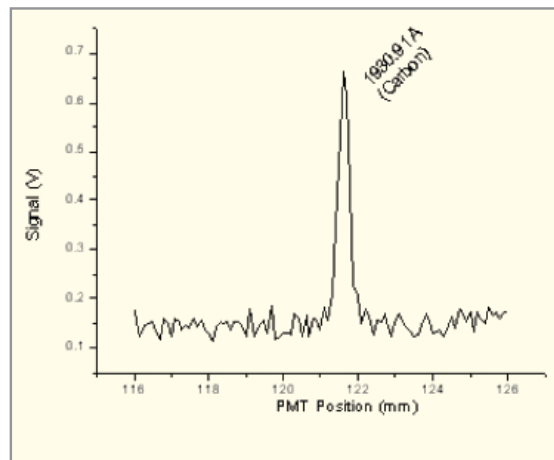
P. Sharma, R. K. Vatsa, B. N. Rajasekhar, N. C. Das, T.K. Ghanty and S. K. Kulshreshtha, Rapid Communications in Mass Spectrometry, Vol. 19, 1522 (2005)

### 11.3 HIGH RESOLUTION VUV BEAMLINE AT INDUS-1

The high-resolution VUV beamline has been designed and developed for recording high-resolution absorption spectra of atomic and molecular vapours using synchrotron beam from Indus-1 as an excitation source of electromagnetic radiation. The beamline consists of three gold-coated cylindrical focusing mirrors for collecting the radiation from the synchrotron and focusing it on the entrance slit of a 6.65 meter off-plane Eagle spectrometer. The absorption cell containing the sample to be studied is coupled between the entrance slit and the third focusing mirror. The spectrometer covers a spectral region of 700 Å – 2000 Å with an average spectral resolution of 0.01 Å. The photoabsorption spectra of atoms and molecules are used to make the following studies:



Photograph of the high resolution VUV spectrometer.



Vacuum UV line of carbon recorded through the spectrometer. The intensity profile is obtained by moving the exit slit and PMT assembly along the Rowland circle.

1. Accurate determination of absorption cross-sections of atoms and molecules which will in turn show the distribution of oscillator strength as a function of photon energy.
2. Determination of vibrational and rotational constants of molecules which will be used to construct potential curves and finding out the symmetry of excited states dissociation energy etc.
3. Observation of long Rydberg series to high principal quantum numbers which will help in the determination of accurate ionization potential and quantum defects.
4. The study of line profiles in the autoionizing range which will give useful information on interchanged interactions.

N. C. Das, R. P. Shukla, D. V. Udupa, N. K. Sahoo, D. Bhattacharyya, K. Sunanda, P. Saraswathy, Sampath Kumar, A. K. Sinha, S. Bhat and V. C. Sahni, Current Science 87, No. 11, 1523-1529 (2004)

#### 11.4 DEVELOPMENT OF A CRYSTAL BENDER FOR EXTENDED X-RAY ABSORPTION FINE STRUCTURE (EXAFS) BEAMLINE AT INDUS-II SYNCHROTRON SOURCE

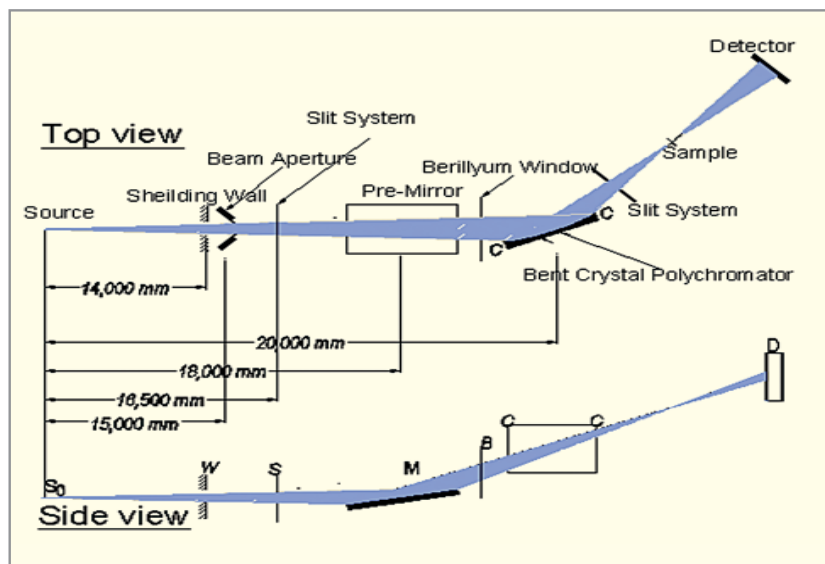
The proposed EXAFS beamline at INDUS-II would carry out the X-ray absorption measurements in energy dispersive



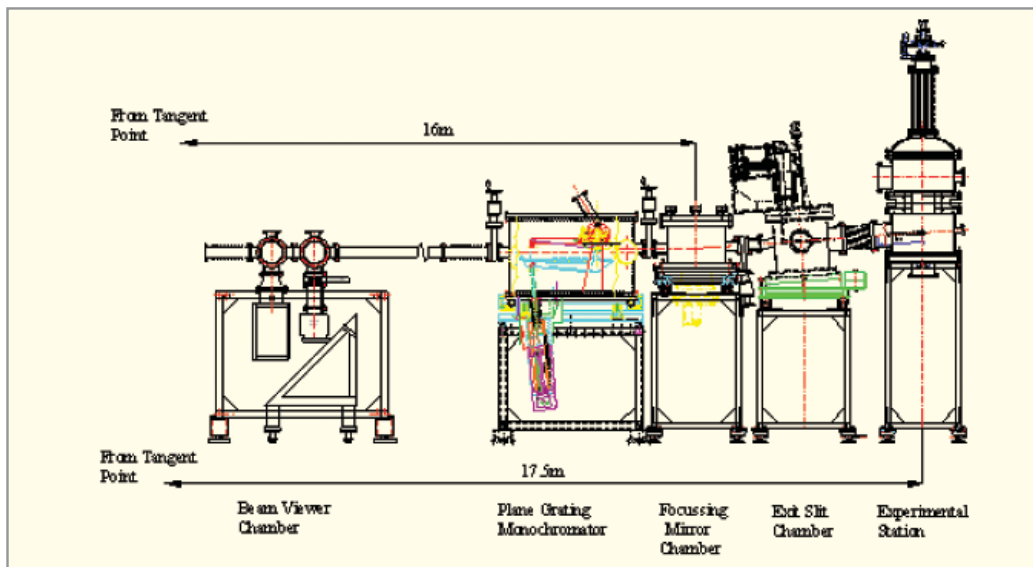
Photograph of the Crystal Bender.

mode involving no time-consuming scanning mechanism and thus can be applied to study in-situ fast and time-resolved processes. The basic idea is to use a single crystal bent in the shape of an ellipse in a particular fashion such that the synchrotron source and the sample positions are situated at the two foci of the ellipse. White synchrotron radiation after reflection from the crystal will be dispersed with a certain band-width depending on the radius of curvature of the crystal and the polychromatic radiation will then be focused at the sample position. The transmitted radiation from the sample will then be detected by a position-sensitive CCD detector. The proposed beam line would cover the photon energy range of 5 keV to 20 keV by a bent Si(111) crystal having 2d value equal to 6.2709 Å and would offer a band width of ~1 keV at 10 keV. The average resolution at the detector has been estimated to be ~ 1 eV per channel.

N. C. Das, S. N. Jha, D. Bhattacharyya, A. K. Poswal, A. K. Sinha and V. K. Mishra, *Sadhana* **29**, 545, (2004)



Optical Lay-out of the EXAFS Beam line



Schematic of PASS beamline on INDUS-1.

### 11.5 PHOTOABSORPTION SPECTROSCOPY STUDIES BEAMLINE

**Monochromator Characteristics:** Plane Grating (SX-700 type) Monochromator design with one long (500 mm) plane mirror, a 130mm long, 1200 l/mm, 1.5° blaze angle, plane grating and an 300 mm long ellipsoidal mirror.

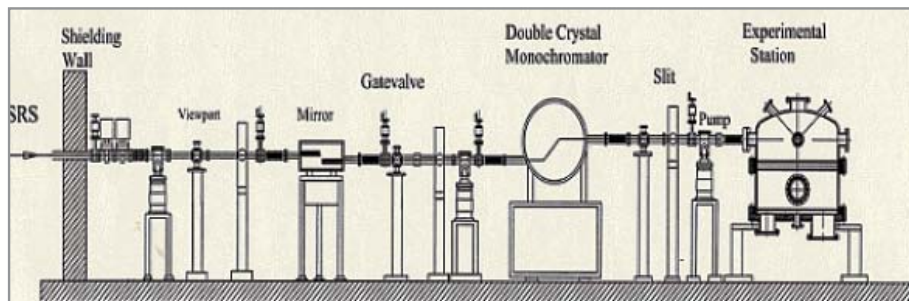
Acceptance	:	0.25 mrad vertical and 2.6 mrad horizontal
Resolution $\lambda/\Delta\lambda$	:	1000
Energy range	:	55 - 840 eV available
Turning ranges	:	11.25°-2.75° for plane mirror, 15.63°-3.8° for plane grating

**Experiments:** Typical experiments include “near to absorption edge” spectrum plus analysis in terms of local electronic structure.

**Experimental Station:** The experimental chamber for the PASS Beamline is of a two-tier design with a preparation and analytical chamber separated by a gate valve. The experimental station includes the following:

- 1) Sample Manipulator: x-y-z- $\theta$ - $\phi$  long z-drive : 400 mm, with heating up to 950°C and cooling up to liquid nitrogen temperature.
- 2) Ion pump, 300 litres/sec
- 3) Turbo pump, 300 litres/sec
- 4) Argon ion gun for in situ sputter cleaning, 500 eV–3 keV
- 5) Calibrated leak valve
- 6) Leed unit: Retractable rear view LEED/Auger
- 7) Evaporators
- 8) Channeltron detector unit (pulse counting / total current) for Total Electron Yield measurements (proportional to the absorption).
- 9) Spherical Sector Analyzer
- 10) Electron Gun, 100 eV - 5 keV (For Auger)

V.C. Sahni, R. Mukund, A. Sequeira, B.N. Karkera, G.P. Das. M. Sanjal and W.C.J. Carvalho, Proc. DAE Solid State Phys. Symp. 36C, 550.



Schematic of PES beamline on INDUS-2.

### 11.6 PHOTO-ELECTRON SPECTROSCOPY BEAMLINE

A beamline for X-ray Photoelectron Spectroscopy (XPS) studies utilizing X-rays in the energy range from 0.8 keV to 15 keV is being developed on Indus-2. The double crystal monochromator being developed indigenously, provides monochromatic X-rays with sufficiently high intensity and requisite monochromaticity for X-ray photoelectron spectroscopy (XPS) studies (Fig.). Exploiting the high chemical specificity and high surface sensitivity ( $\sim 50 \text{ \AA}$ ), XPS station will be used to derive element specific information about composition and electronic structure of surfaces, especially, about chemical shifts and bonding. If required in future, the beamline has a provision to be integrated with a versatile experimental station equipped with additional specialized analyzers and detectors, high resolution X-ray diffraction and Auger electron studies.

#### Specifications of the beamline:

1.	Energy Range	0.8-15 keV
2.	Resolution	$\sim 10^{-4}$
3.	Source	Bending magnet
4.	Divergence	3 mrad
5.	Beam on the target	Focussed
6.	Photon flux	$10^{10}-10^{11}$

Jagannath, R.K. Sharma, S.C. Gadkari, J.V. Yakhmi,  
<ssai@barc.gov.in>



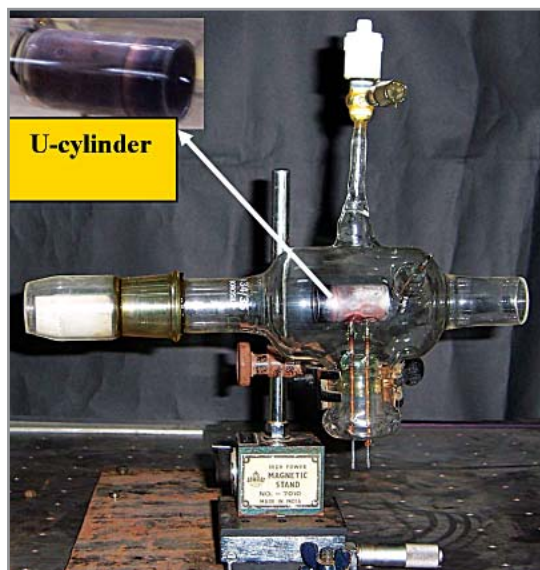
## **12. SPECTROSCOPIC STUDIES**

### **INTRODUCTION**

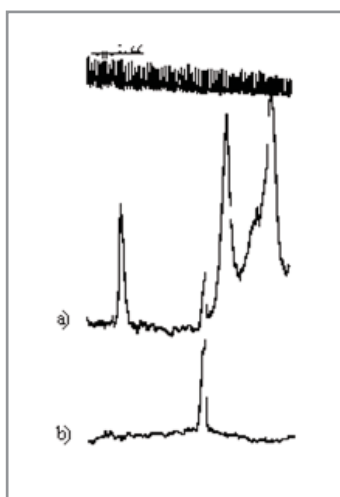
Starting with the aim of developing procedures for spectroscopic analysis of the materials required for nuclear research and utilization program, the activities in BARC have been continuously advanced to take up R&D into the emerging areas in atomic and molecular spectroscopy and cluster physics using supersonic molecular beam, laser spectroscopy, spectroscopy of trapped ions, single molecule spectroscopy, mass spectrometry of bio-molecules and spectroscopy of quantum solids. In the more recent years, three beamlines namely the High Resolution Vacuum Ultra Violet (HRVUV), Photo Physics (PP), Angle Resolved Photo Electron Spectroscopy (ARPES) were established at synchrotron sources at INDUS-I. Another beamline for Extended X-ray Absorption Fine Structure (EXAFS) studies is being currently established at INDUS- II. The success achieved in these areas has been possible due to sustained R&D efforts in the development of specialized optical components, devices, data acquisition and control systems and instruments.

## 12.1 MULTICOLOR PHOTOIONIZATION OPTOGALVANIC SPECTROSCOPY OF URANIUM.

Spectroscopy of highly excited levels, Rydberg levels and autoionisation levels of lanthanides and actinides is of great



U – Ne hollow cathode discharge tube for multi – colour photoionisation spectroscopy



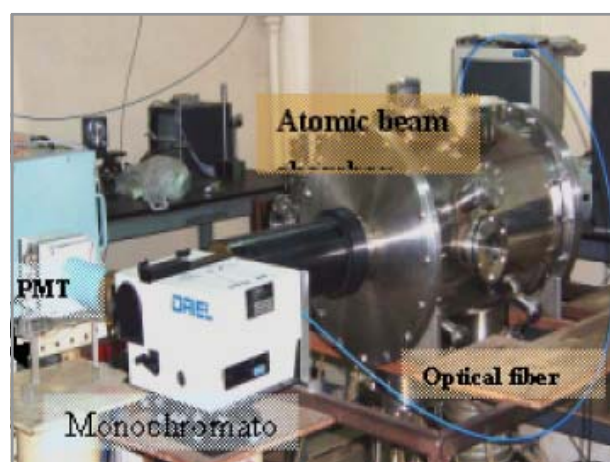
A portion of two color three photon ionization spectrum recorded in a U-Ne hollow cathode discharge with reference optogalvanic spectrum and Fabry- perot fringes

interest to DAE and much of this information is not available from classical spectroscopy. Large volume of new data in this area has been generated, both internationally as well as in our centre, by resonance ionization mass spectrometry. To supplement these efforts two new techniques of multi-color laser induced fluorescence (in atomic beams) and photoionisation optogalvanic spectroscopy have been developed. This is the first reported use of a simple and elegant device of hollow cathode discharge tube for generating new spectroscopic data of uranium. Several new autoionisation resonances of uranium were observed.

Vasdev, M.L.Shah, A.K.Pulhani, B.M.Suri. Appl. Phys. B 80, 587-594 (2005)

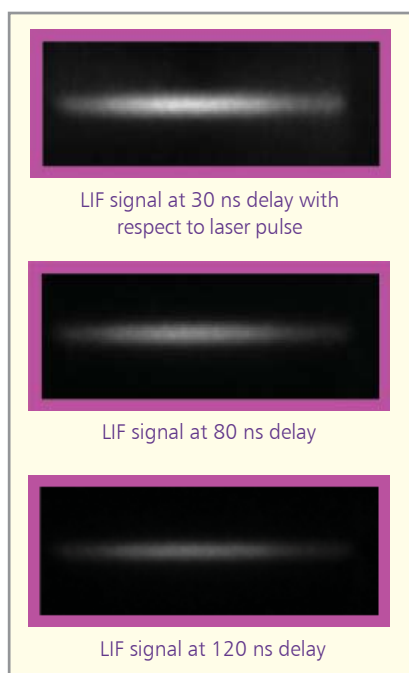
## 12.2 LASER INDUCED FLUORESCENCE SPECTROSCOPY OF LANTHANIDES

Two color laser-induced fluorescence spectrometer have been developed. It employs an atomic beam of elements with reasonable vapor pressure at 1500°C. Fig. shows a photograph of the spectrometer indicating the possibilities of space resolution, time resolution, spectral resolution and remote monitoring. Employing two color laser-induced fluorescence, several new highly excited levels of Samarium were observed which could not be observed using earlier technique of two-color three-photon ionization. Both the tech-

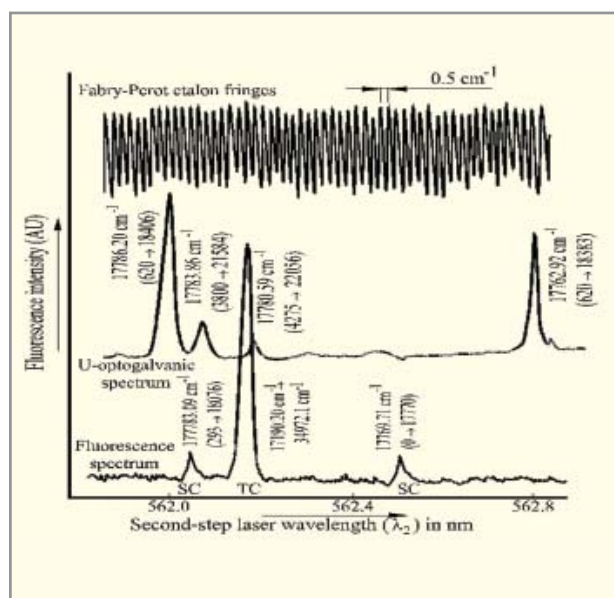


Laser Induced Fluorescence (LIF) spectrometer for single color/ multi color LIF, with provision for temporal resolution (~5 ns), spatial resolution (< 1 mm) and spectrally resolved LIF using fiber optic probe.

niques developed have great potential in atomic spectroscopy of highly excited levels.



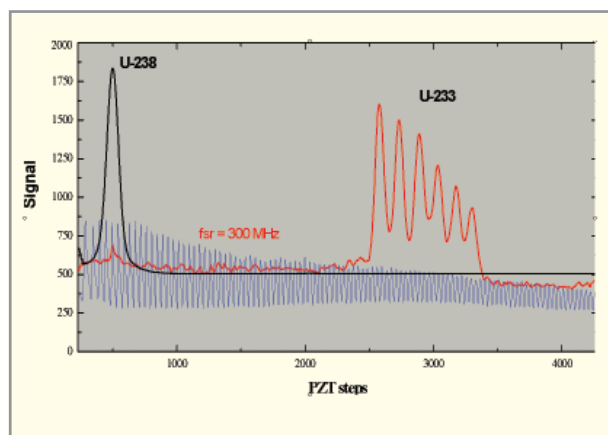
Space and time resolved single color Laser Induced Fluorescence (LIF) in Sm atomic beam



Two color LIF spectrum from Sm atomic beam, showing observation of new highly excited levels

## 12.3 HIGH RESOLUTION LASER SPECTROSCOPY OF ACTINIDES

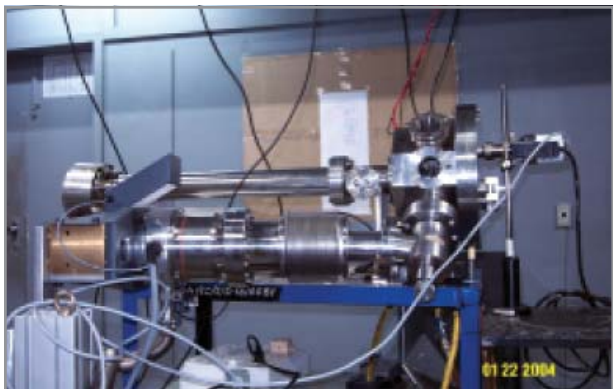
High resolution laser spectroscopy of actinides offers itself as for measurement of isotope shifts and hyperfine structure and consequently information related to nuclear structure. These measurements provide very critical input for development of laser isotope separation technology. Very precise measurements of IS and HFS provide nuclear information such as the spin, multipolar moments, deformation and variation in the mean square charge radius in a chain of isotopes. With the introduction of single mode tunable lasers, a number of laser-based techniques, notably, opto-galvanic spectroscopy, saturated absorption spectroscopy, polarization spectroscopy, laser induced fluorescence spectroscopy are developed and are being utilized. Recent work on high-resolution spectroscopy has been carried out with milligram and microgram quantities of samples and naturally this almost always means rare and radioactive isotopes of interest to nuclear energy programme.



High resolution spectrum of 682 nm line of U-238 and U-233 exhibiting IS  $\delta\nu(233, 238)$  and hyperfine structure of U-233 (Nuclear spin  $I=5/2$ ). The spectrum is obtained using single mode cw laser based opto-galvanic spectroscopy. Frequency scale is provided by the 300 MHz markings of a confocal interferometer.

A K Pulhani, M L Shah, Vas Dev, B M Suri, J. of Opt. Soc. Am B, vol 22, No 5, 1(2005)

A time-of-flight mass spectrometer has been developed for Resonance Ionisation Mass Spectrometry of actinides.



Time of flight mass spectrometer (TOFMS) developed for multi-step, multi-colour photo-ionisation spectroscopy.

A.P. Marathe, A. Venugopalan and B.N. Jagatap, BARC/2004/R/12 and 13

#### 12.4 LASER INDUCED FLUORESCENCE SPECTROSCOPIC STUDIES ON ZIRCONIUM ATOMS AND ZIRCONIUM OXIDE MOLECULES.

The experimental facility for generating supersonic pulsed



Photograph of the supersonic free-jet-laser induced fluorescence setup.

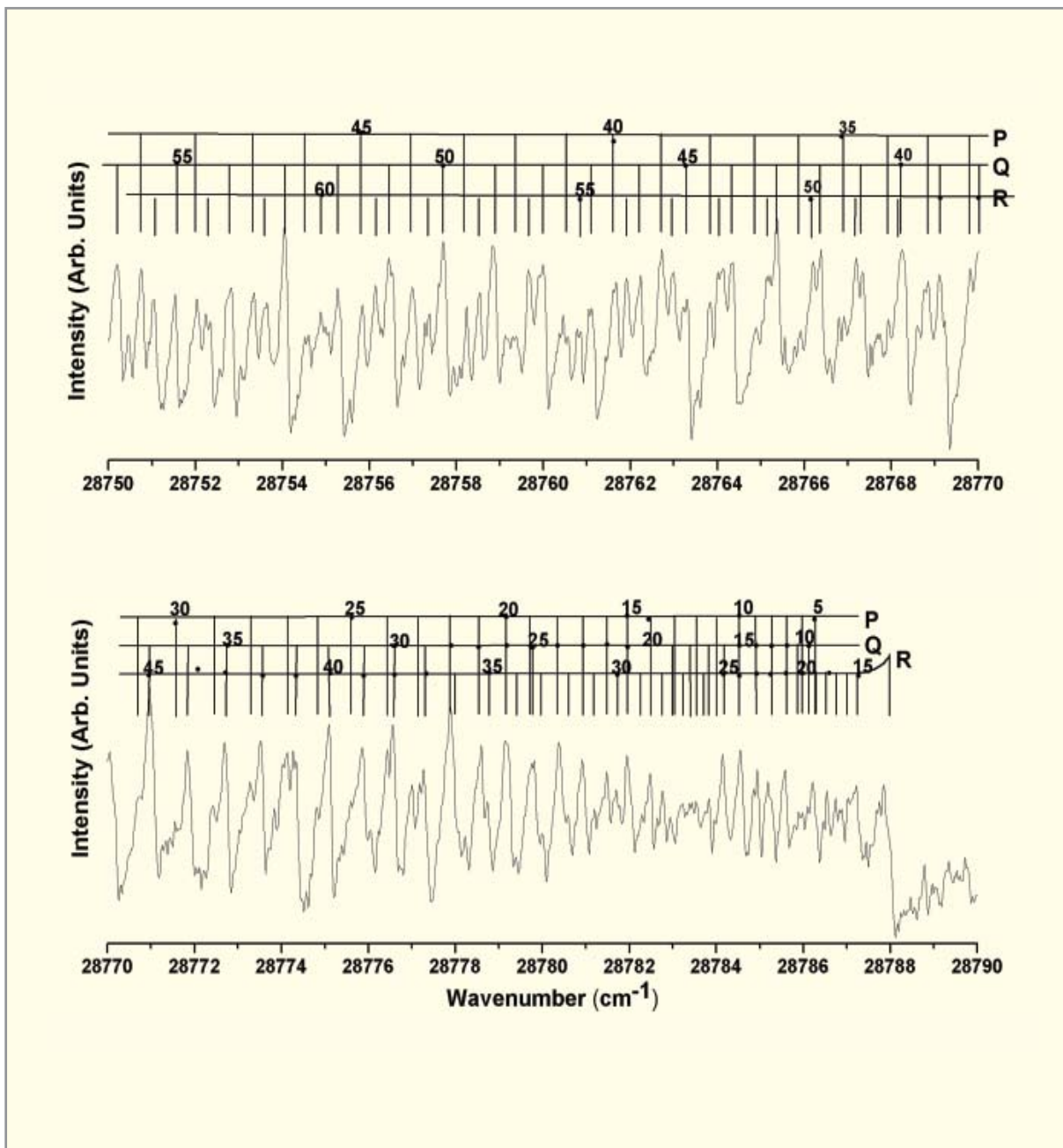
free-jet containing atoms, molecules and clusters of refractory nature has been built, as shown in Fig. The technique of laser vaporization followed by supersonic cooling in conjunction with the technique of laser-induced fluorescence is used to study the electronic structure of atoms and molecules of refractory nature. Although the technique has been applied to the Zr atom, any other refractory species can be studied this way.

The Zr atoms were generated by ablating the rotating and translating Zr metal rod and the zirconium plasma produced by laser ablation was cooled and recombined during supersonic expansion of helium gas pulse generated by home built piezoelectric actuator driven pulse valve. The cooled Zr atoms in supersonic free-jet were probed by laser induced fluorescence (LIF) technique. The LIF excitation spectrum of Zr atom was obtained in 595 nm wavelength region. The dispersed fluorescence spectra provided information on low-lying energy states of Zr atom. The translational temperature of 26 K has been evaluated for Zr atoms from the experimentally obtained Zr atom velocity and velocity distribution in free-jet. This temperature corresponds to the Doppler width of 195 MHz. High-resolution spectroscopy can be carried out on such translationally cooled atomic species to get information like Isotope Shifts (IS) and HyperFine Structure (Hfs).

S. G. Nakhate, BARC Report 2004/E/033

#### 12.5 FOURIER TRANSFORM EMISSION SPECTROSCOPY OF THE $A^1\Pi-X^1\Sigma^+$ TRANSITION IN $^{74}\text{Ge}^{80}\text{Se}$

For the first time, the electronic spectrum of the specific isotopomer  $^{74}\text{Ge}^{80}\text{Se}$  of germanium monoselenide was produced in a microwave discharge through an electrodeless quartz tube containing the single isotopes of  $^{74}\text{Ge}$  and  $^{80}\text{Se}$  and neon as carrier gas. The bands in the  $35000\text{--}25000\text{ cm}^{-1}$  region belonging to the main transition  $A^1\Pi-X^1\Sigma^+$  have been recorded on BOMEM DA8 Fourier transform spectrometer under medium ( $10\text{ cm}^{-1}$ ) and high ( $0.05\text{ cm}^{-1}$ ) resolutions. A large number of bands, including



A portion of the spectrum showing the rotational spectra in the 0-5 band of the  $A^1\Pi - X^1\Sigma^+$  transition in  $^{74}\text{Ge}^{80}\text{Se}$ .

several new bands in the 28000–25000  $\text{cm}^{-1}$  region have been assigned to the A–X system (Fig.). The observation of isotopically pure spectrum has enabled a comprehensive vibrational analysis of the A–X bands. The Franck–Condon Factors (FCF) and  $r$ -centroids were computed and the observed intensities were compared with the FCFs.

A. P. Mishra, B. J. Shetty and R. J. Khirsagar, *J. Molecular Spectroscopy* 232, 284 (2005)

## 12.6 FABRICATION OF PRECISION OPTICAL COMPONENTS

We have developed the technology of fabrication and testing of precision optical components such as plane parallel plates, Fabry-Perot plates, concave spherical mirrors, lenses, prisms, beam splitters needed for various types of optical instruments, spectrometers and monochromators (Fig.). The optical surfaces of diameter upto 200 mm in size can be fabricated with a surface accuracy of  $\lambda/10$ . The plane surfaces of diameter 50 mm can be fabricated with surface accuracy of  $\lambda/100$  at our workshop. These precision Fabry-Perot plates have been used for the stabilization of wavelength in dye lasers required for isotope enrichment program of BARC.

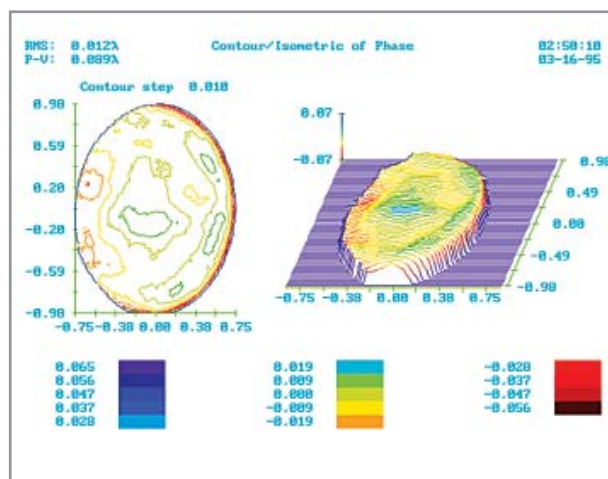


Photograph of various types of optical components.

R.P. Shukla and Dinesh V. Udupa, BARC News Letter No. 215, 7 (2001)

## 12.7 INTERFEROMETRIC TESTING OF OPTICAL COMPONENTS

We have developed a facility for testing the precision optical components. The testing facility consists of classical interferometers such as Fizeau interferometer, Twyman Green interferometer and Newton interferometer using monochromatic sources of light such as sodium lamp and cadmium lamp. We have also developed several laser interferometers such as Jamin interferometer, Mach-Zehnder interferometer for measuring the homogeneity of optical materials in addition to the measurement of wedge angle of nearly parallel plates of glass. We have several parallel plate interferometers using He-Ne laser as a source of light for checking the laser beam collimation of various apertures. For testing of concave spherical surfaces, we have developed Ronchi test and scatter plate interferometer. We have a phase measuring Zygo interferometer using laser source to measure the wavefront emerging out of a good quality lens or spherical mirror. The system accuracy is  $\lambda/20$  for plane surfaces and  $\lambda/10$  for spherical surfaces. The phase map of the actual surface under test can be measured along with Peak-to-Valley (P-V) deviation and the root mean square (rms) deviations from the ideal plane or spherical surface using the Zygo interferometer.



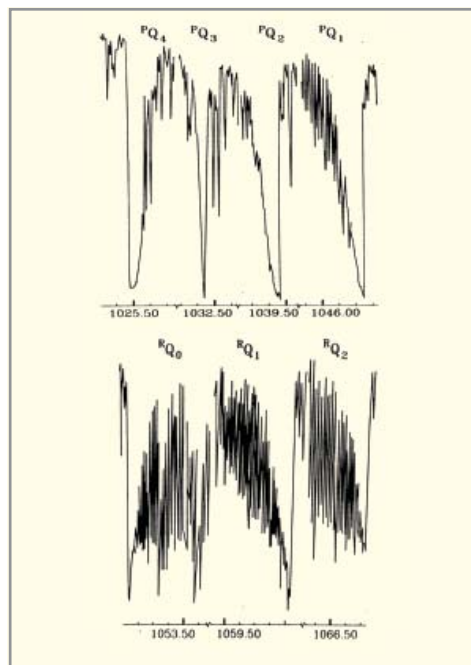
The phase map and surface contour of a flat surface under test recorded using the Zygo interferometer. and  $L_{TC}$  form the zoom lens objective of the periscope.

R.P. Shukla, D.V. Udupa, Optics & Laser Technology 32, 355 (2000)

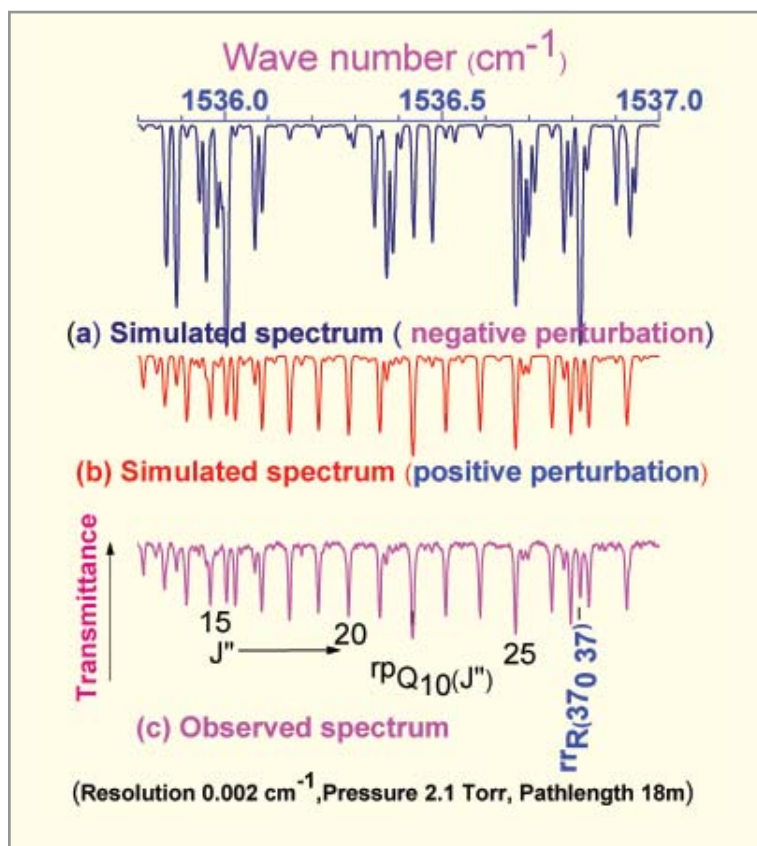
## 12.8 FOURIER TRANSFORM SPECTROSCOPIC STUDIES OF ATOMS, MOLECULES AND TRANSIENT SPECIES

The wide spectral coverage, high resolution capability and high sensitivity of modern Fourier transform instruments permit the studies of atoms, molecules and radicals either in absorption or emission mode. The results of these measurements are useful in applications in atmospheric studies, astrophysics, geophysics, laser development, nuclear properties etc.

We have carried out high resolution absorption studies of several molecules such as Methyl acetylene (Propyne;  $\text{CH}_3\text{CCH}$ ), Phosphine ( $\text{PH}_3$ ),  $\text{PH}_2\text{D}$ , Methylene fluoride ( $\text{CH}_2\text{F}_2$ ) and its isotopomer  $\text{CD}_2\text{F}_2$ ,  $^{13}\text{CF}_3\text{Br}$ , etc. Spectra of these molecules have been recorded with Fourier transform spectrometer in the infrared region. Rotational-vibration



Typical spectrum observed in the  $\nu_2$  band  $\text{CH}_3\text{CCH}$



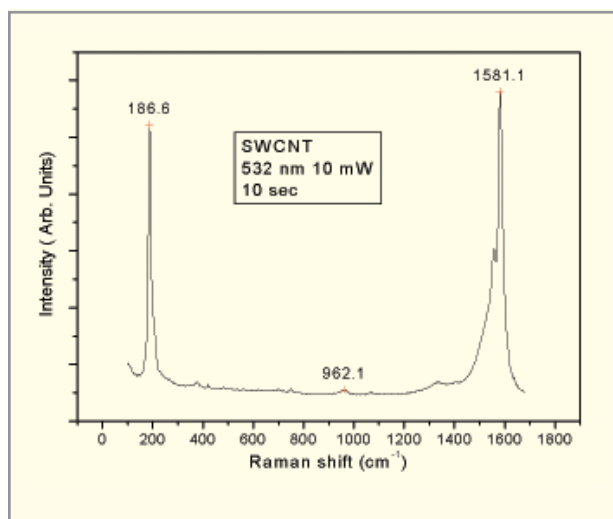
$\nu_2$  band in the region of  $^1Q_{10}$  branch of  $\text{CH}_2\text{F}_2$ , showing the effect of Coriolis coupling.

spectra of these molecules are complicated due to the several perturbations (Coriolis interaction, Fermi resonance etc.) present in the vibrating-rotating molecules. Two such spectra are shown in Fig. ( $\text{CH}_2\text{F}_2$ ) and Fig. ( $\text{CH}_3\text{CCH}$ ). We have successfully analyzed the several spectra taking into account all the possible interactions. Similarly we have also studied the emission spectral of  $\text{CO}$ ,  $\text{N}_2$ ,  $\text{Ar}$ ,  $\text{Ne}$  and transient species ( $\text{SiC}$ ,  $\text{CH}$ ,  $\text{CS}$ ,  $\text{InCl}$ ,  $\text{MgCl}$  produced and excited by MW discharge, DC discharge or hollow cathode discharge etc. We have measured isotope shift of several atomic species such as  $\text{Gd}$ ,  $\text{Sm}$ ,  $\text{Yb}$ , et. Based on the experience in the field, it is proposed to set up an infrared beam line in the Indus-II synchrotron facility which will further enhance the capability of our Fourier transform spectroscopic studies.

Geetha Rajappan and R.J.Kshrisagar, J. Mol.Spectrosc.224, 107-113 (2004)

## 12.9 CCD-BASED RAMAN SPECTROMETER

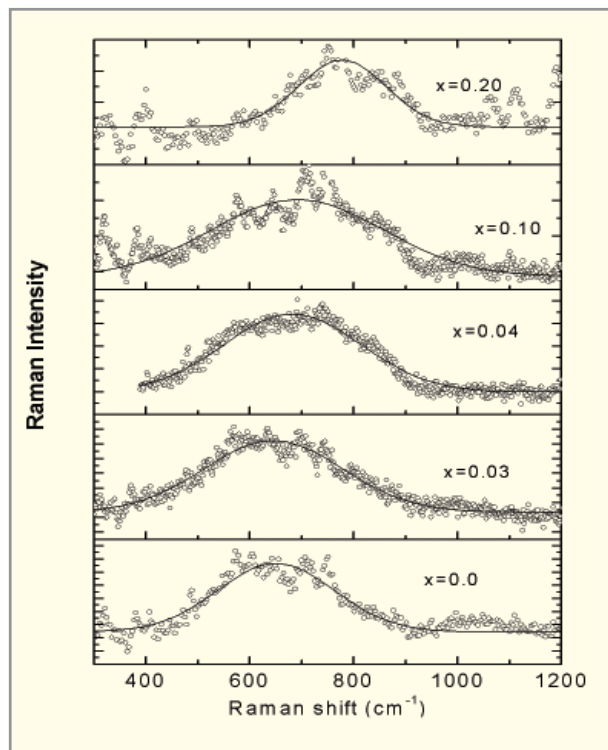
A CCD-based homemade multichannel Raman spectrograph (designed and fabricated at the Center for Design and Manufacturing) has been set up and is currently operational. It can accommodate three different gratings to change the resolution and range of the spectrograph. The highly-sensitive CCD detector with capability for simultaneous acquisition of the spectrum over the full range makes it a very versatile Raman spectrometer. A typical spectrum from



Raman spectrum of Single Walled Carbon Nanotube.

Single Walled Carbon Nanotube is shown and compares very well with that recorded in any commercial spectrometer (Fig.). We have used this spectrograph to obtain data on high-pressure phase transition in organic charge transfer compound TCNE and Carbon doped  $\text{MgB}_2$  superconductor.

$\text{MgB}_2$  is a high-temperature superconductor with a transition temperature  $\approx 40\text{K}$  and carbon doping in  $\text{MgB}_2$  is of current interest to study its effect on critical current density and upper critical field. However, the transition temperature decreases with carbon doping and we have carried out room temperature Raman scattering measurements on well-characterized samples of  $\text{MgB}_{2-x}\text{C}_x$ . From the average mode frequency and the line width of the Raman active  $E_{2g}$  phonon (shown in Fig.) and taking the values of  $N(0)$  obtained from the calculated variation in  $\sigma$



Raman spectrum of  $\text{MgB}_2$  superconductor.

hole density of states in  $\text{MgB}_{2-x}\text{C}_x$ , the electron phonon coupling strength to the  $E_{2g}$  phonon,  $\lambda_{2g}$ , has been evaluated. Using this value of  $\lambda_{2g}$  appropriately weighted,  $T_c$  is obtained using McMillan equation. These values are in good agreement with the experimentally measured  $T_c$  variation in  $\text{MgB}_{2-x}\text{C}_x$ .

T.Sakuntala, A.Bharathi, S.K. Deb, N. Gayathri, C.S. Sundar and Y. Hariharan, J. Phys. Cond. Matter, 17, 3285, (2005)



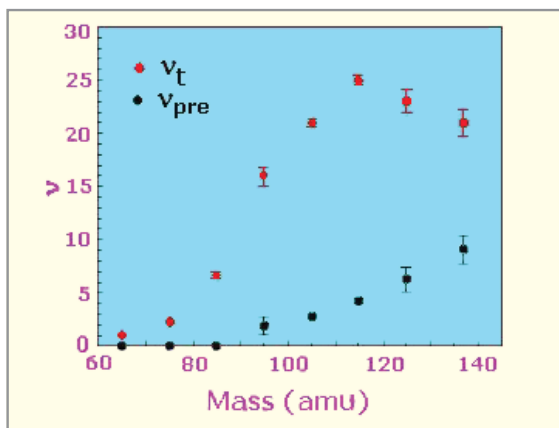
## **13. STUDIES IN NUCLEAR PHYSICS**

### **INTRODUCTION**

Nuclear Physics research is growing broadly in three directions: nuclear collisions at high energies and formation of hot and dense nuclear matter; study of nuclei with large spins and deformations and underlying symmetries; investigation of nuclei away from the line of stability and formation of super-heavy nuclei. Some of these frontier areas of research are covered in this chapter on nuclear physics. Primarily, the experimental programmes have been pursued at the Pelletron accelerator facilities at Mumbai and Delhi. They have been supplemented with measurements carried out using international facilities.

### 13.1 FISSION OF SUPER-HEAVY NUCLEAR SYSTEMS

As part of the ongoing programme to investigate the fission dynamics of super-heavy composite systems, the binary fragmentation of the excited super-heavy system of  $Z=116$  formed in the reaction  $372 \text{ MeV } ^{56}\text{Fe} + ^{232}\text{Th}$  has been investigated. The fragment mass and kinetic energy were determined through measurement of fragment velocity by the time-of-flight method. Neutron spectra measured in coincidence with the fragments at several angles with respect to the fragment direction were analyzed to deduce the total as well as the pre-scission neutron multiplicities.



Total and pre-scission neutron multiplicity as a function of light fragment mass deduced from the fits of the measured fragment-neutron correlations.

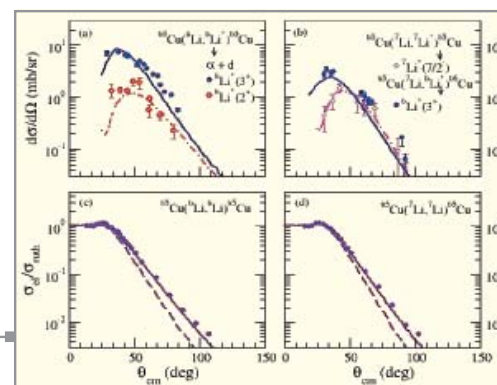
The pre-scission,  $v_{\text{pre}}$  and total neutron multiplicity,  $v_{\text{T}}$  as a function of fragment mass were determined from a moving source fit and these values are shown in figure. It is seen that the value of  $v_{\text{T}}$  increases from about 1 to 25 in going from light fragment mass of 65 to 115, and remains nearly flat in the near-symmetric mass region. On the other hand, the  $v_{\text{pre}}$  is seen to increase monotonically from about 0 to 9 in going from mass 65 to symmetric split. From the observed number of pre-scission neutrons, it is inferred that the time scales of the fission-like reactions leading to near mass-symmetric split are rather large, of the order of several times  $10^{-20}$ s. The events in the near mass-symmetric valley region appear to have a significant contribution from the asymmetric fission of the superheavy compound nucleus

$Z=116$ , due to the influence of the closed proton and neutron shell of  $Z=50$  and  $N=82$  of the light fragments. From the neutron measurements it is inferred that the average number of prompt neutrons emitted in the spontaneous fission of such a superheavy nucleus is about  $(12 \pm 1)$ . Data are now available for  $^{56}\text{Fe} + ^{232}\text{Th}$ ,  $^{80}\text{Se} + ^{232}\text{Th}$ ,  $^{208}\text{Pb}$  and  $^{28}\text{Si} + ^{232}\text{Th}$  and these interesting results are expected to help us in our understanding of the superheavy nuclear formation and decay.

P.K.Sahu, R.G.Thomas, A.Saxena, R.K.Choudhury, S.S.Kapoor, L.M.Pant, M.Barbui, M. Cinausero, G. Prete, V. Rizzi, D. Shetty, D. Fabris, M. Lunardon, S. Moretto, G.Viesti, G. Nebbia, S. Pesente, B. Dalena, G. D'Erasmus, D. Di Santo, E.M. Fiore, M. Palomba, A. Pantaleo, V. Paticchio, G.Simonetti, N.Gelli, F.Lucarelli, A. Brondi, E. Vardaci. Phys. Rev. C. (under publication)

### 13.2 TRANSFER FOLLOWED BY BREAKUP WITH STABLE AND WEAKLY BOUND PROJECTILES

One of the areas of current interest in heavy ion fusion studies is to understand the fusion initiated by weakly bound projectiles. It has been clearly demonstrated that the different degrees of freedom related to nuclear structure of the projectile and the target influence the fusion probability. However, the role of the break up channel associated with the weakly bound projectiles in the fusion process is not clearly understood. With a view to understand



(a) Angular distribution for the resonant states in  $^6\text{Li}$  and (c)  $^7\text{Li}$ . Also plotted in (c) are data for the reaction  $^7\text{Li} + ^{65}\text{Cu} \rightarrow ^6\text{Li}^*(3^-) + ^{66}\text{Cu}$  along with the CCBA calculations (solid curve). Elastic scattering data for both projectiles along with the CDCC calculations is shown in (b) and (d) for the coupled (solid curve) and uncoupled (dashed curve) case.

this aspect, coincidence measurements have been performed at BARC-TIFR Pelletron with  ${}^7\text{Li}$  beam on enriched  ${}^{65}\text{Cu}$ , to study breakup reaction and the two-step reaction mechanism, transfer-breakup ( ${}^7\text{Li} + {}^{65}\text{Cu} \rightarrow {}^6\text{Li}^* + {}^{66}\text{Cu}$ ,  ${}^6\text{Li}^* \rightarrow \alpha + d$ ). This is a complex process that combines the breakup and transfer reactions, both well understood separately.

The coincidence data for  ${}^7\text{Li}$  breakup showed large yields for  $\alpha + d$  events. The origin of these events have been identified as stripping transfer followed by breakup of the excited  ${}^6\text{Li}$  via  $3^+$  state in continuum. To get a deeper insight in the mechanism behind this reaction: direct transfer of the neutron to  ${}^6\text{Li}$ -continuum or transfer to the ground state of  ${}^6\text{Li}$  followed by excitation to continuum, CCBA model predictions were compared with experimental data as shown in Fig. The results provide evidence that the main reaction mechanism is direct transfer to the  $3^+$  state in  ${}^6\text{Li}$ . The reactions with low energy unstable radioactive ion beams from newly available facilities are expected to be of similar complexity. Identification of the reaction processes and development of theoretical understanding for such multi-step reactions is a challenging task. The present study is an important step in this direction.

A. Shrivastava, A. Navin, K. Mahata, K. Ramachandran, V. Nanal, N. Keeley, A. Chatterjee, S. Kailas. ENAM04 Tennessee USA (2003).

### 13.3 HEAVY-ION INDUCED FISSION FRAGMENT MASS, TOTAL KINETIC ENERGY AND ANGULAR DISTRIBUTIONS

Systematic studies of heavy ion fission fragment angular distributions have been carried out for a large number of heavy ion systems with projectiles ranging from B to F and at various bombarding energies. A new model has been developed to understand the fission data from below the Coulomb barrier to above barrier energies. It has been found that the mechanism of pre-equilibrium fission, which is conceptually different from quasi-fission and fast fission, contributes to non-compound-nucleus fission for entrance channel mass asymmetry,  $\alpha < \alpha_{BG}$  systems at all energies and even for  $\alpha > \alpha_{BG}$  at sub-barrier energies. It is also shown that when fusion is initiated at relatively larger distances due to the presence of rotational couplings, the Businaro- Gallone

barrier shifts towards higher mass asymmetry, thus favoring further mass equilibration towards symmetric configurations. This leads to the occurrence of pre-equilibrium fission events for all systems, which affect the fission fragment angular distributions at sub barrier energies. From the fits to the angular distributions,  $K$ -equilibration time is deduced to be  $\sim 6 \times 10^{-20}$  s for a temperature  $\sim 1$  MeV. The fission fragment angular distributions calculated as an admixture of compound nuclear and pre-equilibrium components explains quite well the energy dependence of the angular anisotropies for many systems around the actinide regions irrespective of the entrance channel mass asymmetries at energies both well below and above the Coulomb barrier. Thus the fragment anisotropies serve as a probe of the fusion-fission dynamics and can be used as a guide in selecting optimum entrance channel conditions for the synthesis of super heavy nuclei. Recently, in a fission experiment, the presence of pre-equilibrium fission in  ${}^{14}\text{N} + {}^{232}\text{Th}$  and its absence in  ${}^{11}\text{B} + {}^{235}\text{U}$  reactions, both populating the same compound  ${}^{246}\text{Bk}$  have been clearly demonstrated.

Fission fragment angular distributions and evaporation residue excitation functions have been measured for the systems  ${}^{19}\text{F} + {}^{188,192}\text{Os}$  systems over a range of bombarding energies. From a comprehensive statistical model analysis that included the above data and the pre-fission neutron multiplicity, fission anisotropies and the multi-chance nature of fission, it has been possible to obtain a rather unique set of statistical model parameters. From a large body of fission data spanning a range of fissility values, the effective moment of inertia values at the saddle point of fissioning nuclei have been extracted and these values are found to be in good agreement with the rotating finite range model calculations.

Fission fragment mass and kinetic energy distributions have been measured in  ${}^{12}\text{C} + {}^{\text{nat}}\text{Pb}$ ,  ${}^{209}\text{Bi}$ ,  ${}^{235}\text{U}$ , and  ${}^{11}\text{B} + {}^{209}\text{Bi}$  reactions at above barrier energies. The data were obtained over a range of bombarding energies near and above the Coulomb barrier for all the systems. The average total kinetic energy of the fragments does not show any significant variation with bombarding energy, whereas the mass variance is found to increase with bombarding energy for a given fissioning system. The variance of the fragment

mass distribution ( $\sigma^2_A$ ) has been studied as a function of the temperature and fissility of the compound nucleus by analyzing the present results along with the available data from literature. It is observed that  $\sigma^2_A$  increases exponentially with temperature as well as fissility of the compound nucleus. However, when data are analyzed with respect to the fragment temperature ( $T_f$ ), instead of the temperature of compound nucleus, the dependence of  $\sigma^2_A$  on fissility is greatly reduced for a given value of  $T_f$ . The mass variance shows a universal dependence on  $T_f$  irrespective of the fissility of the compound nucleus. This result implies that the mass variance is decided during the later stage of fission process and is related to the scission configuration of the fissioning nucleus.

R.G.Thomas, R.K.Choudhury, A.K.Mohanty, A.Saxena, and S.S.Kapoor, Phys. Rev. C **67**, 041601 (2003)

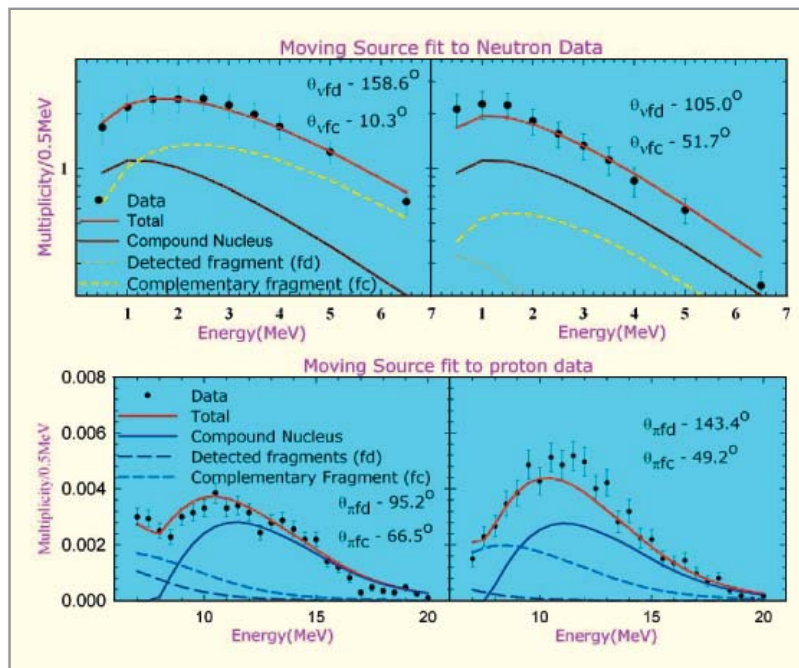
#### 13.4 MEASUREMENT OF PRE-FISSION $\eta$ , $\rho$ , $\alpha$ AND GDR GAMMA-RAY MULTIPLICITIES IN $^{28}\text{Si} + ^{175}\text{Lu}$ SYSTEM

Measurements of fission time scales are very crucial to the understanding of fission dynamics and viscosity of the nuclear medium. An experiment was performed to simultaneously measure the pre-fission neutron, proton, alpha particle and GDR  $\gamma$ -ray multiplicities in coincidence with Fission Fragments (FF), using the Pelletron - LINAC booster accelerator facility at Mumbai. The experiment was done with 159 MeV  $^{28}\text{Si}$  beam on a self-supporting  $^{175}\text{Lu}$  target. A position sensitive silicon strip detector and a  $\Delta E$ -E telescope were used to detect the fission fragments. Two NE213 liquid scintillator detectors were used to detect neutrons. Charged particles were detected using CsI(Tl)

detectors. For the measurement of GDR  $\gamma$ -ray multiplicity, an array of 7  $\text{BaF}_2$  detectors in a hexagonal close packed geometry, having a plastic anti-coincident shield (cosmic veto) and placed at  $90^\circ$  at a distance of 45 cm from the target was used. Neutrons, protons, alpha particles and  $\gamma$ -rays in coincidence with fission were collected on event-by-event basis.

The measured spectra contain both *pre-* and *post-fission* components. The experimental  $\nu$ ,  $\pi$ ,  $\alpha$  spectra were fitted using moving source formula to extract pre-fission multiplicities. The fitted neutron and alpha spectra are shown in figures for two relative angles between fragments and n/p. The preliminary results show a  $\nu_{\text{pre}}$  value of  $3.1 \pm 0.7$ ,  $\pi_{\text{pre}}$  value of  $0.0176 \pm 0.0005$  and  $\alpha_{\text{pre}}$  value of  $0.0203 \pm 0.0004$ . The alpha spectra show that there can be one more component in the spectra, which is having the characteristics of near scission emission.

K.Ramachandran, A.Chatterjee, A.Navin, V.Tripathi, K.Mahata, A.Shrivastava, S.Kailas, V.Nanal, R.G.Pillay, D.R.Chakrabarty, V.M.Datar, Suresh Kumar, A.Mitra, P.K.Sahu, A.Saxena and R.G.Thomas DAE-BRNS Symposium on Nuclear Physics, Dec. 2003 vol.46B, p190



**13.5 STUDY OF GIANT DIPOLE RESONANCE BUILT ON 15.1 MeV T=1 STATE IN <sup>12</sup>C**

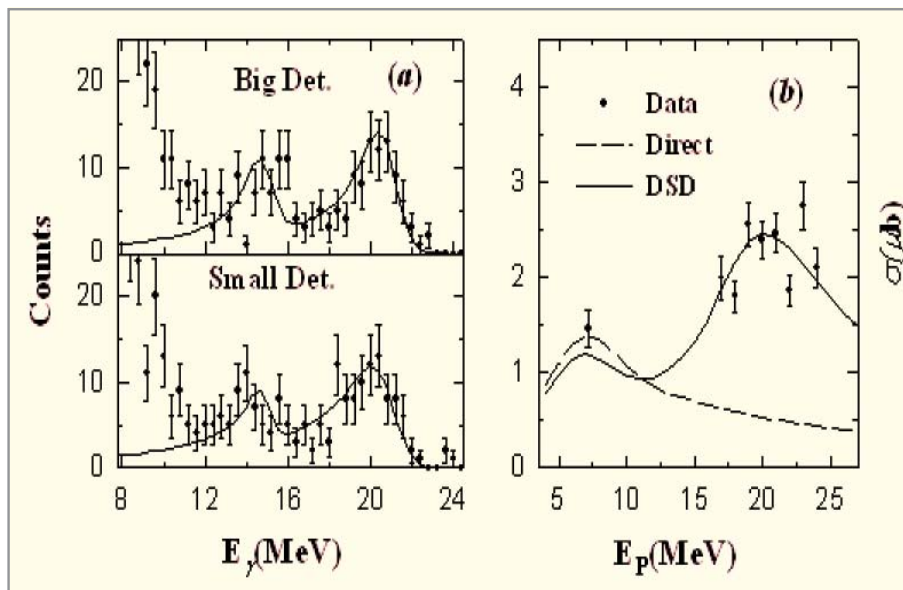
The Giant Dipole Resonance (GDR) in the exotic radioactive nuclei is a challenging topic of current interest. The 15.1 MeV state in <sup>12</sup>C is the isobaric analogue (T=1) of the ground state of radioactive nuclei <sup>12</sup>B and <sup>12</sup>N. A study of the GDR built on this analogue state should provide complementary information on the GDR built on the ground states of these radioactive nuclei. The present work describes such a study from the radiative proton capture to the 15.1 MeV state in the p + <sup>11</sup>B reaction. The capture  $\gamma$ -rays were measured in coincidence with the 15.1 MeV  $\gamma$ -ray arising from the subsequent decay of the T=1 state to the ground state of <sup>12</sup>C. The proton beam energies in the experiment were chosen as 7.2 MeV and 17 to 24 MeV in 1 MeV steps. The experiment was performed with the proton beam from the Mumbai Pelletron bombarding a natural boron target. Gamma rays were detected in two arrays of BaF<sub>2</sub> detectors, each consisting of a close-packed group of seven elements, surrounded by plastic anti-coincidence shields. The projection of the two dimensional coincidence spectra on the energy axis of one detector when the energy window chosen in the other is in the 15.1 MeV region is shown in

Fig. (a). The extracted cross sections are shown in Fig. (b) as a function of proton energy. The calculated direct capture cross-sections are shown by the dashed line in Fig. (b). The measured cross section at 7.2 MeV is close to the calculated value. For proton energy of 17 to 24 MeV, the calculated cross sections are about a factor of five lower than the observed ones. The contribution from the compound nuclear process, even after incorporating a GDR on 15.1 MeV state, is also calculated to be at least a factor of five less.

The result of a Direct Semi-Direct (DSD) model calculation including the GDR excitation on the 15.1 MeV state is shown by the full line in Fig.(b). The volume form factor for the isovector coupling is used in the calculation. The GDR energy of  $(18 \pm 1.5)$  MeV and width  $(12 \pm 5)$  MeV reasonably explain the data whereas the ground state values (22.6 MeV and 4 MeV) fail to reproduce the data. Thus the present results provide evidence for the GDR built on the 15.1 MeV state as seen in the proton capture reaction. The resonance energy is lower and the width higher than the ground state GDR.

Thus the present results provide evidence for the GDR built on the 15.1 MeV state as seen in the proton capture reaction. The resonance energy is lower and the width higher than the ground state GDR.

D.R. Chakrabarty, V.M. Datar, Suresh Kumar, E.T. Mirgule, A.Mitra, H.H. Oza and V. Nanal, Phys. Rev. C 69, 021602(R) (2004).



The gamma spectra and the cross section are shown. The continuous line is the calculation using the direct-semi direct model.

### 13.6 DIRECT OBSERVATION OF $4^+$ TO $2^+$ GAMMA TRANSITION IN ${}^8\text{Be}$

The many body effect in an interacting finite fermionic system is an issue of fundamental importance. One interesting manifestation of the effect, specific to the nucleus, is the phenomenon of clustering. Alpha particles are the most natural building blocks in a cluster model because of their large binding energy. There are possibilities of the occurrence of a very exotic shape like a linear alpha chain in nuclei. The nucleus  ${}^8\text{Be}$  is the simplest alpha cluster system exhibiting a dumbbell-like shape.

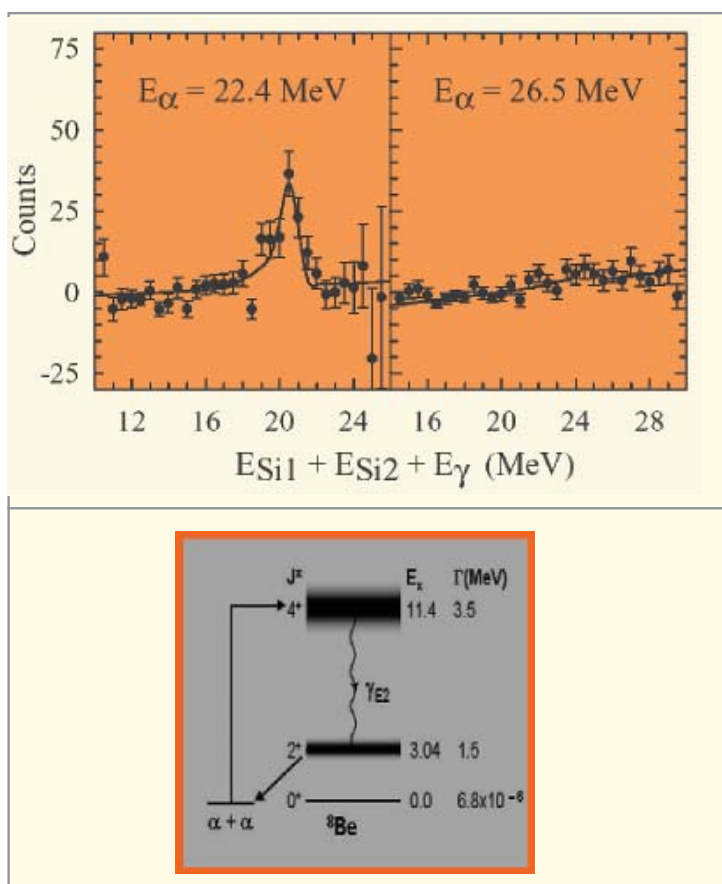
Electromagnetic transition rates provide the important test for nuclear structure models. However, the alpha-cluster

model of  ${}^8\text{Be}$  has not been yet established by gamma decay measurements, because of the extremely low gamma branching of these unbound states. An experiment for measuring the gamma decay of the  $4^+$  to  $2^+$  state has been performed. The gamma branching ratio is very small at  $1.2 \times 10^{-7}$ .

The experiment was done at the Mumbai Pelletron using alpha beams of 22.4 and 26.5 MeV (for ON and OFF resonance measurements) using a helium gas target. Gamma rays were detected in two arrays of BGO detectors. The two  $\alpha$  particles resulting from the decay of the  $2^+$  resonance were detected in an array of six Si PIN diodes placed at forward angles. Data was collected in the event-by-event mode requiring at least two PIN diodes and one BGO in

coincidence. The sum spectra  $E_{\alpha_1} + E_{\alpha_2} + E_{\gamma}$  were generated from the data where  $\alpha_1$  and  $\alpha_2$  refer to diametrically opposite Si PIN diodes and  $E_{\gamma}$  is the energy deposited in one of the gamma detector arrays. Fig. shows random subtracted sum spectra at the two beam energies. The resonant behavior of gamma branch is evident from the figure. The best fits to the data are shown in Figure. The extracted gamma cross sections at the on resonance energy of 22.4 is  $165 \pm 54$  nb and this leads to a  $B(E2)$  value of  $25 \pm 8$  W.u. The observed large value of  $B(E2)$  in the gamma decay rate is consistent with the cluster model calculation.

In summary, we have made the first direct observation of the  $4^+$  to  $2^+$  gamma transition in  ${}^8\text{Be}$  through a  $\gamma$ - $\alpha$ - $\alpha$  triple coincidence measurement. The derived gamma cross sections show a large enhancement supporting the intrinsically deformed alpha-cluster structure of  ${}^8\text{Be}$ . The present experiment demonstrates the feasibility of gamma ray measurements to probe linear chain cluster states in heavier nuclei.

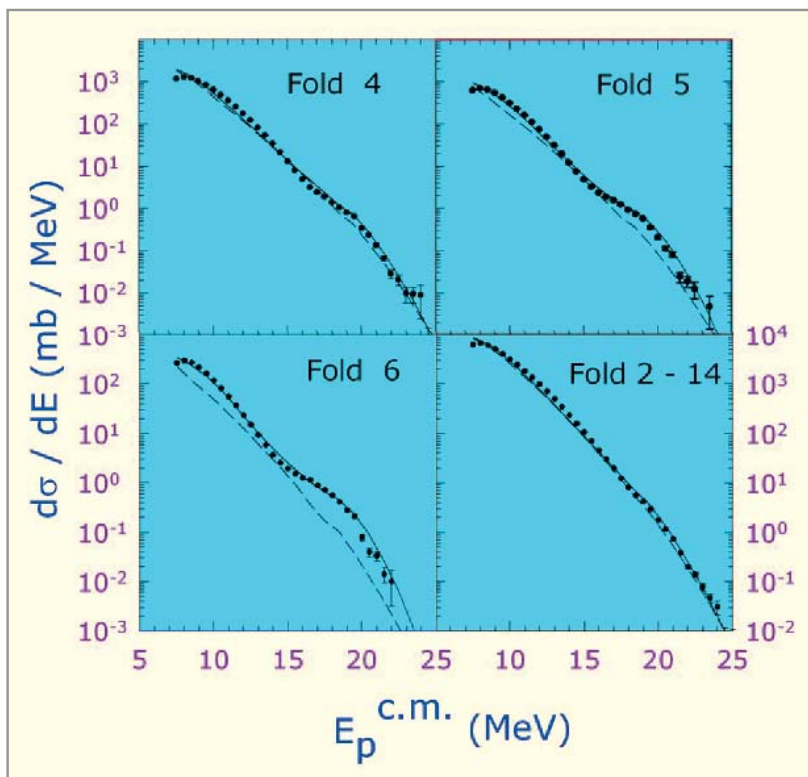


The sum of energies of alphas and the gamma. The decay scheme of  ${}^8\text{Be}$  is also shown in the figure.

V.M. Datar, Suresh Kumar, D. R. Chakrabarty, V. Nanal, E. T. Mirgule, A. Mitra and H.H. Oza Phys. Rev. Lett. **94**, 122502 (2005).

### 13.7 ENIGMA IN ANGULAR MOMENTUM GATED PARTICLE SPECTRUM IN $^{12}\text{C} + ^{93}\text{Nb}$ REACTION

The measurement of multiplicity gated proton evaporation spectra in  $^{12}\text{C} + ^{93}\text{Nb}$  reaction at  $E_{\text{beam}} = 42.5$  MeV exhibited 'bumps' at the higher energy part of the spectrum which could



Fold gated proton spectra and the calculations (see text)

not be explained by the conventional statistical model (CASCADE). A more exclusive measurement at  $E_{\text{beam}} = 40$  MeV was performed with eight INGA (Indian National Gamma Array) clover detectors to tag the fold gated protons from the same reaction in coincidence with particular evaporation residue gamma rays. NaI(Tl) detectors were used to measure proton spectra at backward angles. The gamma multiplicity was measured with a 14-BGO detector array. CASCADE calculations performed with parameterization of enhanced NLD, explained singles (multiplicity gated only) data reasonably well, whereas the conventional NLD prescription failed to reproduce the bumps. This is elaborated in

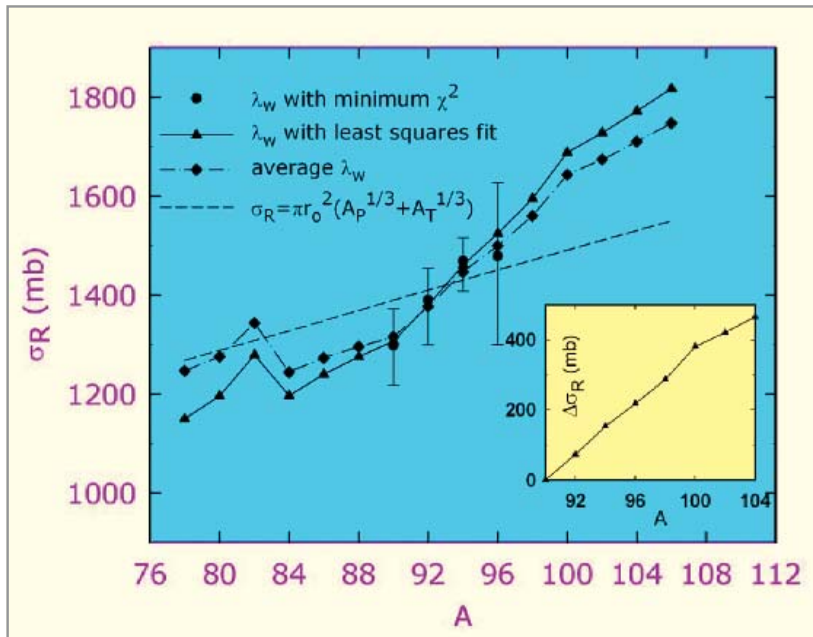
Figure. The other explanation considering a non-statistical process of massive cluster transfer of  $^{11}\text{B}$  from the projectile to the target populating exotic cluster states in  $^{104}\text{Pd}$ , in a certain window of  $E_x$  and  $J$  also reproduced the same effects.

We have also performed measurements in the same system to measure the multiplicity gated alpha spectra at three different beam energies of 37.5, 40 and 45 MeV respectively. The data show the presence of the bump in the multiplicity gated (Fold >3) alpha spectrum also with more prominence compared to that in the proton spectra. Although this may suggest that this could be an exotic cluster transfer, the detailed calculation for proton spectra requires the transfer to occur at relatively large nuclear separation. Thus, both the explanations appear quite unconventional and the observations remain enigmatic.

A. Mitra, D. R. Chakrabarty, V. M. Datar, Suresh Kumar, E. T. Mirgule, V. Nanal, R. G. Pillay, Nucl. Phys. A (under publication).

### 13.8 ANOMALY IN THE NUCLEAR CHARGE RADII OF Zr ISOTOPES

The recent laser spectroscopic measurements of nuclear root-mean-square (rms) charge radii on a chain of Zr isotopes exhibit a rich structure. A prominent kink is observed at  $^{90}\text{Zr}$  and a sharp change is noticed between  $^{98}\text{Zr}$  and  $^{100}\text{Zr}$ , in the neutron rich region. In the present work, the ground state properties of these nuclei are calculated in the Relativistic Mean Field (RMF) framework. The RMF densities are folded with the extended Jeukenne, Lejeune, and Mahaux energy and density-dependent



$\sigma_R$  obtained from analyses of elastic scattering from the chain of even Zr isotopes. The dots with error bars correspond to normalization for the imaginary folded optical model potential ( $\lambda_W$ ) values with minimum  $\chi^2$ . The solid and the dot-dashed lines correspond to the values of  $\lambda_W$  with least squares fit ( $A$  dependent) and average ( $\lambda_W = 1.13$ ) values. The dashed line represents the variation of the geometric  $\sigma_R$  with  $A$ . The inset shows  $\Delta\sigma_R^{A,90}$ , the difference in  $\sigma_R$  for the chain of even Zr isotopes relative to  $^{90}\text{Zr}$ .

nucleon-nucleon interaction to yield the semi-microscopic optical potential which in turn is used to calculate the elastic scattering cross sections for 50 MeV proton scattering from a chain of Zr isotopes.

A definite correlation is observed between the rms charge radii and the corresponding reaction cross sections for  $A=88$ . The Fig. reveals the following interesting results. The calculation shows a kink in the reaction cross-section ( $\sigma_R$ ) at  $A=82$ . It is interesting to note that while  $\sigma_R$  values are significantly larger than the geometrical predictions for neutron rich Zr isotopes, they are suppressed for the neutron deficient Zr isotopes for  $A$  up to 84. From the inset, the jump in  $\Delta\sigma_R^{A,90}$  from  $A=98$  to  $A=100$  is evident which is in tune with the corresponding sudden jump observed in the rms charge radii. We have also predicted

a larger reaction cross section for  $^{82}\text{Zr}$  when compared to the values for  $^{80}\text{Zr}$  and  $^{84}\text{Zr}$ . Experimental verification of the prediction of cross sections for the neutron rich and proton rich Zr isotopes, with the existing Radioactive Ion Beam (RIB) facilities, would be interesting. The analysing power ( $A_V(\hat{e})$ ) calculations for  $p$ -Zr systems ( $E_p = 50$  MeV) have been carried out starting with the real and the imaginary parts of the central potential, using the RMF densities for  $p$  and  $n$  ( $\rho_p$  and  $\rho_n$ ), and the Scheerbaum - Bauge prescription for the spin-orbit part of the interaction.

M. Hemalatha, A. Bhagwat, A. Shrivastava, S. Kailas, and Y. K. Gambhir Phys. Rev. C 70, 044320 (2004); Proceedings of the DAE-BRNS Nuclear Physics Symposium, Mumbai B 47, 334 (2004).

### 13.9 ENSTAR DETECTOR IN THE SEARCH FOR A NEW STATE OF NUCLEAR MATTER

BARC has built a detector ENSTAR (Fig.) to be used at the COSY accelerator, Germany in search of a new and exotic species of nuclei where an eta particle is bound inside a nucleus. The discovery of pionic and kaonic atoms and hyper-nuclei has enriched our understanding of how particles interact with each other. The possibility of the eta particle, which itself is an elusive and difficult to produce entity, to bind itself inside a nucleus has been envisaged by theoreticians but experimental observation of this state, if it exists, has eluded physicists up to now. Using proton beams in the GeV range at COSY, it is possible to devise reactions where the elusive eta particles could be produced. By choosing a reaction and beam energy such that the eta is produced essentially at rest inside the nuclear medium the right conditions can be produced whereby the eta binds itself to a nucleus. The observation of this bound state is extremely challenging.



A new detector, ENSTAR which has been constructed at BARC and assembled at Juelich for this purpose. This detector consists of 122 scintillator elements each with wavelength shifting optical fibers connected to photo-multiplier tubes. The construction, installation, offline and in-beam testing of the detector was completed in 2004.

V. C. Sahni <vcsahni@barc.gov.in>

### 13.10 RELATIVISTIC HEAVY ION COLLISIONS

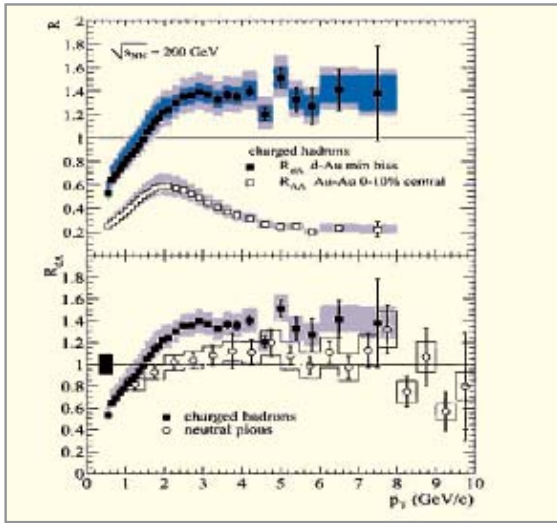
The High Energy group of Nuclear Physics Division is participating both in the PHENIX experiment at BNL Relativistic Heavy Ion Collider (RHIC) and CMS experiment at CERN Large Hadron Collider (LHC). These experiments at RHIC and LHC are designed to create new forms of matter consisting of quarks, anti-quarks and gluons. Under the PHENIX program, BARC has contributed to the fabrication of the Muon Cathode Strip Chambers which are being used at BNL. The striking discoveries at RHIC of strong collective flow, light quark and gluon jet quenching together with the decisive no suppression

control data of d+Au provide strong evidence that a Strongly coupled Quark Gluon Plasma (SQGP) is created in central Au+Au collision at energy 200A GeV. The Fig. (a) shows PHENIX data on the nuclear modification factor  $R_{pA}$  for charged hadrons in d+Au as compared to Au+Au collisions. The bottom panel shows the comparison of  $R_{pA}$  for charged hadrons and neutral pions. The data indicates that the suppression in central Au+Au collisions is not an initial state effects but due to the final state effects of the produced dense medium. The data of the STAR experiments as shown in Fig. (b) also draws similar conclusion.

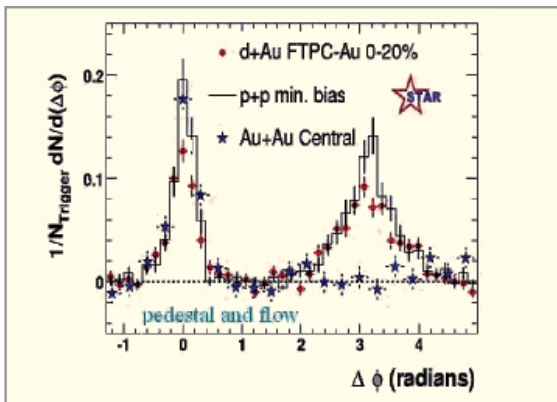
On the theoretical front, the hard photon production from bremsstrahlung and annihilation with scattering that arise at two loop level has been estimated for a chemically non-equilibrated quark-gluon plasma in the framework of Hard Thermal Loop (HTL) effective field theory. The rate of photon production is found to be suppressed due to unsaturated phase space compared to equilibrated plasma. It is also found that the photon production is dominated by bremsstrahlung mechanism, since the phase space

### 13.11 DEVELOPMENT AND UTILIZATION OF ION ACCELERATORS

Accelerators primarily developed for basic research in nuclear and particle physics are now widely used for a variety of studies. Utilising protons and the heavy ion beams from the 14 MV Pelletron and the 6 MV FOTIA facilities, a number of multidisciplinary research programmes have been initiated. Preparation of track etch membranes using heavy ions, high current proton irradiation facility, radiation biology studies using protons in air and radiation damage initiated by protons and accelerator-based mass spectrometry are some of the programmes which are being pursued. Stainless Steels (SS) components exposed to neutron irradiation environment e.g. the core of Light Water

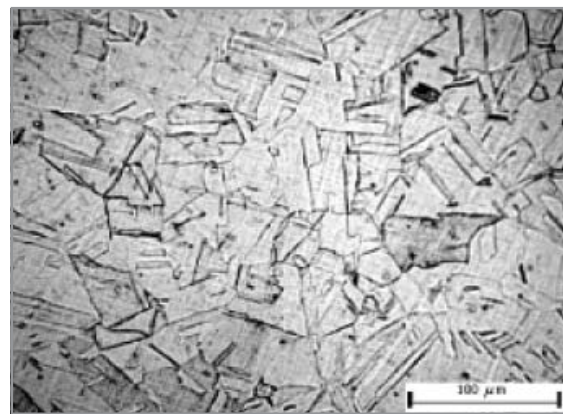


(a) Phenix experiment

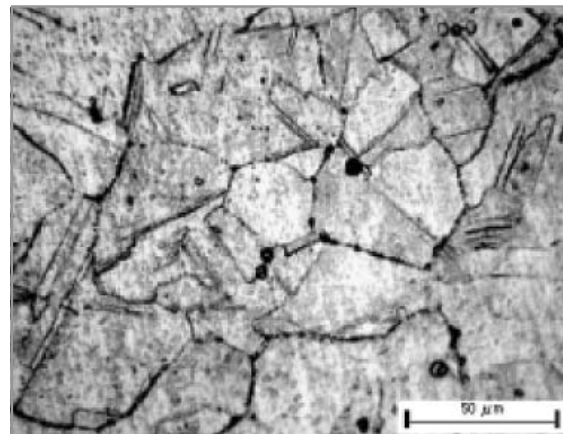


(b) STAR experiment

suppression is higher for annihilation with scattering, in contrast to the equilibrated plasma where annihilation with scattering dominates the photon production. The rate of dynamical growth of the hadron bubbles in a supercooled baryon free Quark Gluon Plasma is evaluated by solving the equations of relativistic fluid dynamics in all regions. For non-viscous plasma, this dynamical growth rate is found to depend only on the range of correlation of order parameter fluctuations and the radius of the critical hadron bubble, the two length scales relevant for the description of the critical phenomena.



As received SS 304.



Irradiated SS 304:  $4.2 \times 10^{16}$  protons/cm<sup>2</sup> (0.2 dpa)

V. C. Sahni <vcsahni@barc.gov.in>

Reactors (LWRs) are susceptible to radiation damage like Radiation-Induced Segregation (RIS). Neutron irradiation results in generation of point defects far in excess of their equilibrium concentration at operating temperature range, i.e., 280–300°C. Diffusion of point defects at grain boundaries and is a major factor contributing to Irradiation Assisted Stress Corrosion Cracking (IASCC). In order to make SS core components more resistant to IASCC, it is essential to study the RIS behavior. Proton irradiation is used to simulate the RIS behavior in SS and it is known to induce the irradiation damage in SS qualitatively similar to that produced by neutron irradiation in a very short span of time. Unlike neutron irradiation, proton irradiation induces less residual radioactivity in the material. RIS behavior in austenitic SS Type 304 at elevated temperature (~ 500°C) was studied using proton irradiation in FOTIA facility. RIS developed during proton irradiation was characterized by an electrochemical technique (Figures).

The Pelletron accelerator has been the workhorse for the nuclear physics programmes of BARC (see studies in nuclear physics section). It has been operational for the last 15 years delivering a variety of beams, at various energies and with high uptime. A superconducting LINAC has been indigenously developed to boost the energy of heavy ions emerging from the Pelletron. The Phase-I of this project having three modules consisting of twelve resonators has been made operational.

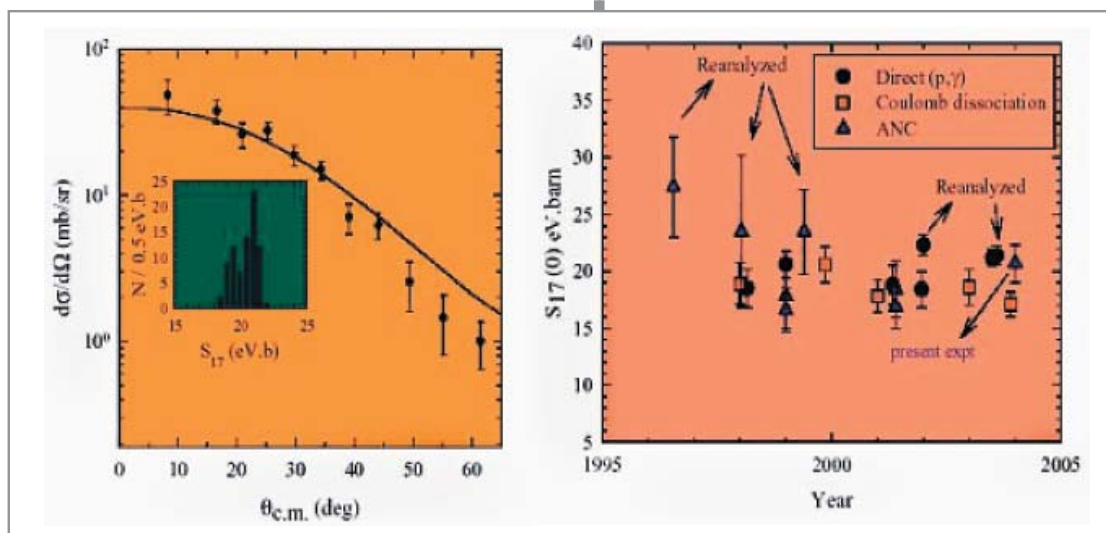
BARC report on "FOTIA", 2003; Report on "BARC-TIFR heavy ion facility", 2004; <http://www.tifr.res.in/~pell>

Ahmedabadi, Vivekanand Kain, S.K. Gupta and P.K. De, Proc. National Symposium on Electrochemical Science and Technology, NSEST-2004 Bangalore, p 10.

### 13.12 ASTROPHYSICAL $S_{17}(0)$ FROM ${}^2\text{H}({}^7\text{Be}, {}^8\text{B})\text{N}$ REACTION AT $E_{c.m.} = 4.5$ MeV

Angular distribution measurements of  ${}^2\text{H}({}^7\text{Be}, {}^8\text{B})\text{N}$  and  ${}^2\text{H}({}^7\text{Be}, {}^8\text{B})\text{n}$  reactions at  $E_{c.m.} = 4.5$  MeV were performed to extract the astrophysical  $S_{17}(0)$  factor, corresponding to the  ${}^7\text{Be}(p, \gamma)$  capture reaction, using the asymptotic normalization coefficient (ANC) method. For this purpose a pure, low emittance  ${}^7\text{Be}$  beam was separated from the primary  ${}^7\text{Li}$  beam by the recoil mass spectrometer (at Nuclear Science Centre, Delhi) operated in a novel mode. A beam

- (a) Measured  ${}^2\text{H}({}^7\text{Be}, {}^8\text{B})\text{n}$  angular distribution together with the folded finite range DWBA + compound nuclear cross sections shown as solid line. The calculated compound nuclear contributions are shown by the dotted line. The inset shows a histogram plot of the extracted  $S_{17}(0)$  using 4,5 and 4 combinations of  ${}^2\text{H}-{}^7\text{Be}$ ,  $\text{n}-{}^8\text{B}$  potentials OMP and  $p-{}^7\text{Be}$  bound state potentials, respectively.
- (b) A comparison of the direct and indirect  $S_{17}(0)$  measurements reported after 1990 for radiative proton capture, Coulomb dissociation and for ANC measurements. The values inferred from more detailed analyses are also shown in this figure marked as reanalyzed.



stopper at  $0^\circ$  allowed the use of higher  $^7\text{Be}$  beam intensity. Measurement of the elastic scattering in the entrance channel using kinematical coincidence facilitated the determination of the optical model parameters needed for the analysis of the transfer data. The transfer data was analyzed using a finite range DWBA code DWUCK5. Eighty combinations of d- and n-OMP and p-bound state potentials were used in the transfer data analysis to get an estimate of the systematic error in the extracted  $S_{17}(0)$ .

The present measurements significantly reduces errors in the extracted  $^7\text{Be}(p,\gamma)$  cross section using the ANC method and resulted in  $S_{17}(0) = 20.7 \pm 1.0(\text{sys}) \pm 1.4(\text{stat})$  eV.b. This demonstrates the capability of the ANC method in determining the S-factor of reactions involving short lived nuclei with a precision similar to that of the  $(p,\gamma)$  measurements.

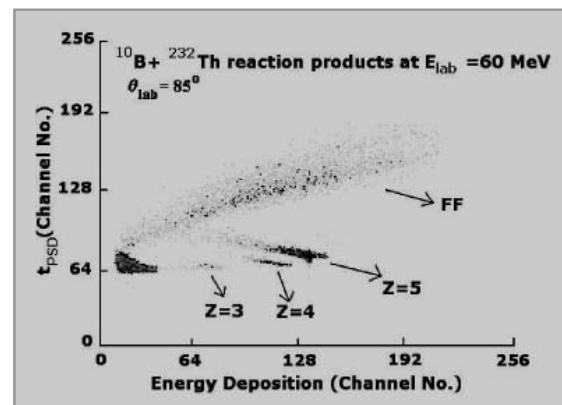
J.J. Das, V.M. Datar, P. Sugathan, N. Madhavan, P.V. Madhusudhana Rao, A. Jhingan, A. Navin, S.K. Dhiman, S. Barua, S. Nath, T. Varughese, A.K. Sinha, R. Singh, A.Ray, D.L. Sastry, R.G. Kulkarni and R. Shyam, Nucl. Phys. A746, 561c (2004).

### 13.13 APPLICATION OF PULSE SHAPE DISCRIMINATION IN Si DETECTOR FOR FISSION FRAGMENT ANGULAR DISTRIBUTION MEASUREMENTS

In case of heavy ion induced fission studies using solid state surface barrier detectors, it is often a problem to identify fission fragments in the presence of large elastic scattering background, if the energy loss of elastically scattered particles in the detector overlaps with the fission fragment energy spectrum. Recently, it has been demonstrated by many researchers that the sensitivity of the pulse shape to density and length of the ionization track is enhanced if the rear contact (reverse mount) of a totally depleted Si-detector is exposed to charged particle irradiation. Since there is a large difference in the length and density of ionization in the silicon detector for fission fragments and elastic products of similar energy, due to the difference in energy loss mechanism, this property can be exploited to identify fission fragments in the presence of large elastic scattering background. With above motivation,

we have investigated the feasibility of Pulse Shape Discrimination (PSD) for identification of fission fragments and projectile like products in heavy ion induced fission reactions.

Simulations are carried out to calculate the pulse shapes of the charge collection in surface barrier detectors for rear-side injection of fission fragments and projectile like particles produced in heavy ion induced fission reactions. It is seen that the pulse shape discrimination method can be used to separate the fission fragments and projectile like particles in heavy ion induced reactions. The experimental result on zero-crossing time versus energy deposition in the detector demonstrates the usefulness of the pulse shape discrimination method using a single surface barrier detector to discriminate fission fragments and heavy ions quite effectively when the detector is used in reverse mount as shown in figure. It is suggested that PSD technique can be



Typical zero-crossing time (PSD) versus energy deposition plot for  $^{10}\text{B} + ^{232}\text{Th}$  reaction at  $\theta_{\text{lab}} = 85^\circ$  and  $E_{\text{lab}} = 60$  MeV.

used to measure the cross sections and angular distributions of fission fragments for cases where the presence of large background of elastic events, introduces sizeable uncertainties in the measurement of cross sections and angular distribution of fission fragments.

B.K. Nayak, E. T. Mirgule and R. K. Choudhury, J. Phys. Pramana (under publication).

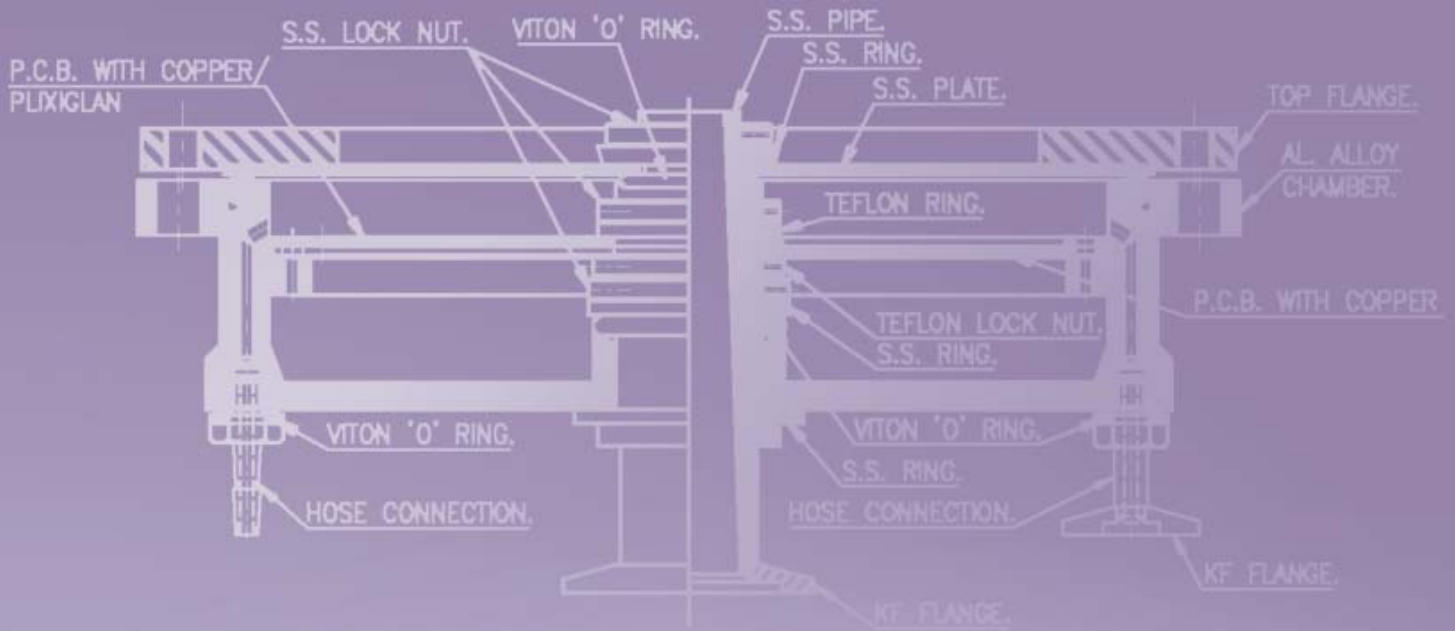


Fig-11 ANNULAR PARALLEL PLATE AVALANCH  
COUNTER

## 14. DESIGN AND FABRICATION OF MECHANICAL ASSEMBLIES

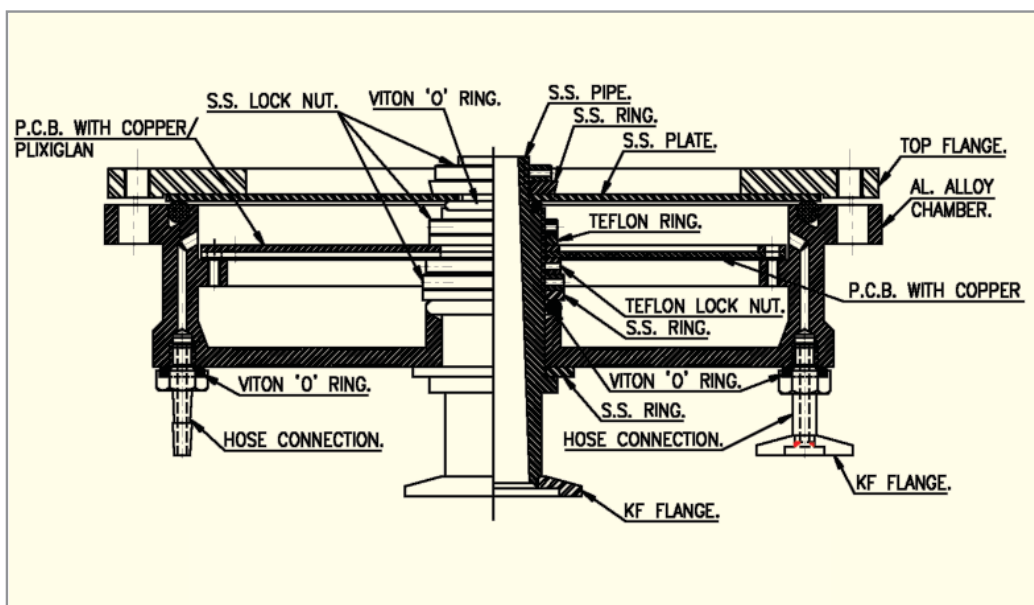
### INTRODUCTION

BARC is involved in the development of several high-tech instruments for in-house deployment as well as for extending the facilities to other users. One of the key requirements for building these facilities has been designing and precision machining of a range of components that includes large-size UHV chambers on side to fine tungsten filament holders for mass spectrometers on the other side. Present chapter describes some the systems fabricated for specialized applications, that include mass spectrometers, nuclear radiation counters and spectrometers.

### 14.1 ANNULAR PARALLEL PLATE AVALANCHE COUNTER

A gas detector of annular shape to provide fast timing pulse i.e., Parallel Plate Avalanche Counter (PPAC) is being developed for detecting the fusion residues in the nuclear reac-

mass and energy. In our investigations of light particle evaporation spectra and high energy gamma ray spectra, to have more exclusive measurements a need for residue tagging in coincidence is required. To meet this requirement an annular PPAC has been designed. The annular chamber for this has been fabricated out of a



Annular parallel plate avalanche counter (PPAC) assembly

tions induced by heavy ion. The body of detector was fabricated in the NPD workshop. To minimize the weight of 240 mm diameter detector, it was fabricated from a block of aluminum alloy of satellite application. To install it at zero degree i.e., in the beam line, a novel variable length KF40 to 6 inch NEC adopter was designed and got fabricated in the workshop. The variable length will enable the installation and removal of the detector without disturbing the rest of experimental setup and the beam line.

The fusion residues with approximately projectile momentum travel in forward direction. The maximum angle of deviation of the residue from projectile depends on the ejectile

special aluminum alloy block, by the workshop. The PPAC angular acceptance is from  $5^\circ$  to  $18^\circ$  at a flight path of 25 cm. The central hole (dia 2 cm) for beam exit at this distance corresponds to  $\pm 2^\circ$ . The parallel electrode to provide high electric field for detector operation consists of copper plate and aluminized mylar stretched foiled supported on a PCB frame, both having annular shape. The gap between the two electrode is to be tried out from 1.5 to 3 mm. An annular mylar foil window of thickness  $\sim 2$  micron will be used. The detector will be operated at about 50 Torr pressure of P10 gas and about 500 Volt across the parallel electrode (plate).

## 14.2 ALPHA SPECTROMETER

It is a device designed and evaluated for carrying out the measurements of plutonium concentration in the irradiated fuel produced by atomic reactors and  $^{238}\text{Pu}$  content and isotope correlation to calculate the specific activity and isotope composition. So the fuel, which is produced in the reactors and its different constituents and concentration are measured.

The device has to work in a pressure range of  $1 \times 10^{-3}$  torr. The sample loading accuracy required with respect to the detector is  $\pm 0.1$  mm. The minimum and maximum distance required between the sample and detector is 10 and 130 mm respectively, which increases in steps of 10 mm.

The chamber is designed to minimize the pump down time taking the above consideration of distance between the detector and sample. This feature enables the user to save the idle time, as the samples need to be changed frequently.

The opening and locking of the chamber door against the flange and loading the sample and placing it at the desired distance is very simple.

The chamber, which is at the heart of the assembly, is fabricated using an SS sheet of 1.5 mm thick, by bending and welding. Two welding joints are at the corners with back cover of SS sheet closing the chamber is welded to the four sides. To the front side of the chamber an SS flange having 'O' ring groove is welded. The inside dimension of the chamber are (79x75x148) mm. The overall size of the assembly is (100x145x300) mm.

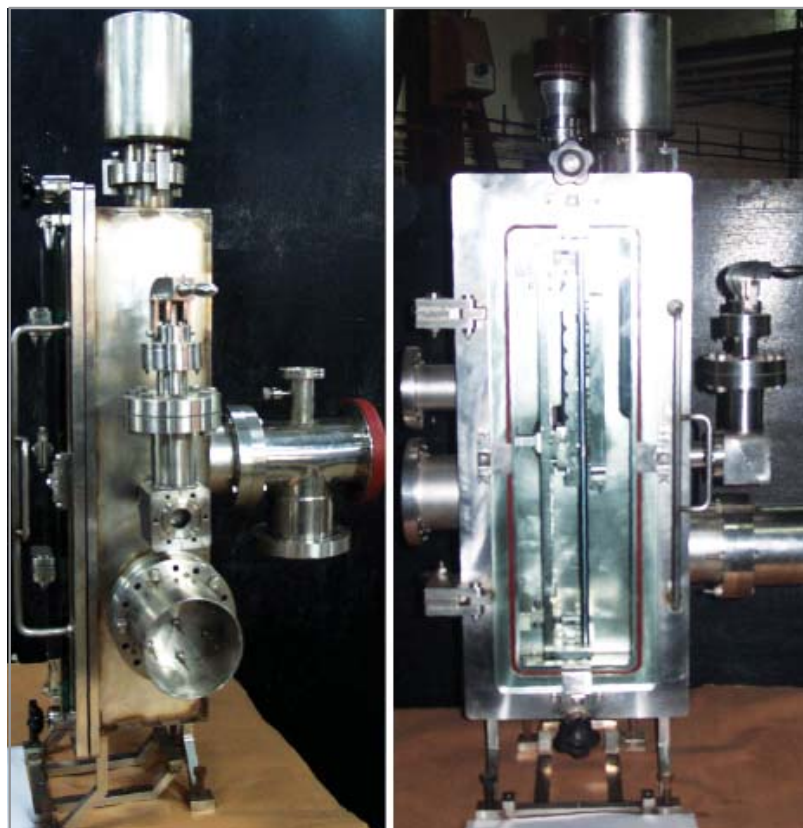
**Working** :-The sample to be evaluated is deposited on SS-304 thin disc called Planchet of 25 mm dia and is placed inside

the chamber. The SSB detector counts the alpha particles emitted by the sample and the output is measured by the computer connected to the microdot connector which gives the percentage of different elements, in the form of graph and data.

The evaluation was done by Fuel Reprocessing Division by comparing the results with another imported device.

## 14.3 ON LINE LINEAR SAMPLE CHANGER FOR (TIMS) MASS-SPECTROMETER

**Linear Sample Changer** - A new concept of computer interfaced filament changeover is introduced in place of existing turret mechanisms used in TIMS mass spectrometers. This mechanism will replace turret mechanisms currently operational in TIMS machines. The prototype developed incorporates in house intricate mechanisms conceptualized and successfully engineered at



MDPDS and validated for accurate and easy operational competence. The mechanism is in TPPED for online performance testing on PGMS-4. This setup is further supposed to be retrofitted in place of present rotary turret chambers on TIMS machines at Tarapur and Kalpakkam.

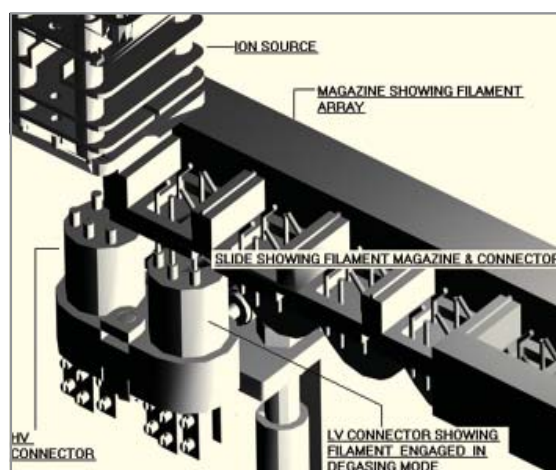
Owing to serious functional errors noted in the Turret type filament changer due to inadequate filament and source slit alignments it was decided to change the turret concept to a linear one. In this newer version the filament slit changeover is oriented lengthwise, therefore, the alignment problems are adequately eliminated. Filament contacts are designed to achieve firm and positive contacts. A degassing mode is also incorporated.

### SALIENT FEATURES

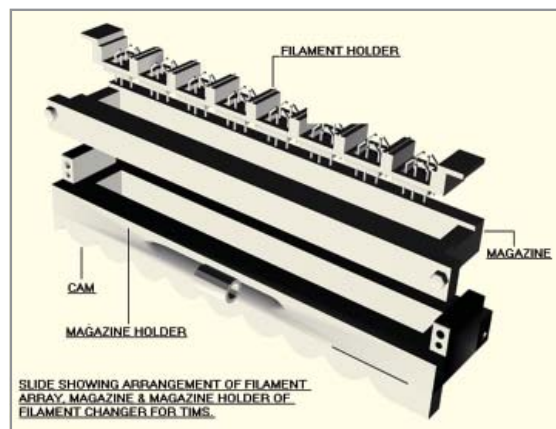
- 1) Linear sample changer is provided with a filament degassing facility, which can be put to use if required.
- 2) Filament to beam valve flange, height of source flange to table top and pumping port configurations are unchanged hence it's a retrofitting setup and no changes are required to be made in the present machine setup.
- 3) An array of eight filaments is loaded in a single magazine, which can be easily assembled and dismantled with the help of two wing nuts. A prepared spare magazine can be immediately put into use for continued further operations.
- 4) Source and shield slits are permanently aligned with theodolite within 15 microns and doweled. Individual spring loading is provided to each filament lead and assembly is tested for firm and positive electrical continuity.
- 5) Contact resistance measured is 10 milli Ohms, and it is within the acceptable limits.
- 6) Filament changeover is oriented lengthwise and through a precisely machined cam and roller mechanism coupled with a computer interfaced

stepper motor drive. It is set to achieve the best slit alignment within the operational requirements.

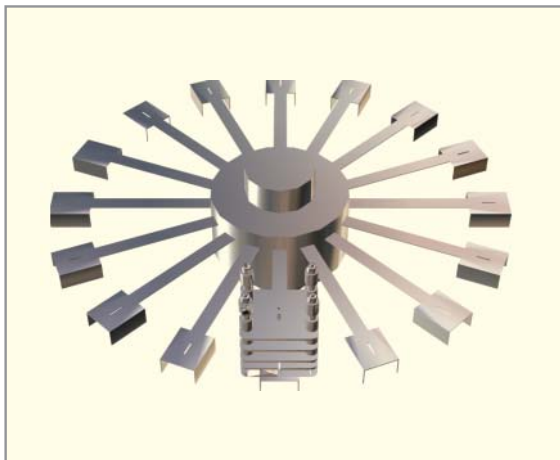
- 7) Filament slider is electrically insulated from the main body and tested at 10 kV.
- 8) Full length viewing window provides easy and convenient maneuvers of filament array in manual changeovers.
- 9) A simple nut and bolt type door lock provides effective and simplest way of door maneuver.



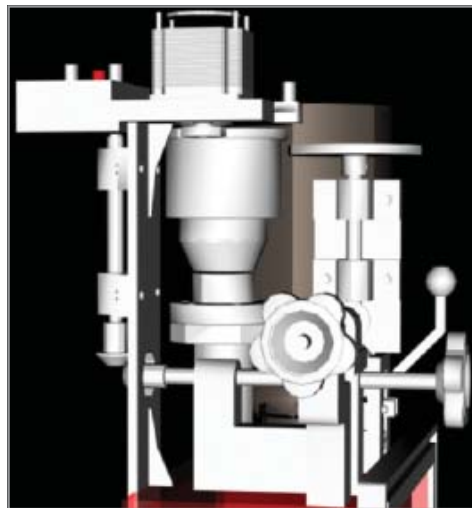
Filament in degassing mode



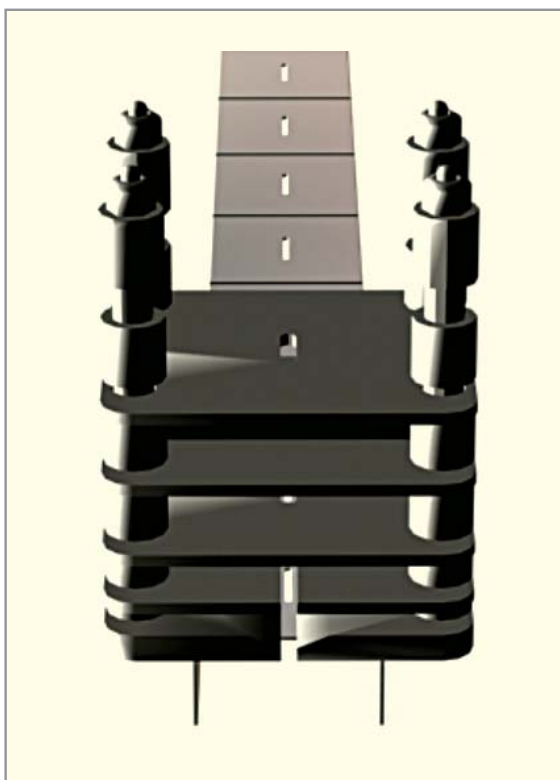
Components of filament array and magazine



Turret array



Gearbox



Linear array

Fig. Shows the turret concept in which filament slits are orientated widthwise. Hence rotation of the turret multiplies the magnitude of slit misalignment since both slits are positioned axially inclined to each other in a plan. This leads to serious errors in overall machine sensitivity and performance. Fig. shows the new concept where the alignment is made lengthwise and the filament array is moved in a straight line against ion source eliminating the alignment problems well within acceptable limits.

Filament changeover is accomplished through a rotary feed connected to a lead screw driven by a stepper motor and computer interface. Fig. shows the gearbox developed and deployed to rotate the feed through. A manual mode is also provided which disengages stepper motor from the feed through to facilitate manual work environment.